Investigation of the Effects of Soot on the Wear of Automotive Engine Components

PhD Thesis

Lawal Babatunde **Abdulqadir**

A thesis submitted in partial fulfilment of the requirements for the degree of Doctor of Philosophy

November 2017

Supervisors: Prof. Roger Lewis and Dr. Tom Slatter

Department of Mechanical Engineering

The Leonardo Centre of Tribology

University of Sheffield

Acknowledgement

First and foremost, I wish to acknowledge my greatest indebtedness to Allah (SWT) for abundantly blessing me right from the origination of my creation till now and for consistently keeping me secure from excess and lack. Thy blessings and favours on me are too numerous to count. I would continue to praise Thee everlastingly and remain grateful forever!

I must express my obligation and thanks to my supervisory team; Prof. Roger Lewis, my first supervisor, was highly supportive and his deep interest in my work which he always displayed by going through any of my submissions meticulously with constructive feedbacks were sources of encouragement for me. Dr. Tom Slatter, my second supervisor, was equally supportive and always readily available to offer useful and timely suggestions as at when required. My experience in working with both of them has been very inspiring and immensely rewarding.

I also appreciate Dave Butcher and Luke Callaghan, both members of the technical team of the Leonardo Centre for Tribology, who readily offered their expertise whenever required. I must also mention Leslie Morton whose period of replacing the timing chain of his lovely Benz car was so timely that I could use the old chain as part of my research work.

I must express my heartfelt gratitude to the Management of Kwara State Polytechnic, Ilorin and Nigerian Tertiary Education Trust Fund (TETFund) for jointly sponsoring me for this programme, which has positively impacted me, professionally and intellectually.

My profound gratitude also goes to the late Amir of Al-Harakatul Islamiyyah, Dr. Muhammad Ali Olukade, who ceaselessly encouraged me to pursue a PhD, even, when on his death bed. May Allah (SWT) continue to shower His Mercy on him. Aameen!

I must also appreciate, most sincerely, the support, encouragement, advice and prayers accorded to me by my friends who are too numerous to mention; you are all appreciated.

Finally and most importantly, my sincere appreciation and gratitude go to my loving wives who kept the home-front stable in my absence, Hajiya Rodiyat Titilayo Lawal and Mallama Hamdalat Funmilayo Lawal (my treasures and jewels of inestimable values), my darling children (the comfort of my eyes-Qurrata a'yuni) and the entire members of my family (immediate and extended) for their sacrifice, encouragement, prayers and unflinching moral and emotional supports which they have all been rendering over the years.

Summary

This study is motivated by the current trends in the automotive industry where an increasing level of soot is becoming a challenge to the internal combustion engine (ICE) components. Factors responsible for increasing soot level can be grouped into those explicitly driven by regulations and those driven by technological developments; as well as the requirements of extended drain intervals which lessen the overall maintenance cost of running a vehicle and reduce the environmental impacts of disposed oils.

The research work basically involves a multi-pronged approach to evaluate the behaviour of sooty-oil surrogates (blends of fully formulated engine oil, HX5 SAE15W-40, and carbon black particles) under various conditions, using laboratory specimens and real engine components. Laboratory specimens are appropriate for evaluating systemic changes in various parameters; they, however, tend to be more homogeneous and have smoother surfaces than real specimens [1]. Real component testing affords more realistic surface contacts and contact geometries; and therefore loading conditions.

Increasing soot-loading affects virtually every component involved in the combustion process; the most vulnerable are, however, the valve-train components. Consequently, the focus of the research was on the components within the engine's valve-train related specifically to diesel engine.

Based on the specific component simulations that were proposed, two standard commercial tribometers were used; namely, the High Frequency Reciprocating Rig (HFRR-Plint TE77) and the Mini Traction Machine (MTM-Plint TE54). Two others were designed and built as part of this research; these are: a Pin-in-Bush (PIB) Rig and a Chain Rig.

The generic tests involving the basic geometric contacts, non-conformal point (ball-on-flat) and non-conformal line (ring-on-ring), were designed to mimic specific contact conditions in an internal combustion engine (ICE). The elephant's foot/valve tip contact of the automotive engine valve train is perfectly simulated by the ball-on-flat test with a small stroke length; while ring-on-ring test undergoing sliding and rolling concurrently perfectly mimics the valvetrain's cam lobe/roller follower contact geometry.

The pin-in-bush conformal contact reciprocating sliding rig was designed to have conformal interacting surfaces which provides area contact for the pin and bush moving with sliding action on the lubricant film at the interface. The rig was also adapted, with minimum modifications, for the chain rig which was used for the real engine component test; specifically, Mercedes Benz M271 timing chain and sprocket. The results obtained from the chain were compared with a similar component that has undergone about 206,000 kilometres in a real engine.

The results obtained in this study are comparable with other reported studies using carbon black to mimic engine soot. Although loads of data were generated in the course of various tests and post-test analysis, space limitation would not allow all of these to be presented. For the quantitative (friction coefficients, viscosity, wear volume and roughness profile) results, averages of the measured values were determined and used to present the results in various formats. However, only few of the qualitative analysis (microscopy, SEM, ContourGT and Alicona) results were presented in this thesis.

Generally, the behavioural pattern of increasing volume of wear, viscosity, frictional force and coefficient of friction with increasing carbon black content remain essentially consistent with all the tests carried out under this study. However, the surface roughness revealed a somewhat smoother surface profile for moderate carbon black content (3-5wt%CB), especially

at moderate normal load. Also, traction coefficient values decreased progressively and consistently with increasing carbon black content for mixed lubrication tests.

Wear analysis revealed that the carbon black contamination effects in the contact are substantial at high concentration levels, high temperature and high normal loads as wear scar volume increased with these parameters. Evolution of the wear test further reveals that the progression of wear is a function of time. The severity of wear is more pronounced in the ball-on-flat tests operating under boundary lubrication as compared to the ring-on-ring (mixed lubrication) tests. Though, both contacts are non-conformal, but the load distribution was over a wider surface area with a line contact as against what happens with point contact, where a small area of contact carries the full load.

Observed wear mechanisms can be interpreted as mild three-body abrasive wear at moderate carbon black contents (3-5wt%CB) where the well-dispersed carbon black particles freely roll and slide between the contacting specimens. While at higher carbon contents (7-12wt%CB) where agglomeration is more likely, the resultant wear mechanism is metal-to-metal contact due to starvation of lubricant which access into the contact is restricted by the carbon particle agglomerates, and thus resulting in two-body abrasion. Another possible mechanism at higher content is that some of these hard particles get into the contact zone where they become squeezed and get embedded into the surfaces. The embedded hard particles burrow through the contacting surfaces, forming grooves along the sliding direction. This is also classified as two-body abrasion.

For the mini-traction machine (MTM) test, there was also cyclic stress-induced surface fatigue due to the combined effects of high contact pressure resulting from Hertzian line contact and high load and occurrence of fatigue-induced incipient damage in the subsurface, along the plane of maximum shear stress.

The real engine component tests revealed multiple effects on the contacting bodies. These range from sliding and rolling actions between the sprocket teeth and the chain rollers along with the carbon black particles. There was also the effects of the impact stresses induced by the collision of chain with the sprocket teeth during engagement. The emerging results from various post-test analysis have also revealed the damaging effects any particle infiltration into the contact between various moving parts of the timing chain system can cause.

The analysis of the 'L' (denoting the initial of the owner of real engine components) vehicle components also gives some valuable and instructive indications of possible damages that prolonged usage can cause to a component, particularly timing drive components which constitute parts of the most durable and lifetime components in an internal combustion engine (ICE).

The novel idea on the use of ultrasound technique to measure the instantaneous film thickness (between the contacting specimens) of selected sooty-oil surrogates also recorded a significant level of success in terms of the obtained results which are comparable with analytical results in behavioural trends and numerical values. Notably, being a pioneering move towards determining the real-time film thickness of soot-contaminated oil, this indicates a potential for future research.

Table of Contents

Nomenclature

a, b Contact area dimensions (m)

c Speed of sound (m/s)

D_U Diameter of the upper disc (m)

D_L Diameter of the lower disc (m)

E Young's modulus (MPa)

E' Reduced Young's modulus (MPa)

f Resonant frequency (Hz)

F Force (N)

G Non-dimensional material parameter

H_{min} Non-dimensional minimum film parameter

H_c Non-dimensional central film parameter

h Depth of the wear scar (m)

h_{min} Minimum film thickness (m)

h_c Central film thickness (m)

k Non-dimensional ellipticity parameter

P Nominal Load (N)

P Gauge pressure, (kg/cm^2)

p_o Maximum contact pressure (GPa)

p_{mean} Mean Average contact pressure (GPa)

N_U Rotation of the upper disc (rpm)

N_L Rotation of the lower disc (rpm)

r Radius (m)

R' Reduced radius of curvature in the direction of sliding (m)

R_q Root mean square (r.m.s) surface roughness (m)

R_a Average surface roughness (m)

T Torque (N-mm)

U Non-dimensional speed parameter

u Mean surface velocity in x direction (m/s)

W non-dimensional load parameter

w_n Width of the wear scar (m)

z Depth at which τ_{max} occurs (m)

z	Acoustic impedance of a material (Pa.s/m^3)
Z	Viscosity-pressure index (dimensionless)
α	Pressure viscosity coefficient (GPa^{-1})
η	Absolute viscosity, (cP or Pa.s)
η_o	Absolute viscosity at atmospheric pressure and constant temperature (Pa.s)
υ	Kinematic viscosity (cSt)
λ	Lambda ratio (dimensionless)
ρ	Density of the material, in kg/m^3,
μ	Coefficient of friction (dimensionless)
μ_o	Initial coefficient of friction
μ_{ss}	Steady state coefficient of friction
τ_{max}	Maximum shear stress (MPa)
υ	Poisson's ratio (dimensionless)

List of Figures

List of Tables

Chapter 1

Introduction

This chapter deals with the motivation for this research along with its main aims and objectives. The roles of European emission regulations in controlling vehicle exhaust emission are highlighted. The challenges posed by the emerging engine technology trends are also discussed as well as the proposed new lubricant formulations to confront their expected consequences.

1.1   Statement of the problem

The progressive increase in demand for automobiles in the last few decades has resulted in the rapid rise of the automotive industry; and this was consequently accompanied by advances in lubrication and transmission technology.

Automotive manufacturers are regularly attempting to extend the service intervals of internal combustion engines (ICEs) [2-8] to reduce both the long-term vehicle maintenance costs and the environmental impact of disposed oil. The clear consequence of this is that lubricating oil will become increasingly contaminated with soot, the effect of which is detrimental to the components in tribological contacts. Exhaust gas recirculation (EGR) is increasingly being used to minimize oxides of nitrogen (NOx) emissions in compliance with emission regulations, and the resulting recirculation of combustion products back into the combustion system further contaminates the oil. The implication of this is that while the EGR is effectively reducing emission of NOx, it is inadvertently increasing soot levels in the lubricating oil; a covert trade-off between NOx and soot [2, 9, 10]. Singh et al. [10] in investigating soot generation and wear of an engine suggested the use of a soot trap along with EGR as the solution to simultaneously control the level of soot and emission of NOx whilst minimising wear. Although, soot is not specifically governed by legislative requirements [11]; it can be considered to be so governed indirectly through particulate matter (PM) limitations. Consideration of this along with its debilitating effect on engine oil lubricity and the wear of engine components have made its control an important focus for automotive manufacturers.

It has been reported that less than 30% of the soot generated in the engine actually gets into the atmosphere through the exhaust pipe [12]; the remainder are retained within the engine due to blow-by gases, being deposited on the cylinder walls, exhaust ports, piston crowns. The continuous circulation of the lubricant along with the piston rings scrapping results in the significant quantity of the retained soot ending in the lubricant sump.

In terms of their properties, while there are no significant differences between their particle sizes and structure [13], the exhaust soot is more oxidized than soot extracted from the lubricant sump [13, 14]. This chemical differences which is attributable to after-effects of primary particles formation processes influence their polarity and hardness with possible impact on the resultant wear effects.

European vehicle exhaust emission legislation plays a role in the level of soot contamination of engine lubricants. European emission standards are a set of progressively increasing stringent emission regulations governing the EU member states automobiles exhaust emissions. Substances currently under these regulations

1

are: nitrogen oxides (NOx), carbon monoxide (CO), total hydrocarbons (THC), non-methane hydrocarbons (NMHC) and particulate matter (PM) [15]. Whenever the standards are set it behoves the automobile manufacturers to develop the technologies to meet the standards. Failure to do this has serious implications, in terms of financial sanctions and other punitive measures. The most recent of which is the notorious case of Volkswagen which manipulated its diesel cars, through an illegal software installation, to run emissions controls only during emissions tests [16]. The Environmental Protection Agency (EPA) revelations showed that the full emissions control system was turned off by the software during normal operating conditions of the vehicles, especially when being driven on highways and byways; thus allowing spewing of harmful pollutants at up to 40 times the legal limit. This discovery has not only tainted the company's corporate reputation, it has also incurred massive financial liabilities in terms of payment of compensations running into billions of dollars, declining stock price and thousands of job cuts.

Figure 1.1 shows the various stages of light-duty vehicle (LDV) standards including latest Euro 6 emission limits while Figure 1.2 shows more recent global version of the emission implementation schedules where Euro pathway is updated to latest standard (Euro 6). Passenger cars comprising gasoline, diesel and light commercial vehicles with gross vehicle mass (GVM) not above 3500 kg are considered as LDV [17]. Table 1.1 presents the emission standards for heavy-duty vehicles (HDV), which generally include goods vehicles and buses. It is worth pointing out that while the standards for light-duty vehicles are defined by driving distance of the vehicle (g/km), engine energy output (g/kWh) is used to define the heavy-duty vehicles.

Most emissions are attributable to heavy-duty vehicles. In the US, for instance, while heavy-duty vehicles constitute only 2% of the country's overall fleet, they account for 30% of the NOx and 50-60% of the black smoke emissions [18, 19].
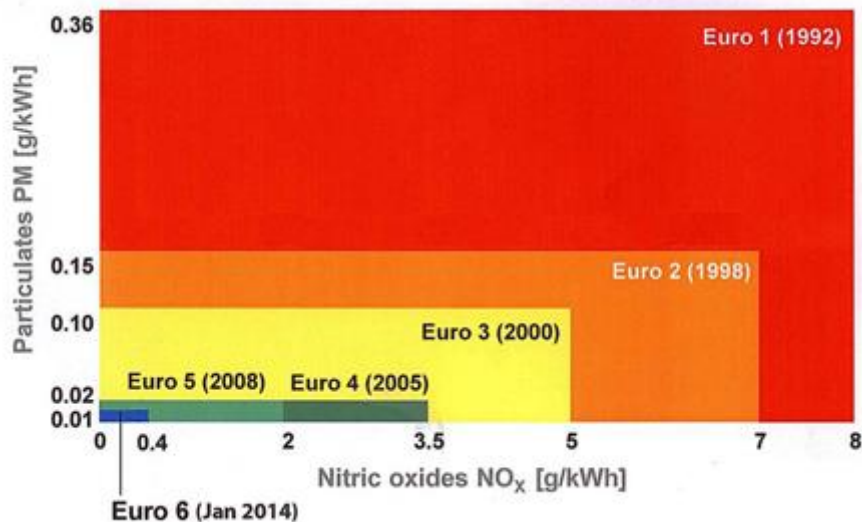
Figure 1.1: European NOx and PM emission standards for diesel vehicles [20]

	2005	2006	2007	2008	2009	2010	2011	2012	2013	2014
Brazil	PROCONVE L-3		PROCONVE L-4			PROCONVE L-5			PROCONVE L-6	
China(1)	China II		China III			China IV				
Europe	Euro 4						Euro 5			Euro 6
India(1)	Bharat II					Bharat III				
Japan	FY 2005 Emission Regulation					Post New Long Term Emission Regulation				
Mexico	Standard A (US 1994)					Standard B: Tier 2 Bin 10, 11 / Euro 4-Euro 3 (diesel)			Standard C(2)	
Russia	Euro 1	Euro 2					Euro 3		Euro 4	
S. Korea	US NLEV	CARB K-ULEV and Euro 4 (diesel)				CARB LEV-2 and Euro 5 (diesel)				
Taiwan	Euro 3			Euro 4 – Tier 2 Bin 7				Euro 5		
Thailand	Euro 2	Euro 3						Euro 4		
U.S.	US Tier 2									

(1) Major cities have introduced accelerated adoption schedules – timelines in this table reflect nationwide adoption
(2) Implementation schedule dependent on the availability of low sulphur fuel nationwide

Figure 1.2: Global implementation schedule for emission regulations in light-duty vehicles [17]

Expectedly, the inclusion of emission control system adds to the cost of vehicle production; and this accounts for the reluctance in the implementation of the emissions regulations. Sanchez et al. [17] worked out some incremental costs estimates for meeting each level of the emission standards for light-duty vehicles. The estimates, representing the cost of technology for different engine size to meet each regulatory level, are presented in Tables 1.2 and 1.3 for Europe and United States respectively.

Table 1.1: European emission standards for HD diesel engines, g/kWh [21]

Tier	Date	Test cycle	CO	HC	NOx	PM	Smoke
Euro I	1992, < 85 kW	ECE R-49	4.5	1.1	8.0	0.612	
	1992, > 85 kW		4.5	1.1	8.0	0.36	
Euro II	October 1996		4.0	1.1	7.0	0.25	
	October 1998		4.0	1.1	7.0	0.15	
Euro III	*October 1999 EEVs only*	*ESC & ELR*	*1.0*	*0.25*	*2.0*	*0.02*	*0.15*
	October 2000		2.1	0.66	5.0	0.10 0.13*	0.8
Euro IV	October 2005	ESC & ELR	1.5	0.46	3.5	0.02	0.5
Euro V	October 2008		1.5	0.46	2.0	0.02	0.5
Euro VI	31 December 2013		1.5	0.13	0.4	0.01	

* for engines of less than 0.75 dm³ swept volume per cylinder and a rated power speed of more than 3,000 per minute. EEV is "Enhanced environmentally friendly vehicle".

Table 1.2: Incremental costs for LDVs meeting European standards (2010 dollars) [17]

ENGINE TYPE	VEHICLE CLASS	EURO 1 (BASELINE)	EURO 1 TO EURO 2	EURO 2 TO EURO 3	EURO 3 TO EURO 4	EURO 4 TO EURO 5	EURO 5 TO EURO 6	NO CONTROL TO EURO 6
Gasoline	4 cylinders Vd= 1.5 L	$142	$63	$122	$25	$10	--	$362
Gasoline	4 cylinders Vd = 2.5 L	$232	$3	$137	$15	$30	--	$417
Diesel	4 cylinders Vd = 1.5 L	$56	$84	$337	$145	$306	$471	$1,399
Diesel	4 cylinders Vd = 2.5 L	$56	$89	$419	$164	$508	$626	$1,862

Table 1.3: Incremental costs for LDVs meeting US standards [17]

ENGINE TYPE	VEHICLE CLASS	TIER 1 (BASELINE)	TIER 1 TO NLEV	NLEV TO TIER 2	TIER 1 TO TIER 2	NO CONTROL TO TIER 2
Gasoline	4-cylinders Vd=2.3 L	$260	$80	$65	$145	$405
Gasoline	6-cylinders Vd= 3.2 L	$313	$115	$81	$197	$510
Gasoline	8-cylinders Vd= 4.5L	$381	$185	$124	$309	$690
Diesel	4-cylinders Vd=2.0 L	-	-	-	-	$1,609
Diesel	4-cylinders Vd=3.0 L	-	-	-	-	$2,086

1.2 Automotive engine technology trends

Current trends in automotive research that consider soot in the broadest sense can be grouped into those explicitly driven by regulation and those driven by technology development required to measure its presence.

1.2.1 Regulation-induced

Automotive manufacturers (both OEM and in the supply chain) are introducing many changes to engine design to fulfil current and future requirements of reduced fuel consumption, elongated service intervals and emissions reduction. These include retarded injection timing, raised piston rings, selective catalytic reduction (SCR) and the use of exhaust gas recirculation (EGR) [22].

Tackling the issue of fuel consumption through downsizing implies an increase in specific power output, accompanied by higher cylinder pressures (increased dynamic load) and oil temperatures (increased thermal load) [23]. Controlling the formation and emission of NOx by reducing combustion chamber temperatures and retarding the fuel injection timing during the combustion cycle, however, traps more soot in the chamber. EGR also assists in controlling the combustion process temperature as some of the normal intake charges are displaced by the recycled gas, the resultant effect of which is also soot build-up.

Any design change that increases the soot content is very likely to also increase the viscosity of the lubricating oil, leading to increased oil pump loads and increased fuel consumption.

Furthermore, interdependencies are seen throughout an engine where some of the combustion residues actually form some protective films ameliorating the severe contact conditions in some of the components [24], for example in the valve and seat

insert contact where the legislation for lead-free fuels resulted in the elimination of beneficial tribofilms [25-27]. Similarly, lubricant additives, such as zinc dialkydithiophosphate (ZDDP), play a major role in protecting the components from wear by forming tribofilms at contact points but as it has been discovered, for example that the lifetime of catalytic converters is shortened by ZDDP breakdown products [28].

The recent aim of the EU Commission [29] to introduce Real Driving Emission (RDE) tests further increases the operating range of the emissions regulations with consequences on the technology to comply. The RDE tests are carried out in real-time using Portable Emission Measurement Systems (PEMS) which according to Vlachos [30] have been very effective in vehicle emissions control and a novel approach towards emission abatement with potentials to improve air quality globally.

The new test is aimed at determining, more accurately, pollutant emissions in real driving conditions. This was consequent upon discovering that the emissions generated by vehicles on the road are substantially higher than in laboratory conditions.

This measure has the likely effect of increasing the level of soot generated in the engine as the EGR would become more widely used, even by gasoline engines, in order to comply with the new regulations.

More generally, the move towards lower viscosity lubricants (e.g., SAE 0w7, 0w15) to satisfy the quest for more efficient automotive engines, through reduced friction, has significant tribological implications due to the thinner lubricating films formed in the engine contacts and the attendant wear behaviour of components [31].

1.2.2 Timing drive system

The technology adopted for the timing drive system of an automotive engine has wider implications on the entire engine [23]. The choice is often between toothed belts and chain. Schoeffmann [23] carried out an in-depth comparative analysis of these alternative technologies with a view to creating a basis for a right choice in designing an automotive engine.

Gasoline Direct Injection (GDI) technology developed to achieve fuel economy goals is now confronted with a challenge of low-speed pre-ignition (LSPI). There is high possibility of occurrence of LSPI at low engine speed and high loads which are common in GDI and turbocharged gasoline direct injection (TGDI) engines [32]. The timing chain wear test is thus being developed to tackle the imminent problems of timing chain wear that may emanate from soot particles generated by these engines.

1.3 Paradigm shift in engine lubricant formulations

Fuel economy performance is now rated based on the periodic length of durability of the engine [32]. To tackle the challenges of new engine technologies and efficiency performance mandates, lubricant formulators have to develop products with novel additive chemistry and lower viscosities to meet up with the emerging engine technology trends. Figure 1.3 shows the desirable features of the additives for new lubricant formulations.

Three current specification upgrades with tremendous impact on the industry are: GF-6 for passenger car motor oils (PCMOs), PC-11 for heavy-duty engine oils (HDEOs) and GM specifications. The new formulations are enabled with backward compatibility. While GF-6A covers the existing engine oil grades in that category, GF-6B covers the new grades with lower viscosities (less than SAE XW-20). Similarly, PC-11A is

compatible with existing HDEO (API CJ-4) with an HTHS (high-temperature high-shear) of 3.5 minimum, while PC-11B covers new lower viscosity oils with an HTHS of 2.9-3.2 [32].

1.3.1 GF-6 formulations

GF-6 extended drain intervals are to be achieved with the use of more oxidation resistant base oils, accompanied by more effective anti-oxidants and additives capable of sustaining boundary lubrication over a long period. Such base oils include: gas-to-liquid synthetic oils, polyalphaolefins, polyolesters or polyalkylene glycols [32].

GF-6B is to deliver improved fuel economy as well as lower green-house gas (GHG) emissions. However, the gain of improved fuel economy performance obtained from the use of low viscosity GF-6B may be overshadowed by the resultant negative effect of excessive wear and durability concerns especially at extreme loading and high-temperature conditions. There may therefore be the need to formulate the lower viscosity GF-6B oils with more effective friction modifiers and anti-wear additives. With this, enhanced fuel economy can be achieved without trading-off surface protection against wear.

MAXIMIZING EFFICIENCY

TECHNICAL PARAMETERS (ENVIRONMENT-CONDITIONS)	BOUNDARY	MIXED	EHD/HD
ADDITIVE FEATURE	Surface Protection	Compression Resistance	Fluid Protection
ADDITIVE BENEFIT (DESCRIPTORS/DEFINITION)	Wear Reduction protects surfaces regardless of friction need for optimal friction management	Surface Separation maintains fluid strength and delivers surface repulsion	Fluid Integrity protects against fluid degradation
SOLUTIONS	Extreme Pressure Agents Surface Activated Additive Systems Anti-wear Agents	Film Strengtheners Friction Modifiers	Anti-oxidation Agents Contamination Control Agents Viscosity Management Agents

Figure 1.3: Features of the additives suitable for emerging lubricants [32]

1.3.2 Proposed category 11 (PC-11)

With proposed category 11 (PC-11) intended to replace API CJ-4 oils, the transition from traditional heavy-duty oil, SAE 15W-40 to other grades, such as, 10W-30, 5W-XX and 0W-XX, is in the offing. PC-11 was designed to satisfy the continuous drive for higher engine performance, improved fuel economy and reduced carbon dioxide emissions with efficient engine oils delivering a good HTHS performance without compromising durability [32, 33].

PC-11 is targeted at improved fuel efficiency performance and green environmental compatibility with evolving automotive technology and its attendant emission complexity. Aside better fuel economy and reduction of greenhouse gas emissions, PC-11 is also driven by increasing biodiesel use and necessity for enhanced engine protection from higher temperatures, better shear stability, reduction or elimination from of engine oil aeration and protection from adhesive wear [32].

As a result of the challenges of oil thinning and occurrence of oxidation consequent upon running an engine consistently at high temperature, which is common with heavy-duty diesel engine, oxidative and thermal stabilities of PC-11 engine oils are therefore required to be strengthened.

1.3.3 Dexos1

The Dexos1 specification also aims at optimizing vehicle operational performance with respect to low-speed pre-ignition (LSPI) and fuel economy, especially with GDI/TGDI technology. And to achieve these without trading-off oxidation, component wear, deposit and sludge control [32].

The implementation date for Dexos1 is September 2016, PC-11 is December 2016 and GF-6 is March 2018 [32]. While GF-6A and PC-11A oils are both backward compatible, the same may not be said for GF-6B and PC-11B oils both of which have little or no back serviceability and are therefore not expected to be recommended at the start.

1.3.4 Additive challenges

The biggest challenge of these new formulations is developing additive chemistry that will guarantee effective wear performance with lower viscosities. The challenge becomes more daunting with a tighter specification on the phosphorus limit (from 0.12%P to 0.08%P) for engine lubricants to ensure exhaust catalyst compatibility [32].

Realization of the lofty goals of these new formulations is therefore dependent on the effective combination of base oils improvements along with enhanced anti-wear additives, friction modifiers and antioxidants.

The traditional SAE 15W-40 lubricants have been able to satisfy the need of heavy-duty diesel engines over the years and for any replacement to sustain the confidence of the consumers, it must prove its ability to protect their equipment in an identical fashion [32].

Confronted with the contemporary challenges of maximizing energy efficiency with minimal impact on the environment, the automotive industry and lubricant formulators have shown great interest in research that brings about tribological improvements. Consequently, automotive researchers have intensified investigations to develop engines with better fuel economy, improved performance and efficiency with the ultimate aim of achieving a better combustion system in an engine [11, 34].

1.4 Research aim and objectives

The main aim of this research is to evaluate the effects increasing soot levels have on the wear of internal combustion engines (ICEs) components with a view to understanding the factors responsible for its build-up and the mechanisms involved in its interactions with engine components; and ultimately coming up with suggestions on how to mitigate its inherent damaging consequences on engine performance by

identifying the critical threshold for components wear that may affect ICE performances.

Generally, all the components involved in the combustion process are affected by the effects of the increasing soot loading; however, the most vulnerable are the valve-train components. Hence, the focus of the research will be on the components within the engine's valve-train related specifically to diesel engines.

To achieve this overall goals, the following objectives are proposed:

i. Understanding effects of soot on a simple specimen non-conformal point contacts (simulating elephant's foot/valve tip contact).

ii. Understanding effects of soot on a simple specimen non-conformal line contacts (simulating rocker arm/cam nose contact).

iii. Designing and producing a new rig to study the effects of soot on conformal contacts (Pin-In-Bush (PIB) set-up).

iv. Understanding effects of soot on a simple specimen conformal contacts (using PIB set-up).

v. Designing and producing a new rig to study the effects on a mini-chain arrangement.

vi. Studying the effects of soot on "mini" chain-drive systems (using Mercedes Benz M271 engine components).

vii. A novel use of ultrasound technique for in-situ measurement of sooty-oil film thickness.

1.5 Novel aspects of this work

The novelties of this research can be itemised thus:

➢ The specimen tests were based on realistic automotive engine contacts using appropriate materials, rather than generic laboratory tests that cannot be related to real engine contacts.
➢ The use of the ring-on-ring arrangement which perfectly simulate the contact between the camlobe and roller follower.
➢ The design and development of pin-in-bush (PIB) rig to simulate chain link articulation under load, which was done as part of this researcher.
➢ The design and development of chain rig to study the effects of soot on the wear of a timing-chain system using real engine components, which was also carried out as part of this researcher.
➢ The development of a test platform to measure the sooty-oil film thickness instantaneously using an ultrasound technique.

1.6 Thesis layout

This section gives a brief summary for all the subsequent chapters presented in this thesis.

Chapter 2: **Wear, Friction and Lubrication.** This chapter gives fundamental knowledge of the concept of tribology and its related terms, such as wear, friction and lubrication. Various types of wear mechanisms are

discussed; particularly, those attributable to soot-contaminated contacts in an internal combustion engine (ICE).

Chapter 3: **Literature Review.** This chapter broadly covers previous research works that have been carried out on automotive soot. The chapter starts with the basic definition of soot, its formation, removal and reduction along with the mechanisms of its wear and effects on automotive engine components. Geometric conformity of different tribological contacts in an ICE was also discussed along with the analysis of various levels of tribological studies; relating this research work to different simulation approaches. Finally, comparison of the previous research was done, highlighting common trends in research techniques and findings and identifying possible gaps that can be explored.

Chapter 4: This chapter gives detailed report on the preparation of the sooty-oil surrogates along with measurement of their viscosity at different temperature. The procedure adopted in characterisation of the specimen surfaces was also discussed.

Chapter 5: **Non-conformal Point Contact Reciprocating Test.** This chapter describes non-conformal ball-on-flat experiments. Details of the test rig, specimens, theoretical calculations of the contact parameters and test procedure are presented along with post-test analysis and the obtained results. Report of the innovative use of ultrasound technique in the instantaneous measurement of the film thickness of varying compositions of sooty-oil surrogates is also presented.

Chapter 6: **Non-conformal Line Contact MTM Test.** A detailed investigation of the non-conformal ring-on-ring test using a mini traction machine (MTM) are presented in this chapter. Items highlighted in Chapter 4 are also captured.

Chapter 7: **Conformal Contact (PIB) Test.** This chapter discusses the conformal contact test using the in-house designed and manufactured pin-in-bush rig. Details of the rig, specimens, testing method and results obtained are presented.

Chapter 8: **Automotive Engine Real Component (Chain Rig) Test.** This chapter outlines the real component test using a chain rig, adapted from the PIB rig with some modifications. In depth analysis of the results are highlighted along with results obtained from a similar component that has undergone several thousands of miles on a real engine.

Chapter 9: **General Discussion, Conclusions and Recommendations.** In this chapter, the results and findings of the study are outlined along with recommendations and suggestions for future works.

Chapter 2

Wear, Friction and Lubrication

This chapter discusses the basic terms that make up the concept of tribology, namely: wear, friction and lubrication. Each of these terms are discussed along with their types, especially as related to this research work. Contact mechanics, which deals with how distribution of contact pressure between two bodies is influenced by their geometric area of contact was discussed in each chapter, based on the operating contact condition.

2.1 Wear

Wear is damage to a surface resulting from progressive removal of materials from the contacting asperities due to relative motion between that surface and a contacting surface or substances [35, 36] or surface damage resulting from material displacement without any alteration to the original mass [37]. The extent of this removal or displacement is dependent on the conditions under which the material operates, such as the contact pressure which, in turn, is influenced by the size of the asperity (contact area).

Blau [36] highlights two main types of wear transitions, namely natural and induced. While a natural transition is a change to the tribosystem caused by no external influence, induced transition is caused by external operating factors, such as load, speed, temperature, acceleration, environment.

While there are many types of wear, the discussion in this thesis will be limited to those types that are envisaged may result from the contact conditions in this research work; namely: abrasive, adhesive and fatigue.

2.1.1 Abrasive wear

Abrasive wear occurs when the harder of the two rubbing bodies induces a sort of scraping or displacement of the surface materials of the softer body. Ludema [38] analysed the abrasive processes itemizing the elements involved in a simple flow chart, Figure 2.1.
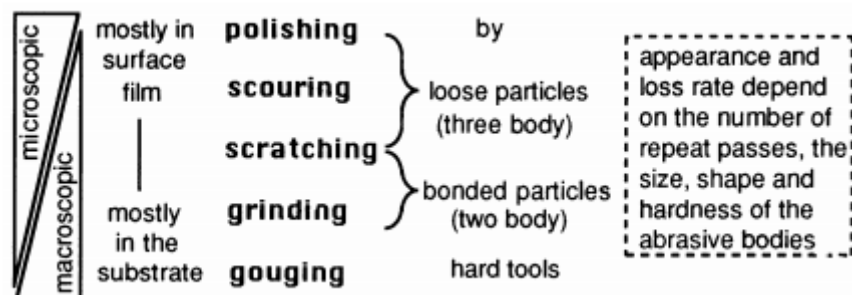
Figure 2.1: Abrasive processes [38]

Figure 2.2a shows the mechanisms of abrasive wear between two materials of different hardness; two-body abrasion and three-body abrasion with an infiltrating hard particle.
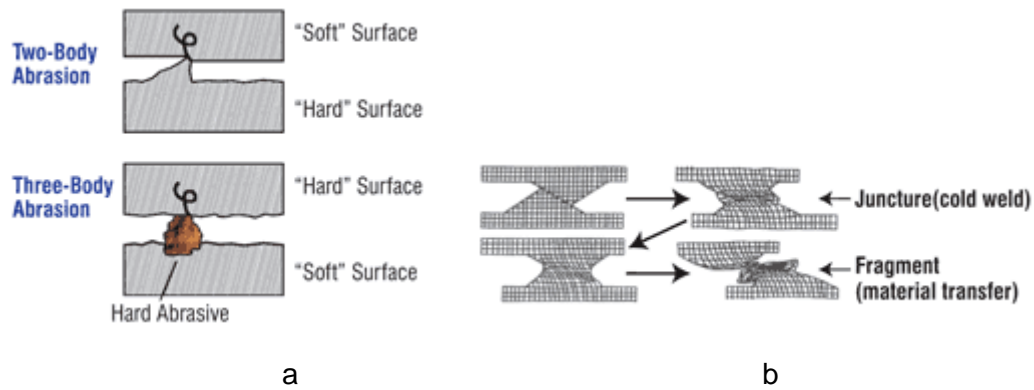
Figure 2.2: Mechanisms of wear: (a) abrasive and (b) adhesive [39]

2.1.2 Adhesive wear

As the name suggests, this involves material loss between contacting bodies due to high local friction.

Adhesive wear occurs when there is near dry contact between surfaces resulting from the absence of lubricating oil as a result of starvation at high soot content or at high contact pressure when the applied load between the surfaces is very high. Either of these results in material transfer between the contacting surfaces. Figure 2.2b shows the mechanisms of adhesive wear between two materials.

2.1.3 Fatigue wear

Fatigue wear occurs when surface material is displaced by the action of cyclic sliding. It often leads to substrate failure through crack formation and propagation. Fatigue wear may occur even in adequately lubricated contacts when high contact pressures are applied between surfaces in repeated rolling or sliding action results in very high local stresses [40].

2.2 Friction

It may not be adequate to give friction a definitive meaning because of the wide range of interactive variables influencing its manifestation. Succinctly put, the effect of interacting surfaces in relative motion or interlocking asperities of the two bodies in rubbing contact culminates in tangential force countering the motion [27]. This force is known as friction and is influenced by several parameters, such as, normal load (contact pressure), material, surface roughness, contact geometry, lubrication, temperature, sliding speed, etc.

In automotive engines, the effective power, P_e, at the output shaft is always lower than the indicated power, P_i, at the piston. The difference is referred to as friction loss, P_r. Approximately, about one-third of fuel energy is lost to friction in a combustion engine [41]

$$P_r = P_i - P_e$$ Equation 2.1

This friction loss comprises the losses at each tribological contact, such as engine block (crank shaft, connecting rods and piston with piston rings) and valve train system (camshaft, valves, timing system and other auxiliaries); thus reducing the available engine power at the output shaft. It accounts for about half of the total developed energy consumption in an automotive engine [42] and also influences the fuel consumption of the engine [43]. Consequently, fuel efficiency is improved when the friction between moving parts is reduced. The major source of the frictional and

11

parasitic losses in an automotive engine is the piston assembly [44]; single-handedly accounting for about 50% of mechanical losses. Figure 2.3 shows how mechanical losses are distributed in a diesel engine.
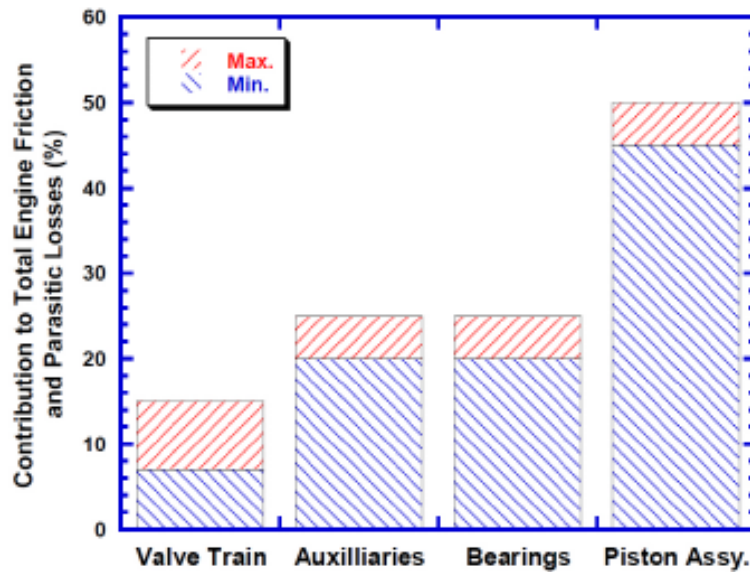
Figure 2.3: Distribution of mechanical losses in a diesel engine [44]

In tribological testing, friction is not primarily a material property as its manifestation is dictated by the operational tribosystem [45]. This explains why a specific material exhibits different frictional values when tested under different tribological conditions.

The coefficient of friction, μ is often estimated from the ratio between this resisting tangential force, F and the applied normal load, N.

$$\mu = \frac{F}{N}$$
Equation 2.2

2.3 Stribeck curve

The Stribeck curve is an essential tribological tool which indicates frictional behaviour observed for lubricated surfaces under different lubrication regimes.
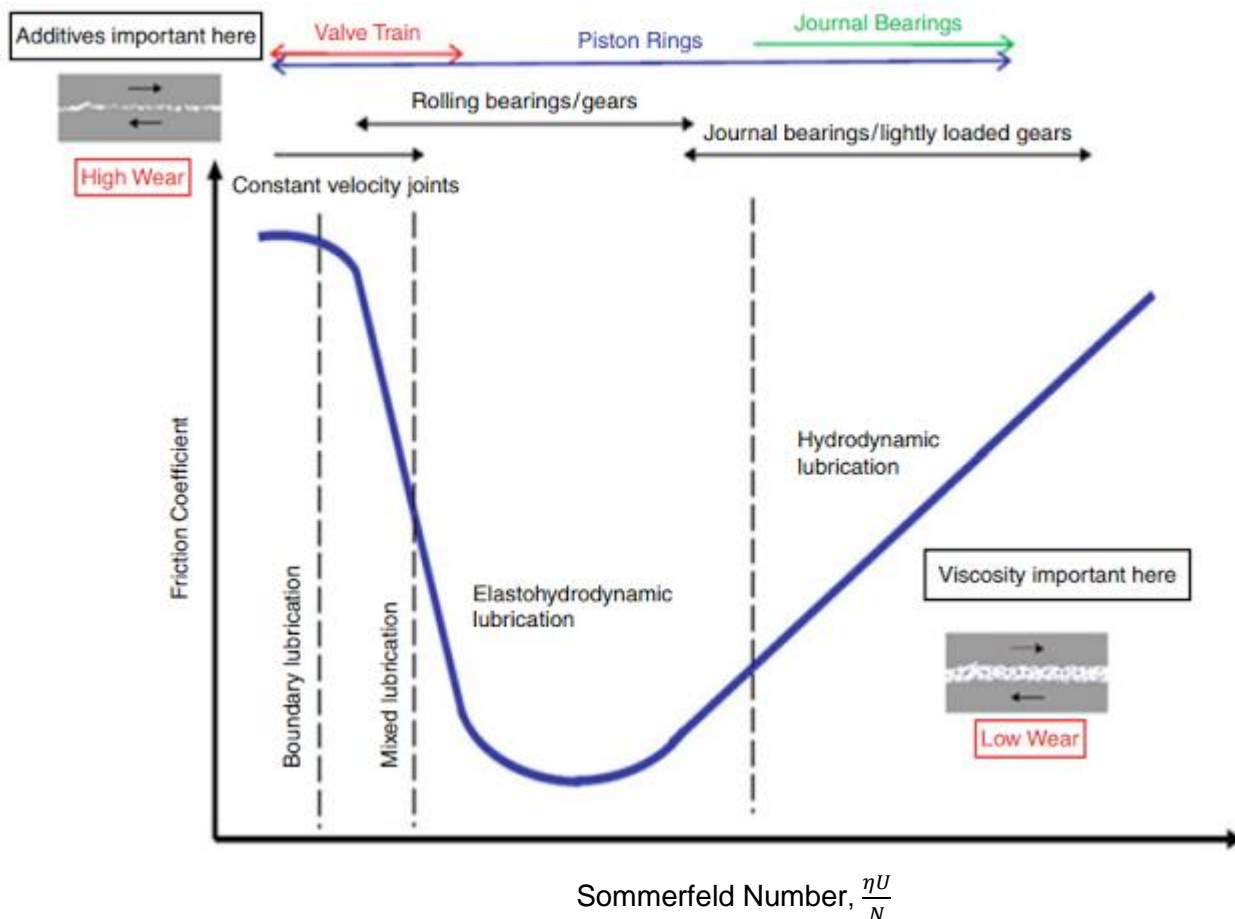
Figure 2.4: A sample of the Stribeck curve showing various regimes of lubrication [46]

In this curve, shown in Figure 2.4, the coefficient of friction, μ is displayed as a function of dynamic viscosity (η) multiplied by the tangential velocity (U), and divided by the normal load (N). The curve normally shows the four lubrication regimes:

2.3.1 Boundary lubrication

The asperities of the contacting surfaces are apparently in direct contact here. This may be due to high load or low speed or both.

2.3.2 Mixed lubrication

Here, the surface asperities are not fully separated, but interact only partially. This is the operational regime between hydrodynamic and boundary lubrication. This may be due to any or combination of these factors: very low viscosity or velocity and too high load preventing complete separation of the contacting surfaces.

2.3.3 EHD lubrication

The surfaces are fully separated by a very thin (0.1 µm to 1 µm) fluid film lubrication; though, the elastic deformation of the surfaces and the effects of pressure on viscosity lead to physical interactions between the contacting bodies [40].

2.3.4 Hydrodynamic lubrication

Ideally, the fluid film lubrication ensures the surfaces are completely separated and that there is no asperity contact. In hydrodynamic lubrication, there must be adequate

velocity to generate a load-carrying lubricating film which sustains the relative motion between the two contacting surfaces.

In hydrostatic, separation of the contacting surfaces is achieved through the pressurized lubricant which is continuously supplied by an external pump.

2.4   Oil film thickness

The main function of a lubricating oil is to form and maintain a lubrication film between two bodies in relative motion and the effectiveness this function depends on the viscosity of the oil; which means the higher the viscosity, the thicker the film and better protection. However, there is a limit to viscosity increase to prevent its side effects. The best choice is a lubricant with sufficient viscosity to generate adequate film thickness that prevents direct interaction of the contacting bodies asperities and low enough to avoid dragging and overheating [47]. As indicated on the Stribeck curve, Figure 2.4, viscosity is the most influencing factor in the no asperity contact regime; shear stability of the lubricant is therefore important for minimizing shear-related viscosity losses.

Film thickness, therefore, plays an important role in lubricated contacts [48]. It determines the level of protection the contacting bodies enjoy. Hence the need to estimate its numerical values in order to determine the extent of separation of the contacting bodies.

2.5   Surface roughness

Quantification of surface roughness plays a major role in the assessment of tribological contacts [42]. Apart from its usefulness for comparison with minimum film thicknesses to estimate lubrication regime, it also indicates the extent of contact reduction due to peaks and valleys of the surface asperities resulting in the actual contact area being less than the apparent contact area as postulated by Bowen and Tabor [49].

This becomes critical with the current quest for energy efficient systems, which requires automotive engines to work under increasingly severe conditions such as thinner lubrication, minimum lubrication and higher temperatures.

An illustration of magnified view of surfaces in contact is presented in Figure 2.5, showing that at the microscopic level, seemingly smooth surfaces contain a lot of irregularities (asperities); this implies that area of contact between the two bodies may actually just be a fraction of nominally estimated contact area [36]. Hence the apparent contact area is always significantly larger than the true contact area.
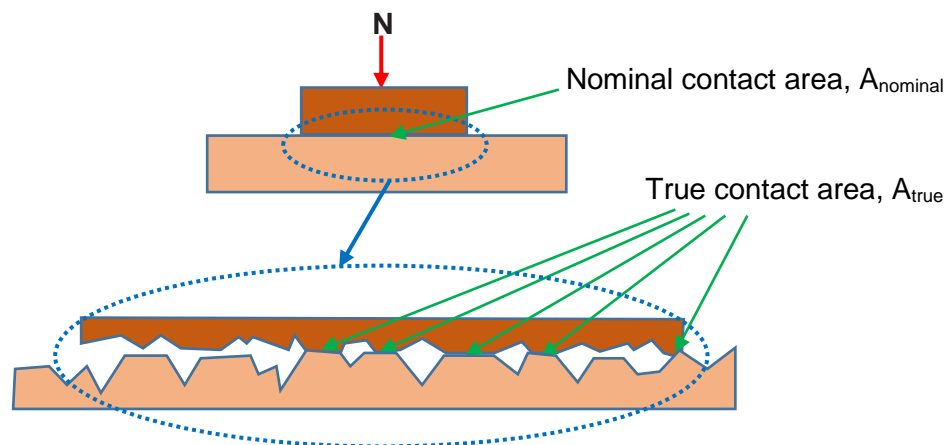
Figure 2.5: An illustration of magnified view of surfaces in contact

2.6   Conclusions

Wear, friction and lubrication which are the basic concepts of tribology have been discussed. Starting with their basic definitions, brief explanations of their various modes and factors influencing their occurrence are presented with relevant diagrams. Some illustrations on the mechanisms of abrasive and adhesive wears are also presented.

The Stribeck curve highlights the regime of lubrication under which different components within the automotive engines operate. The roles played by the surface roughness and the lubricant film thickness in protecting the contacting components are also discussed.

Chapter 3

Literature Review

This chapter presents a broad literature review on the research topic highlighting previously undertaken related works. The chapter aims to present some insight into soot: its formation, removal and reduction along with the mechanisms of its wear and effects on automotive engine components. In addition, justifications for the use of carbon black in soot wear studies are highlighted along with a brief discussion on the geometric conformity of different tribological contacts in an internal combustion engine (ICE) and the adoption of chain-driven timing drive system by original equipment manufacturers (OEMs). It further analyses the advantages, applications and limitations of various levels of tribological studies; relating this research work to different simulation approaches. The review finally compares observations from previous research works under such headings as wear, wear mechanisms, wear rate and viscosity among others with a view to looking at common trends and gaps in order to identify area of automotive soot study that can be explored.

3.1 Background on soot wear

3.1.1 Soot formation

Soot is microscopic hard amorphous carbon particles, the concentration of which can be as high as 8% in automotive lubricants [50]. As elemental particles, soot presents as small but hard spherical particles of 10-35 nm [51]; however, they can aggregate into secondary particles which are 'soft' and 'slippery' due to their agglomerated structure with average size of 120 nm [52] or more than 400 nm [53]. Soot clusters can build up to thousands of spherules in size. Each spherule comprises hydrocarbon material and inorganic material (mostly sulfates), which are responsible for the abrasive behaviour of soot. There are as much variations between the hardness of soot particles produced by light-duty and heavy-duty vehicles as there are within those produced by the same engine; however, their hardness is reported to be similar to [54] or even higher than [55, 56] the hardness of automotive engine components.

One of the reasons attributed for the variations in the hardness is the difference in carbon density which influences the hardness of the carbon material [54], a major constituent of soot. Another is the similar engine design that are operated under different conditions, for example, EURO I and EURO II heavy-duty diesel engines which produced soot of different hardness [54].

Figure 3.1 shows soot in its various forms as elemental particles and sticking together to form an agglomerate in a chain-like structure; while, Figure 3.2 presents the transmission electron microscopy (TEM) images for diesel soot in both two-dimensions and three-dimensions.

Figure 3.1: The depictions of: (a) Soot as elemental particles and (b) a chain agglomerate of soot particles

(a)   (b)
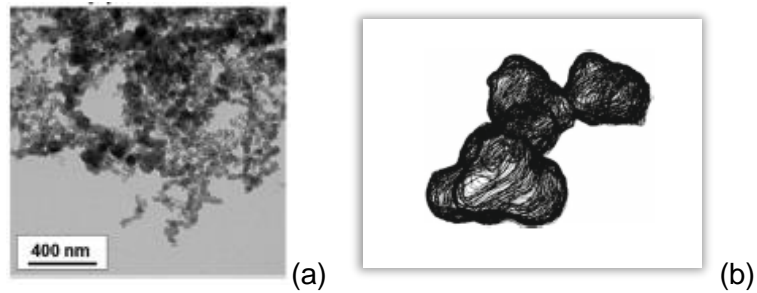
Figure 3.2: Transmission electron microscopy (TEM) images of diesel soot
(a) in two-dimensions [53] and (b) three-dimensional visualisation [57].

Soot, though undesirable because of its harmful effects, is an inevitable combustion product of partially combusted fuel in an internal combustion engine (especially diesel) [58]. Soot is formed mainly in the fuel-rich regions of the combustion chamber at elevated temperatures. It can also be formed to some extent at lean combustion when some unburned oxygen passes through the flame. This normally occurs during cold starting, low speed engine and other circumstances, such as deceleration and acceleration, mostly common especially in urban traffic.

For diesel engines, the complex combustion process is further aggravated by the non-uniformity of fuel distribution and air-fuel mixing process [59]. This combustion initiates close to the injection point around the top dead centre (TDC) when the mixture is fully compressed and occurs very rapidly and spontaneously as a diffusion flame. Since the mixture (air-fuel) is very fuel-rich, this results in the production of high level of soot. Figure 3.3 illustrates how air-fuel ratio influences the formation of soot in a diesel engine.

The blue region represents the ideal stoichiometric operating conditions where there is just enough air to completely burn the available fuel. This is, however, not achievable mainly because the available time for each combustion cycle is very short. Stoichiometric air-fuel ratio for diesel engine is 14.5:1. Lean operation, represented by the smaller red region, means more air than 14.5 (fuel lean), this generates some level of soot; while the bigger red region which represent the rich operation indicates less air than 14.5 (fuel rich) where much more soot is generated.

$\phi = Equivalent\ ratio$

$\lambda = Air - fuel\ ratio;\ \lambda = \dfrac{1}{\phi}$
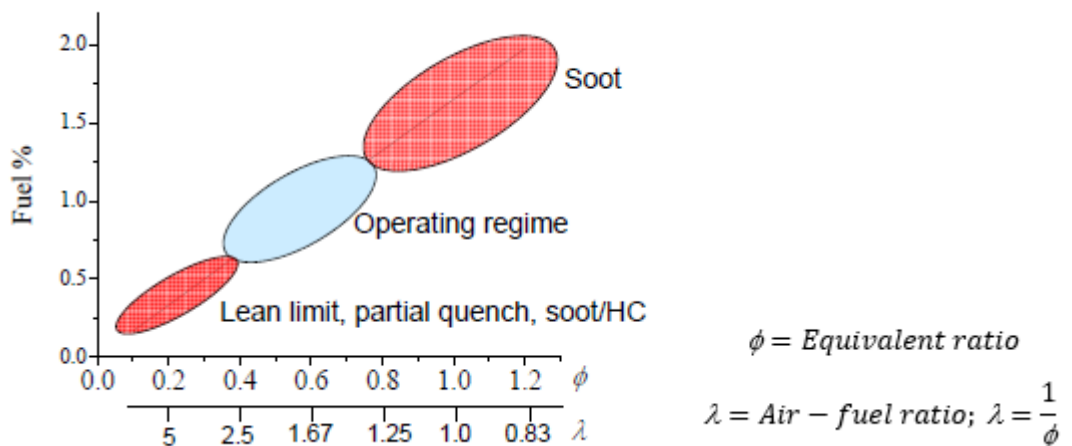
Figure 3.3: Soot formation process in a diesel engine [60]

Obviously, it can be seen from Figure 3.3 that:

17

$\phi < 1$, $\lambda > 1$ when there is fuel lean mixture,

$\phi = 1$, $\lambda = 1$ for stoichiometric mixture and

$\phi > 1$, $\lambda < 1$ when there is fuel rich mixture [61].

Soot generation is, therefore, an indication of reduced combustion efficiency caused by disproportionate mixture of fuel and air (resulting from over-fuelling and/or air restrictions), excessive stop/start situation and excessive exhaust back pressure.

3.1.2 Morphology, structure and chemistry of diesel soot

As mentioned above, the formation of diesel soot occurs during the high temperature combustion of diesel fuel. The main composition of diesel soot is carbon, while oxygen and hydrogen are also present in small quantities [62]. Patel et al. [63] carried out an elaborate examination of the diesel soot structure and presented an high resolution transmission electron microscopy (HRTEM) image, Figure 3.4 where the graphite-like layers are shown in amorphous (marked as *A*) and turbostratic (marked as *T*) fashions. The primary particle size of the turbostratic structure ranges between 10 nm to 30 nm in diameter. Raman spectroscopy of the diesel soot showed the presence of ordered and disordered carbon with graphene layer edges. The work further analysed the chemical composition of diesel soot using the energy dispersive X-ray spectroscopy (EDS). The spectra of the dispersed soot region indicated the presence of carbon, calcium, phosphorus, sulphur, zinc and oxygen on the larger agglomerates but only carbon and oxygen were present on the primary soot particle. The observed calcium, phosphorus, sulphur and zinc are obviously constituents of lubricating oil additives.
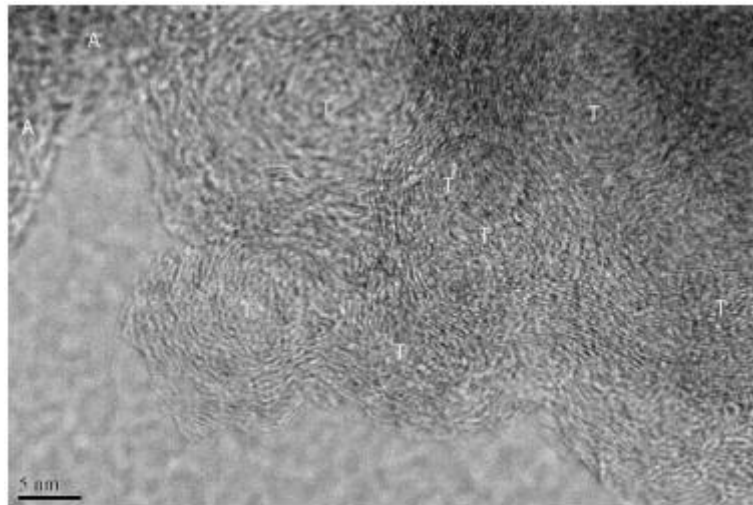
Figure 3.4: HRTEM micrograph of diesel soot showing turbostratic and amorphous regions [63]

3.2   Soot monitoring, removal and reduction

3.2.1 Field-based condition monitoring of soot

The ASTM designed standard for field testing is ASTM D7686 [64] and is designed to measure soot build-up (up to 12%) in diesel crankcases of in-service hydrocarbon-based lubricants using fixed-filter infrared spectroscopy. Absorption intensity measurement is used to determine the soot level after which direct or differential (using a new lubricating oil as reference) trend analysis is used to compare and correlate with the engine performance [65]. Figure 3.5 shows an infrared absorbance spectra for diesel crankcase oils over a range of 4000 to 550 cm^{-1} using FTIR spectroscopy. From

the baseline offset at 2000 cm^{-1}, the figure indicates the increasing soot loading levels for low to very high (increasing from 1 to 5).
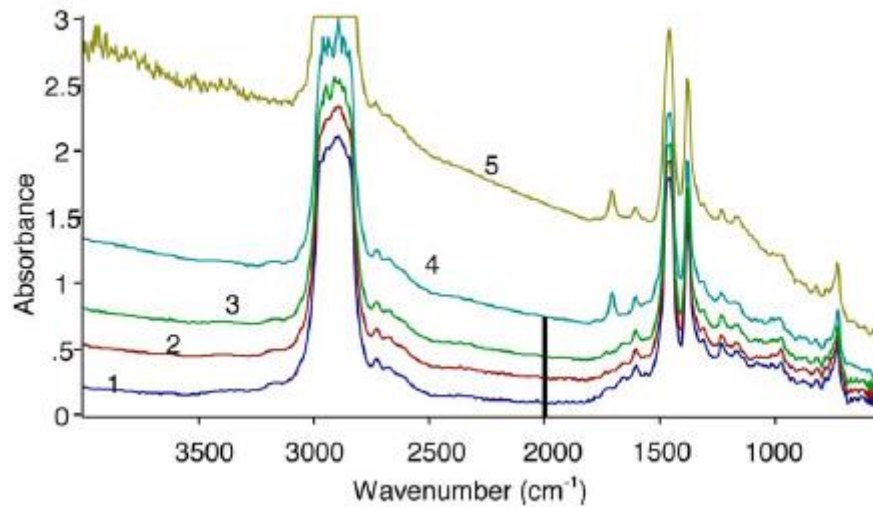
Figure 3.5: Trend analysis of soot measurements in diesel crankcase oils [65]

Although this standard evaluates only the soot content, ASTM E2412-10 [66] is designed for more complex condition monitoring such as, additive depletion, contaminant build-up and base stocks' oxidation, nitration and sulfation as evidence of degradation. Figure 3.6 shows the measurement areas for oxidation and nitration (1800 to 1670 and 1650 to 1600 respectively) accumulation monitoring in crankcase oils, and Figure 3.7 shows measurement area of sulfation.
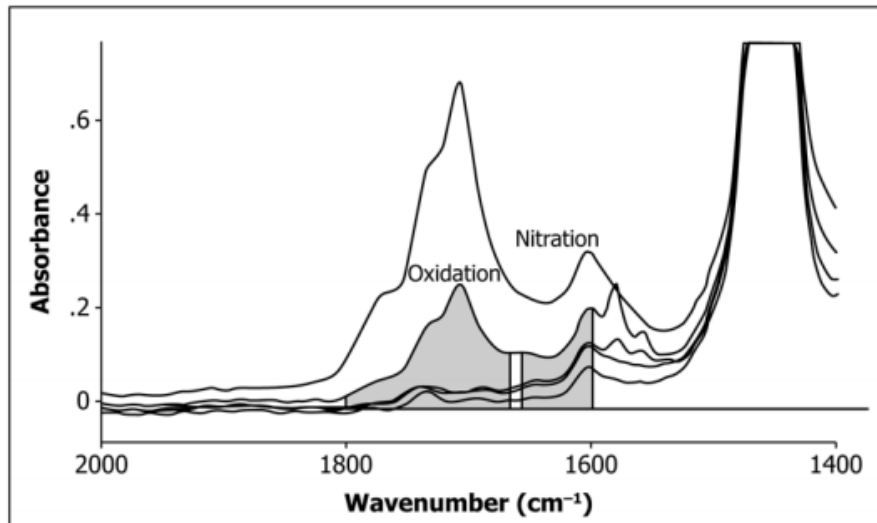
Figure 3.6: Measurements of Oxidation and Nitration in crankcase oils [66]
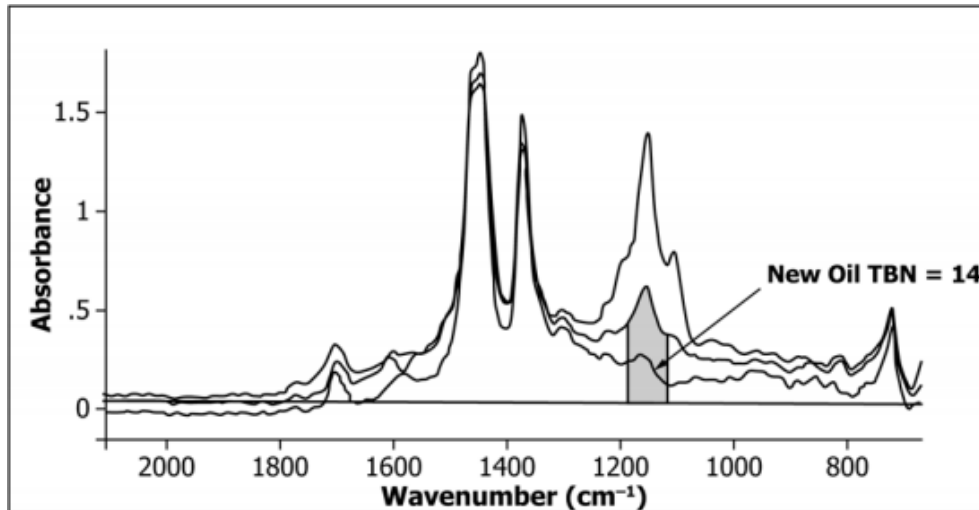
Figure 3.7: Measurement Sulfation in crankcase oils [66]

Oxidation occurs as a result of oil reaction with oxygen which is usually accelerated by high temperature, water and acids. While nitration is a degradation of oil resulting from a reaction with NOx, sulfation results from the reaction of oxygen, heat, water and sulfur from diesel fuel or base oil additives. Each of these causes premature oil thickening which increases oil viscosity, deposits of varnish and sludge.

3.2.2 Removal of soot

Effective and efficient soot removal from the recirculating lubricating oil in the sump can help achieve the desired engine performance and durability and prolong oil drain intervals, a significant current trend driven by users [67].

The two main removal approaches to date have been through mechanical filtration and centrifugal filtration. Mechanical filtration involves efficient single-pass filtering using coarse filter (mainly used for petrol engines) and/or by-pass filtering with a finer filter (mainly used for diesel engines). Centrifugal filtration involves the use of high speed rotating chambers to separate the contaminating particulates from the lubricant [2]. Cheekala et al. [67] used a new approach involving the utilization of electric field on the soot particles to stabilize the weakly bound soot cake. This method achieved appreciably higher filtration efficiency as compared to mechanical and centrifugal filtration.

3.2.3 Soot reduction

There are a number of measures to control generation and build-up of soot in order to ameliorate its deleterious effects on lubricant and engine components. Some of these measures are listed below:

- Improving the combustion process through the use of direct fuel injection and swirl within the combustion chamber to assist air-fuel mixing and increasing the amount of air supply to burn all the fuel,

- Fitting particle filters:
    - Bypass filters with increasingly finer grade filter elements,
    - Deep-bed filters,
    - Use of soot trap along with EGR,

- Use of Lean NOx Trap (LNT) catalyst and Selective Catalytic Reduction (SCR) as alternative to EGR; due mainly to the trade-off between NOx and Particulate Matters (PM) and PM emissions limit [68].

- Improving driving style: Soot emission can be substantially reduced by reducing stop/start driving,

- Intelligent Traffic Systems (ITS) which comprises real-time monitoring of soot generation and emission and traffic flow can keep traffic flowing and reduce emissions.

3.3 Overview of soot effects on automotive engines

The damaging effects of lubricating oil contamination by soot particles have been discovered for long. Research has confirmed that soot contributes significantly to the wear of various specimen/components, when taken through various forms of laboratory/components experimental investigations [2-9].

Soot effects on ICEs are multi-dimensional and the mechanism of soot-induced wear is thought to be either one or combination of some of the following elements:

1) Soot can either directly entrain into the contact between two components and with its hard particles abrade or scratch the surfaces in three-body abrasion [2-4] or block oil entrance into the contact zone of rubbing components when its size, through agglomeration, is larger than the oil film thickness or indirectly degrades the oil through alteration of its chemical properties thus rendering it ineffective [69].

2) Soot acts as an abrasive on the anti-wear solid film, comprising calcium, oxygen, phosphorus and sulphur, formed by the oil on the metal surface [70-72]. The idea of preferential adsorption and chemisorption of anti-wear additives in the lubricants by the soot [73-75] still subsists.

3) Soot contaminants produce large increases in oil viscosity [6, 9, 76-79] and thus hinder the effectiveness of the oil pump which consequently affects the rate and amount of lubricant getting into tribological contacts when required.

3.3.1 Soot microstructure and tribochemical activity

It is also thought that the microstructure of the soot has an effect on its chemical reactivity due to the arrangement of carbon structure influencing its oxidation resistance. Thermal ageing transforms soot structure from disordered amorphous carbon to more orderly polyaromatics with higher oxidation resistance [80]. Ivleva et al. [81], in a study of soot samples from gasoline and diesel engines, observed that their carbon structures, amorphous and graphitized respectively, have an impact on their chemical reactivity during the process of oxidation and gasification, with well-graphitized diesel soot oxidizing less readily.

The temperature at which soot forms also influences its properties (chemical composition, surface area and morphology) and hence its reactivity behaviour [82]. The higher the temperature of formation, the more ordered and less reactive are the soot samples.

Antusch et al. [73] studied the tribochemical action of various sooty oil mixtures from diesel engine, gasoline engine and laboratory produced carbon black, and reached a conclusion that soot particulate concentration is not solely responsible for wear properties with soot morphology, surface chemistry, and reactivity playing more significant roles. They also proposed a new wear model specifically for sooty oil from gasoline engines (Figure 3.8); where the unpaired reactive electrons (dangling bonds) of the highly disordered soot particle surface compete with anti-wear additives for the

21

metal surface. The soot particulates, being more polar, have a more likely chance of reacting with the metal surface first and also attract the polar additives to itself, thereby increasing wear. By reacting with the metal surface, the soot particles prevent the anti-wear additives from protecting the metal surface; and by attracting the additives, they render them ineffective. This was corroborated by Uy et al. [14] in their comparison of samples of soot from gasoline and diesel engines, concluding that the more amorphous structure of the gasoline engine is responsible for its high level of polarity and reactivity with metal surface and other polar additives in the lubricating oil. Hence, the level of disorder in the soot microstructure is proportional to its chemical reactivity.

All these ideas should be seen as complementary rather than contradictory as each comes to strengthen our understanding of the behaviour of soot in an automotive engine.
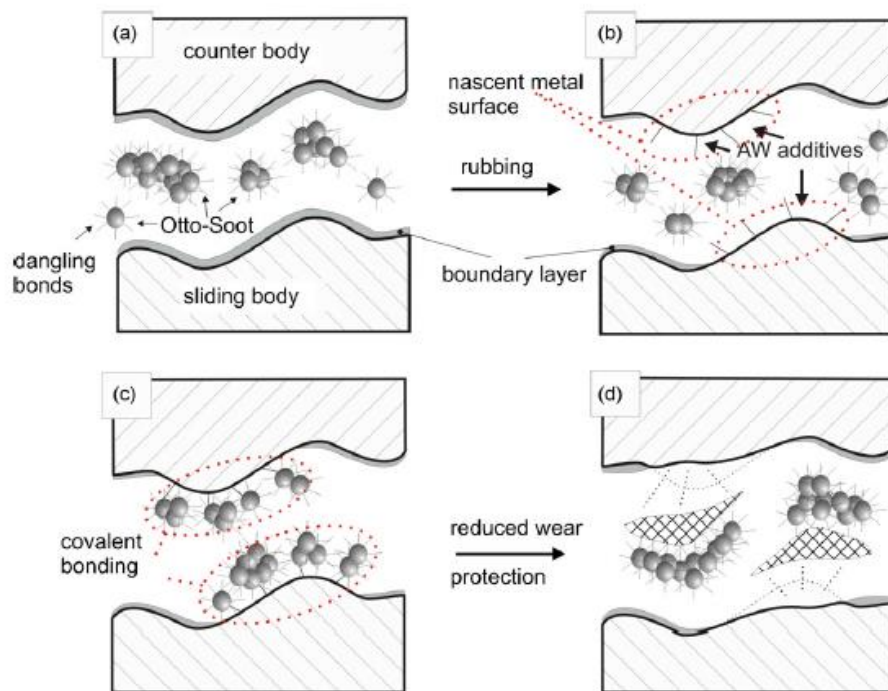
Figure 3.8: New wear model for gasoline soot [73]

3.3.2 Soot effects on wear and friction of metals

The detrimental effects of lubricant contamination cannot be overemphasized; apart from causing wear of engine components, it also adds to frictional losses in the contacts of the engine components moving relative to each other (rubbing surfaces). Soot contributes significantly to the wear of engine components; the most vulnerable being components in tribological contacts, such as: cylinder liners, piston rings, valve train system, bearings. Many researchers [2-9] have shown that the infiltration of soot particles into contacts between these components is largely responsible for increased wear of rubbing surfaces. In some cases, soot like any other detached abrasive material, embeds in the softer body at the point of contact with the harder body and then scratches the harder body while serving as protective layer for the softer body.

Extensive research in this area has investigated various lubricants, soot types (including varying composition of surrogates) and numerous testing methods ranging from specimen, components to engine and has built confidence and a high level of acceptance of these theories by automotive stakeholders (engine manufacturers and lubricant formulators).

Nagai et al. [72] presented the results of the engine component tests where increasing the EGR efficiency level aggravates the level of wear of the tribological components correspondingly (Figure 3.9) and is attributed to progressive soot build up as EGR level increases. Findings from other researchers [9, 71, 83] corroborate this with the assertion that life span of an engine may be shortened by EGR as a result of rapid oil contamination and degradation from exhaust products.
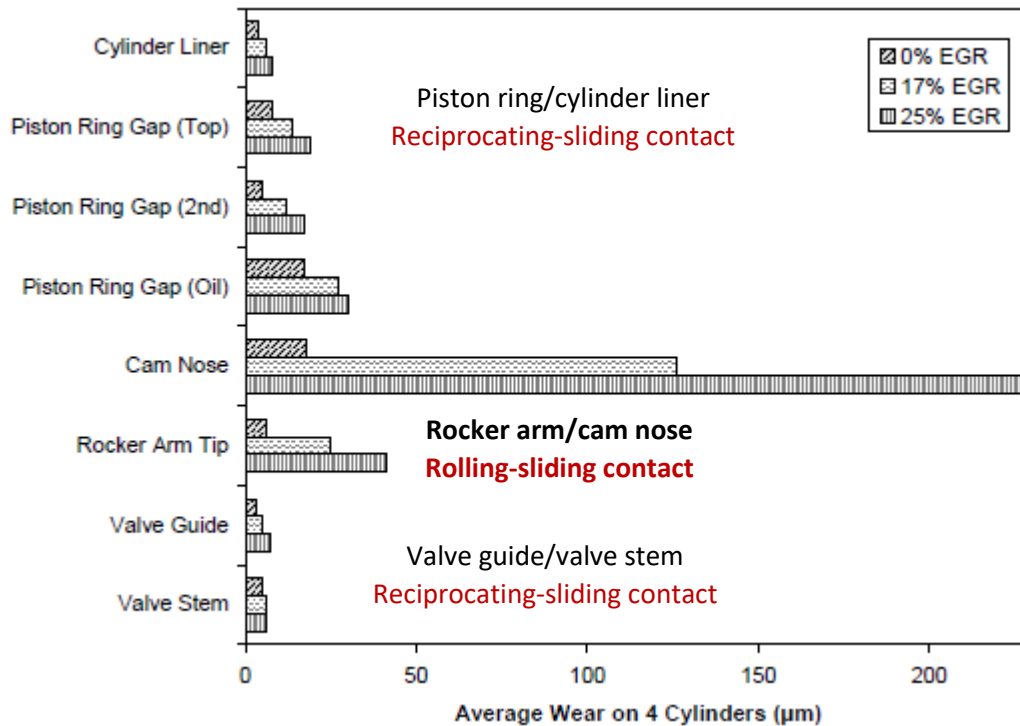
Figure 3.9: A depiction of the influence of EGR on the wear of tribological components (with their respective kinematics) in a 4-cylinder engine [72]

A number of studies have been carried out to understand the effects of soot on ferrous materials such as steel and cast iron that are commonly used in engine components [5, 6, 31, 34, 39, 40, 53]. It is known that the presence of soot causes high wear and also affects friction in contacts.

Soot is known to also affect friction in contacts. Through a four-ball-tribometer, George et al. [74] discovered that the average friction coefficient increases proportionally with carbon black concentration. Hu et al. [84] observed the same trend in a similar experiment using CD SAE 15W40 lubricating oil, especially for carbon black content above 2wt%. They attributed the reduction in the coefficient of friction at 2wt% to the fact that the carbon black particles are well-dispersed in the mineral oil. Green and Lewis [2], using a carbon black contamination level of 0-7wt% in a reciprocating ball-on-flat test rig, found that increasing levels of carbon black in engine oil increases the friction coefficient. Similar work has also shown that friction fluctuates and increases in case of contaminated oil with soot [70]. Other studies have reported that the presence of soot decreases the coefficient of friction. Aldajah et al. [9] discovered that friction slightly decreased in a four-ball wear test with used diesel engine oil from a Cummins-11 engine, but the wear volume increased significantly. While Antusch et al. [73] found that high soot concentration decreased the friction in a pin-on-disc (PoD) tribometer using carbon black-contaminated oil and soot-contaminated used oils from

Otto and diesel engines. These conflicting reports on the effects of soot on friction suggest further investigations are required.

Most of the work considering soot wear of ferrous metals shows that all specimens (arbitrary or real components) tested have shown signs of abrasive wear starting from low percentage of soot/carbon black in the lubricant with evidence of lubricant starvation at higher concentrations [4, 6, 73, 84, 85]. Using data from three-body wear tests, Gautam et al. [71, 86] discovered that the level of wear from soot contaminated lubricants was higher than that of uncontaminated oils. It was also found that abrasion wear mechanism was the major cause of the wear increase. Green et al. [4] similarly observed, from a ball-on-flat test, that the carbon black particles in the contact was responsible for the lubricated sliding wear at low content and starvation of lubricant from the contact resulting in adhesive scuffing/galling at higher content. Images depicting these wear mechanisms are shown in Figure 3.10.
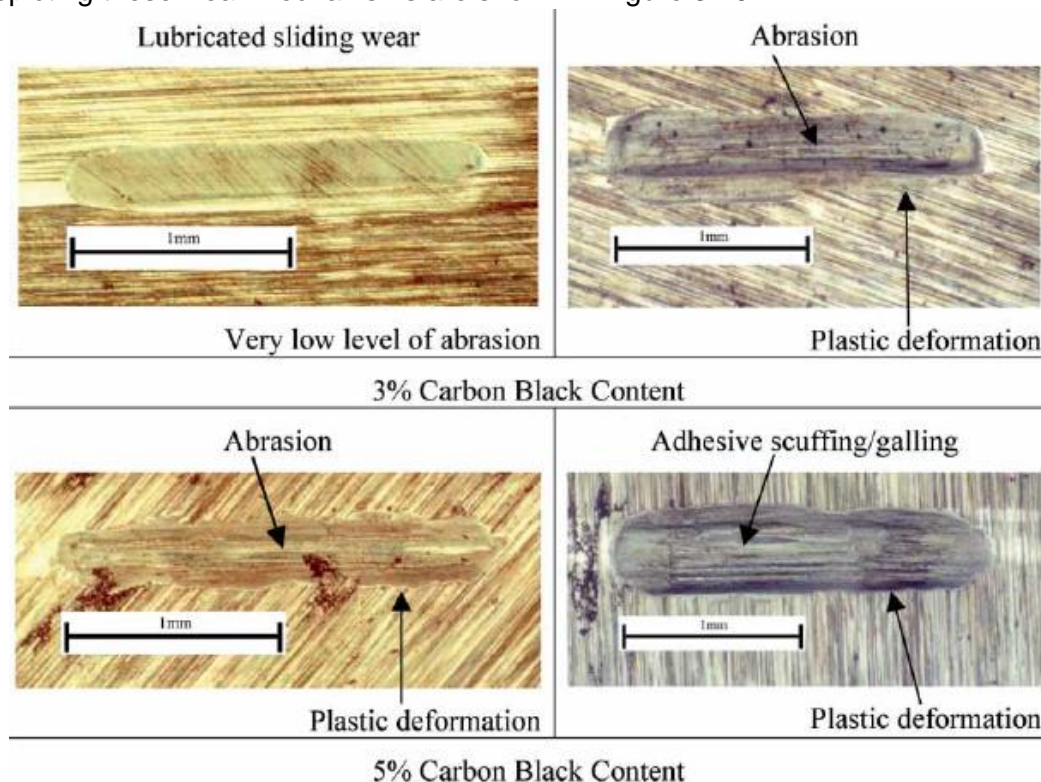
Figure 3.10: Images of abrasion mechanism at 3% and 5% carbon black content [4]

Soot size relative to the film thickness also plays a major role in determining whether wear would occur or not. If the lubricant film is thicker than the soot particle sizes, the metal surfaces can be separated by the lubricant film and no wear will occur. Contrarily, if the film thickness is less than the soot size, then abrasive wear will occur [9, 56, 87]. Li et al. [56] discovered that soot is harder than steel or cast iron thus the soot is hard enough to abrade metal engine parts. The investigation also shows that a number of groove widths are larger than the soot sizes, Figure 3.11. It is suggested that (wear debris) from the cast iron may have been responsible for these.
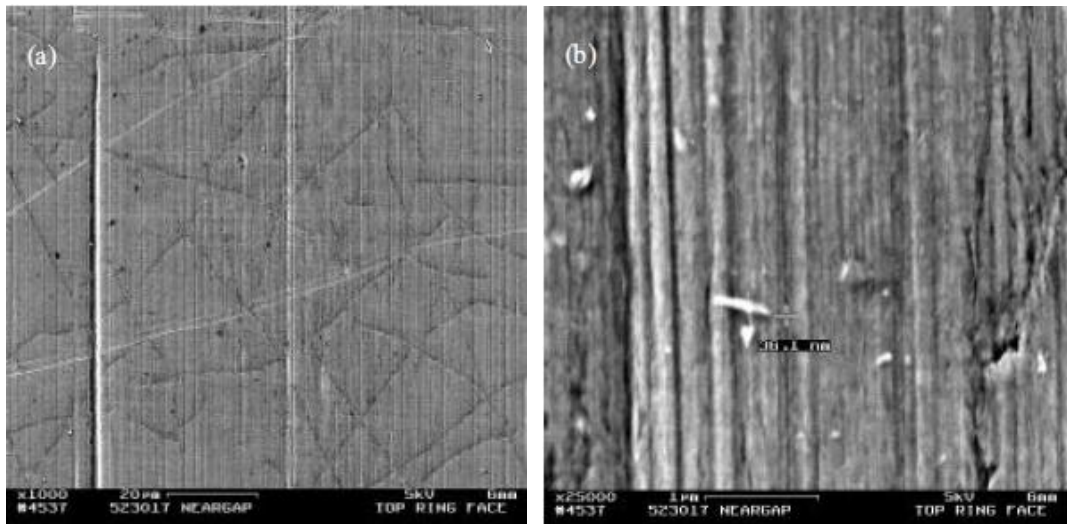
Figure 3.11: SEM micrographs of M-11/EGR top ring face showing massive vertical, parallel grooves

3.4   Carbon black as a diesel soot surrogate

Running a real-life engine investigation of diesel soot would be very herculean in terms of cost and time as it takes very long for soot to build up to appreciable level for meaningful results [2, 53, 88]. Similarly, extraction of real soot (for experimental studies) from used engine oil can be very laborious just as getting enough quantity for series of experiments can be a challenge. Also pertinent is the fact that the quality of generated soot varies from engine to engine, in terms of carbon graphitisation, size, chemical composition and dispersion properties [89]. The use of commercial carbon black therefore comes handy, as surrogate for engine soot, in the study of soot influence on the wear of engine components and performance of the lubricating oils [90]. And, it has continue to achieve this purpose with remarkable opportunities for repeatable experiments from which reliable data are obtained [2-4, 6-8, 84, 91-93]. One very important advantage of using carbon black as soot surrogate is that it gives an evaluation of the direct effect of soot in wear and friction studies. Since the real-engine lubricant undergoes various changes in the course of the engine operations, isolating the direct effect of soot may be difficult if not impossible.

Figure 3.12 is an illustration of comparative images (taken with high resolution transmission electron microscopy) of carbon black and diesel soot showing their morphology, chemical composition and particulate diameters.

25
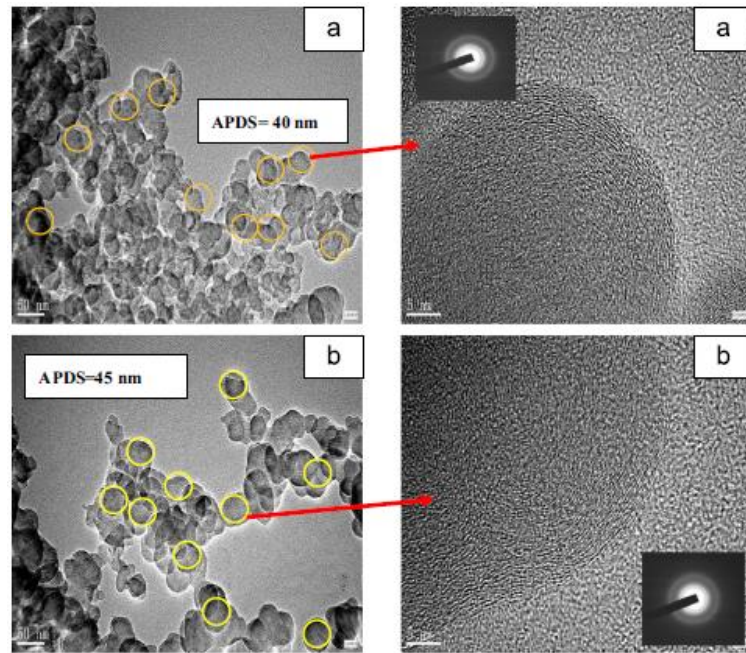
Figure 3.12: HRTEM images of (a) carbon black and (b) engine soot [91]

Clague et al. [13] carried out an extensive comparative analysis of real diesel engine oil soot as well as exhaust soot with 5 different types of commercial carbon black and arrived at the conclusion that there is strong semblance between both soot types and carbon black samples, especially, regarding their primary particle sizes and structure; hence they can effectively mimic some behavioural patterns of diesel engine soot.

Uy et al. [14] compared six samples of soot (from exhaust and extracted from used oil) from gasoline turbocharged direct injection (GTDI) with tendency to generate more soot and diesel engines, along with a sample of carbon black (Mogul L); looking at their morphology and chemical compositions in relation to wear effect on the engine components. Although the results show that the carbon content was highest for Mogul L, followed by diesel soot and then GTDI soot; nonetheless, they still exhibit similarities in their primary particle sizes and structure, while their chemical compositions are the main difference. The authors concluded that their chemical differences, attributable to after-effects of primary particles formation processes, influence their polarity and hardness with possible impact on the observable component wear and wear mechanism in the two engines.

Leveraging on this, Growney et al. [53] carried out an all-encompassing comparison of diesel soot with Regal 250R carbon black. The parameters examined include particle size, morphology, surface chemistry and specific surface area among others. The results revealed significant similarities in their morphologies, grain sizes (70 nm for CB and 50 nm for diesel soot) and densities (1.89 g/cm^3 for CB and 1.94 g/cm^3 for diesel soot) with some noticeable differences in their surface elemental compositions. Their conclusion, though with some reservations, was that some carbon black grades can be suitable as a surrogate for studying the behaviour of diesel soot. Presumably, their reservations were based on the fact that the work was limited to a specific grade of carbon black (Regal 250R). Pahalagedara et al. [94] carried out a rigorous investigation of two diesel soot samples and 10 different commercial carbon black samples looking at the correlations between their oxidation activity and structural characteristics, like primary particle size, specific surface area, amorphous nature and degree of crystallinity. The work established that higher particle size and lower surface area are linked with lower oxidation activity and vice versa. The same trend was

observed by Sharma et al. [95] in their study of oxidation kinetics of over a dozen samples of commercial carbon black and a diesel engine soot sample. Both groups concluded with a verdict of strong link between the oxidation activity and structures for all the samples investigated.

However, Muller et al. [88], in comparing the raw exhaust sample of black smoke soot generated from a Euro III stationary heavy duty Diesel D2876 CR-Engine at 30% load with commercial lamp black from Degussa (FR 101 33/D), have a contrary opinion. The focus was on their physical and chemical differences with emphasis on their oxidation behaviours. They concluded that carbon black could not be suitable as the diesel engine soot model. A similar observation was made from their study of Euro IV HD diesel soot and selected industrial carbon black [96].

It can be seen from the foregoing that so many of the research works so far tilt towards the similarity and this is not unexpected as formation processes of carbon blacks and automotive engine soot have so many common features [13].

Table 3.1 presents a summarised comparison of diesel soot and carbon black where their key properties are contrasted.

Table 3.1: A comparison of the key properties of diesel soot and carbon black

Parameter	Diesel soot	Carbon black
Primary particle size (nm)	10 – 30	20 – 50
Agglomerates (nm)	120 – 800	200 – 500
Density (g/cm^3)	1.94	1.89
Surface area (m^2/g)	55	43
Chemical composition		
Carbon (%)	$\cong 90$	> 95
Hydrogen (%)	$\cong 2 - 3$	$\cong 0.5 - 0.7$
Oxygen (%)	$\cong 3 - 4$	$\cong 1 - 2$
Nitrogen (%)	$\cong 0.3 - 0.4$	$\cong 0.3$

3.5   Conformal and non-conformal contacts

Geometric conformity of contacts plays major roles in their tribological behaviours. Conformal contact occurs when nominal area of contact is large enough to maintain uniform contact pressure under constant load, despite occurrence of wear [45]. While for non-conformal contact, the area of contact is small compared to the contacting bodies sizes; contact pressure, therefore, continuously varies under constant load as wear enlarges nominal area of contact. Consequently, a test which begins with non-conformal point contact eventually ends with conformal contact as a result of wear; thus reducing the initial contact pressure. Table 3.2 presents a list of conformal and non-conformal components in automotive engine.

Table 3.2: Conformal and non-conformal components in automotive engine

Conformal (fit perfectly together)	Non-conformal (touch at a point or along a line)
Piston rings and bushes	Gears
Bearings (Journal/sleeve/shell, plain, deep groove)	Bearings (Roller/ball element)
Chain linkages	Cams
Clutches	

Conformal contact failures are very rare under ideal lubrication and operating conditions (such as sustainable load, speed and temperature ranges); however, non-conformal contacts eventually fail even under a scrupulously maintained lubrication and operating conditions. The failure mode here is mainly due to fatigue resulting from subsurface voids and cracks.

Warmuth et al. [97] observed that contact geometry influences fretting wear behaviour in terms of the level of wear, the type of debris formed and the retention of formed debris within the contact region. There was more wear with less-conforming contacts; more-conforming contacts have a higher tendency to form metallic debris, while the debris was predominantly oxide for less-conforming contacts. An increase in contact conformity also increases the period of debris entrapment within the contact [97-99].

3.6   Chain drives and wear problems

Automotive timing drives constitute one of the most critical components within the engine. The chain-drive is the preferred mechanism for torque transmission in internal combustion engines due to its high strength to wear ratio [100-102], which implies less damage to the chain because of its relatively better mechanical properties [103]. The chain-drive is of importance to automotive industry because of the advantages of non-slip, less weight and cost, high reliability and durability and more compact transmission when compared to belts and gears, though, at the expense of increased noise and vibration [104].

In recent years, more automotive manufacturers have been adopting chain-driven timing drive systems [23]. Figure 3.13 gives an illustration of the sales of passenger cars according to the timing drive used with a projection into the possible trends in the nearest future. The engines with chain-driven mechanism include, but not limited to Jaguar V8, Chevy LS1, Lexus V8, VW VR6, Ford Modular V8, all current BMW and Mercedes Benz.
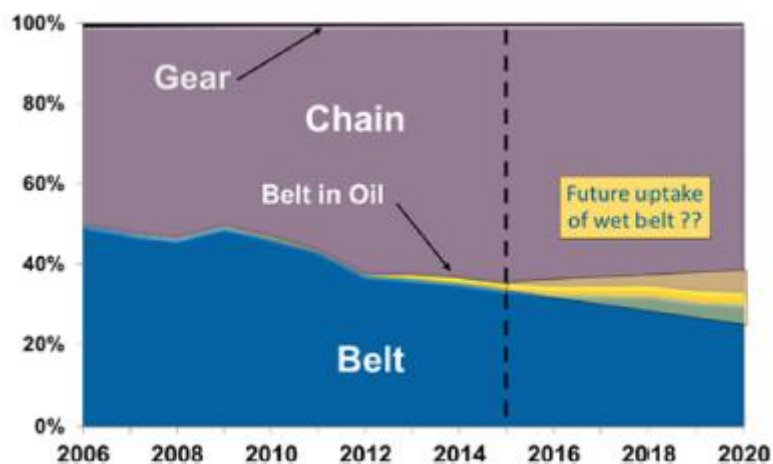
Figure 3.13: Passenger Cars by timing drive system as at 2015 with projection into the future [23]

In automobiles, the chain meshes with sprockets to drive some components; such as the timing mechanism comprising camshaft and crankshaft. As with any metal-to-metal contact where relative motion exists, consideration of wear becomes essential. The chain-drive system is a less investigated part of the automotive engine with tribological contacts; although, there had been a fair share of research on chain-drive involving wear, however, there is dearth of research specifically on soot effects on its wear. Incidentally, the chain is sensitive to lubrication contaminants [101] through increased noise, rough engagement with the sprocket and breakage.

28

The critical failure mode that can affect chain drives is the elongation resulting from prolonged abrasive wear of the joints between pins and plates [23]; and the rate of chain elongation is highly influenced by the oil deterioration and soot content. Chain stretch leads to angular timing error between camshaft and crankshaft resulting in valve timing offset with consequences on the engine cycle. This may not be noticeable until the vehicle covers several thousand kilometres; starting with timing offset of a few degrees which may aggravate to jumping the sprocket teeth leading eventually to valves break. Figure 3.14 illustrates the effect of chain elongation on valve timing and clearance.
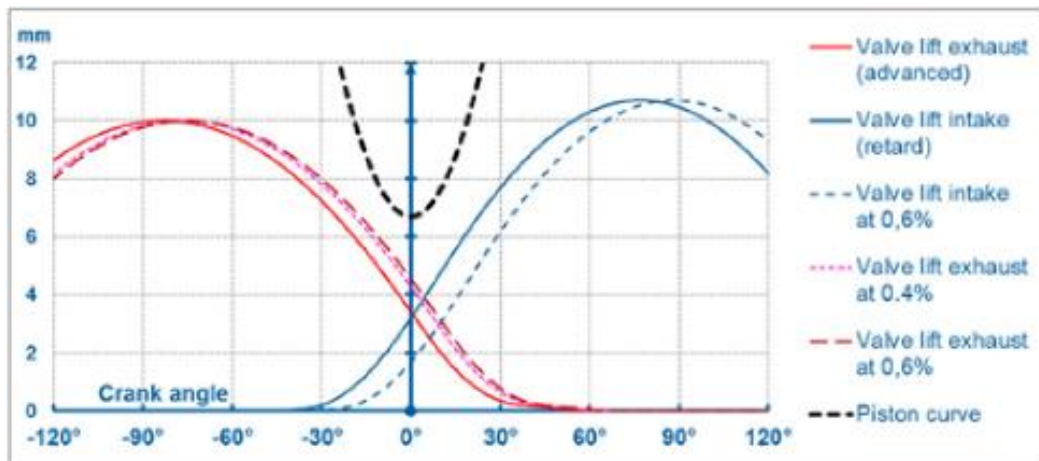
Figure 3.14: Effect of chain elongation on valve timing and clearance [23]

The inconsistency of valve timing, as shown in Figure 3.14, is a major disadvantage of chain drives compared to belt drives. However, on-board detection of the failure mode using sensors to monitor cam timing errors is now being incorporated into automotive engine control systems by some OEMs [23].

The dynamic load distribution of a chain-drive has been studied at a moderate and high speeds theoretically, using modelling techniques [105]; and experimentally by evaluating how it is influenced by material elastic properties [106, 107], lubrication [107, 108], misalignment and speed [108] and geometric variations [107]. The results show that while load distribution is independent of the elastic properties of the chain and sprocket [107], it is dependent on the friction between the sprocket teeth and chain roller [108]. Peeken and Coenen [109] studied the influence of different lubrication conditions on the wear of roller chain investigating application modes, lubricant volumes and viscosities and anti-wear additives. They concluded that with optimal lubrication, wear does not limit the life of a chain; it is rather more influenced by the fatigue strength of the chain component. Radcliffe [110] carried out wear tests on unlubricated articulating chains studying the effects of load, friction, material and environment on wear. It was observed that wear was mainly caused by friction between pin and bushing and variation in wear rate was attributed to wear debris behaving like a solid lubricant of varying effectiveness.

Wada et al. [111] effectively tackled the challenges of noise, weight, size and friction in a cam drive system by developing a single-stage silent chain drive with enhanced wear resistance. Ward and Dwyer-Joyce [112] investigated the failure of the chain tensioner which maintains a constant tension, minimise noise and reduce wear in chain-drive systems. Lee and Priest [113] evaluated different lubricants using a designed test rig to drive chains and sprocket. The measured parameters were power saved and mass loss with each lubricant. Polat et al. [101] also investigated the

performances of different lubricants on a standard type endless bushing chain using accelerated dynamometer to simulate the engine running lifetime. The results show progressive failure resulting from timing chain elongation due to wear between pins and bushings.

Torrance et al. [114] investigated soot effect in conforming contacts using a pin-in-bush set-up to simulate a chain link. The result indicated that carbon black principally causes wear by removing the protective anti-wear film between the contacts. This was discovered through the use of high resolution SEM which revealed the presence of boundary lubricant film for uncontaminated lubricant; there was little evidence of this film when carbon black-contaminated lubricant was used.

3.7   Automotive engine tribological testing simulation approaches

The load and speed of automotive engines vary continuously due to the actions and reactions of different components interacting with one another. The upward and downward movements of the piston rotate the crankshaft through which torque is transmitted to the camshaft through the timing drive system. Over the cycle, the impulses of various pistons influence the speed of the crankshaft while the torque demand of the camshaft may also be influenced by the cam profiles on one hand and the reaction torque of the valve springs on the other [23].

This is just a glimpse of the complex dynamics that numerous components within the automotive engine undergo and this explains why it would be inappropriate to attribute observed failures on a component to a particular cause in an engine test.

Tribological investigation of automotive engine components can be carried out at various levels ranging from specimens in a bench test to vehicle tests in the field. While a specimen test gives good control and repeatability, but less complexities and less representative, the real engine test produces less repeatability and control but more complexities and therefore more representative [2]. Figure 3.15 illustrates various automotive engine simulation approaches.

Laboratory tests, specimen or component, involve testing under varying conditions where different parameters (temperature, speed, mass, stroke length, lubricant, etc) can be changed at will; the results obtained can then be compared with previous tests that have been done under similar conditions. Apart from being relatively quick and less costly, this approach gives room for screening of materials for application suitability, monitoring performance over time and quantifying the effects of changing each parameter. All these are, obviously, not feasible with real-world testing.

	TEST CONDITIONS	PARAMETER PROPENSITY	RESULTS INTERPRETATION	RESULTS UTILISATION	REPEATABILITY OF TESTS	RESULTS SIGNIFICANCE	COST IMPLICATION
Real-world Test (Actual vehicle)	Complex	Good	Difficult	Easy	Poor	Poor	Expensive
System Test (e.g., Engine dynamo-test							
Sub-system Test (e.g., motorised cylinder-head)							
Component Test (Bench Test)							
Specimen Test (Bench Test)	Simple	Poor	Easy	Difficult	Good	Good	Cheap

Figure 3.15: Simulation approaches in automotive engine [2]

Laboratory tests generally provide platforms for the evaluation of the effect of varying parameters (normal load, sliding speed, temperature, contact geometry, lubrication, etc.) on the extent of wear and wear mechanism attributable to each. They are, however, not an adequate representation of the real situation. Combination of automotive engine operations often yield more severe wear on individual components than when a component is isolated for laboratory observation, however, close the simulation condition is to the real situation. Nonetheless, the use of actual engine components may be the preferred approach towards getting a good representation when evaluating the effect of various parameters on individual components. Unfortunately, only few researches are actual engine components based; and even fewer are soot-related. Specifically, there is a dearth of research on chain-drive system wear emanating from soot effects.

3.7.1 Research methodology

The research methodology adopted is sequential, moving from specimen to component. The initial set of tests which involved ball-on-flat specimen was aimed at replicating some previous work to ascertain the behavioural patterns of various compositions of the sooty-oil as well as build confidence in this test method; this simulates contact between elephant's foot and valve tip of the automotive engine valve-train system. The test then moves to disc-on-disc, mini traction machine (MTM) test, which simulates automotive engine's cam lobe and roller follower contact. Although both test are non-conformal, ball-on-flat operates under initial Hertzian point contact while geometric contact condition for disc-on-disc is line contact.

The test then graduated to conformal contact using pin-in-bush (PIB) to simulate chain link articulation. This approach was utilized in a component test using a dedicated design of chain-sprocket rig.

Figure 3.16 shows a flow-chart illustrating the proposed research methodology for this study with indicators of how various testing approaches vary in complexity, representation, control, repeatability and cost effectiveness.

Specimen Testing	Component Test	System Test
Non-conformal **Ball-on-flat HFRR (Plint TE77)**		**Chain System (from real engine)**
Non-conformal **Disc-on-disc MTM (Plint TE54)**	**Chain-Sprocket Rig**	
Conformal **Pin-in-bush (Chain link simulation)**		
Increasing complexity, more realistic		
Increasing control, repeatability, cost effectiveness		
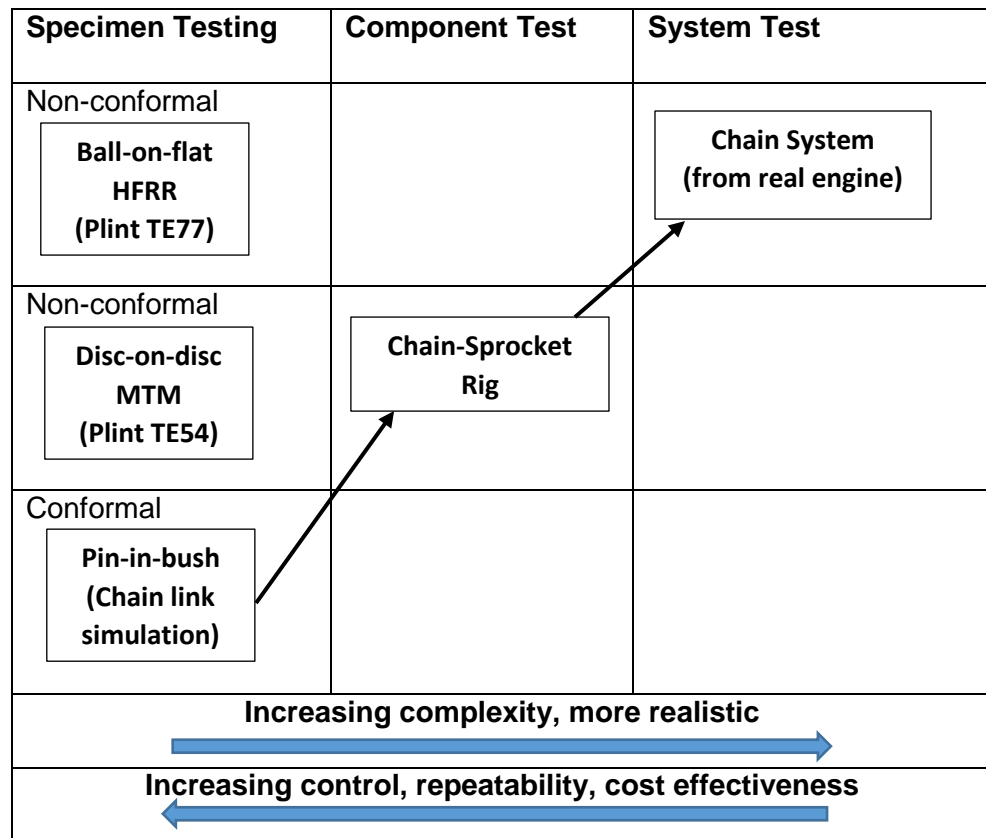
Figure 3.16: A flow-chart illustrating simulation stages for tribological testing

3.8   Comparison of the observations

This section looks at some previous research works in the area of soot-contaminated lubricants with a view to identifying common trends and gaps associated with various parameters.

3.8.1 Common trends

Virtually, all the researchers in this area observed that increase in wear is a direct consequence of increasing levels of carbon content in oil. In fact, Sato et al. [87] assertively stated that wear increases proportionally to the soot concentration when the characters of soot and fresh oil are the same.

On wear mechanisms, Abrasive wear is mostly common in the observations attributive to the soot content and starvation of lubricant in the contact. In addition, Penchaliah et al. [76] observed that oxidation produced polishing wear along with abrasion, while corrosive wear emanated from sulphuric acid and moisture.

Adhesive wear may be experienced with higher load or higher soot levels when soot agglomeration blocks lubricant access to contact zones resulting in material transfer between the contacting bodies, especially from the softer material to the relatively harder one. While fatigue wear may result when high contact pressures are applied between surfaces in repeated rolling or sliding action due to very high local stresses [40].

Green and Lewis [6] using the valve train components test, observed that high levels of abrasive wear were exhibited by worn rocker pads and valve tips. While Truhan et al. [79] testing with cylinder liner/ring contact, observed that liner wear rate was relatively higher than that of the ring; asserting that, quantitatively, wear rates for the liner was about double that of the ring.

In the estimation of the friction coefficient and viscosity, there is a strong correlation between soot or its surrogate content and lubricant viscosity/friction coefficient [6, 76, 79, 115] tough not necessarily linearly [77].

On the use of exhaust gas recirculation (EGR), Nagai et al. [72] highlighted the detrimental effects of EGR as it increased valve train wear, oil degradation and piston deposits. A similar trend was noted by Aldajah et al. [9] who observed that while EGR effectively reduces NOx emissions it negatively deteriorates engine oil as a result of increased soot loading and acid content. They also observed that EGR tests, though noisier, recorded about 10% reduction in average friction coefficient. Singh et al. [10] corroborated these findings with their observations that EGR operated engine produced higher soot deposits and higher soot loading than the engine without EGR. In addition, used lubricating oil from the EGR operated engine contained more heavy metals content; an indication that wears are more severe in an engine with EGR.

3.8.2 Research gaps and unknowns

A few gaps are noted in some of the works; for instance, Aldajah et al. [9] and George et al. [77] observed nonlinearity in this correlation between wear level and carbon black content of the lubricant. Also, Antusch et al. [73] observed that soot particulate concentration is not solely responsible for wear properties seen as soot morphology, surface chemistry, and reactivity play more significant roles. He further observed that the materials abrasion is significantly influenced by additives adsorption and chemisorption from sliding surfaces.

In the estimation of the friction coefficient when carbon black was used in the CDSAE15W-40 formulated lubricant, Hu et al. [84] found that the coefficient of friction decreased to a contamination level of 4wt%. This was attributed to the combined effects of uniformity in the dispersion of carbon black and the additives in the lubricant.

From these observations, it can be summarized that:

➢ Linearity of wear relationship with soot content is dependent on the mixture homogeneity level,

➢ Observed wear mechanisms range from abrasive, polishing and corrosive wear to adsorption and chemisorption,

➢ Wear rate of automotive components also varies from one tribological contact to the other,

➢ The variation of viscosity/coefficient of friction with soot content is dependent on the level of dispersancy of the soot or its surrogate,

➢ EGR effectively serves the purpose of reducing the atmospheric pollution through NOx reduction but increases soot loading, acid and metal contents in the engines thereby shortening the life span of the engine.

The areas of research that have not been explored in the study of automotive soot are: numerical simulation and modelling of soot wear, soot effects on wear of actual engine

components and the wear and friction performance of non-metallic materials used in ICEs.

The literature on numerical simulation and modelling of soot has been limited to its formation [116-119], oxidation [120, 121] and particle size distribution [122, 123]. An area of automotive soot study that has not received any attention is modelling of soot wear mechanisms, because they are still not fully understood. The complexity of soot wear mechanism makes the task of accurately simulating and predicting soot wear behaviour very difficult [124]. Nonetheless, work in this direction is overdue.

The use of actual engine components may be the preferred approach towards getting a good representation when evaluating the effect of various parameters on individual components. Unfortunately, only few researches are actual engine components based. Green et al. [6] studied the effects of soot build-up on the elephant's foot and valve tip; while Truhan et al. [73] used segments of piston rings on flat specimen (as cylinder liner) to evaluate friction and wear behaviour of soot-contaminated lubricant. These are the only available literatures on soot-related component-based wear test.

3.8.3 General conditions in a diesel engine

Diesel engine, generally, operates under a harsh environment; in terms of high temperature and reactive decomposition of lubricating oil. Soot level in such an engine can be as high as 8% [50] or more. The decision to simulate up to a carbon black contamination level of 12wt% was to study the anticipated trends that may emanate from the requirements of extended drain intervals which has been predicted to raise the engine soot level to 10% or more [2]. The choice of SAE 15W-40 was also based on the fact that it has been an effective mineral oil-based lubricant satisfying the needs of heavy-duty diesel engines over the years [32]. The selected speed for the ball-on-flat test, 2000 rpm (33.33 Hz), is the average operating speed of the valve train when the engine operate at the speed of 4000 rpm [7]. The load range selection was similarly hinged on the fact that at an average engine speed of 2000 to 4000 rpm, the thrust force generated on the cam base circle can range between 50 N and 250 N [125].

3.9 Conclusions

One fact that is clear from the literature is that the knowledge of soot-induced wear mechanism is still evolving as new revelations are unfolding year in year out. The reasons for the rather conflicting and somewhat contradictory observations by various researchers are understandable. Firstly, automotive soot has a variety of structural complexities which depends on the type of engine and its operation. The consequence of this is that, though, soot particulate comprises basically similar elements, but in varying degrees and sizes. Their structural arrangement and ordering is another point of departure. Commercial carbon black is also affected by the same challenge as its production process dictates its final properties. Hence, the need to always give adequate information, in terms of the parameters of the materials used for any research work.

Researches has shown that an abrasive wear mechanism is the most dominant of all the postulated theories of soot-induced wear of ICE components. The impact of variations in the hardness of soot produced by light-duty and heavy-duty vehicles, as well as those produced by the same engine therefore becomes a major concern when using real engine soot in wear studies. A further justification for the use of carbon black as soot surrogate in laboratory investigation of soot.

The focus of the automotive manufacturers, now targeted at designing and producing highly efficient and environmentally friendly vehicles in fulfilment of the requirements of fuel consumption reduction, extended drain intervals and more importantly emission

reduction which are achieved through retarded timing, raised piston rings, selective catalytic reduction (SCR) and the use of exhaust gas recirculation (EGR). However, these emerging technologies come with their attendant consequences.

A more compact engine to minimize fuel consumption implies increase in specific power accompanied by higher cylinder pressures and oil temperatures; while emission reduction through the use of EGR results in soot build-up with consequent increase in lubricating oil viscosity which in-turn may lead to pumpability problems and increase fuel consumption.

The challenge of formulating thinner oils in fulfilment of demand for improved fuel economy comes with the risk of engine component wear resulting from solid-to-solid contact.

In the same veins, use of lead-free fuel and the recently proposed replacement of ZDDP additives to enhance performance of catalytic converters in emissions reduction could threaten critical engine components as the beneficial tribofilms formed by lead and ZDDP to ameliorate the severe tribo-pairs contact conditions are eliminated.

The deleterious effects of soot build-up are obvious and the role that the evolving automotive technology, as dictated by the need to comply with stringent emission legislations that continue to be periodically regularly reviewed, will play in furthering that build-up is enough justification for continuous research aimed at ameliorating its effects on engine performance.

The purpose of this research work which is focused on diesel engines and diesel soot is, therefore, to determine the effects increasing soot levels have on wear of simple specimen conformal and non-conformal contacts. Secondly, it will study the wear effect on a chain-sprocket contact, being real engine component test and further extend this to a real application (system). The overall aim is to reduce soot-related wear in internal combustion engines (ICEs) by identifying critical threshold for components wear.

To fulfil the aspect of this research work that concerns studying how increasing soot levels affect wear of valve train components involves conformal and non-conformal tests of various specimens, simulating progressive engine wear processes with different materials and contact conditions using carbon black as soot surrogate. These tests are illustrated in Figure 3.16, comprising: ball-on-flat (point contact) and disc-on-disc (line contact) both non-conformal simulation of elephant's foot/valve tip contact and cam lobe/roller follower contact respectively. Also, conformal pin-in-bush set-up was designed to simulate chain link contact; this rig was adapted for component test involving chain and sprocket specifically from Mercedes Benz M271 engine (2005 C180 Kompressor Model).

Interestingly, a chain was obtained from an engine of the same model that has covered 206,000km mileage in the real-world. The chain along with the oil drained while changing it were subjected to various types of analysis, giving us a unique opportunity for comparison with the laboratory-tested components.

Chapter 4

Sooty-oil Preparation and Viscosity Measurement

This chapter deals with the processes involved in the preparation of the sooty oil, analysis of the relationship of viscosity with pressure and temperature; and the measurement of the viscosities of sooty-oil surrogates at different temperature. The procedure adopted in characterisation of the specimen surfaces was also highlighted.

4.1   Sooty-oil surrogate constituents

The sooty-oil surrogate is a blend of fully formulated automotive mineral oil, Shell Helix-HX5 SAE 15W-40 and carbon black particles mixed in varying proportions. Table 4.1 shows the properties of the lubricant and carbon black which was obtained from Alfa Aesar Company. The data sheets of the mineral oil and carbon black are attached as Appendix I and Appendix II respectively.

Table 4.1: Test lubricant and carbon black

Substance	Name	Description
Lubricant	Shell Helix-HX5, 15W40 (formulated mineral oil)	Kinematic viscosity @ 40°C = 106.00 cSt; Kinematic viscosity @ 100°C = 14.27 cSt; Density @ 15°C = 865.8 kg/m^3.
Carbon black	Carbon black, acetylene, 100% compressed.	**Physical and Chemical Properties** Form: Powder, Colour: Black, Smell: Odourless, Purity: 99.9+%, Melting point/range: 3652-3697°C, Boiling point/range: 4200°C, Ignition temperature: 900°C, Surface area: 75m^2/g, Particle density @ 20°C: 1.8-2.1g/cm^3, Solubility in water: Insoluble.

4.2   Sooty-oil mixing process

Sooty-oil surrogates of varying percentage compositions, 0wt%-12wt%, were prepared using an ultrasonic agitation at 60°C for 20 minutes. The use of the ultrasonic bath (Camlab CamSonix C950T) was to reduce the chances of oil aeration. A digital overhead stirrer (SciQuip Pro-40) was also used to mechanically homogenize the mixture; adjusting its speed from 60 rpm to 100 rpm in 10 rpm steps after every 4 minutes. Figure 4.1 shows the pictorial view of this arrangement.

A visual assessment of the mixtures showed that the level of homogeneity appeared uniform except for 10wt%CB and 12wt%CB where there were some agglomerations. This obviously results from high carbon black concentration.
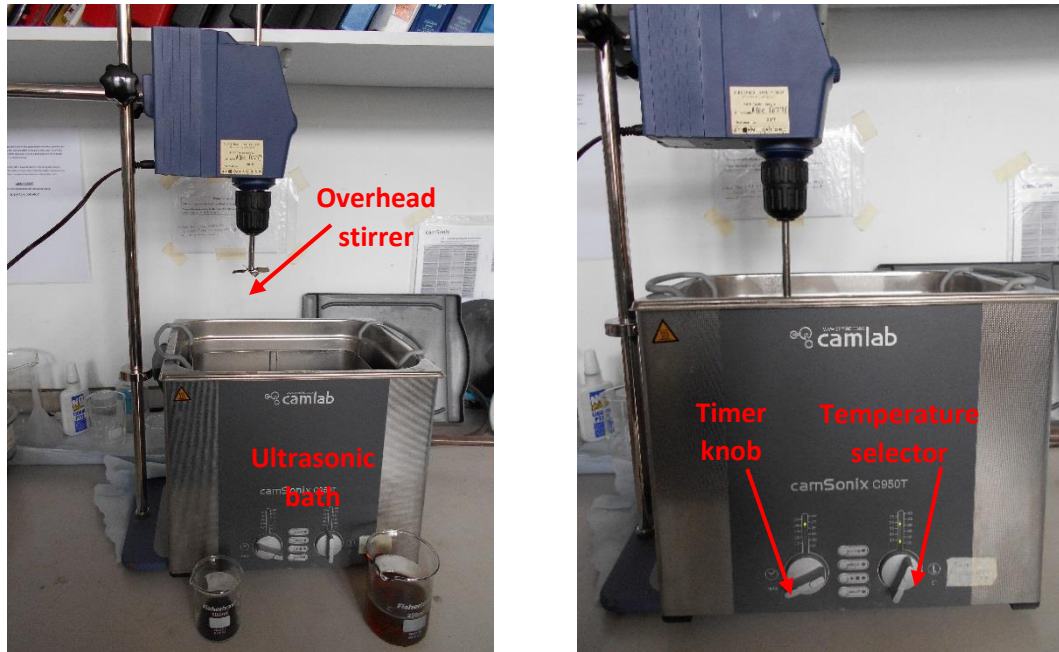
Figure 4.1: Pictorial views of sooty oil mixing process

Previous studies on soot have always been limited to less than 10wt% soot contamination. However, the idea of as high as 12wt% carbon black contamination was primarily mooted since the ultimate focus is to study the effect of soot on chain-drive systems where materials can take a very long time to wear. So, for a laboratory test, an acceleration of wear rate is necessary to produce some measurable wear within a reasonable length of time.

Secondly, it could also serve the purpose of revealing the anticipated trends with the requirement of elongated oil drain intervals mentioned earlier whence it is expected that soot contamination levels in real engine may be as high as 10wt% and above [2].

The sooty oil preparation methods described here were replicated for all subsequent studies reported in the thesis. They surrogates were actually prepared in two batches; the first was prepared in appropriate proportions and stored in 100 ml bottles. This was used for ball-on-flat tests. The second batch was similarly prepared, but in larger quantity and stored in 500 ml bottles. This was used for all other tests and they appeared quite stable throughout the testing period, spanning 15-18 months.

4.3 Sooty-oil viscosity measurement

Oil viscosity is one of the most important parameters in the lubrication system of a tribological contact. The main function of a lubricating oil is to form and maintain a film thickness between two rubbing surfaces and this vital function depends mainly on the viscosity of the lubricating oil. Whenever this parameter is not within a specified range in any automotive tribological contact, the resultant effect can be catastrophic failure emanating from increased friction, wear and heat.

At low concentration, sooty oils possess enhanced viscosity behaving like a solid lubricant especially when well-dispersed; however, high soot concentration can result in oil thickening [5] and excessive increase in oil viscosity which causes pumpability problems [77] due to reduced fluidity [126].

To broaden the understanding of how sooty oil causes wear, the need to measure the correlation between viscosity and various carbon black compositions arises.

A Brookfield DV-II + Pro rotary viscometer manufactured by Brookfield Engineering Laboratories Inc., Germany and supplied by Brookfield Viscometers Limited in Essex, UK, was used to measure the dynamic viscosity of the sooty oil samples. The viscometer is usually used in conjunction with the PC Brookfield application software, RHEOCALC32, which remotely controls the device and enables automatic result display on the dashboard. The unit of viscosity displayed by the dashboard is in centipoise (cP), hence, the specific gravity is required to convert to kinematic viscosity in centistoke (cSt) using Equation 4.1. The specific gravity (which is the dimensionless density value) of each sooty-oil surrogate at a given temperature, T, was derived from Equation 4.2.

$$Kinematic\ viscosity,\ \upsilon = \frac{Dynamic\ viscosity,\ \eta}{Specific\ gravity,\ \rho} \qquad \text{Equation 4.1}$$

$$\rho_T = \rho_{15}[1 - 0.00063(T - 15)] \qquad \text{Equation 4.2}$$

A constant volume of 350 ml in a standard beaker of 600 ml (as recommended) was maintained for each of the samples. The spindle size/speed combination was carefully selected to obtain the torque value of above 10% for all the readings; this is the recommended condition for a valid viscosity reading. Spindle No RV3 at 70rpm was selected based on the fact that it gives a value comparable with the pure lubricant data sheet at 40°C (90.35 cP compared with measured value of 94.86 cP). This was the combination used for all the tests except 12wt%CB where RV6 at 120rpm was used. While measuring the viscosity at various temperatures, the distilled water used for the water bath, Thermo Haake's Circulator DC10, could not heat the samples to 100°C; the highest attainable temperature was 94°C. Consequently, values for 100°C was determined by extrapolation; this was to enable comparison with values on the lubricant's data sheet. The arrangement is shown in Figure 4.2.

A reasonable length of time, about 10 minutes, was allowed to stabilize the readings before recording and test was repeated for each sample thrice and average reading taken. The beaker, temperature probe and spindle were thoroughly washed and wiped dry after each sample test.
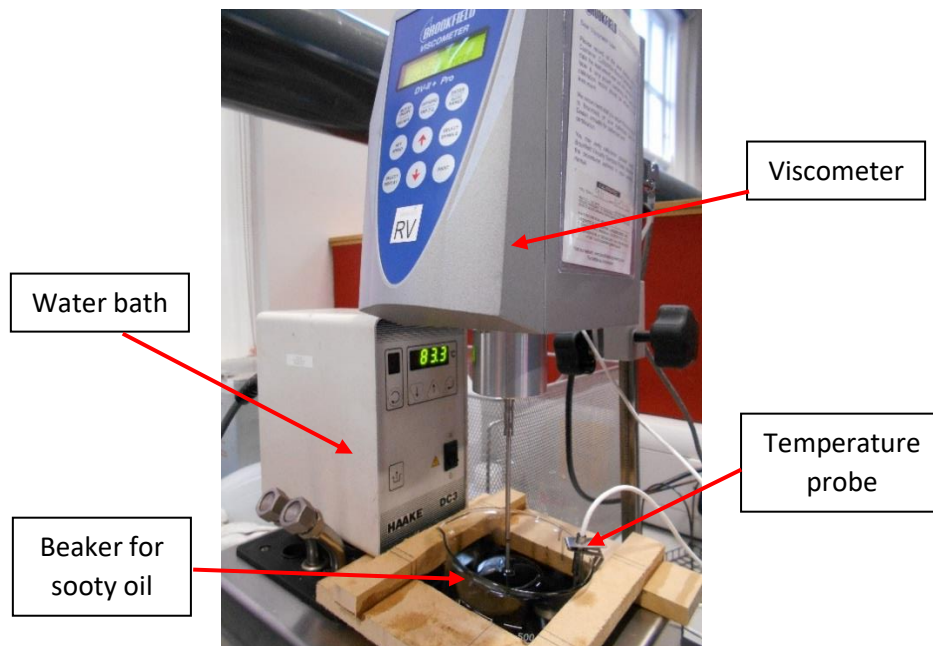
Figure 4.2: Sooty oil viscosity measurement arrangement

4.3.1 Viscosity-temperature relations

The relationship between viscosity and temperature for most lubricant is, generally, inverse. The viscosity of a lubricant at a particular temperature can be estimated by drawing a line through its viscosity values at any two temperatures (typically, 40°C and 100°C). Walther equation, Equation 4.3, relates kinematic viscosity, υ to absolute temperature, T (°C + 273) through such line [127].

$$\log\log(\upsilon + 0.7) = A - B\ log\ T \qquad \text{Equation 4.3}$$

where A and B are constants for any given lubricant

4.3.2 Viscosity-pressure relations

The dynamic viscosity, η of a lubricant to pressure over a wide range of gauge pressure, P can be accurately represented by Roelands equation, Equation 4.4 [128].

$$log_{10}\ \eta + 1.200 = \left(log_{10}\ \eta_0 + 1.200\right).\left(1 + \frac{P}{2000}\right)^z \qquad \text{Equation 4.4}$$

where

η is the absolute viscosity, (cP)

η_0 is the absolute viscosity at $P = 0$ (atmospheric pressure) and a constant temperature, (cP)

P is the gauge pressure, (kg/cm^2)

Z is the viscosity-pressure index, a dimensionless constant.

The viscosity-pressure index, Z, is a characteristic of the lubricant and be estimated for most mineral oils, synthetic hydrocarbons and polyesters from their 40°C and 100°C viscosities by the use of the following relations, Equation 4.5.

$$Z = [7.81(H_{40} - H_{100})^{1.5}\ (F_{40}) \qquad \text{Equation 4.5}$$

where

$$H_{40} = \log(\log(\eta_{40}) + 1.200) \qquad \text{Equation 4.6}$$

$$H_{100} = \log(\log(\eta_{100}) + 1.200) \qquad \text{Equation 4.7}$$

$$F_{40} = (0.885 - 0.864\ H_{40}) \qquad \text{Equation 4.8}$$

The EHL pressure viscosity coefficient, α_{EHL} can be estimated using an empirical equation, Equation 4.9, that involves absolute viscosity at atmospheric (zero) pressure and Roelands' pressure-viscosity index, Z [127].

$$\alpha_{EHL} = Z[5.1 \text{ x } 10^{-9}(\ln \eta_0 + 9.67)] \qquad \text{Equation 4.9}$$

4.3.3 Sooty-oil viscosity

Figure 4.3 presents the kinematic viscosity for different carbon black composition at various temperatures. It is clear from the figure that while viscosity increases with increasing carbon black content, it decreases with increasing temperature; though, the relationship is non-linear. That is, the rate of change in viscosity is not constant with respect to temperature changes. The detailed results are presented as Appendix III.
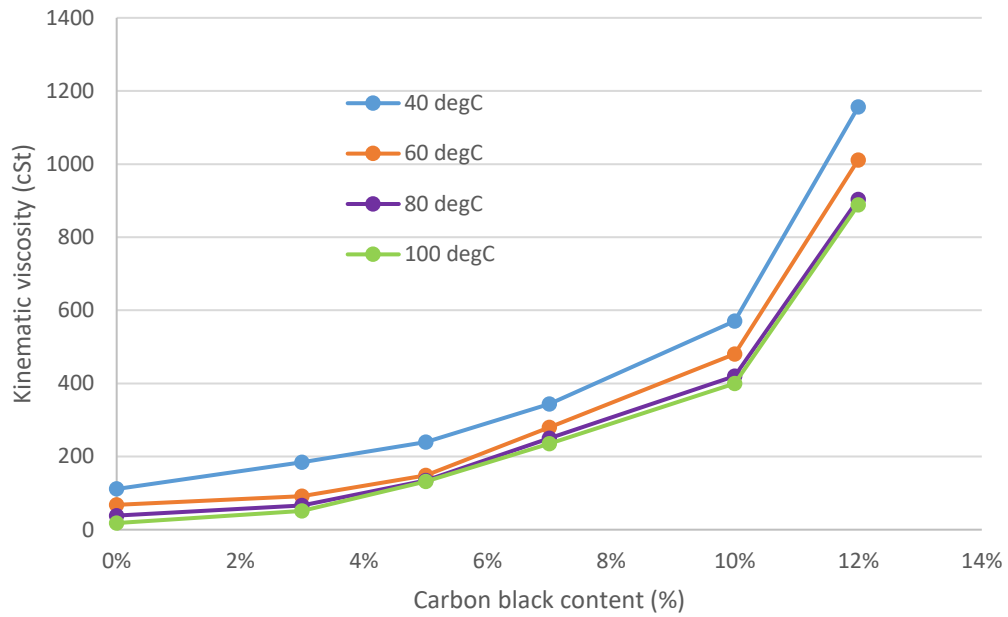
Figure 4.3: Kinematic viscosity of sooty oils at various temperature

Figure 4.4 shows the viscosity measurements for various compositions of sooty oil at 40°C and 100°C. The values obtained are comparable with those of Green and Lewis [6] for 0wt% to 7wt% carbon black contents, the extent to which they measured.
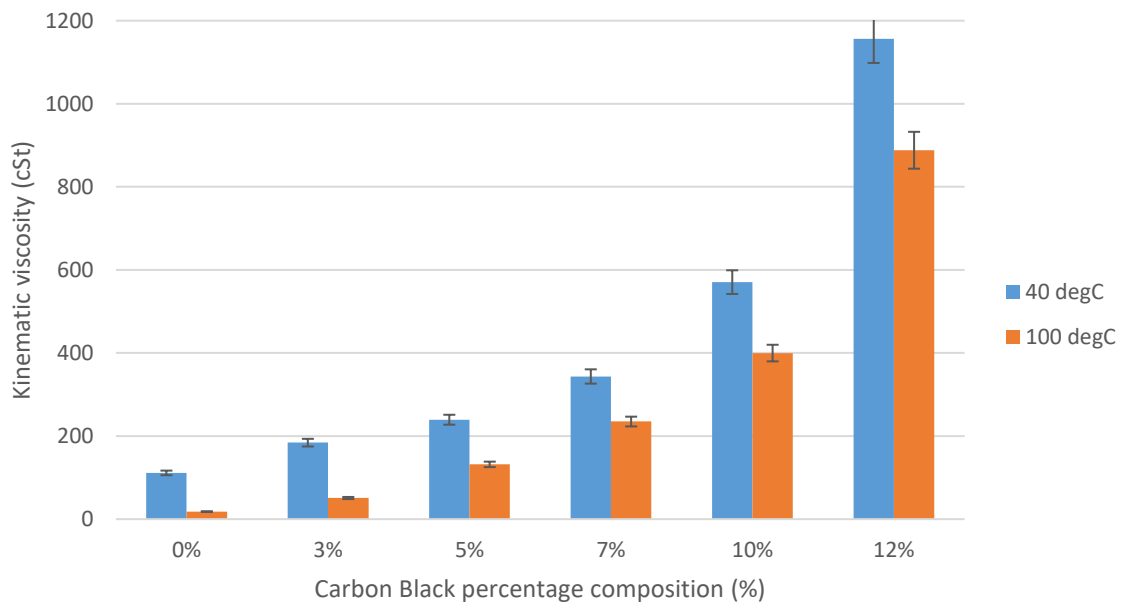
Figure 4.4: Kinematic viscosity values at 40°C and 100°C for various carbon black compositions with percentage error bars

4.4   Characterisation of specimen surfaces

The section highlights the general procedures followed in the characterisation of the specimen surfaces. The peculiarity of each specimen is further discussed at appropriate chapter.

The manufactured specimens, namely: flat specimen, rings, pin and bush were produced through machining and grinding. These specimens along with as purchased (ball specimens) and real engine components (chains and sprockets) were subjected to the following cleaning procedure in line with standard test method [129]:

i.   Washing with a mild liquid laboratory glassware cleaner,

ii.   Drying in hot air,

iii.   Cleaning ultrasonically in acetone for 2 minutes,

iv.   Drying in hot air,

v.   Cleaning ultrasonically in heptane for 2 minutes,

vi.   Drying in hot air.

The specimens were then given a final cleaning after been securely mounted on the testing rigs by wiping their contacting surfaces with heptane-soaked cotton swabs.

Chapter 5

Non-conformal Point Contact Reciprocating Test

Soot-related wear tests have been carried out using several different approaches in the past. These include the four-ball test rig [9, 84] where contact is achieved with a rotating ball loaded against three stationary balls. There are also other methods such as: ball-on-flat [3, 4, 7, 8, 115], pin-on-disc [71, 73, 74, 76, 130] and the Mini Traction Machine (MTM) [6, 131] where ball-on-flat rolling and sliding conditions can be achieved. These tests can replicate aspects of some engine components contacts; for example, the elephant's foot/valve tip contact of the automotive engine valve train is perfectly simulated by the ball-on-flat method with a small stroke length [4, 7].

To partially fulfil an aim of this research work that concerns studying how increasing soot levels affect wear of valve train components, a non-conformal point contact was investigated first. This involved studying the progressive wear processes from cold-starting to full operation with a small stroke (2 mm) ball-on-flat contact condition with boundary lubrication using carbon black as soot surrogate.

Carbon black has become a standard for simulating soot contamination due to its close similarity with diesel engine soot in microstructure, morphology, particle size, porosity and density [132] especially at the primary particle level [13] as variations are manifested in these properties between soot and carbon blacks when aggregated.

5.1   Test equipment

A Cameron-Plint High Frequency Reciprocating Rig (TE77), manufactured and supplied by Plint & Partners Limited, England, was employed for all the tests. This is a standard tribometer, initially used for measuring the lubricity of fuels but is also commonly used as a testing machine for friction and wear measurements [131]. Due to its versatility, this equipment has been adopted by various researchers in modelling and simulating different components of automotive engines [3, 4, 6-8, 78, 79, 131, 133-135]. Elephant foot/valve tip contact and piston rings/cylinder liner contact are some of the ICE components that have been such simulated.

The TE77, shown in Figure 5.1, uses a mechanical drive through a scotch yoke mechanism which converts rotary motion into linear reciprocating motion. The machine has a normal load range of 10 N to 250 N, frequency range of 2.5 Hz to 50 Hz, the stroke length ranges from 0.1 mm to 15 mm manually adjustable through the eccentric mechanism and a temperature range of room to 600°C maximum achievable through a block heater mounted beneath the oil bath where the flat specimen is firmly screwed down.

The desired temperature and mode of test (ramping/dwelling) are pre-set by the programmer for each test. Meanwhile, the calibration is done before each test. Also, a hygro-thermometer was used to measure and record ambient humidity and temperature.

The ball specimen is rigidly mounted into the ball holder after which it is lowered into the oil bath to engage the flat specimen and the loading stirrup clamped to ensure the positioning remains unaltered during testing. The normal load is manually applied through a lever. Figure 5.2 presents the schematics of the ball-on-flat arrangement.
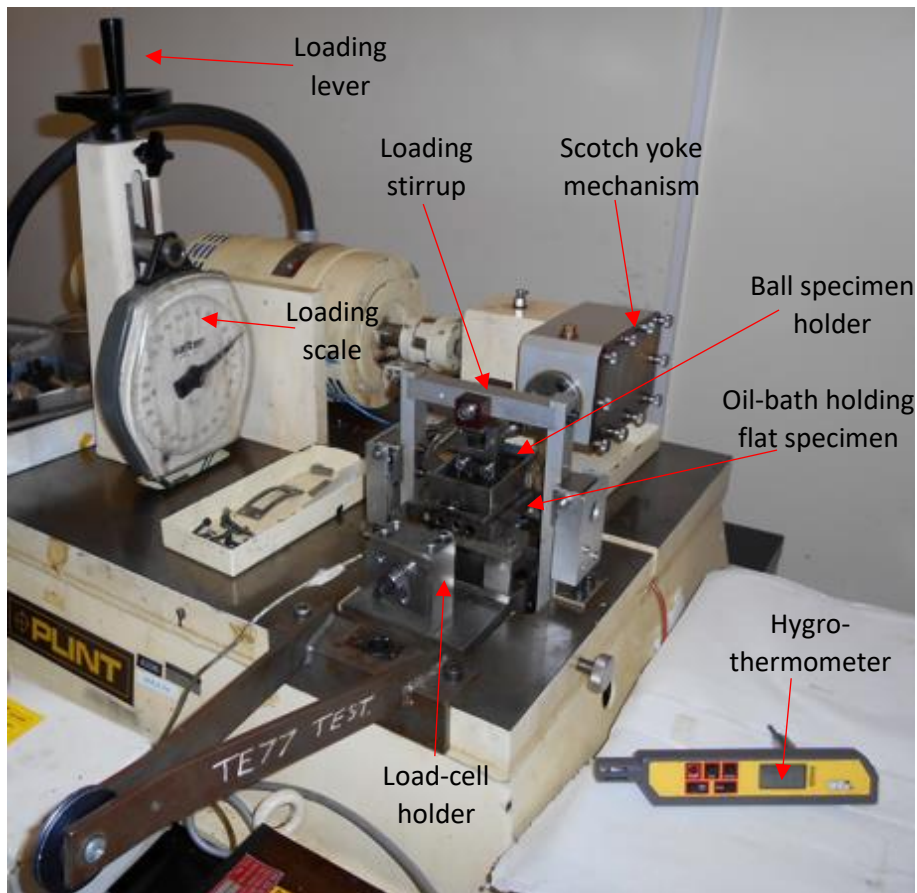
Figure 5.1: Plint TE77 testing machine
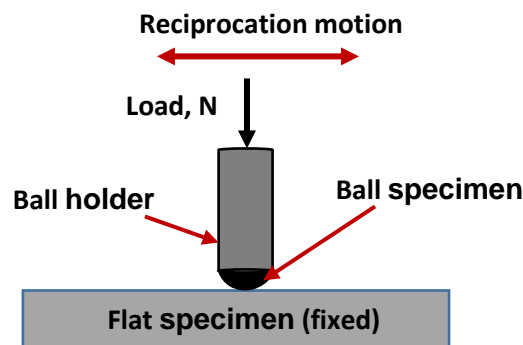
Figure 5.2: Schematics of the ball-on-flat arrangement

The piezo-electric force transducer, which is mounted in line with the contact resists the movement in the horizontal direction, measures the friction forces (positive and negative values) in the oscillating contact. The output is transferred to the data acquisition system and finally captured by the LabView Software. These are subsequently analysed using Microsoft Excel Software and coefficient of friction can be determined using the basic formula in Equation 5.1.

$$\mu = \frac{F}{N} \qquad\qquad\qquad \text{Equation 5.1}$$

5.2　Test specimens

The ball specimen used for this test was made of Chrome Steel EN31 having chemical composition of high carbon and about 1.5% chromium content which offers high degree of hardness with compressive strength and abrasion resistance. Typical application of chrome steel in automobiles is in bearings; however, elephant's feet are also manufactured from heat-treated Chromoly alloy (AISI 4130, majorly comprising chromium and molybdenum including 0.30% carbon) with an enlarged elephant foot surface to reduce valve tip wear [136, 137]. While the flat specimen was EN1561-Grey Cast-Iron which contains 1.5-4.3% carbon and 0.3-5% silicon plus manganese, sulphur and phosphorus. It has a moderate tensile strength and good wear resistance and is easy to cast with excellent surface finish. Its application areas in automobiles include: cylinder heads, cylinder blocks, connecting rods and gearbox cases. Table 5.1 shows their respective mechanical properties, while Figure 5.3 shows their pictorial views with dimensions.

While the flat specimen was drawn to scale and produced through machining, grinding and appropriate labelling in the mechanical workshop of the University, the ball specimen was as purchased. They were thoroughly cleaned using acetone in an ultrasonic bath for 2 minutes, after which they were dried in hot air before testing.

Table 5.1: Mechanical properties of the ball and flat specimens

	Ball Specimen	Flat Specimen
Material	**Chrome Steel EN31**	**Grey Cast Iron EN1561**
Tensile Strength (MPa)	750	250
Average Hardness (HRC)	63	25
Young's Modulus, E (GPa)	215	103
Poisson's Ratio, υ	0.3	0.26
*Average Roughness (μm)	0.05	0.52
*Dimension (metric)	ϕ6mm	66mm x 25mm x 4mm

*Measured values

(a)　　　　　　　　　　　　　　(b)
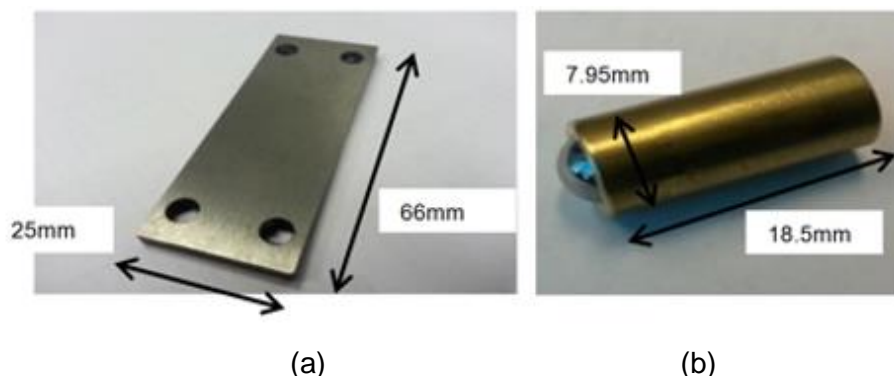
Figure 5.3: Pictorial views of the specimen: (a) flat and (b) ball

The average surface roughness of the ball and flat specimens were measured using a Veeco Dektak 150 profilometer and the average values found to be 0.05 μm and 0.52 μm respectively.

5.3   Calculation of contact parameters

5.3.1 Contact pressure

The maximum contact pressure, p_o, to be used in specimen tests can be determined using Herzian's contact formula:

$$p_o = \frac{3P}{2\pi a^2}$$

Equation 5.2

Average contact pressure, $p_{average}$, is:

$$p_{average} = \frac{P}{\pi a^2}$$

Equation 5.3

Contact area dimensions, a, is given by:

$$a = \sqrt[3]{\frac{3PR'}{E'}}$$

Equation 5.4

Some of these parameters are defined later in this section.

Figure 5.4 shows a schematic diagram of the ball-on-flat contact (a) along with the contact pressure distribution (b) where the contact pressure rises from zero at the edges of contact (where x = ±a) to a maximum value of p_0 at the axis of symmetry (x = 0) with an elliptical form of the contact distribution.
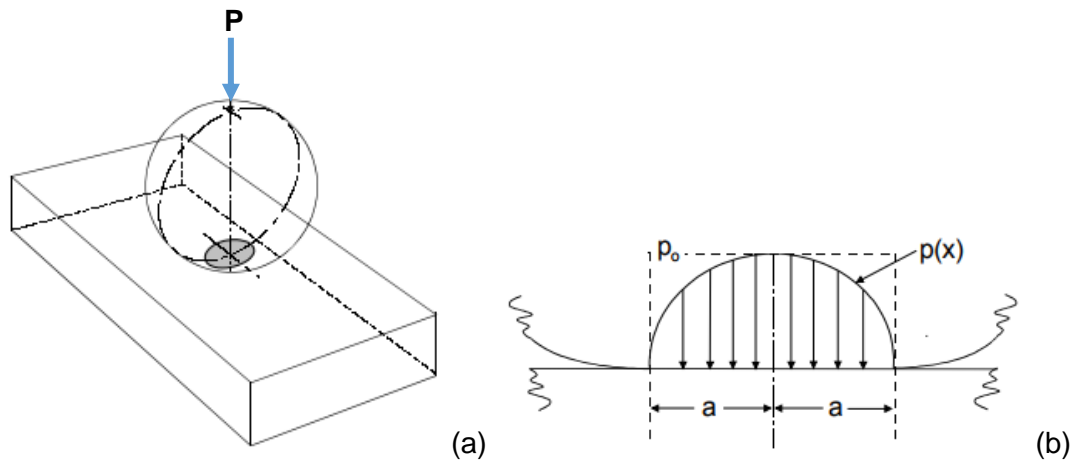
Figure 5.4: Schematic of (a) ball-on-flat specimens and (b) contact pressure distribution [138]

5.3.1.1 Hertzian contact pressure

The initial Hertzian contact pressures (maximum and mean) were theoretically calculated for the normal load of 50N using Equations 5.2 and 5.3 respectively; and then calculated for other loads used in subsequent tests (varying loads). The results are presented in Table 5.2 and Appendix IV shows the detailed calculations. As expected, the contact pressure increases with nominal load and from the values obtained, being higher than 1 GPa, the contact will operate under boundary lubrication conditions. These are the initial contact pressures and it is expected that when contact area increases due to progressive wear, the contact pressure will reduce correspondingly [139].

Table 5.2: Contact pressures at various nominal loads

Nominal Load, P (N)	Maximum Contact Pressure, p_o (GPa)	Mean Contact Pressure, p_m (GPa)
50	1.83	1.22
75	2.09	1.39
100	2.30	1.53
125	2.48	1.65
150	2.63	1.76

5.3.2 Film thickness

To adequately analyse the tribological behaviour of surfaces in contact, it is necessary to determine, theoretically, the oil film thickness of the sooty-oil surrogates. The minimum film thickness (h_{min}) is stated below, Equation 5.5 [40], comprising five non-dimensional parameters. It is obvious from the equation that oil film thickness is directly proportional to the speed at contact point and the viscosity, but inversely proportional to contact load. The formulae derived by Hamrock and Dowson can be applied to any contact [40].

    i.   Minimum-Film-Thickness, h_{min} is determined from:

$$\frac{h_{min}}{R^{'}} = 3.63U^{0.68}G^{0.49}W^{-0.073}\left(1 - e^{-0.68k}\right) \qquad \text{Equation 5.5}$$

where,

    h_{min} is the minimum film thickness, m

    R' is the reduced radius of curvature in the direction of sliding, m

Derived from, $\dfrac{1}{R'} = \dfrac{1}{R_x} + \dfrac{1}{R_y} = \dfrac{1}{R_{x1}} + \dfrac{1}{R_{x2}} + \dfrac{1}{R_{y1}} + \dfrac{1}{R_{y2}}$

Since the contact is between a spherical ball (body 1) and a flat surface (body 2)

Then, $R_{x2} = R_{y2} = \infty$ and $R_{x1} = R_{y1} = R$

$$\therefore \ \frac{1}{R'} = \frac{1}{R_x} + \frac{1}{R_y} = \frac{1}{R} + \frac{1}{\infty} + \frac{1}{R} + \frac{1}{\infty} = \frac{2}{R}$$

Hence, $R' = \dfrac{R}{2}$ Equation 5.6

    R_x and R_y are the reduced radii of curvature in the x and y directions, respectively, m

    R is the Radius of the ball specimen, m

non-dimensional film parameter, H_{min} is:

$$H_{\min} = \frac{h_{\min}}{R'}$$

Equation 5.7

non-dimensional speed parameter, U is:

$$U = \frac{\eta_o u}{E'R'}$$

Equation 5.8

non-dimensional material parameter, G is:

$$G = \alpha E'$$

Equation 5.9

non-dimensional load parameter, W is:

$$W = \frac{P}{E'R'^2}$$

Equation 5.10

non-dimensional ellipticity parameter, k is:

$$k = 1.034\left(\frac{R_y}{R_x}\right)^{2/\pi}$$

Equation 5.11

u is the mean surface velocity in x direction, m/s

$$= \frac{u_1 + u_2}{2}$$

Equation 5.12

E' is the reduced Young's modulus, Pa

$$= \left\{ \frac{1}{2}\left[\left(\frac{1-\upsilon_1^2}{E_1}\right)+\left(\frac{1-\upsilon_2^2}{E_2}\right)\right]\right\}^{-1}$$

Equation 5.13

where,

α is the pressure viscosity coefficient, m²/N

υ_1 and υ_2 are the Poisson's ratios of the respective contacting bodies

E_1 and E_2 are the Young's modulus of the respective contacting bodies

u_1 and u_2 are the velocities of the respective contacting bodies in x direction, m/s

η_o is the absolute viscosity at atmospheric pressure and constant temperature, Pa.s

5.3.3 Lambda ratio

Lambda ratio, λ, is a useful tool in determining the severity of asperity interactions in a lubricated sliding [140]. This ratio is given by the fractional relationship between the minimum film thickness of the lubricant and root mean square of the surface roughness [128],

$$\lambda = \frac{h_{min}}{\sigma^*} \qquad\qquad \text{Equation 5.14}$$

where, $\qquad \sigma^* = \sqrt{R_{q1}^2 + R_{q2}^2} \qquad\qquad$ Equation 5.15

which is the root mean square (r.m.s) of two surfaces, m

R_{q1} and R_{q2} are the r.m.s. surface roughness values for bodies 1 and 2 respectively

$R_q = 1.25R_a$ and is the r.m.s of surface roughness, m

R_a is the average surface roughness, m

The value of λ gives an indication of the lubrication regime operational in the contact. For $\lambda>3$, asperity contact is negligible because a full film prevents both surfaces from touching each other and the lubrication regime is termed hydrodynamic. While for $1<\lambda<3$, where some contact between asperities occurs, the lubrication regime becomes mixed or elastohydrodynamics. Also, for $\lambda<1$, there are significant asperity interactions leading to the boundary lubrication regime.

5.3.3.1 Minimum film thickness and Lambda ratio

The estimated minimum film thickness and lambda ratios at 100°C, using Equations 5.5 and 5.14, are presented in Table 5.3. It clearly shows that each of the parameters increase with carbon black content. The fact that the lambda ratio values are less than one is a clear indication that all the sooty-oil surrogates are expected to operate under boundary lubrication. The spreadsheet showing the detailed calculations is in Appendix V.

Table 5.3: Minimum film thickness and Lambda ratio of sooty oils

Sooty oils	Minimum Film Thickness (nm)	Lambda Ratio, λ
0wt%CB	3.61	0.00553
3wt%CB	6.12	0.00937
5wt%CB	6.80	0.01041
7wt%CB	4.07	0.01113
10wt%CB	9.69	0.01484
12wt%CB	13.10	0.02002

The diameter of primary soot particles are estimated to be approximately 30-50 nm [3, 4, 6, 13, 87, 115, 132]; this is similar to the particle size of the carbon black [13]. While mean soot particle and aggregation sizes are estimated to be 0.2 μm and 0.5 μm respectively [3, 4, 6]. When this is compared with the calculated film thickness above, it is obvious that the carbon particles will greatly influence the amount of wear expected as the minimum particle size is far greater than the maximum film thickness obtainable from the sooty oil compositions used.

5.4   Experimental procedures

The lubricant was used separately in a ball-on-flat specimen contact uncontaminated (0wt%CB) and mixed with varying percentages (3-12wt%CB) of carbon black as soot substitute. Two temperature conditions were adopted, namely controlled linear heating (ramping from room temperature to 100°C) test and high temperature (100°C) test to simulate engine start-up and normal engine working conditions respectively [6, 7]. The steady state temperatures when the engine lubricants are most efficient range between 100°C and 110°C [141]. The contact load range selected was based on the thrust force generated on the cam base circle for an average speed of 2000 to 4000 rpm [125].

Each test was performed three times and measurements taken which proved to be repeatable with an error of ± 3%. The test conditions were as outlined in Table 5.4, while Table 5.5 indicates the plan for the tests.

Table 5.4: General test conditions

S/N	Parameter	Test Conditions
1.	Ball Specimen Radius (mm)	3
2.	Ambient Temperature (°C)	21±2
3.	Relative Humidity (%)	45-55
4.	Normal Force (N)	50
5.	Stroke Length (mm)	2
6.	Oscillating Frequency (Hz)	33.33
7.	Sliding Linear Speed (m/s)	0.133
8.	Test Duration (min)	20
9.	Lubrication	All lubricated

Table 5.5: Specific test plans

Formulated Oil + %Carbon Black							
Set	Test No	0wt%	3wt%	5wt%	7wt%	10wt%	12wt%
A (Ramped Temp.)	1	CLH					
	2		CLH				
	3			CLH			
	4				CLH		
B High Temp. (100ºC)	1	100ºC					
	2		100ºC				
	3			100ºC			
	4				100ºC		
	5					100ºC	
	6						100ºC
C Varying load (100ºC)	1		75N				
	2		100N				
	3		125N				
	4		150N				
D Wear evolution (100ºC)	1		5 mins				
	2		10 mins				
	3		15 mins				
	4		20 mins				
	5		25 mins				
	6		30 mins				

5.4.1 Test A: Controlled linear heating (CLH)-Ramping test

For this set of tests, the Plint TE77 machine was programmed to ramp from room temperature to 100ºC in 10 minutes (while the machine is running, simulating engine warm-up condition represented by CLH1 in Figure 5.5), then to dwell at that temperature for 50 minutes, though the machine was to run at the stabilized temperature of 100ºC for only 10 minutes. The extra minutes were to allow for the stabilization of the temperature as the temperature continues to rise until it reaches a maximum temperature of 125ºC in 13 minutes and stabilizes at 100ºC in 25 minutes. The concluding 10 minutes of this test was done from the 30th minute after the temperature had fully stabilized at 100ºC, represented by CLH2 in Figure 5.5.

The engine warm-up was simulated to assess the level of wear the specimen will likely experience. Lubricant viscosity is, normally, temperature-dependent; hence, at cold start, the increased viscosity at low operating temperatures implies lower thermal efficiency of the ICE [142]. This results in frictional losses [143] and possible increase in fuel consumption [144].
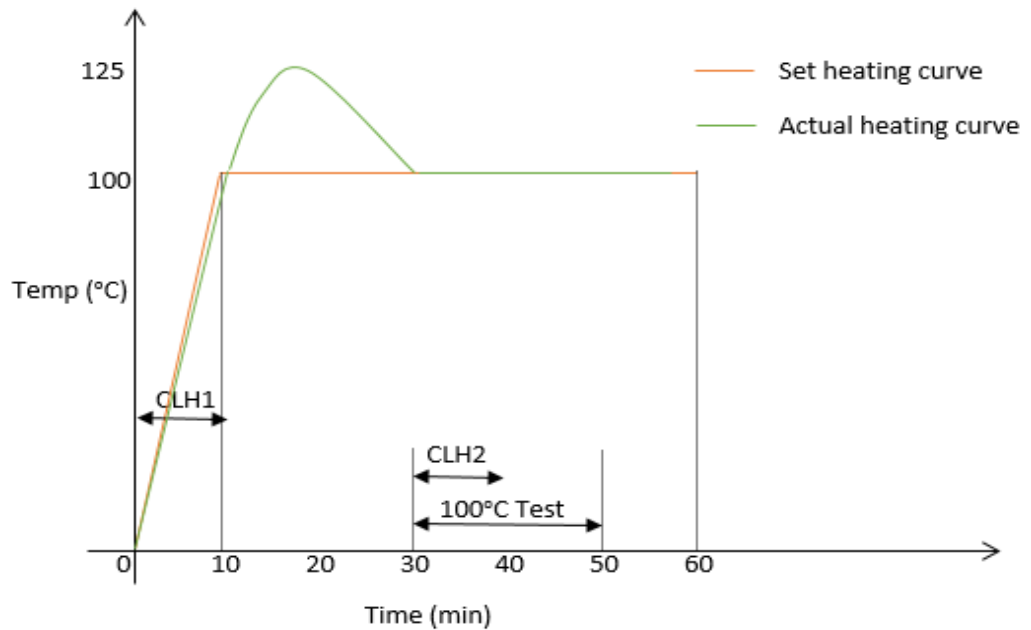
Figure 5.5: Ramping Curve

5.4.2 Test B: High temperature (100°C)

The same programme was maintained for testing at this temperature. However, since the test was to run continuously for 20 minutes at a stabilized temperature of 100°C, the running of the machine only commenced after the first 30 minutes as, by then, the temperature would have fully stabilized. Meanwhile, the ball specimen was lowered into the oil bath to make contact with the flat specimen after the first 20 minutes, this was to ensure that the two specimens run at the same temperature throughout the testing period.

5.4.3 Test C: High temperature (100°C) at different normal loads

Further tests were carried out with varying normal loads using the same carbon black composition of 3wt%CB; this is to study the consistency of the observed trends. These are highlighted below:

C1-4: High Temperature testing for 20 minutes @ 2000 rpm, Normal Load = 75 N, 100 N, 125 N and 150 N.

5.4.4 Test D: High temperature (100°C) tests for different lengths of time

In a tribotest, wear evolves gradually in respect of the conditions under which it is operating. In furtherance of efforts to understand how wear evolves in soot-contaminated contacts, tests were carried out at different durations (5-30 mins) under the same conditions; namely, 0.133 m/s, 100°C, 3wt%CB and 50 N. The aim was to enhance the fundamental understanding of the mechanisms of wear and friction in this contact.

5.4.5 Wear analysis

A series of a priori and a posteriori wear measurements were designed to be carried out to examine the wear resulting from these tests using Veeco Dektak 150 Profilometry and Digital Microscopy (optical and scanning electron). While profilometry is mainly to generate data for numerical analysis of the wear scar, digital microscopy is to generate images for visual observation and interpretation of wear mechanisms.

In wear analysis, the most common method is gravimetric (mass loss) analysis [145]. However, its main limitation occurs when the wear volume is very small. There is also three-dimensional surface profiling which is accurate and reliable, though rigorous in analysing as a result of the number of data obtainable from multiple profiling.

5.4.5.1 Wear scar volume measurement

Qu and Truhan [146] adopted a "single-trace" approach where wear volume is determined from closed-form algebraic equations. The method is more accurate with lesser limitations. Furthermore, Sharma et al. [145] introduced a model where measured width is used to determine wear volume using an improved geometric equation shown as Equation 5.16 below. This model is simple and effective in generating accurate and quick results as only the wear scar width, *w*, is required to be measured while other parameters are the stroke length, *L*, and the radius of the ball specimen, *r*, both of which are known. Figure 5.6 shows the wear scar, assumed to be uniform in shape with measured width and stroke length.

Volumetric calculation of wear scar:

$$V_{total} = L \left[r^2 sin^{-1} \left(\frac{w}{2r} \right) - \frac{w}{2} \left(r^2 - \frac{w^2}{4} \right)^{\frac{1}{2}} \right] +$$

$$\frac{\pi}{3} \left[2r^3 - 2r^2 \left(r^2 - \frac{w^2}{4} \right)^{\frac{1}{2}} - \frac{w^2}{4} \left(r^2 - \frac{w^2}{4} \right)^{1/2} \right] \qquad \text{Equation 5.16}$$
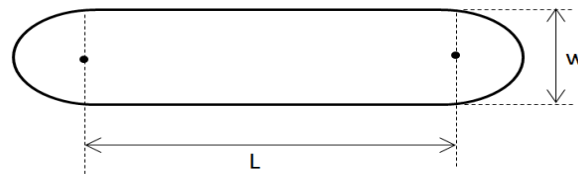
Figure 5.6: Wear scar profile showing measured width and stroke length

The wear scar profile was measured both transverse and parallel to the sliding direction using the profilometer to determine the width and roughness profile respectively. While width measurement was taken at five locations that of roughness profile was taken at three locations.

There are two major reasons why wear here cannot be quantified by mass-loss measurement which involves measuring the mass before and after the test and determining the net mass reduction. Firstly, the wear scar is relatively very small ($\cong$ 2mm) relative to the size of the specimen; secondly, the materials are displaced to the sides of the wear scar rather than being fully removed. This is not unexpected when grey cast iron, which is porous, undergoes lubricated testing [147]. Ductility of grey cast iron may have also contributed to this observation.

5.5   Sooty-oil film thickness measurement

The importance of the lubricant film thickness in determining the level of protection the contacting bodies enjoy has earlier been mentioned. This role could be maximized with the continuous monitoring of the lubricant film thickness, automatically, during operation. An attempt was, therefore, made at measuring the instantaneous film thickness of selected compositions of the sooty-oil surrogates using ultrasonic

technique with embedded sensors connected to the FMS-100 and fitted to the Plint TE77 head. The purpose of this test is to measure the film thickness of sooty-oil surrogates in real time. The surrogate compositions tested were 0wt%, 1wt%, 3wt% and 5wt%CB, to simulate used oils with varying soot contents.

One major hindrance to the experimental measurement of film thickness in used oil is that the soot content prevents transmitting of the light when using optical method, especially at high content [87]. Ultrasound can, however, be reflected from a layer of liquid between two contacting bodies [148]. This reflection is influenced by acoustic properties of the liquid and the contacting solids, as well as the ultrasonic frequency and the liquid thickness layer. If the other parameters are known, the thickness of the liquid layer can be determined from the resonant response.

5.5.1 Theory of ultrasound

Sound is a travelling wave which propagates through a host medium. An ultrasonic wave is a sound wave with a frequency beyond the human audible range, typically taken as 20kHz and above [149]. Ultrasonic transducers can be used to generate longitudinal waves and transverse waves, both of which support sound wave propagation through a solid medium. In longitudinal waves, the particles oscillates parallel to the direction of wave propagation; while in transverse waves, the oscillation of the particles is perpendicular to the wave propagation direction.

5.5.2 Speed of sound

If the speed, c, that sound takes to travel through a material is known, then, an ultrasonic pulse can be used to determine the thickness, d, of the material using the speed, distance and time relationship; to and fro movement implies twice the thickness of the material.

$$d = \frac{ct}{2}$$
Equation 5.17

5.5.3 Acoustic impedance

Acoustic impedance, z, of a material is a measure of the resistance the sound wave encounters while passing through the material; and is defined by:

$$z = \rho c$$
Equation 5.18

where,

ρ is the density of the material, in kg/m^3,

and c is the speed of sound, in m/s

The SI unit of acoustic impedance is pascal second per cubic metre (Pa.s/m^3) or rayl/m^2.

A sound wave passing between two materials is partly reflected and partly transmitted at the interface. The reflected portion is referred to as the reflection coefficient, R. And, this is influenced by the difference in the acoustic impedance between the materials.

For two dissimilar materials, if the wave is assumed to be perpendicular to the interface, the reflection coefficient, in relation to acoustic impedance, is given by:

$$R = \frac{z_1 - z_2}{z_1 + z_2}$$
Equation 5.19

where,

z_1 is the acoustic impedance of the upper material,

and z_2 is the acoustic impedance of the lower material

Acoustic impedance of the tool steel (pin specimen) was estimated to be 4.60 x 10^7 rayl/m^2 while the value for the cast iron (counterface specimen) was 3.74 x 10^7 rayl/m^2.

5.5.4 Measuring film thickness using ultrasonic

The film thickness formed between specimens contact is influenced by the load, speed and surface temperature of the specimens [150]. Consequently, tests are proposed to be carried out varying some of these parameters.

The theoretical estimation of the film thickness for all the sooty-oil surrogates reveals very thin lubricant films. The appropriate method suitable for measuring the lubricant film thickness practically is, therefore, the spring model. This model as expressed in a derivation from Dwyer-Joyce et al. [148] is shown in Equation 5.20:

$$h = \frac{\rho c^2}{2\pi f z_1 z_2} \sqrt{\left(\frac{R^2(z_1+z_2)^2 - (z_1-z_2)^2}{1-R^2}\right)} \qquad \text{Equation 5.20}$$

where,

h is the film thickness,

f is the resonant frequency (in Hz),

and other terms are as defined earlier.

There is also the need to note the reference measurement, in which the reflected surface is made free of any lubricant. The test and reference A-Scan reflections must, therefore, be captured and compared. The reflection coefficient, at any frequency index, is then given by the proportional difference between their frequency amplitudes. Figure 5.7 displays a sample of this. The peak frequency, which gives the highest signal to noise ratio (SNR), is usually the best choice [151].
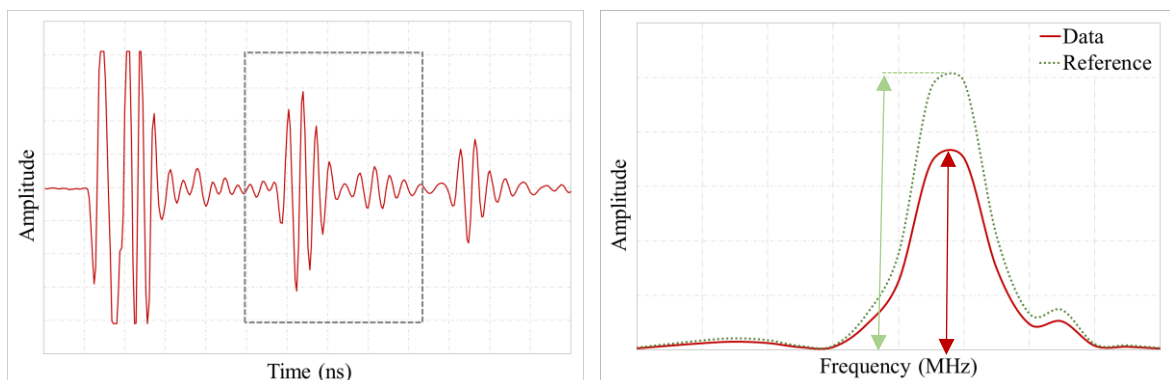
Figure 5.7 Method to determine reflection coefficient [151]

5.5.5 Wave velocity characterisation

The lubricants were first characterised as a prelude to film thickness measurements; this was to determine their wave velocities with respect to temperature. Wave velocity test rig, shown in Figure 5.8 was used for this purpose.

A sample of each oil was filled into the rig and then carefully positioned in a programmable oven. The temperature readings were taken from the thermocouples and the corresponding time-of-flight was measured by an ultrasonic transducer. The time-of-flight, which is the time between reflections and the path length, the distance covered by the wave between reflections, were then used to calculate the wave velocity [151].
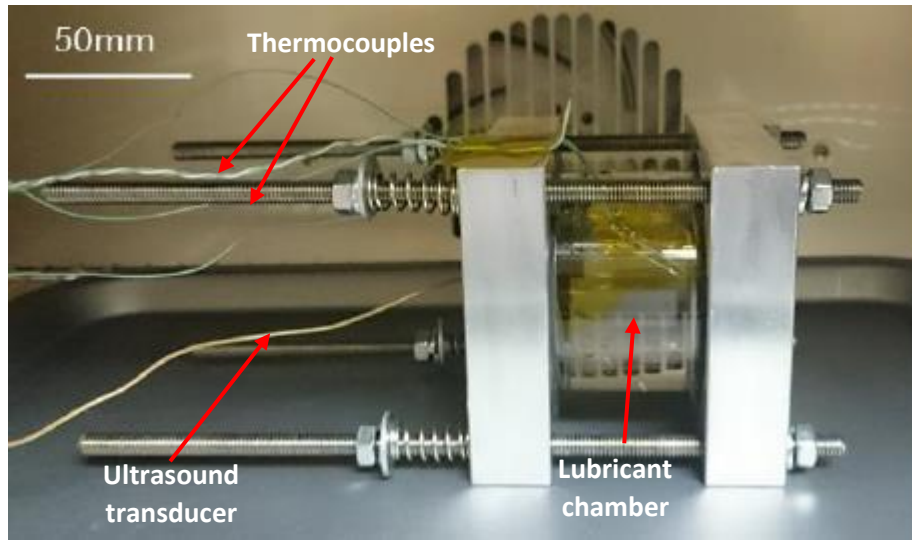
Figure 5.8: Assembled wave velocity test rig in oven [151]

Figure 5.9 presents the results obtained for the 0wt%CB and 1wt%CB oils between 25°C and 120°C. These were the two samples whose speed of sound could be determined before the test rig broke down. Subsequent follow-up will make up for this as the department is currently building a new wave velocity rig.
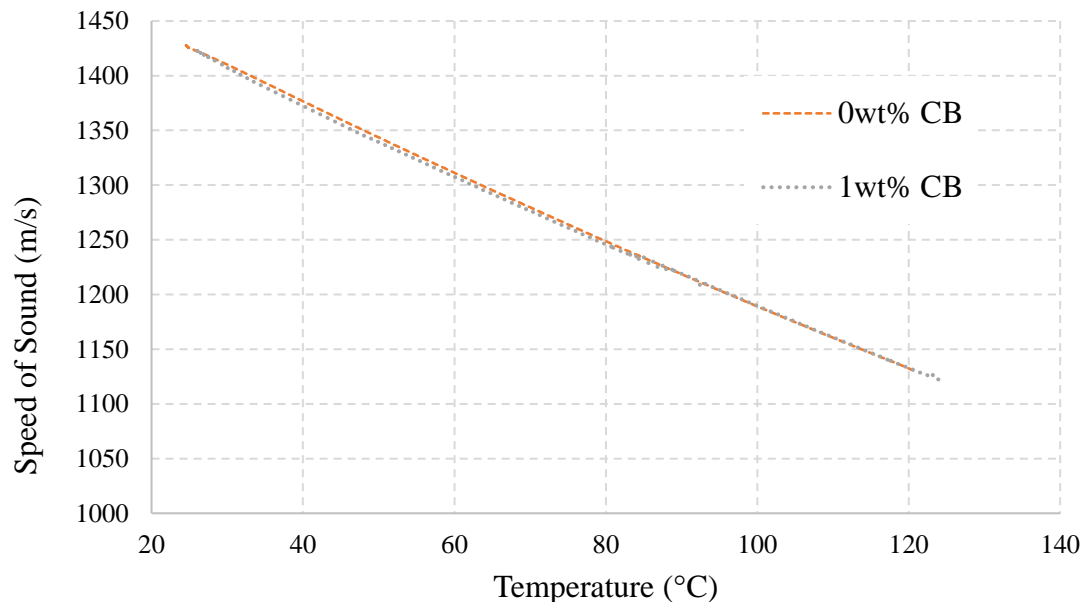
Figure 5.9: Wave velocity of 0wt%CB and 1wt%CB against temperature

5.5.6 FMS-100

The FMS-100 is a PC based ultrasonic measurement device equipped with facilities to transmit and receive ultrasonic signals in pulse/echo mode. The device has a 100 ms/s digitiser for the digitisation of reflected ultrasonic waves which allows real-time processing of the time-domain data to calculate lubricant film thickness. The system uses LabVIEW allowing the system to be easily configured to also capture and record analogue signals such as temperature and load.

5.5.7 Pin specimen

The pin specimen was made of O1 tool steel and it is a segment of a large cylinder with a radius of 750 mm for the hardened contacting surface and the width is 11 mm, about the same with the counter-face; this was to achieve a line contact. The pin, instrumented with longitudinal and shear sensors, was fitted to the reciprocating head of Plint TE77. Ten DL-50 sensors, of 10 MHz frequency each, was used; five on either side. With an average hardness of 64 HRC and Young's modulus of 214 GPa, the tool steel is similar to the chrome steel used for the ball-on-flat test. Ditto for the counter-face, except that the thickness was halved here.

Figure 5.10 presents a schematic and photograph of the sensors layout, five on either side of the pin specimen, along with the photograph of the instrumented pin after been coupled to the holder. A profile of the pin specimen showing the front and side views is presented in Figure 5.11.
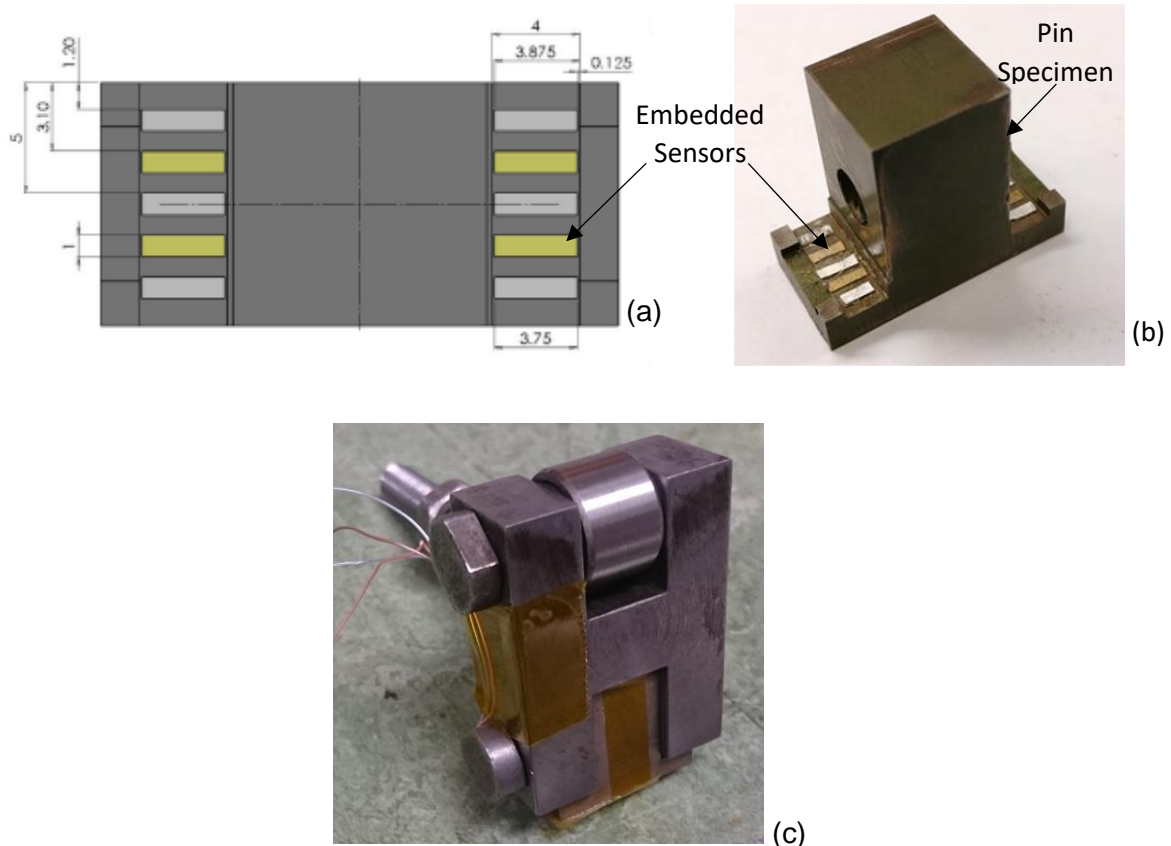
Figure 5.10: (a) schematic of the sensors layout, (b) photograph of the pin specimen showing the sensors and (c) Instrumented pin after been coupled to the holder
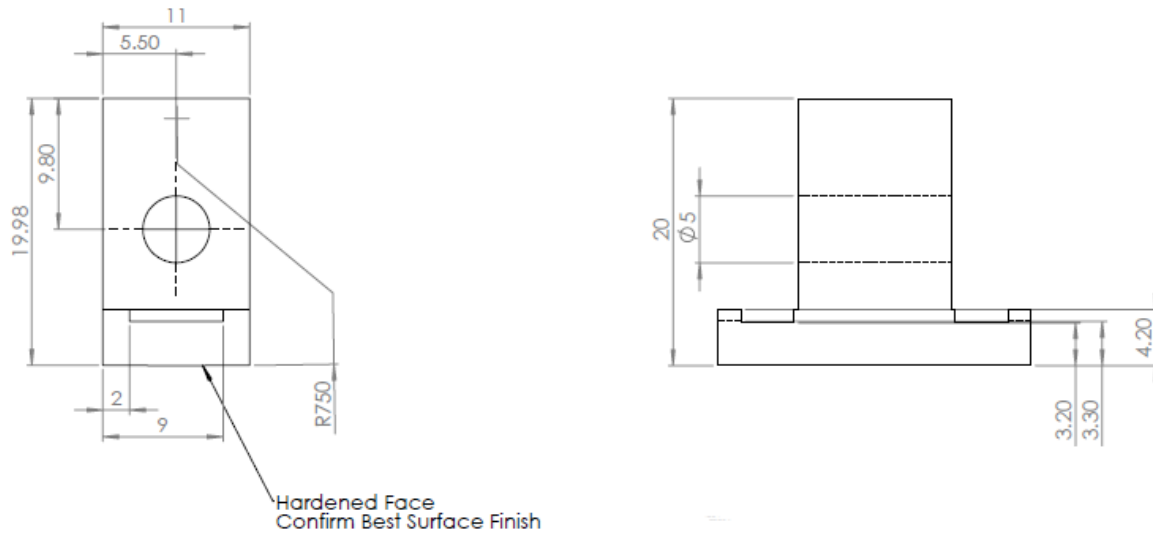
Figure 5.11: A profile of the pin specimen showing the front and side views

The process of extracting the signal from the ultrasonic sensors can be described as follows. When a sound wave hits a sensor, it causes the sensor to vibrate. Due to the piezoelectric effect this vibration results in a voltage output of the same frequency. However, a 10MHz sensor (or a sensor of any other frequency) does not just vibrate at 10MHz; it vibrates at a range of frequencies, with 10MHz being the centre frequency. This signal might be quite messy because there is often low and high frequency content within the signal. In this case, the next step is to apply a filter which reduces the weighting of particular frequencies within a signal. Consequently, the selected FFT index signal frequencies were 8, 9, 10, 11 and 12 MHz and the "Filter" tab on the FMS software was configured to choose the filter to apply.

5.5.8 Analytical predictions

5.5.8.1 Contact pressure

In estimating the Hertzian contact pressure, the pin is treated as a cylinder with a radius of 750 mm and contact length of 24 mm, while the counter-face is a cylinder of with an infinitely large radius. The result of this estimation for different normal loads is presented in Figure 5.12.

	Maximum Hertzian contact pressure (MPa)
20 N	5.2
30 N	6.3
40 N	7.3
50 N	8.2
60 N	8.9
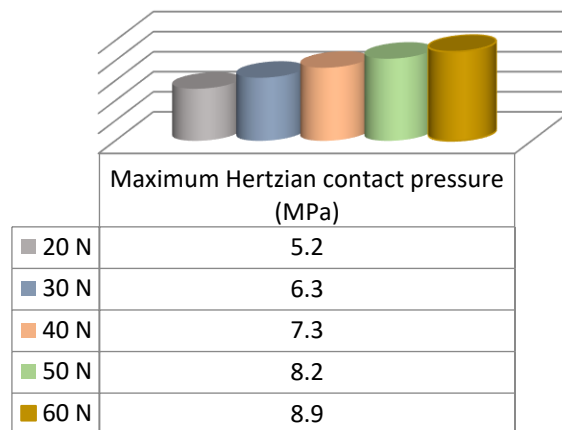
Figure 5.12: Theoretical estimation of the maximum contact pressure versus normal load

5.5.8.2 Film thickness

The central film thickness formula, Equation 5.21, was used to estimate the theoretical film thickness for the uncontaminated oil at 100°C under varying conditions. This is in line with elastohydrodynamic lubrication proposed for this contact, based on the fact that it is a line contact and the estimated Hertzian contact pressures are greater than 5 MPa. The results of the estimation are presented in Figures 5.13 and 5.14 for varying normal loads and varying entrainment speeds respectively. The results indicate that entraining speed and film thickness are positively linearly correlated, while normal load and film thickness are negatively correlated.

$$\frac{h_c}{R'} = 2.69U^{0.67}G^{0.53}W^{-0.067}\left(1 - 0.61e^{-0.73k}\right)$$ Equation 5.21

h_c is the central film thickness, and other parameters are as defined earlier.
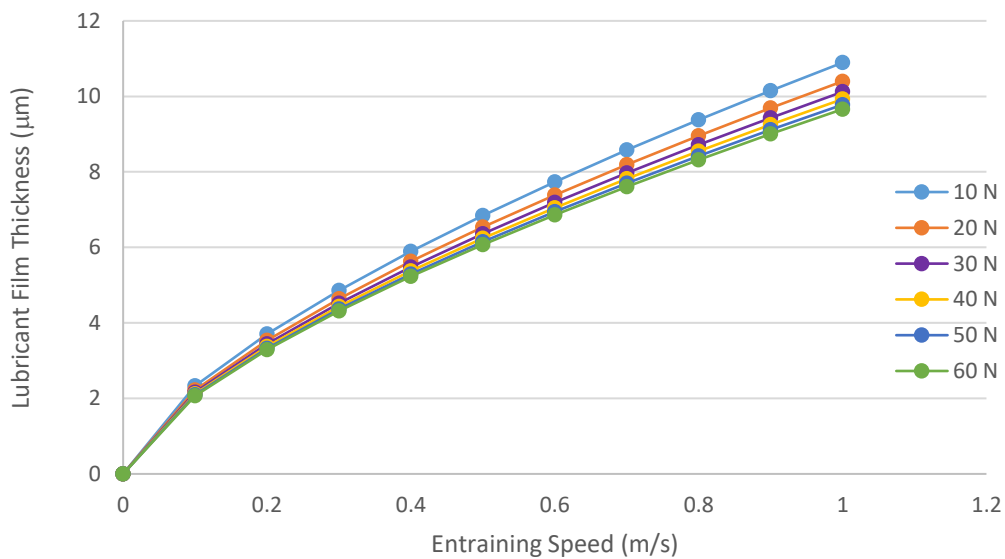
Figure 5.13: Theoretical estimation of the film thickness versus entraining speed for various normal loads
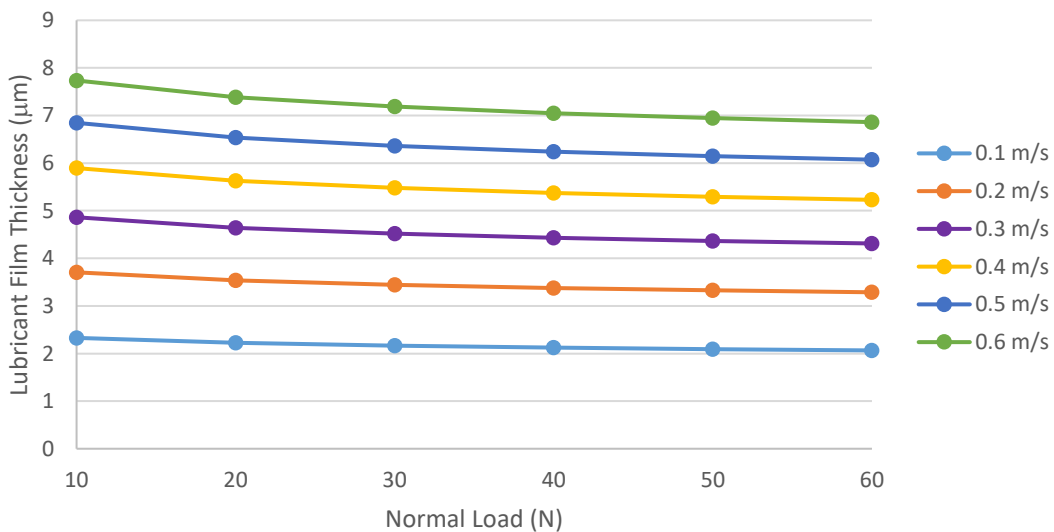
Figure 5.14: Theoretical estimation of the film thickness versus normal load for various entraining speeds

5.5.9 Test procedure

The instrumented pin ran through a series of sliding tests against cast-iron counter-faces. Three sets of tests were carried out. One at varying speeds (2-20 Hz) using uncontaminated oil, the second one was at varying loads (20-50 N) with uncontaminated oil and the last was at same load (20 N) and speed (10 Hz) with varying levels of contamination. All the tests were done at the oil-bath temperature of 100°C and the stroke length of 15 mm. Each test was run for 300 seconds, with measurement pulse repetition rate of 25 kHz; the data for each test was only recorded for 10 seconds at 2 minutes into the test, after reaching equilibrium. Reference measurement was taken before the commencement of each test. Figure 5.15 shows the specimens setup on the Plint with the schematics of the reciprocating head; while Figure 5.16 presents the complete view of the experimental setup with the FMS-100.

At the end of the tests, the generated data from each test was post-processed using a LabView program purposely designed for this testing. With this software, the reflection coefficient for each sensor was exported as a .tdms file; which when opened in Excel using Excel TDM importer, converts the reflection coefficient to film thickness.
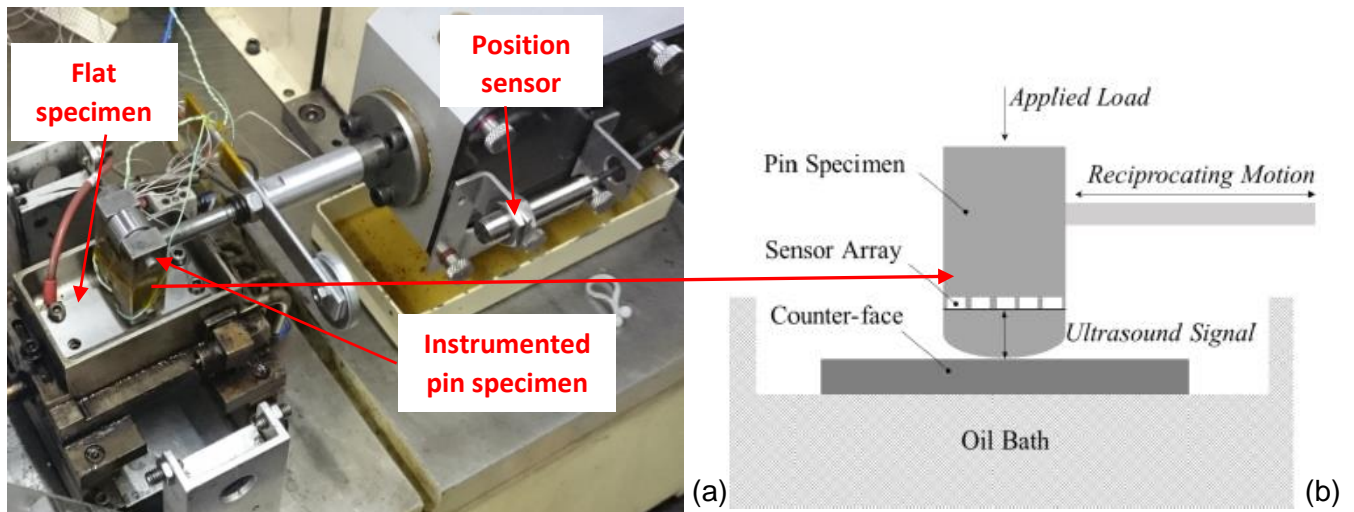
Figure 5.15: (a) Specimen setup on Plint TE77 (b) schematics of the reciprocating head
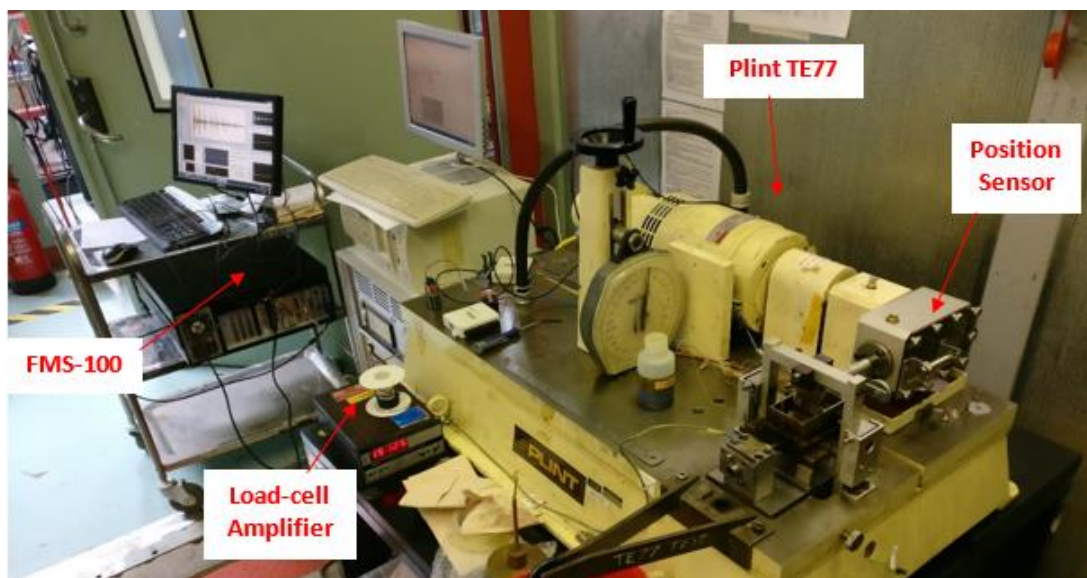
Figure 5.16: A complete view of the setup with the FMS-100

5.6   Results

5.6.1   Friction measurement

5.6.1.1 Friction force and coefficient of friction

Using Equation 5.1, the friction force was converted to coefficient of friction. Figure 5.17 shows the graph of coefficient of friction against time for different carbon black contents with the error bars. It can be seen from the figure that initial fluctuation of friction, due to wear scar development, was immediately followed by a gradual increase before steady state was achieved for the most part of the test. This is because sliding wear is generally characterized by the initial unstable behaviour and long-term stable behaviour in terms of changing surface conditions and wear processes [152]. The average standard deviation is 0.0016, which indicates high level of consistency and repeatability.
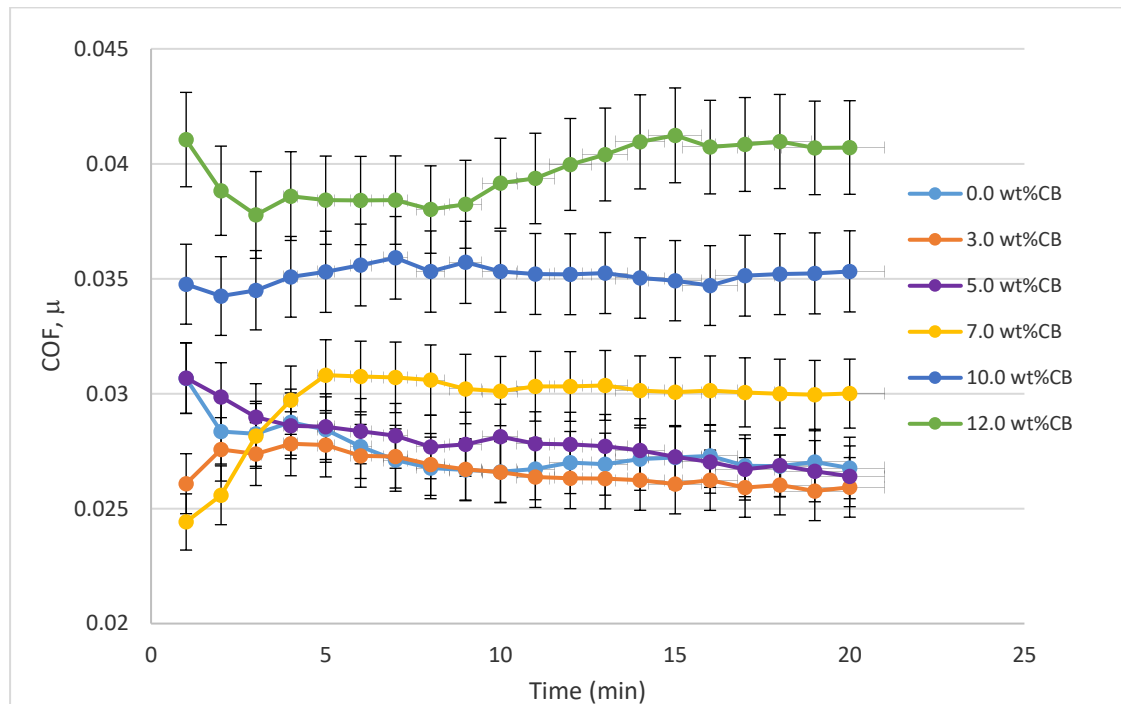
Figure 5.17: Results of coefficient of friction against time for various carbon black contents at 100°C, 0.133m/s, 1.8 GPa with the percentage error bars

Figures 5.18 and 5.19 show the graphs of friction force against time and coefficient of friction against time respectively for 3wt%CB carbon black content at various loads and hence contact pressures. As expected, friction force rises progressively as the normal load increases. While there was an appreciable increase in friction force with normal load, the coefficient of friction does not vary significantly (ranging between 0.030 and 0.034).

A similar close range was observed for the evolution of wear tests, Figure 5.20. It is obvious from that figure that the longer the test runs, the more steady the frictional behaviour.
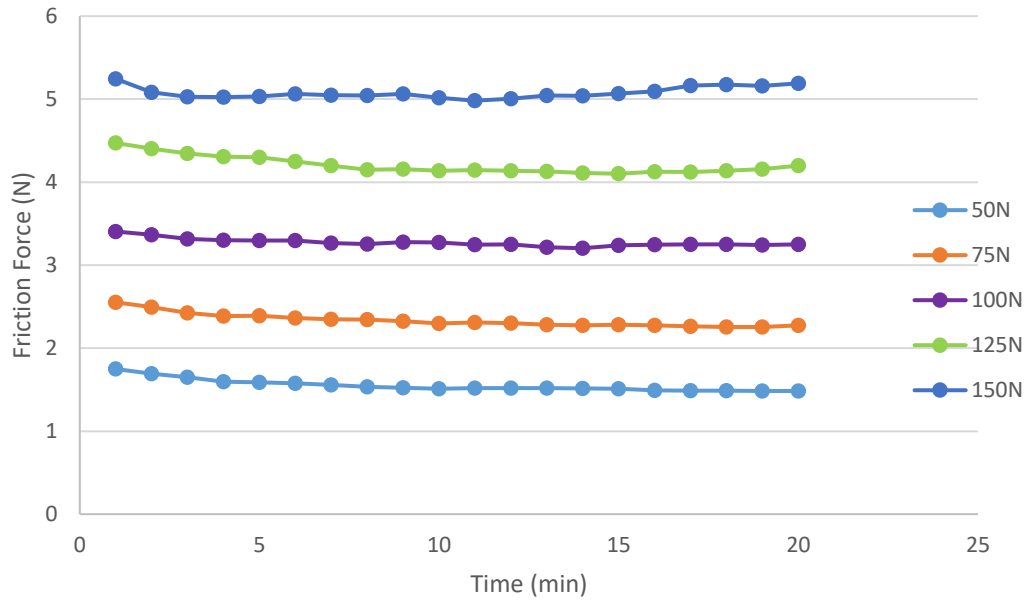
Figure 5.18: Friction force against time for 3wt%CB content at different loads
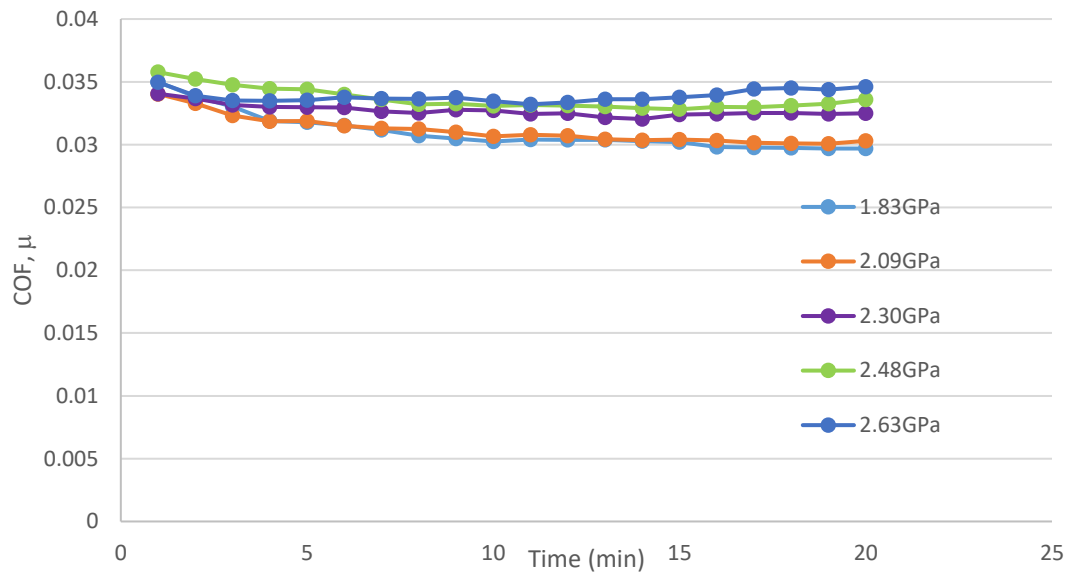
Figure 5.19: Coefficient of friction against time for 3wt%CB content at different contact pressures
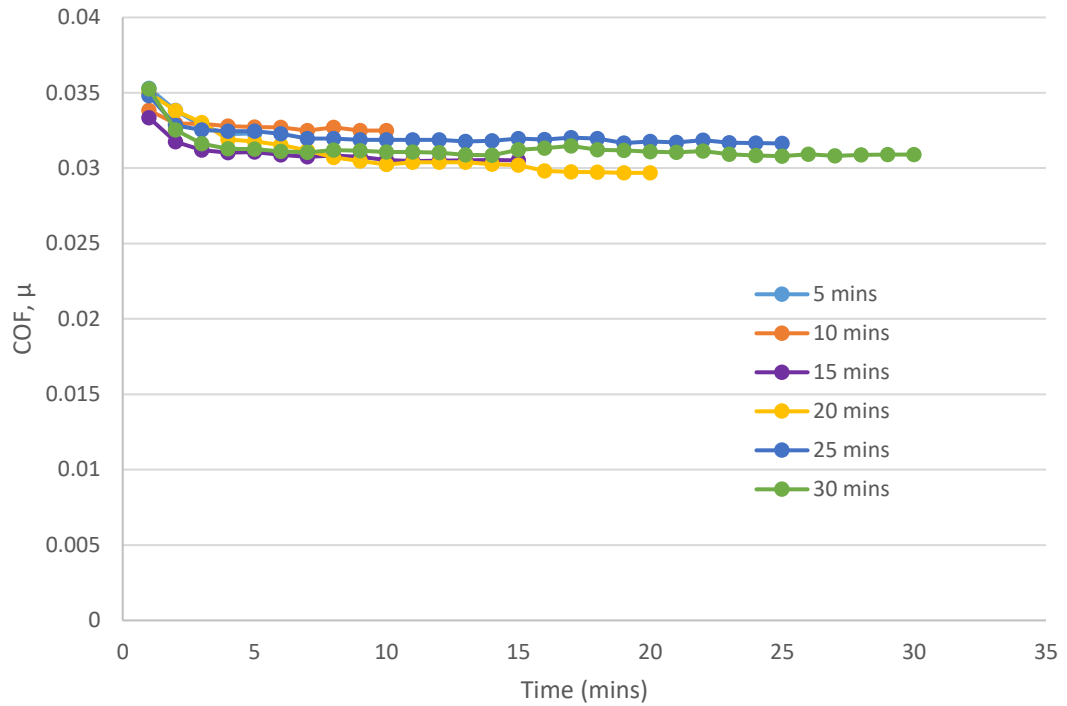
Figure 5.20: Results of coefficient of friction against time for 3wt%CB content running for different durations

Figure 5.21 shows the evolutionary friction behaviour in the sliding contact where the initial coefficient of friction (derived from the mean coefficient of friction for each time of testing) is usually the maximum before getting to the steady state condition where the coefficient of friction becomes stable as the sliding surfaces come into a more conforming contact [153]. This behaviour is illustrated with the line of best fit (polyline).
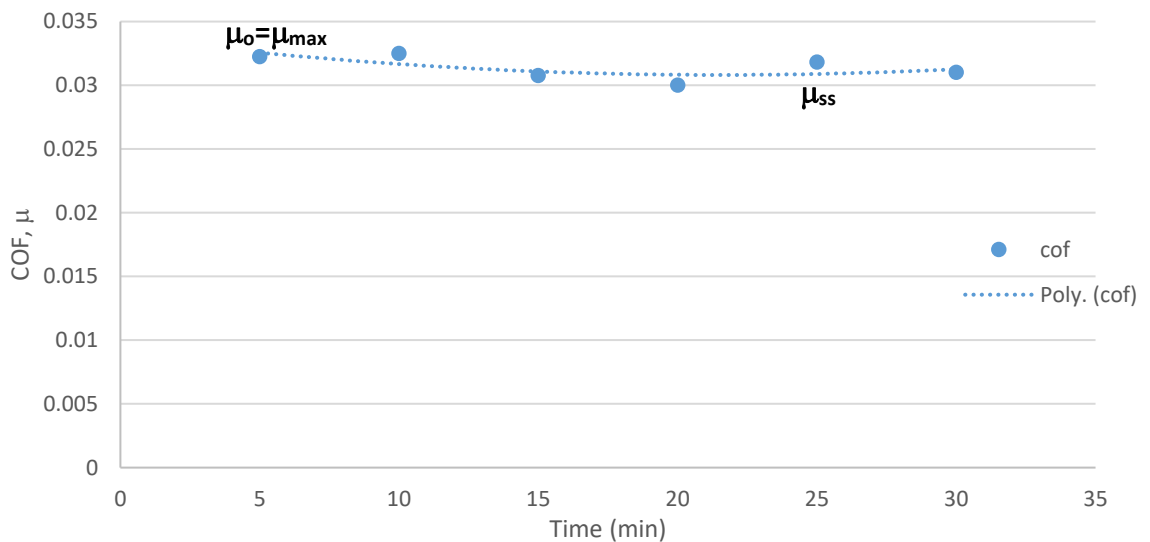
Figure 5.21: Evolutionary friction behaviour in sliding contact

5.6.2 Wear analysis

5.6.2.1 Wear scar volume

Figure 5.22, derived from Equation 5.16, depicts the variation of the actual wear volume with carbon black content for controlled linear heating and high temperature tests while Figure 5.23 presents the percentage volume increase from 0wt%CB. The results reveal typical non-linear sliding wear behaviour, one can see a sudden jump at the beginning between 0wt%CB and 3wt%CB, a semblance of relative steady-state behaviour between 3wt%CB to 7%wtCB; and another swift rise from 7%wtCB through 10wt%CB to 12wt%CB. It is obvious from the figures that both parameters (wear volume and percentage increase in wear volume) increased with temperature and carbon content, but more sharply at higher contents, especially 10%wtCB and 12%wtCB.

For the evolution of wear tests, Figure 5.24, the wear behaviour is relatively linear for 5-minute to 20-minute tests before rapid wear-rate sets in at 25-minute and 30-minute tests. The former observation may not be unconnected within the fact that the same carbon black composition (3wt%CB) was used, while the latter may be due to the breakdown of the protective surface layers resulting from prolonged testing period.

	0wt%CB	3wt%CB	5wt%CB	7wt%CB	10wt%CB	12wt%CB
■ CLH (22-100oC)	0.208	0.224	0.250	0.273		
■ 100oC	0.237	0.418	0.469	0.502	0.531	0.625
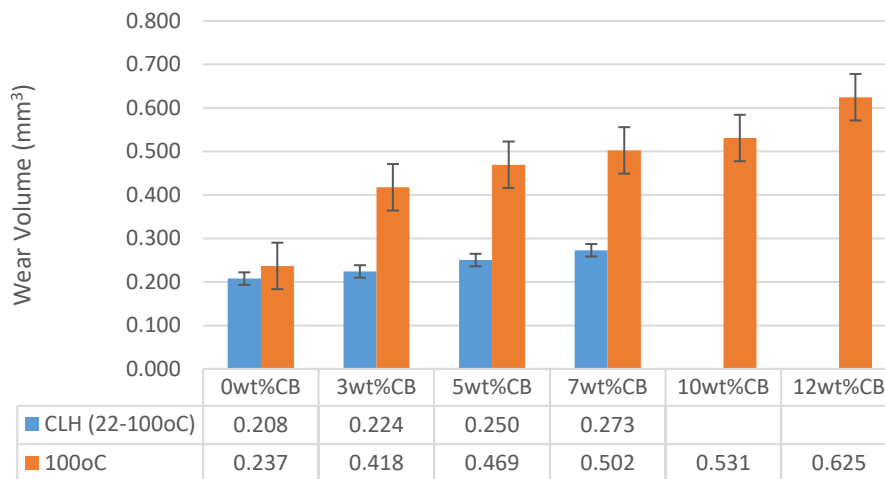
Figure 5.22: Actual wear volume variation with Carbon Black content for CLH and 100°C tests (with standard error bars)
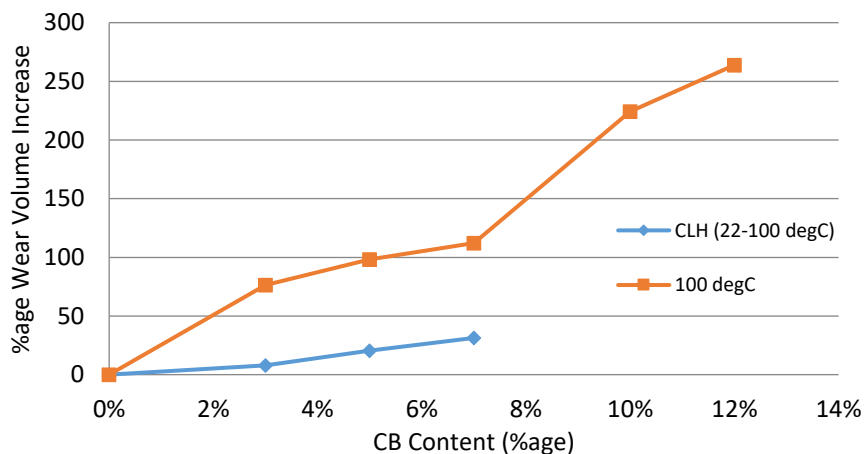
Figure 5.23: Percentage wear volume increase variation with Carbon Black content for CLH and 100°C tests

63

	5mins	10mins	15mins	20mins	25mins	30mins
Wear Volume	0.232	0.287	0.344	0.451	0.814	1.01
%age Increase	0	23.8	48.1	94.5	251	334
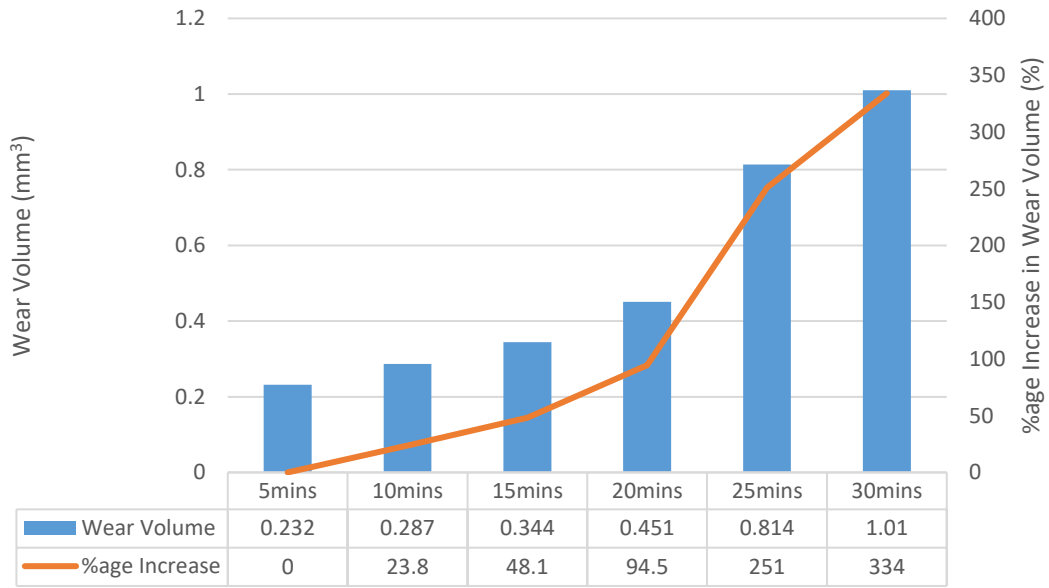
Figure 5.24: Actual volume and percentage wear volume increase for 3wt%CB for different running times

Figure 5.25 presents the variations of actual wear volume and film thickness with contact pressure for 3wt% carbon black content at 0.133 m/s and 100°C. Expectedly, the wear volume and percentage increase in wear volume increased correspondingly with contact pressure resulting from increase in normal load with noticeable very sharp increase at maximum contact pressure of 2.63 GPa. This is because as contact pressure increases, the oil film thickness decreases as clearly indicated in theoretical film thickness calculations, shown in the figure.
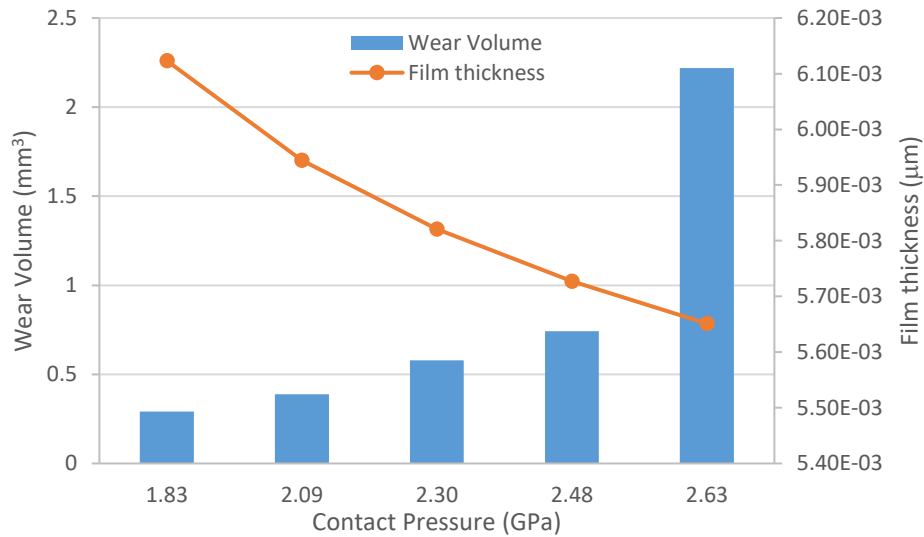
Figure 5.25: Variations of actual wear volume and film thickness with contact pressure for 3wt% Carbon Black at 0.133 m/s and 100°C

5.6.2.2 Post-test contact pressure

The use of a non-conformal contact configuration to estimate the initial Hertzian contact pressure is very common in most tribological papers [139, 154]. Practically, only a fraction of the total test time is spent under Hertzian conditions as the nominal

contact area increases with the occurrence and development of wear over time which correspondingly decreases the nominal contact pressure as the test progresses [139]. Figure 5.26 shows the wear scar profile obtained from Veeco Dektak 150 Profilometry where the contact area has increased significantly. The Veeco Dektak 150 Profilometer was produced by Veeco Instruments Inc., USA.
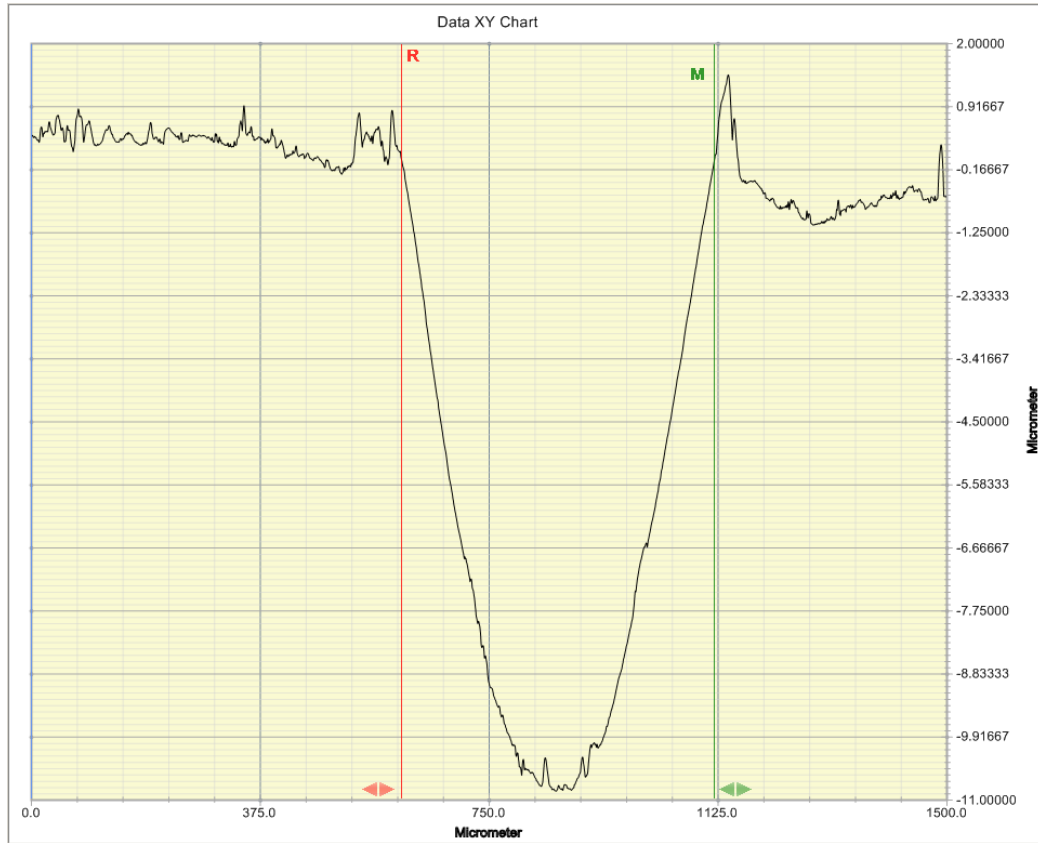
Figure 5.26: Wear scar profile showing significant increase in nominal contact area

Ideally, it would be useful to know the real area of contact at every instant during the test to help in accurately determining the instantaneous contact pressure and thus have a more realistic estimation of the lubrication regime in which the contact operates; this is obviously a herculean task. However, the contact pressure at the end of each test may be determined using the post-test wear scar dimensions. Since the shape of the wear scars obtained in these tests is elliptical, Figure 5.27, the nominal contact pressure is estimated using the expression obtained from Ajayi and Erck [139] for elliptically shaped scars presented below as Equation 5.22.
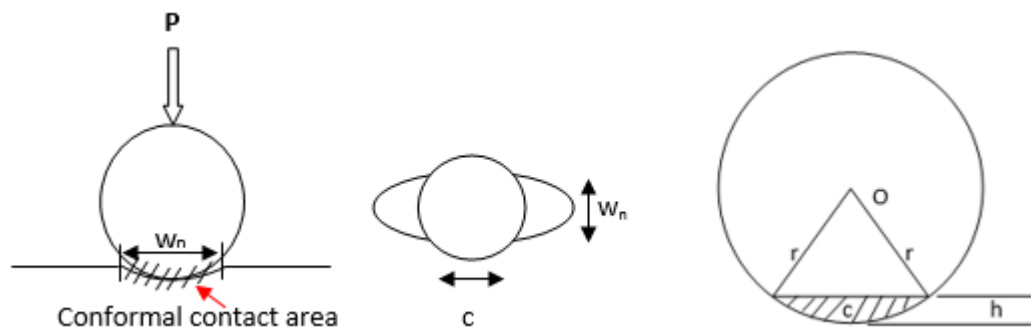
Figure 5.27: Schematic diagrams of conformal contact

65

$$P_n = P/_{\pi ab}$$ <div align="right">Equation 5.22</div>

where,

P_n is the nominal contact pressure, N/m^2

P is the normal load, N

a and b are the half-lengths of the major and minor axes respectively, m.

From Figure 5.27 above, the major axis is the wear scar width and the minor axis is the diameter of the ball segment embedded in the wear scar.

Therefore,

$$a = {}^1/_2\, w_n$$ <div align="right">Equation 5.23</div>

$$b = {}^1/_2\, x\, c = {}^1/_2 \left(2\sqrt{2rh - h^2}\right)$$

$$b = \sqrt{2rh - h^2}$$ <div align="right">Equation 5.24</div>

where,

w_n is the width of the wear scar, m

h is the depth of the wear scar, m

r is the radius of the ball specimen, m

5.6.2.3 End-of-test contact pressure

The contact pressure at the end of each test was determined with the post-test wear scar dimensions using Equation 5.22. The results of this estimation are presented in Figure 5.28 and they indicated that the end-of-test contact pressure values obtained are less than the initial Hertzian contact pressure shown in Table 5.2. The reduction is by an average of 5 times for 50 N to 125 N normal loads and 15 times for 150 N normal load. The detailed calculations are shown in Appendix VI.

For various sooty oils with 50 N normal load, Figure 5.28(a), the post-test contact pressure showed progressive decrease from 0wt% to 12wt% carbon black contents. This is due to the fact that the volume of wear scar increases with carbon black content. The same trend was maintained for 3wt% carbon black composition with various loads, Figure 5.28(b); where there was marginal variations in the estimated contact pressure between 50 N and 75 N normal loads as well as between 100 N and 125 N normal loads. There was, however, a sharp decrease in contact pressure at the highest load (150 N) which may be due to the excessive wear observed at this level.
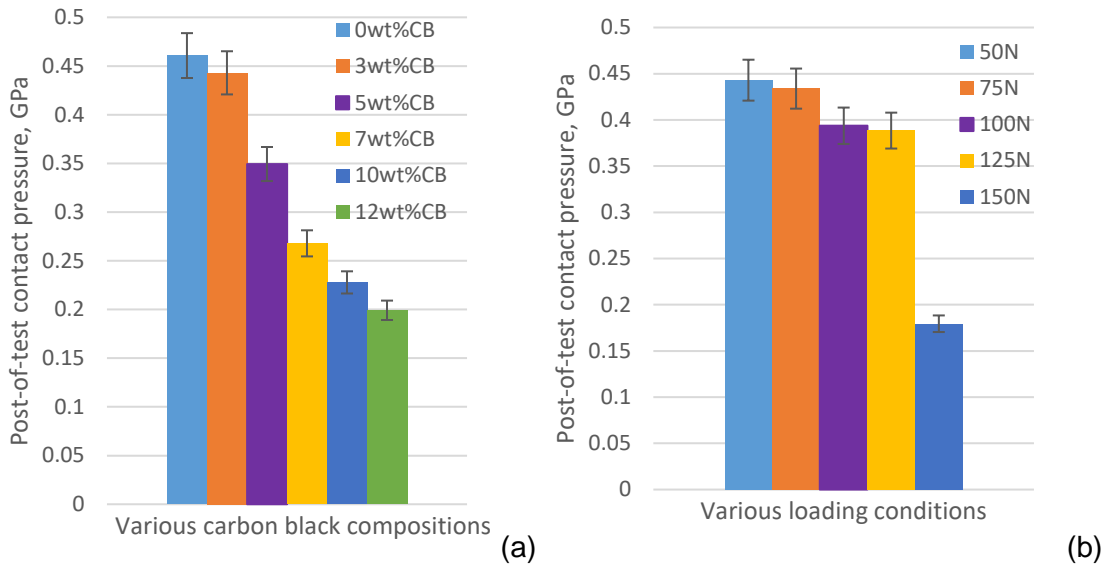
Figure 5.28: End-of-test nominal contact pressure for various contact conditions: (a) 0-12wt%CB contents and (b) normal loads with 3wt%CB content with percentage error bars

Figure 5.29 depicts how the post-test contact pressure varies with wear scar width for the evolution of wear tests; the figure is purposely plotted on log scale to reduce the contact pressure range of values within different durations. Expectedly, the figures indicate an inverse relationship between the contact pressure and the wear scar width.

Figure 5.29: Relationship between post-test contact pressure (in log scale) and wear scar width for 3wt%CB content running for different durations with standard error bars

5.6.2.4 Wear scar roughness profiles

To assess the effect of different tests on the roughness, post-test roughness of the wear scars was measured using the Veeco Dektak 150 profilometer. This was done by moving the stylus longitudinally in the direction of sliding operation. Though, the centre line average value, R_a and root mean square value, R_q were taken, R_q values were used for the computation, being more accurate as its square term is a good discriminator for surface variations [155].

The results obtained for various carbon black contents at 100°C and that of different loads with 3wt% carbon black composition are presented in Figure 5.30. The data, Figure 5.30(a), shows marginal variations in wear scar roughness for 0wt% to 7wt% carbon black contents, while there is appreciable increase for 10wt% and 12wt% carbon black contents. For different loads, Figure 5.30(b), the minimum wear scar roughness was for 2.30 GPa (100N) contact pressure, but sharply increased by about five times and fifteen times for 2.48 GPa and 2.63 GPa respectively. This is suggestive of the effects of two-body abrasion due to lubricant starvation as a result of high contact pressure between the contacting specimens.

	Rq (um)
0wt%CB	0.587
3wt%CB	0.590
5wt%CB	0.621
7wt%CB	0.653
10wt%CB	0.906
12wt%CB	0.955

(a)

	Rq (um)
1.83 GPa	0.590
2.09 GPa	0.553
2.30 GPa	0.522
2.48 GPa	2.554
2.63 GPa	7.828

(b)

Figure 5.30: Post-test roughness profile of the wear scar for (a) varying CB contents and (b) varying contact pressure using 3wt% CB content

5.6.2.5 Wear scar optical microscope images

The optical microscopic images of the wear scars generated by the tests are presented in Figures 5.31-5.34.

Figure 5.31 shows the wear scar microscopic images for the ramped (controlled linear heating) and 100°C tests for various carbon black contents. The observed wear mechanisms move from lubricated sliding wear at 0wt%CB to mild metal-to-metal abrasion at 3wt%CB. Abrasive wear with patches of pits were observed for 5wt%CB and pronounced abrasion with plastic deformation at the edges for 7wt%CB.
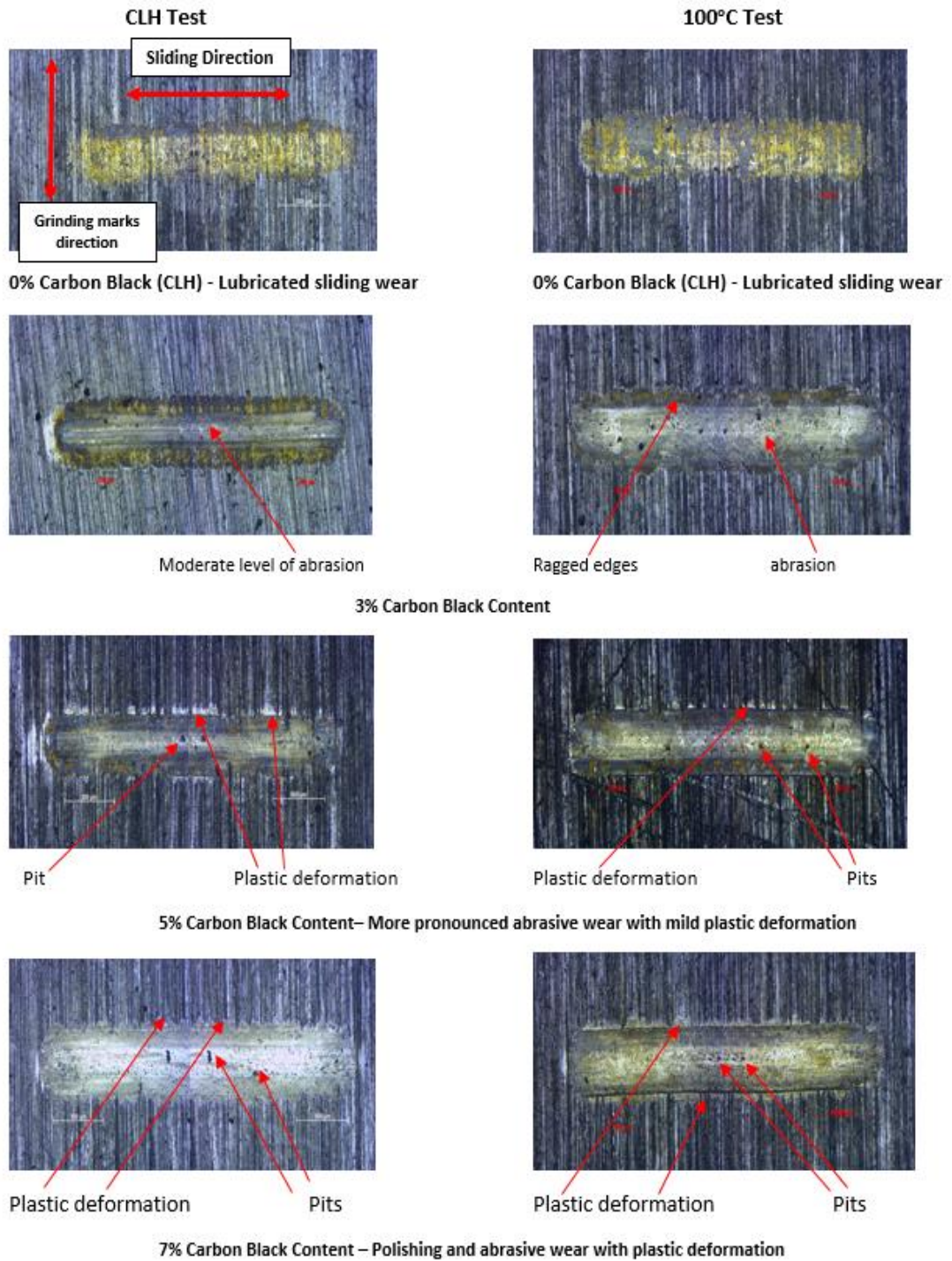
Figure 5.31: Optical microscopic images of 0-7%wtCB contents for CLH and 100°C tests at 1.83 GPa contact pressure

Figure 5.32 shows the wear scar microscopic images of 10wt% and 12wt% carbon black contents for the 100°C test. The wear mechanisms observed here are abrasion with plastic deformation around the edges of the wear scar. A magnification of selected spots shows evidences of patches of pits, crack formation and propagation leading eventually to adhesive scuffing especially for 12wt% carbon black content. Evidences of plastic flow from the sliding track to the sides can also be clearly seen from the figures.
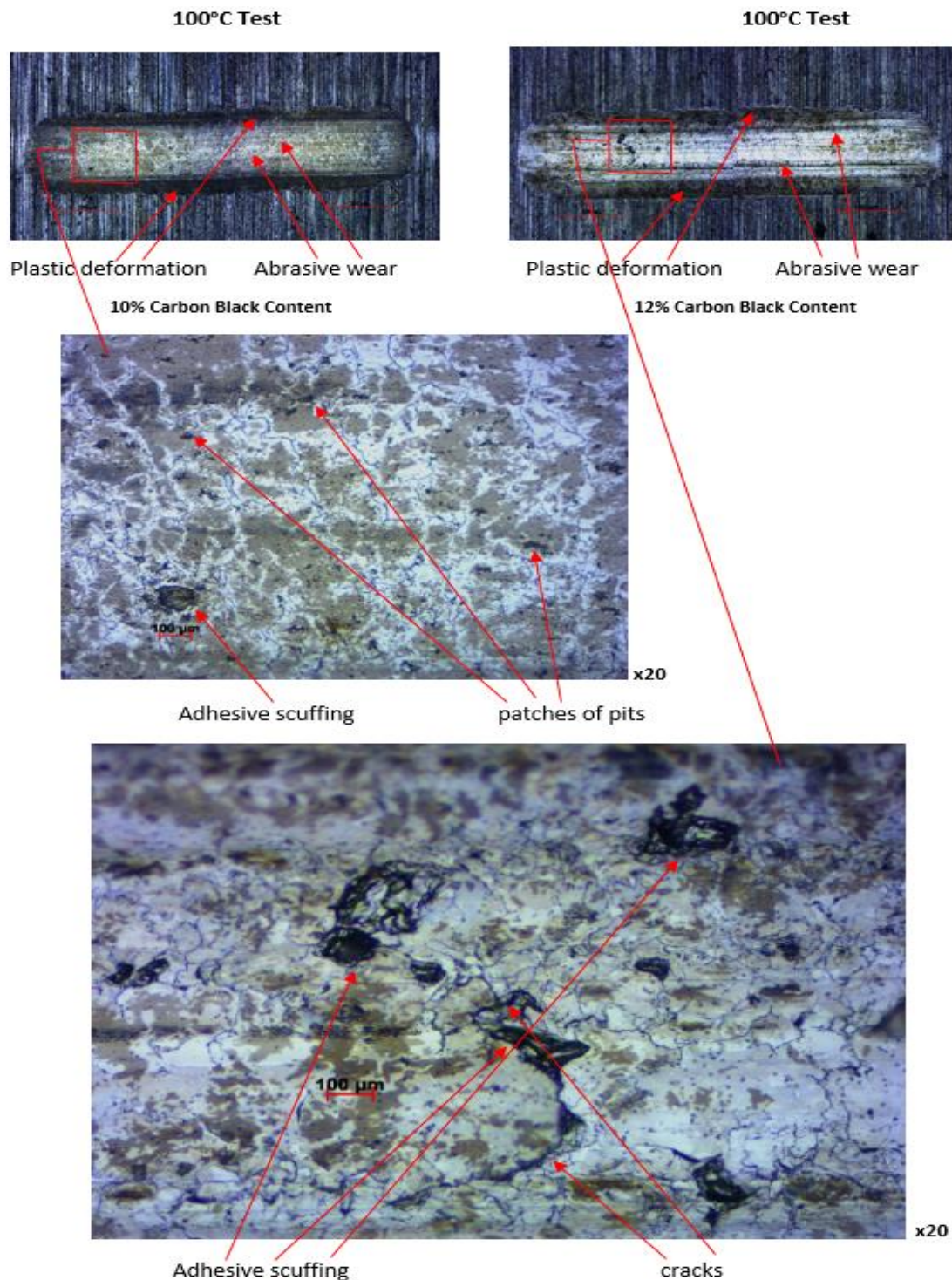
Figure 5.32: Optical microscopic images of 10wt%CB and 12wt%CB contents for 100°C tests with magnification of selected spots

For higher loads (with consequent higher contact pressures) using 3wt% carbon black content at 100°C, there is pronounced abrasion and plastic deformation at 2.09 GPa and 2.30 GPa contact pressures, Figure 5.33; while images for 2.48 GPa and 2.63 GPa contact pressures, Figure 5.34(a), clearly shows evidences of excessive adhesion and material transfer, known as galling, between the surfaces in sliding contact as a result of total breakdown of lubrication at the points of contact.

The scanning electron microscope images were taken for 2.48 GPa and 2.63 GPa using Hitachi TM3030Plus Tabletop Microscope. The images, Figure 5.34(b), clearly shows the level of severity of damages to the surfaces at these very high contact pressures where the test can be likened to a worst-case scenario comprising lubricant contamination at high temperature, high load and boundary lubrication.

Plastic deformation   Abrasion   Plastic deformation   Abrasion

75N (2.09 GPa)   **100N (2.30 GPa)**
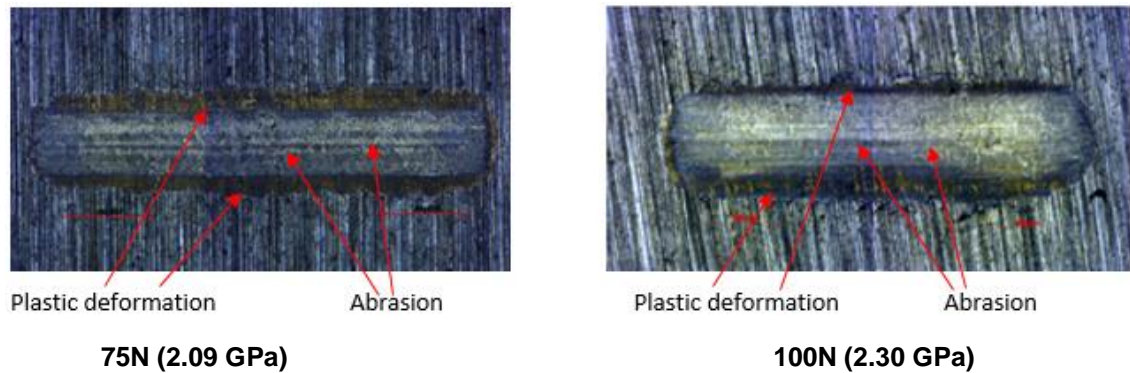
Figure 5.33: Optical microscopic images for 2.09 and 2.30 GPa using 3%CB content at 100°C

Adhesive scuffing/galling   cracks   Highly pronounced adhesive scuffing/tearing

125N (2.48 GPa)   **150N (2.63 GPa)**
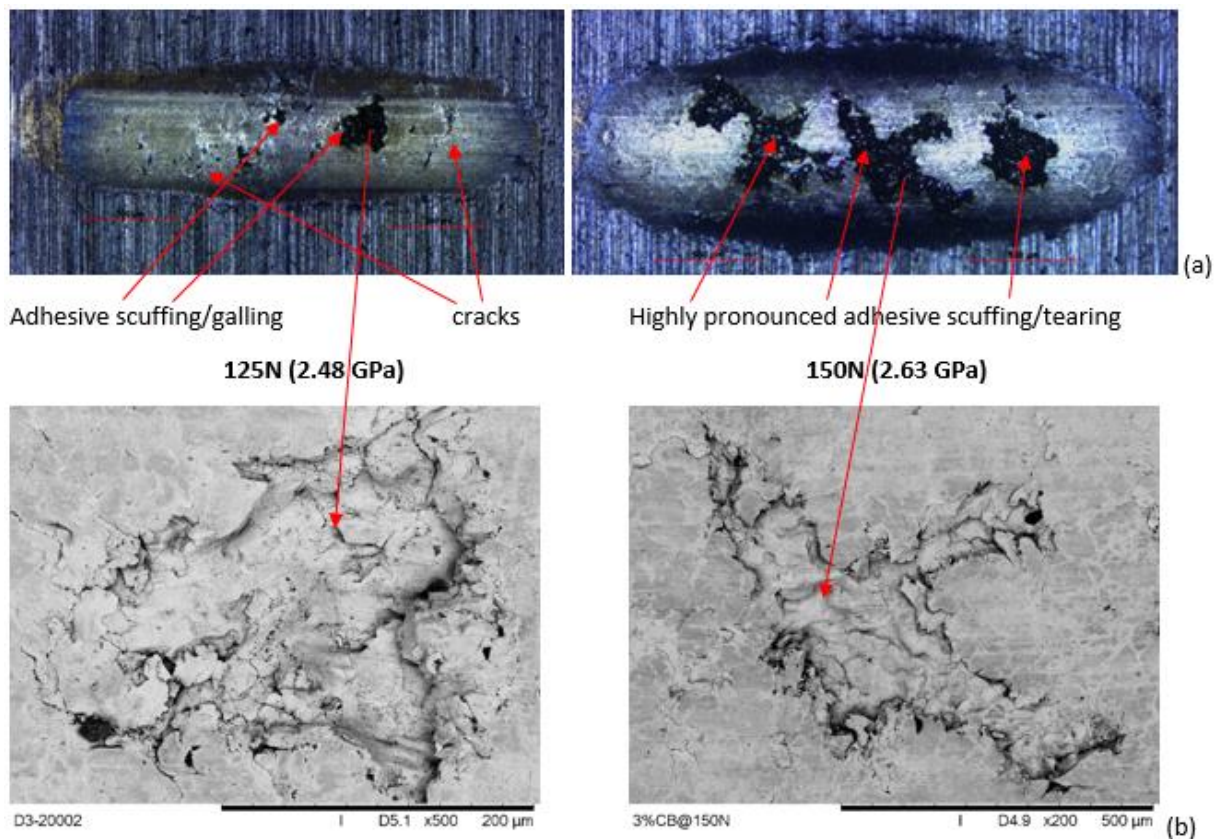
Figure 5.34: Images for 2.48 and 2.63 GPa using 3%CB content at 100°C with SEM images of selected spots showing the scuffing/tearing more clearly

The microscopic images obtained from evolution of wear tests, Figure 5.35, show a progressive level of wear from mild abrasive wear within the first ten minutes to more pronounced abrasion for 15-20 minutes tests and obvious evidence of polishing wear for 25-30 minutes tests. The scanning electron microscopy images, Figure 5.36, further reveal evidence of crack formation from 10-minute test, which propagates further as time progresses before culminating in peeling and mild scuffing at 25-30 minutes tests.
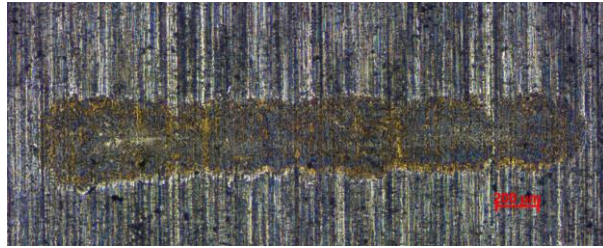
5-minute test with little scratches
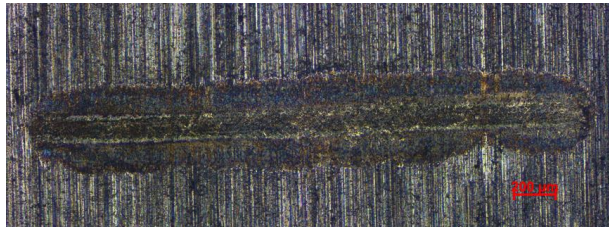
10-minute test with mild abrasive wear
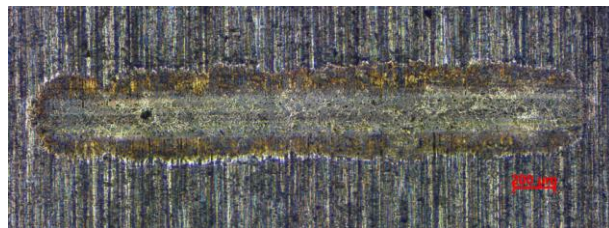
15-minute test with pronounced abrasive wear
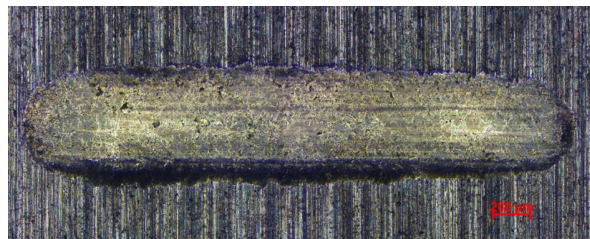
20-minute test with severe abrasive wear
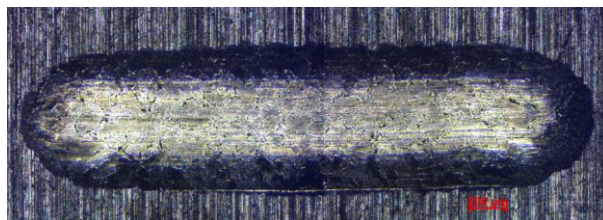
25-minute test showing evidence of polishing wear
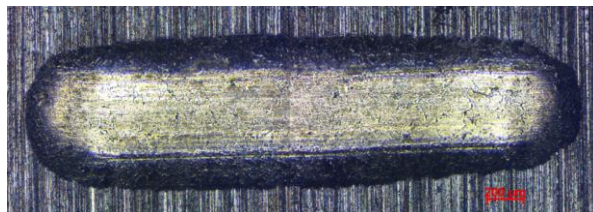
30-minute test showing evidence of more pronounced polishing wear

Figure 5.35: Optical microscopic images for 3%CB content at different running times
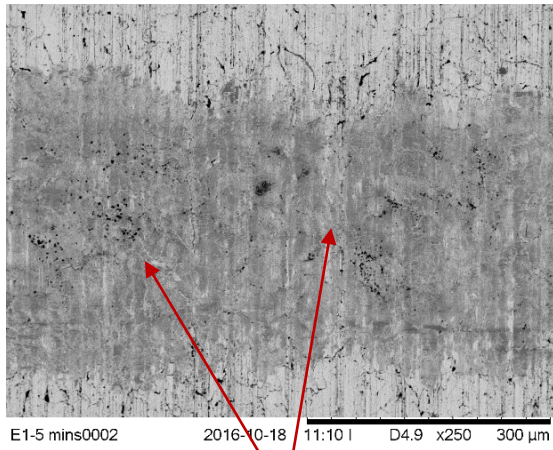
Wear track with visible grinding marks

5-minute
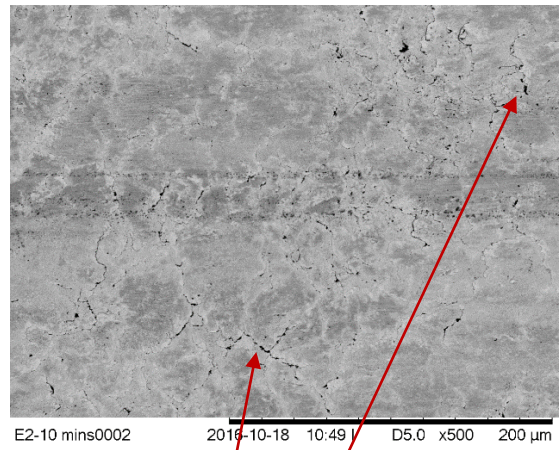
Cracks formation

10-minute
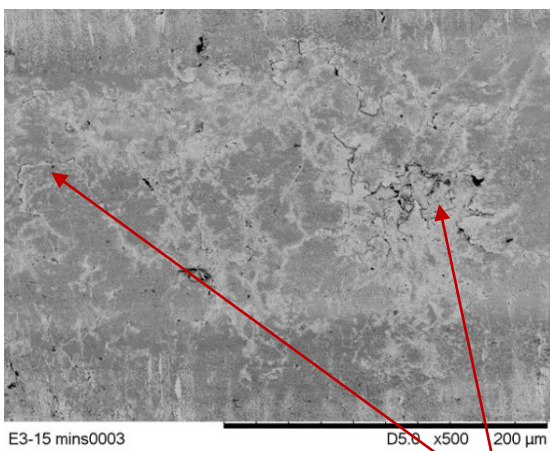
Cracks formation/peeling

15-minute
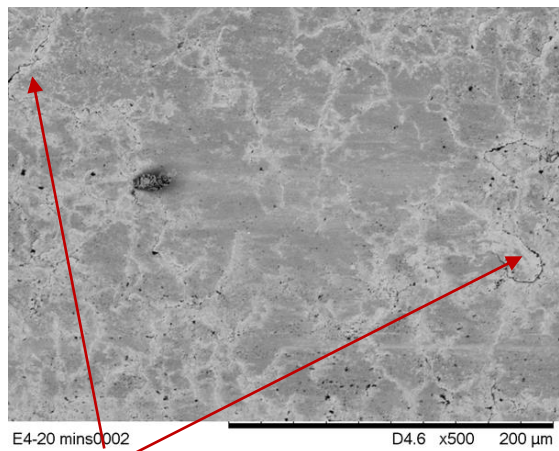
20-minute
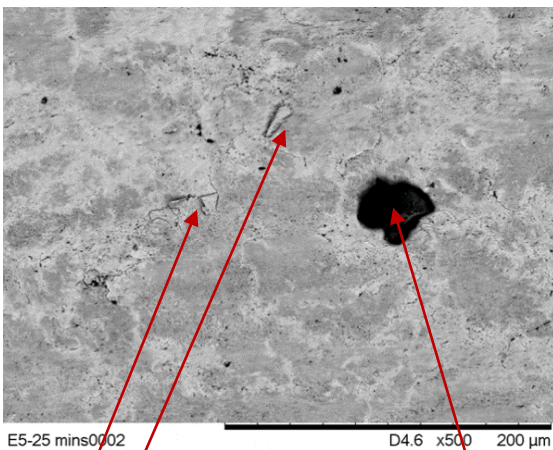
Peeling

particle embedment/scuffing
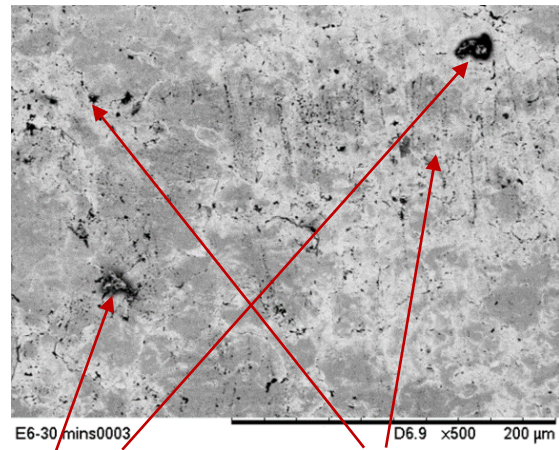
pits

25-minute

30-minute

Figure 5.36: SEM Images for 3wt%CB content at different running times

5.6.2.6 Ball specimen

On examination, the ball specimens used for different normal loads also present varying degrees of surface damages, as shown in Figure 5.37. From mild scratches at 1.83 GPa, the surface alterations gradually moved to roughed surface, abrasion, minor scuffing and pronounced scuffing as the contact pressures increased.
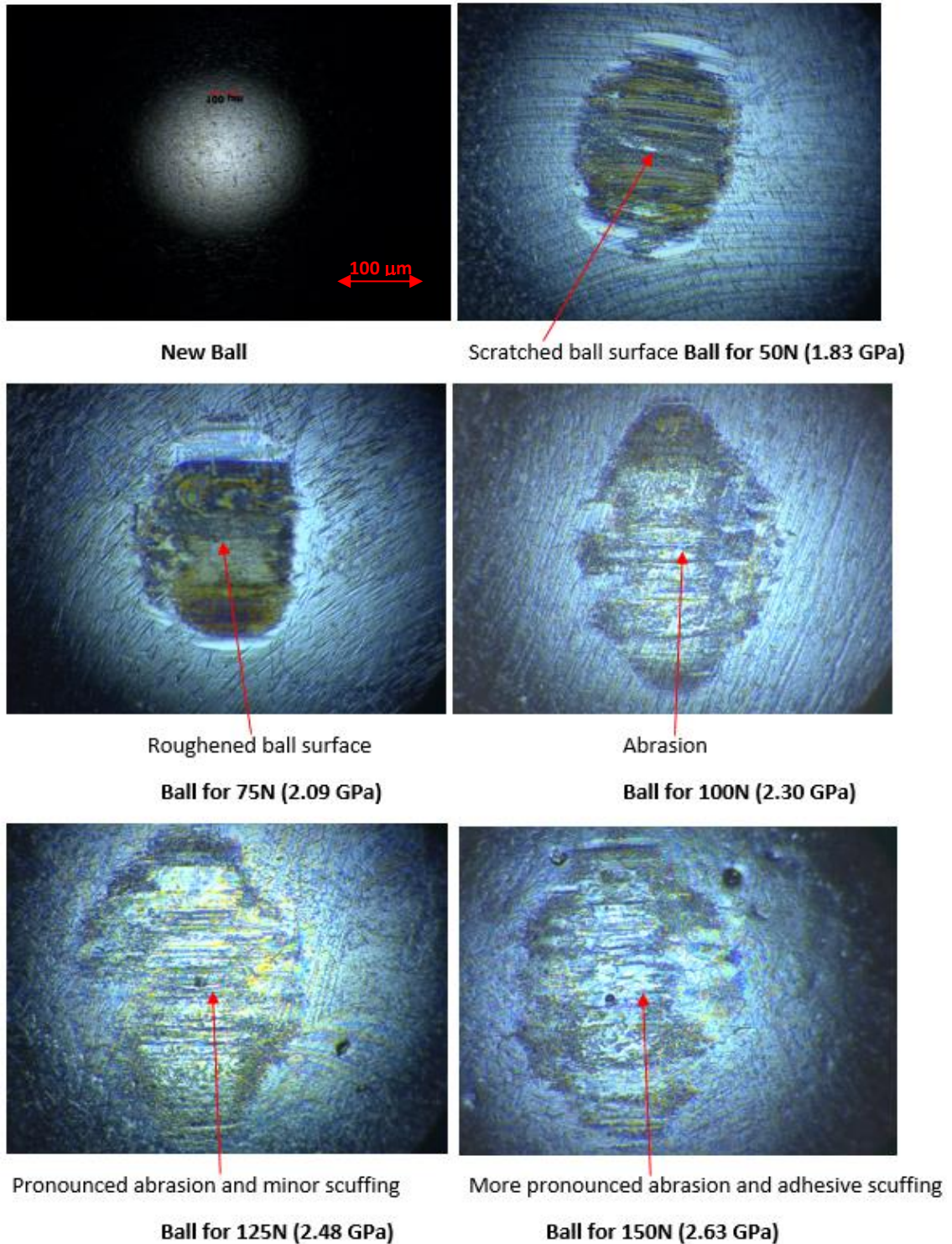
Figure 5.37: Optical microscopic images of ball specimen used for higher normal load tests using 3wt%CB content at 100°C

5.6.3 Film thickness measurement

The results of the first sets of test are presented in Figure 5.38 where the comparison of the mean film thickness over the full cycle for varying reciprocating frequencies is shown. From the result, it can be seen that the film thickness increased with increasing speed. And, for the load variation tests, presented in Figure 5.39, an increase in load decreases the film thickness. Figure 5.40 shows the result from varying carbon black content from 0wt%CB to 5wt%C. The result indicates insignificant variation between the uncontaminated oil, 0wt%CB, and 1wt%CB; however, there was noticeable variation between 3wt%CB and 5wt%CB.

The cam angle indicates the position of the pin specimen, attached to the reciprocating arm of the TE77, as it slides on the counterface. It is 0º at the starting end (BDC) and 180º at the other end (TDC) at its half cycle. The reverse motion completes the cycle at 360º.

A combined result, pulling together the tests conducted under the same condition of 10 Hz speed and the load of 20 N using uncontaminated oil is displayed in Figure 5.41; and the level of comparability indicates that the tests are repeatable.
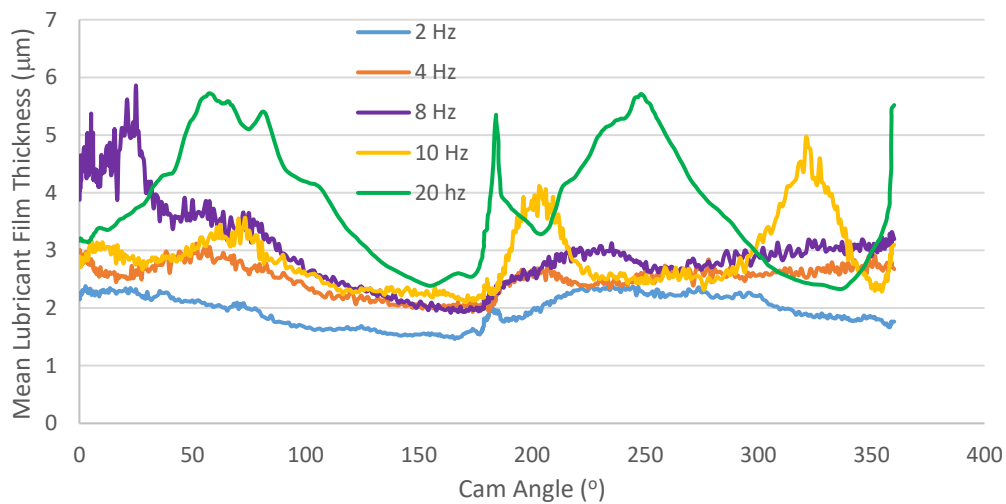
Figure 5.38: Mean film thickness at varying reciprocating frequencies
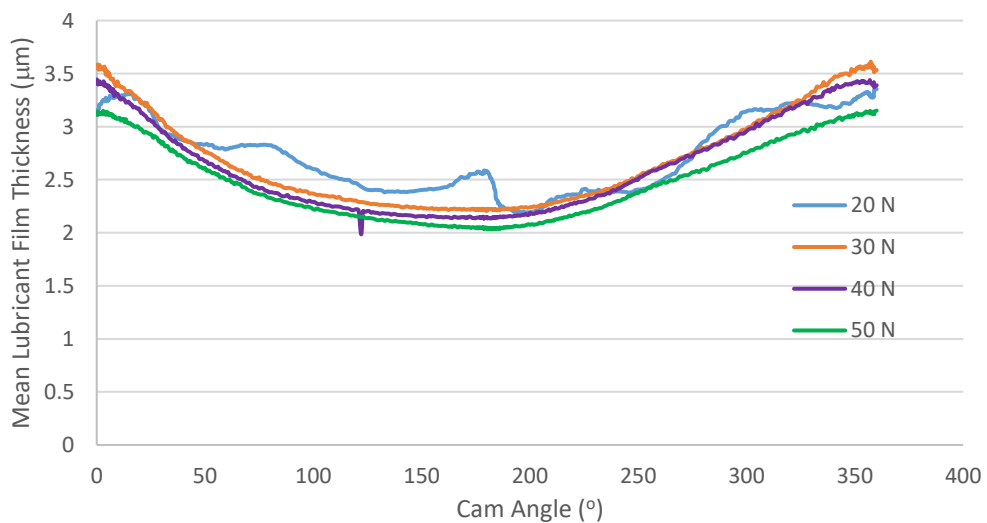
Figure 5.39: Mean film thickness at varying normal loads
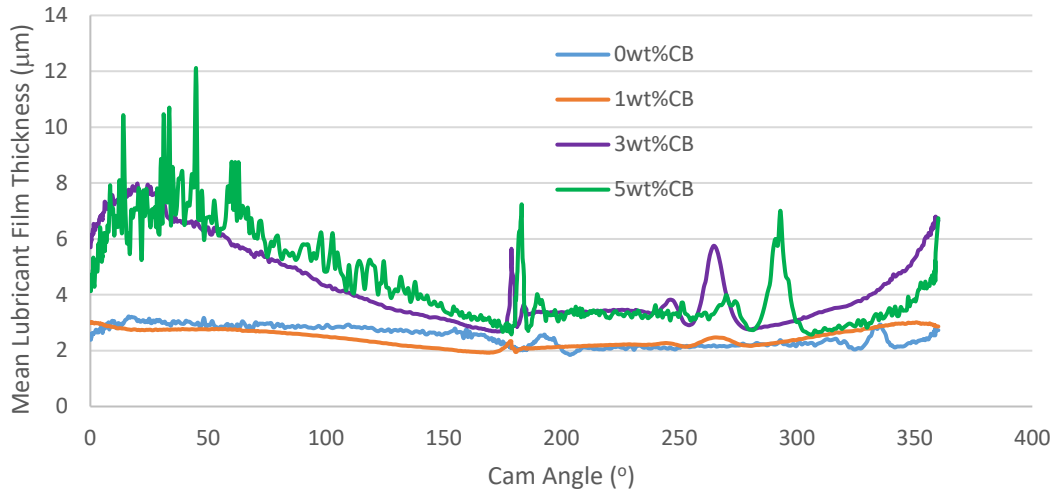
Figure 5.40: Mean film thickness at different carbon black contents
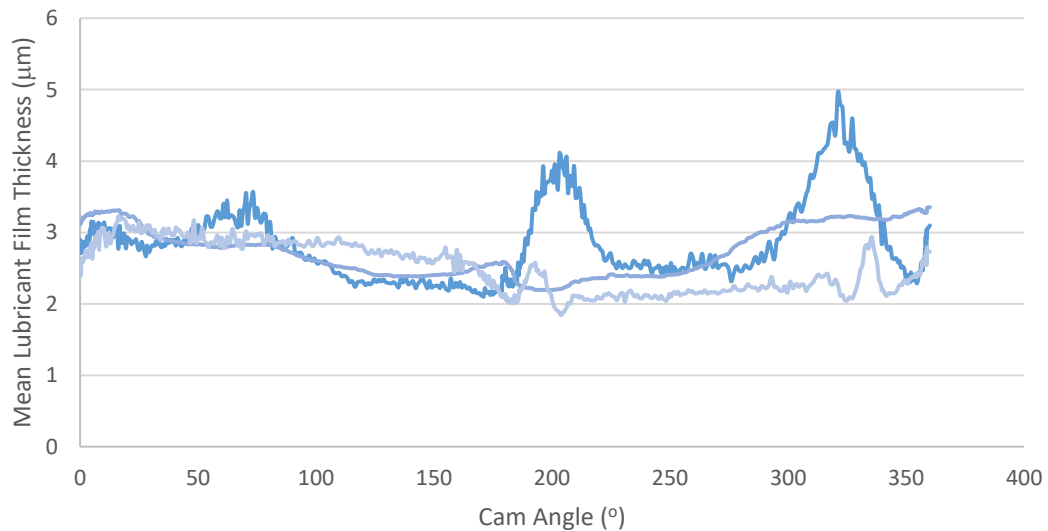
Figure 5.41: A combined graphs of tests at the same condition of 10 Hz and 20 N using uncontaminated oil

5.7 Discussion

5.7.1 Sooty-oil viscosity

The result from sooty oil viscosity as presented earlier shows that viscosity increases with increasing carbon black content, but decreases with increasing temperature. The rate of change of viscosity is, however, not proportional to the change in temperature. This is similar to results obtained by Asango et al. [156], Green and Lewis [6], George et al. [77] and Truhan et al. [78]. Also, Aworanti et al. [157] observed the same trend with binary and ternary blends of Soybean, Biodiesel and Petroleum oils. The reason for this trend is attributable to the fact that oils are thinner at higher temperatures which impacts the film thickness resulting in transition from one lubrication regime to another. For boundary lubrication, the resultant effect is more severe wear.

The implication of the first aspect of this result is that the theoretical oil film thickness would increase correspondingly and this was actually confirmed with the calculation of

the film thicknesses of sooty-oil surrogates. However, while the increased film thickness is expected to protect the rubbing surfaces in contact; that did not manifest here because firstly, the sliding operation was carried out under a boundary lubrication condition and secondly, soot is generally believed to cause break down of film thickness under this condition [6]; probably, by abrading the anti-wear additive films (tribofilm) formed on the interface between the contacting bodies.

5.7.2 Friction force and coefficient of friction

The sudden rise in frictional values at the initial stage which was followed by steady state in the subsequent duration of the tests could be attributed to the wear debris formation and entrainment at the sliding contact zone [158]. This is because sliding wear is generally characterized by an initial unstable behaviour and long-term stable behaviour in terms of changing surface conditions and wear processes [152]. For 3wt% to 7wt% carbon black contaminations, it is obvious that the sooty oils exhibit non-conformal behaviour at the initial phase. But as the test progresses beyond the first ten minutes, the level of conformity between the rubbing surfaces increases. It can also be seen that at this level of contamination, the effect on the contact friction is insignificant especially at higher rubbing surface conformity.

The sliding friction results indicated that friction force and coefficient of friction vary with carbon black content levels. The variation was a minima at moderate carbon black content (3wt%-7wt%) and virtually became insignificant as the test progressed and the level of conformity between the contacting surfaces increased. Green and Lewis [2-4] had a similar observation with formulated oil mixed with carbon black. This is attributed to the lubricant's ability to retain and evenly disperse the carbon black particles. It should, however, be noted that 3wt%CB consistently maintained the lowest coefficient of friction value, especially after the initial wear-in period. This is similar to Hu et al. [84] observation which was also linked to the uniformity in the dispersion of the carbon black particles assisted by the additives in the formulated lubricant. Real engine soot also has the tendency to exhibit this friction modifying behaviour at a more homogeneous aggregates level [159], behaving like a solid lubricant.

However, at higher carbon content, 10wt% and 12wt% carbon black contamination, the friction force and coefficient of friction rise significantly. This is attributable to the thickening effect resulting from an appreciable increase in viscosity. In addition, the ability of the lubricant to disperse the carbon black particles reduces with percentage increase in concentration; the consequence of which is increase friction and coefficient of friction due to restriction of lubricant flow into the contact by carbon black agglomerates with the consequence of increased metal-to-metal contact between the rubbing surfaces.

When the normal load was sequentially increased there was a corresponding rise in the friction force. This is adduced to the fact that film thickness decreases with increasing load which consequently increases the friction between the rubbing surfaces. There was, however, insignificant change in the coefficient of friction. An indication that the coefficient of friction is less dependent on the normal load [48] at this extreme condition of lubricant contamination at high temperature, high load and boundary lubrication; but rather on the viscosity since the same carbon black content (3wt%CB) was used at various loads.

5.7.3 Wear analysis

5.7.3.1 Wear scar volume

The influence of carbon black particles in increasing wear was manifested in wear scar volume analysis. The volume of the wear scar increased steadily with temperature and carbon content but very sharply at higher contents, especially 10wt% and 12wt%. The reasons for these may be attributed to the facts that temperature increase results in thermal thinning of the lubricant which manifests as oil film thickness reduction; secondly, there are more carbon black particles at higher levels which could lead to more three-body abrasion or blockage of lubricant into the contact resulting in more metal-to-metal contact and therefore more wear. This is in line with previous findings [2, 4-6, 87, 160].

A similar observation was noted when normal load was sequentially increased using 3wt% carbon black content where the wear scar volume increased correspondingly with load increase but extremely sharply at 2.63 GPa. This is due to the fact that load increase causes reduction in the lubricant film thickness, leading to increasing metal-to-metal contact and, hence, more wear.

The progressive increase in wear volume with carbon black content is an indication that formation of boundary film decreases with increase in soot content as the presence of soot is suspected of inhibiting the formation of protective boundary layer at the interface between the contacting bodies [14].

5.7.3.2 End-of-test contact pressure

The initial Hertzian contact pressures are indicative of a contact operating under boundary lubrication. Though, with the level of reductions observed from post-test contact pressure estimations, the contact may experience some level of hard elastohydrodynamic lubrication too. This may be due to the fact that the materials in contacts, being metals, have high elastic modulus [128].

Nevertheless, the combined effects of the contact pressure, being higher than 1 GPa and the minimum film thickness lower than 0.1 μm are indicative of the ball-on-flat contact operating under boundary lubrication conditions for all the tests here. The estimated lambda ratio values for all the sooty-oil surrogates with 50 N normal load also corroborates this.

The results obtained for end-of-test contact pressure clearly showed that nominal contact pressure is dependent on the area of contact. However, to have a proper understanding of how nominal contact pressure varies during test, there is the need to establish a relationship between contact pressure and sliding distance/time with a view to having an enhanced ability to propose and predict wear mechanisms and other tribological phenomena that may occur in the course of the test. Figure 5.42 presents this correlation for the evolution of wear tests where the wear scar width increases with the test duration while, as would be expected, the post-test contact pressure decreases correspondingly.
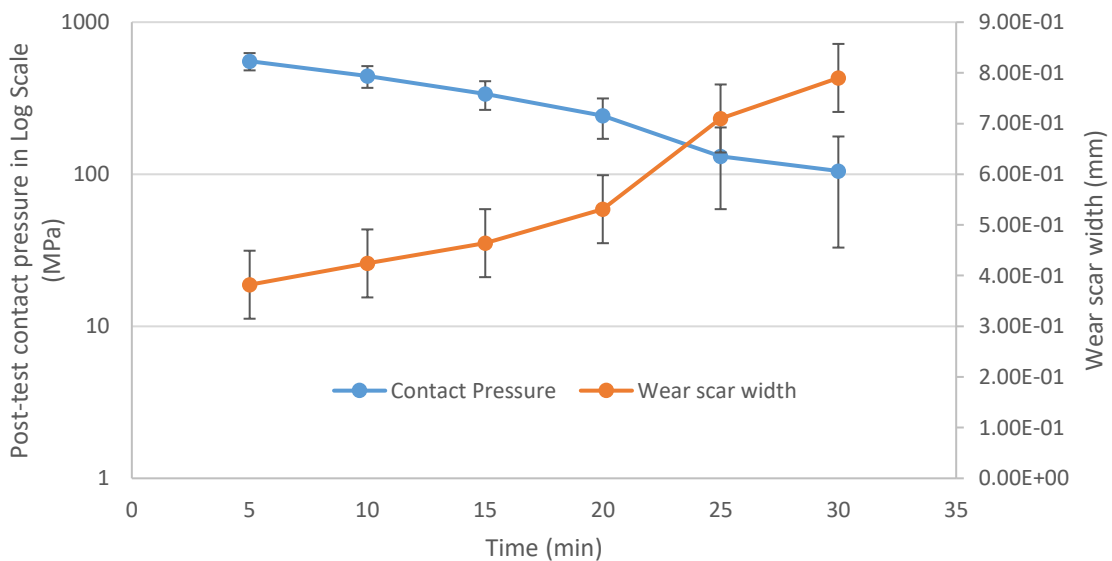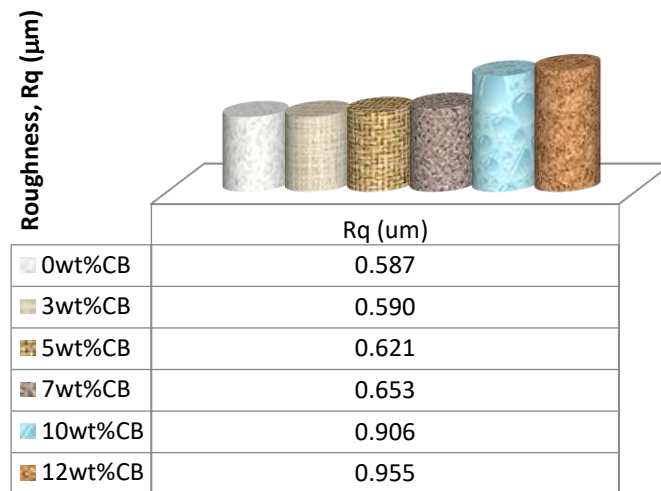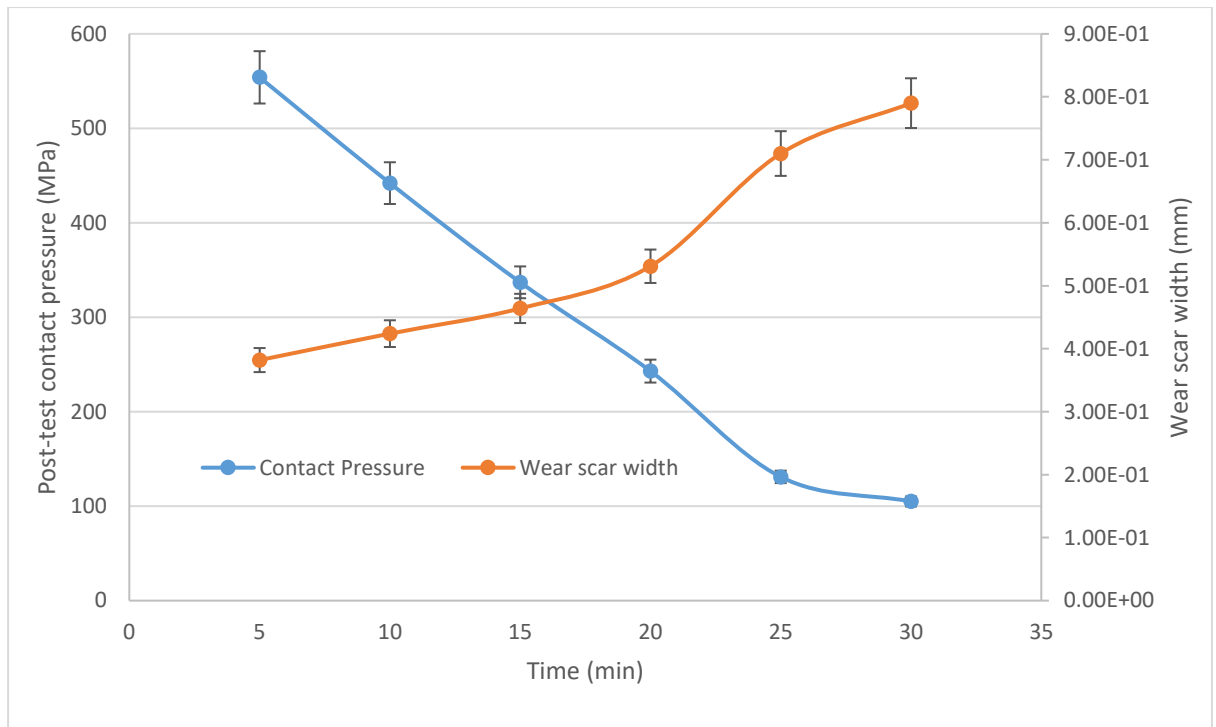
Figure 5.42: Relationship between post-test contact pressure and wear scar width for 3wt%CB content running for different durations percentage error bars
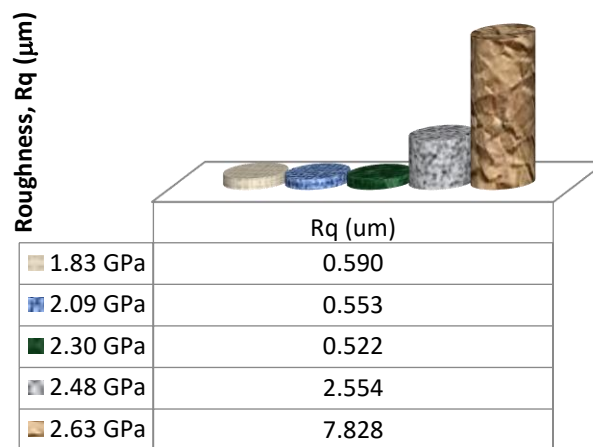
5.7.3.3 Wear scar roughness profile

The result obtained from wear scar roughness indicated marginal, but noticeable variations in post-test surface roughness values for the flat specimen used for 0wt% to 7wt% CB contents; the values for 10wt% and 12wt% contents are relatively higher. This shows that as carbon black particles abrade the softer surface it also exhibits its polishing effect especially at moderate contamination levels while the abrasion could be detrimental at higher percentage of contamination. It should be particularly noted that the wear scar roughness for 3wt% carbon black content at different normal loads was minimum at 2.09 GPa and 2.30 GPa normal loads, but increased in multiple folds at higher contact pressures, specifically 2.48 GPa and 2.63 GPa. This is suggestive of the combined effects of moderately high normal load with the level of homogeneity of 3wt% carbon black content used, resulting in three-body abrasive polishing. A clear manifestation of polishing effect of carbon black, especially at high level of homogeneity and moderate loads [2, 6, 71, 74, 79, 161, 162]. While for higher loads, the surface roughness could be extremely detrimental despite high level of sooty-oil homogeneity.

5.7.3.4 Wear mechanisms

Apart from the fact that the wear volume increases with carbon black contamination, there is also an obvious transition in wear mechanism as influenced by carbon black content levels. The wear mechanism observed in these tests are predominantly abrasion. Abrasive wear are basically of two types: two-body abrasion or three-body abrasion.

For 0wt% carbon black content, the wear was mainly boundary lubricated metal-to-metal contact. The material of the ball specimen, being harder, sliding against the relatively soft flat specimen; thus resulting in two-body abrasive wear, illustrated in

Figure 5.43(a). At moderate normal load of 50N [125] and carbon black contents, 3wt% to 7wt%, the observed wear mechanism was three-body abrasion resulting from carbon black particles entrainment with scratch marks and plastic deformation at the edges; this is depicted in Figure 5.43(b). However, at higher carbon black content (10wt% and 12wt%), high levels of abrasive wear and pronounced plastic deformation at the edges were dominant ostensibly due to starvation of lubricant caused by carbon black agglomerates, formed at higher contents, either restricting easy flow of the lubricant or completely preventing the lubricant from getting access to the contact region of the specimens. This may also result in two-body abrasive wear. The resultant crack formation and propagation leading eventually to localized adhesive scuffing is an indication of extreme damages that high soot retention can cause in an engine as predicted by Green and Lewis [2]. This is a clear indication of how wear mechanisms are dependent on carbon black content and temperature (hence oil film thickness).

(a)

Two-body abrasive wear

(b)

Three-body abrasive wear
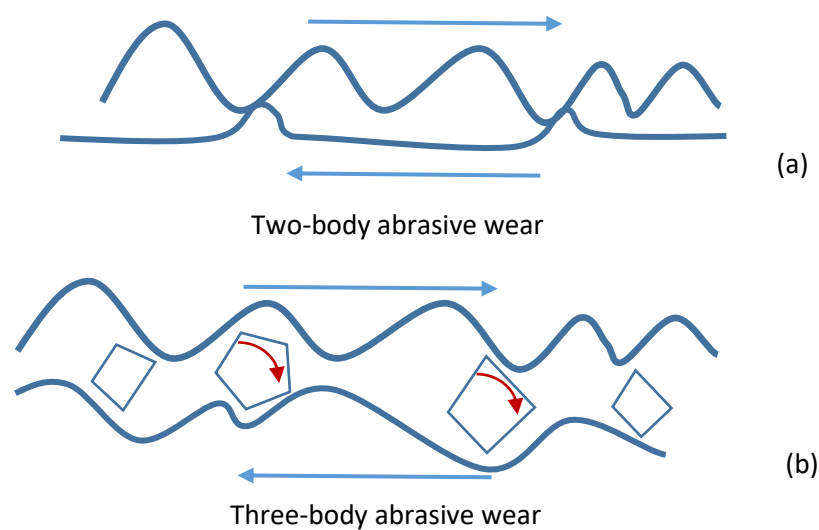
Figure 5.43: Abrasive wear mechanisms [163]

At progressive normal load increase, there was pronounced abrasion and plastic deformation at 2.09 GPa and 2.30 GPa while there were excessive adhesion, crack formation and propagation and material transfer between the surfaces at 2.48 GPa and 2.63 GPa. This is a manifestation of total breakdown of lubrication in that area. The cracks are obviously caused by high shear stress resulting from friction forces. At higher contact pressures, carbon black particles possibly got trapped between the sliding surfaces, thus enhancing two-body abrasion resulting in larger wear scar and transfer of large fragments of the material from the flat specimen, known as galling.

Apart from soot contamination, oxidation can also increase lubricant viscosity and cause abrasive polishing [76]; while corrosive wear can result from sulphuric acid and moisture.

The ball specimen, originally assumed to be hard enough to resist any deformation, was re-examined when this level of damage was noticed on the flat specimen. And, it showed similar features with severe obliteration of its original surface especially at higher contact pressures. This is obviously due to high contact pressures resulting in the trapped hard carbon black particles subjecting the two contacting surfaces to three-body abrasive wear [37]. This phenomena, according to Williams [164], is regarded as localized damage resulting from the occurrence of solid-phase welding between the

surfaces in contact. This is attributable to the fact that as the friction force increases due to high normal load, there is corresponding increase in shear stress at the interface [40]. It should, however, be noted that the test here combined cogent factors that can cause detrimental damage to tribological contacts, namely: lubricant contamination, high temperature, high load and boundary lubrication and is therefore considered as the "worst-case" conditions.

5.7.3.5 Evolution of wear

Evidence from the "evolution of wear" test proves that wear generation and progression occur in stages and is a function of time. Interestingly, the rate of progression can be linear especially if the viscosity of the lubricating fluid is moderate as shown by the percentage increase curve for the first 20 minutes.

The combined effects of normal and tangential loads emanating from applied normal load and sliding action exerted by the harder ball specimen on the softer flat specimen results in the deformation of the surface layer through the removal of the asperities of the softer surface. This process eventually generates a relative smooth surface as revealed by the measured post-test roughness at 2.09 and 2.30 GPa.

Under the severity of the worst-case scenario earlier mentioned, deformation resulting from frictional forces could displace surface material in the direction of sliding resulting in crack formation. Figure 5.44 shows the wear scar profile for test at 2.63 GPa obtained from Veeco Dektak 150 Profilometry where the direction of propagation of cracks can be seen. Cracks continuously build-up in a sort of networking through formation, propagation and connection with other cracks or subsurface cracks eventually leading to crack nucleation and consequent void formation through wear particle detachment [165] manifesting as surface damage with the level of deformation governed by the tribological conditions and material properties [36, 166-169].
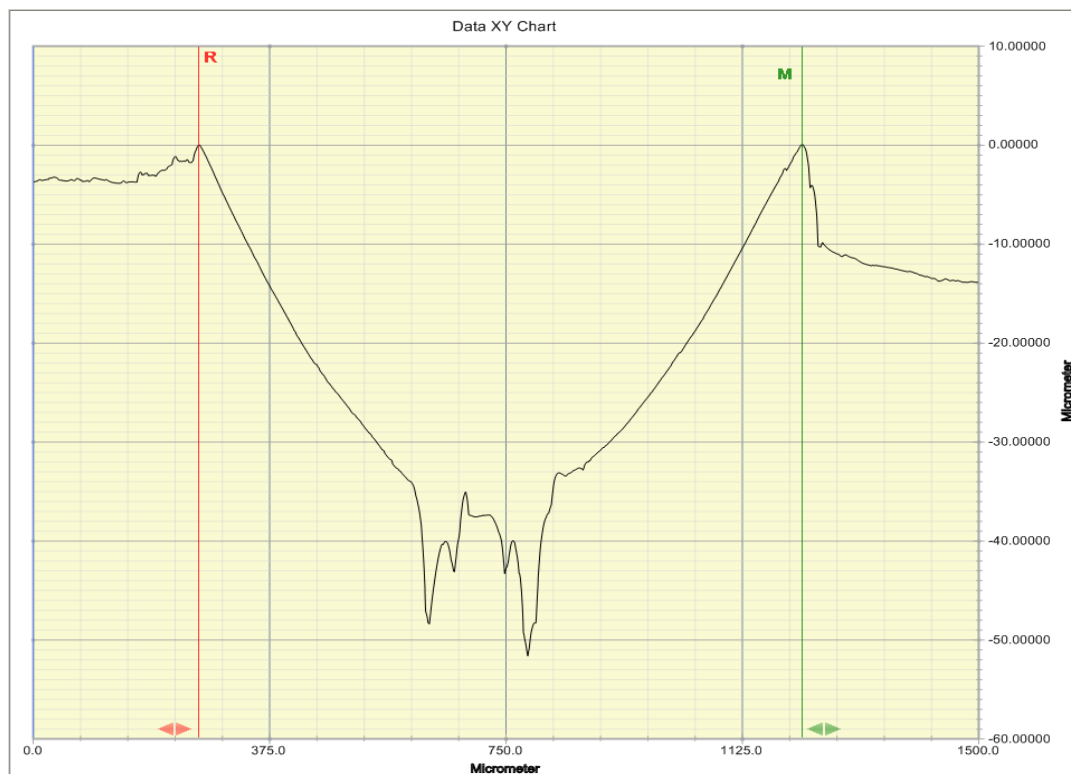
Figure 5.44: Wear scar profile showing void formation through cracks connection

81

5.7.4 Film thickness measurement

The lowest film thickness values occurred at 180°, and this was consistent for all the tests. Ordinarily, with a perfectly aligned set-up, the reciprocating motion is expected to produce minimum film thickness at both ends (0° and 180°), which are the points of zero sliding velocity; and maximum at the centre of the stroke (90° and 270°), where sliding velocity is maximum. This may have been caused by misalignment which pushes the pin specimen into the counter-face, increasing the load towards the end of the forward stroke. The reason for this misalignment was suspected to be because the point of connecting the pin specimen holder to the Plint reciprocating head was not centre as the available holder was just adapted for the testing. A follow-up test may need a re-designed holder suitable for the peculiarity of this set-up. Nonetheless, the 20 Hz curve tends to generate the expected trend; this may be due to the fact that as the speed is increased, the contact inclines towards the full film conditions.

In line with the analytical estimations, the experimental results indicated that increasing the speed generates increasing film thickness; while increasing the normal load reduces the film thickness. For the variable carbon black content, the film thickness values for the 0wt% and 1wt% are quite close; there is, however, significant increase in the film thickness with 3wt% and 5wt%. It is therefore obvious that increasing carbon content tends to increase the film thickness. This is attributable to their tendency to increase the viscosity of the lubricant; and thus, increase its load carrying capacity.

Apart from high level of repeatability as revealed by the combined result of the tests conducted under the same conditions (10 Hz, 20 N and 0wt%CB), the numerical film thickness values are also comparable to the analytical predictions. The analytical estimation of the lubricant film thickness under those conditions, with an entraining speed of 0.236 m/s, yields 3.67 μm; while the average of the experimental film thickness under the same condition is 2.81 μm.

There is noticeable spikes in the curve obtained for the 5wt%CB, this may be due to the presence of more carbon black particles at this level of concentration. Though minimal, the presence of electrical noise was also noted in some of the curves; this may have come from the connecting cables, which are necessarily long for this test. Acting as antennas, these cables can thus pick up external electromagnetic energy from surrounding rotating equipment.

5.8 Conclusions

From the series of outlined experiments conducted in this chapter, the following conclusions can be drawn:

Though, with the progressive increase in viscosity of sooty oil as the carbon black content increases, the friction is normally expected to be reduced. While the theoretical calculations of the film thickness and contact pressure indicated that the sliding process operated under boundary lubrication regime which is expected to generate higher friction. The fact that friction increases with carbon black content, especially at higher compositions of 10wt% and 12wt% implies that the lubrication regime under which a tribosystem operates takes precedence over the viscosity of the lubricating medium.

Also, when friction is compared with coefficient of friction, it can be deduced that viscosity within 200cSt (0 – 5wt%CB) where the coefficient of friction values are similar is the best boundary lubrication conditions. Beyond these levels, oil thickening sets in

due to increase in viscosity; thus increasing the contact friction which ultimately reduces the efficiency of the automotive engine.

Wear scar roughness measurement revealed that roughness changes with wear with an exhibition of abrasive polishing effect of carbon black particularly when the level of homogeneity is high at moderate normal loads.

Optical microscopic images of the wear scar showed that wear mechanisms progressed from lubricated metal-to-metal sliding wear at no contamination to moderate three-body abrasion and pronounced two-body abrasive wear with plastic deformation as the tests progressed with increasing carbon black content levels.

At high carbon black contents, starvation was the major cause of the observed wear mechanism resulting in crack formation and propagation leading eventually to localized adhesive scuffing and material removal. The results also revealed that there could be significant wear due to debris entrainment especially under severe adhesive wear conditions.

High load test provides evidences of how deleterious soot can be at very high contact pressures where the contact conditions can be likened to a worst-case scenario comprising lubricant contamination at high temperature, high load and boundary lubrication. The combination of these factors contributes to crack initiation and propagation which subsequently results in material removal and severe damage to the contacting surfaces.

From the wear analysis, it is clear that the carbon black contamination effects in the contact are substantial at high concentration levels, high temperature and high normal loads as wear scar volume increased with these parameters. Evolution of wear test further reveals that the progression of wear is a function of time.

At moderate carbon black contents, the wear behaviour is as a result of three-body abrasive wear where the suspended carbon black particles freely roll and slide between the contacting ball and flat specimens. Another observed features of the wear scars is plastic deformation (pile-ups on both sides of wear groove) resulting from the material of the ball specimen being much harder than that of the flat specimen. While at higher carbon contents where agglomeration is more likely, the resultant wear track was a product of mechanical interaction between the ball and flat specimens (metal-to-metal contact) due to starvation of lubricant which access into the contact is restricted by the carbon particle agglomerates, and thus resulting in two-body abrasion. A combination of such factors as: carbon black quantity, relative hardness of the contacting bodies, normal load among others influenced the resultant wear mechanisms, wear scar volume and severity of the wear.

The instantaneous measurement of the film thickness of varying compositions of the sooty-oil surrogates showed that the adopted ultrasonic technique is very effective. Tests under varying speeds and loads produced the same trends with the analytical prediction; and the numerical values of the film thickness obtained experimentally also indicated closeness to the analytical results.

Chapter 6

Non-conformal Line Contact Mini Traction Test

A ring-on-ring test was conducted using a Plint TE 54 mini traction machine; this is to further reveal sooty-oil surrogate behaviour under a different lubrication regime. The ring-on-ring contact using twin-disc arrangement was designed to simulate a tribocontact situation between an automotive engine's cam lobe and roller follower under mixed lubrication conditions. With the contact undergoing sliding and rolling concurrently, this arrangement perfectly mimics this contact's geometry with a non-conformal line contact arising from the profiles of the contacting bodies conforming in a longitudinal direction and non-conforming in the perpendicular direction; thus resulting in high contact pressure in the interface [170]. Figure 6.1 presents the valve train system showing a cam lobe and roller follower rolling/sliding contact along with the ring-on-ring arrangement idealising the contact.
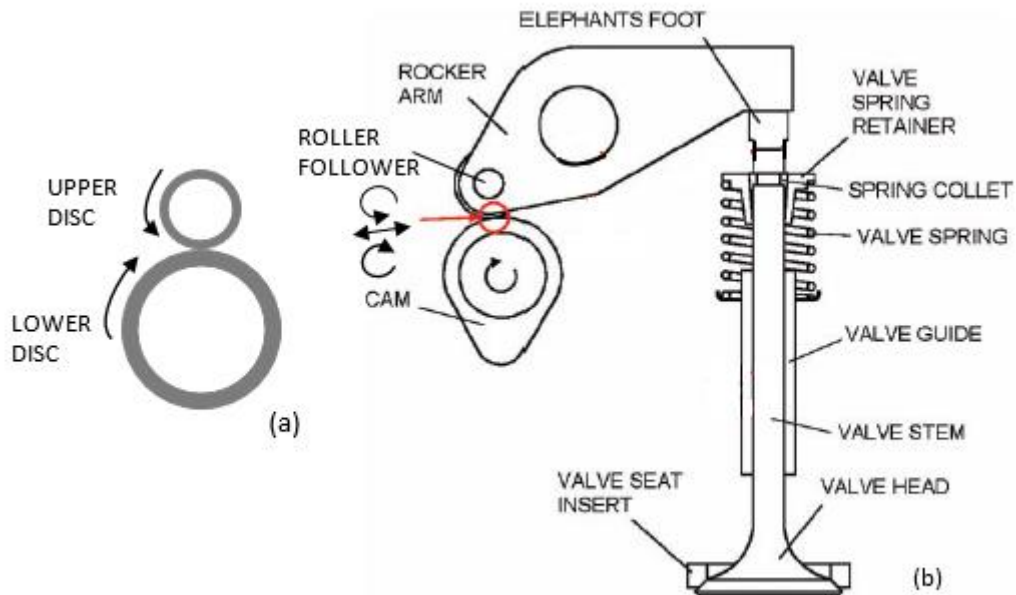
Figure 6.1: Schematics of the the experimental arrangement (a) ring-on-ring simulation (b) valve train's cam lobe/roller follower contact geometry [2]

6.1 Test equipment

The TE 54 Mini Traction Machine (MTM), manufactured and supplied by Phoenix Tribology Limited, UK, is a versatile tribometer provided with a self-aligning carrier which allows a 25 mm diameter by 8 mm wide disc to be mounted and roll on a 50 mm diameter by 10 mm wide disc, thus resulting in an 8 mm wide line contact. In this arrangement, both specimens rotate on vertical plane, thereby eliminating the possibility of spin or skew which is common with horizontal plane-rotating ball on disc arrangement. Figure 6.2 presents the pictorial view of the machine with the arrangement of the specimens in the test chamber; while the basic specifications of the machine are presented in Table 6.1.
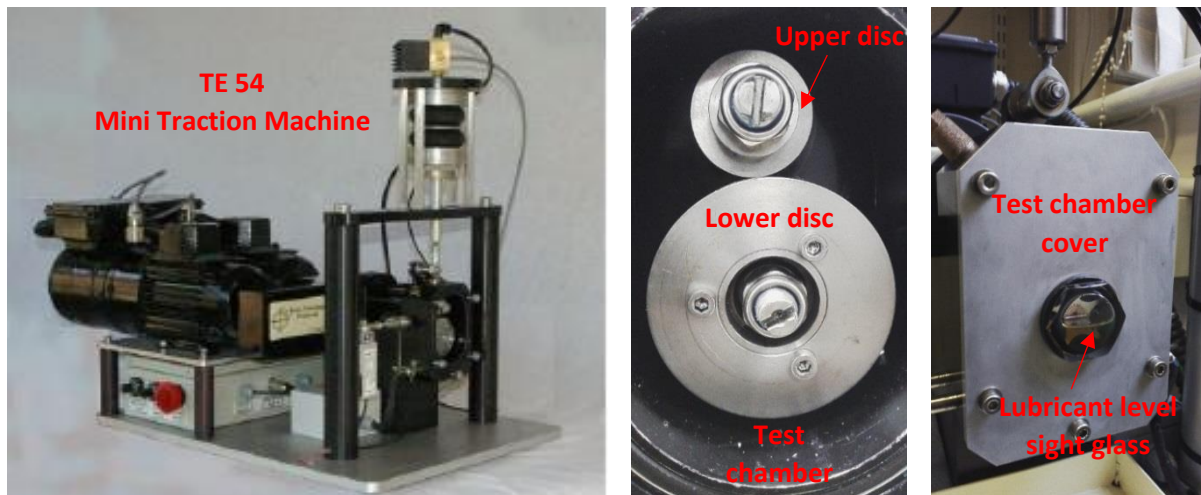
Figure 6.2: TE 54 mini traction machine with specimen arrangement in the test chamber [171] (uncovered and covered)

Table 6.1: The specifications of TE 54 MTM [171]

Upper Disc Specimen Diameter (mm)	25
Upper Disc Specimen Width (mm)	8
Lower Disc Specimen Diameter (mm)	50
Lower Disc Specimen Width (mm)	10
Maximum Upper Disc Speed (rpm)	4000
Maximum Lower Disc Speed (rpm)	2000
Maximum Surface Speed (m/s)	5.24
Maximum Load (N)	500
Maximum Hertzian Pressure (Steel)	2.0
Oil Bath Temperature (^{o}C)	Ambient to 150
Heater Power (W)	250
Temperature Sensor	k-type thermocouple
Loading System	Pneumatic bellows with force feedback
Drive Ratio	2:1
Interface	SUPERSLIM Serial Link Interface Module
Software	COMPEND 2000

In order to adjust both the mean speed and the slide/roll ratio, the upper and lower discs are independently driven by variable speed motors; while the upper disc (25 mm diameter) is driven directly through a shaft connected to its drive motor through flexible couplings, the lower disc (50 mm diameter) is driven by the second motor through a toothed belt with a 2:1 reduction. In addition, the upper specimen shaft is carried on a pivoted arm and trunnion assembly, enabling both load actuation and traction/friction force measurement. The lower specimen is mounted on a holder before being inserted into the shaft within the chamber. There are two such holders supplied with the machine, fixed and self-aligning, shown in Figure 6.3. The fixed specimen holder ensures a point contact between upper ball and lower disc, while the self-aligning gives a perfect line contact whose length is determined by the width of the upper disc.
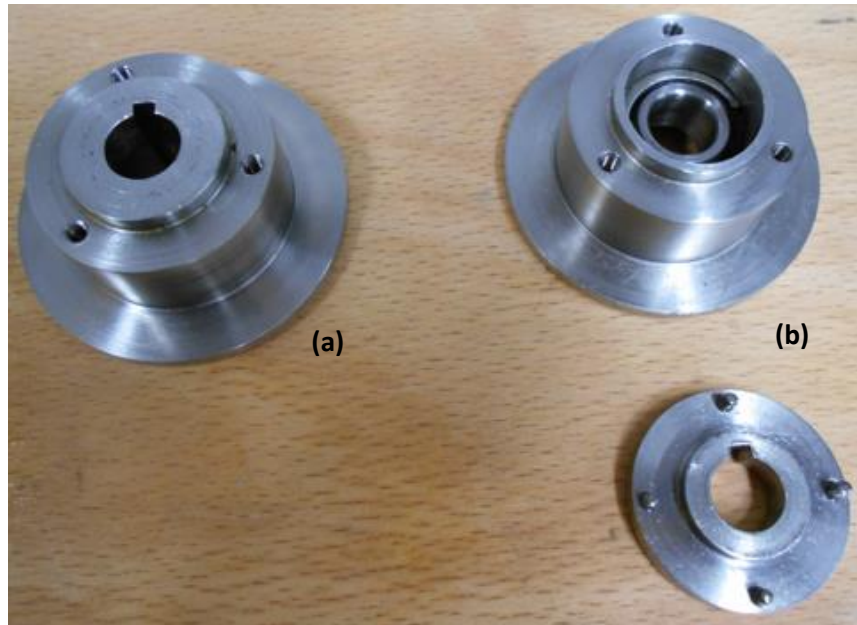
Figure 6.3: Pictorial views of the lower disc holders (a) fixed (b) flexible and its key-slot attachment

The two discs are rolling against each other with tangential traction between them resulting from the upper disc rotating at double the speeds of rotation of the lower disc. Figure 6.4 shows how the discs are held together by the normal load and a depiction of the ideal elastohydrodynamic (EHD) lubrication contact condition for the discs.
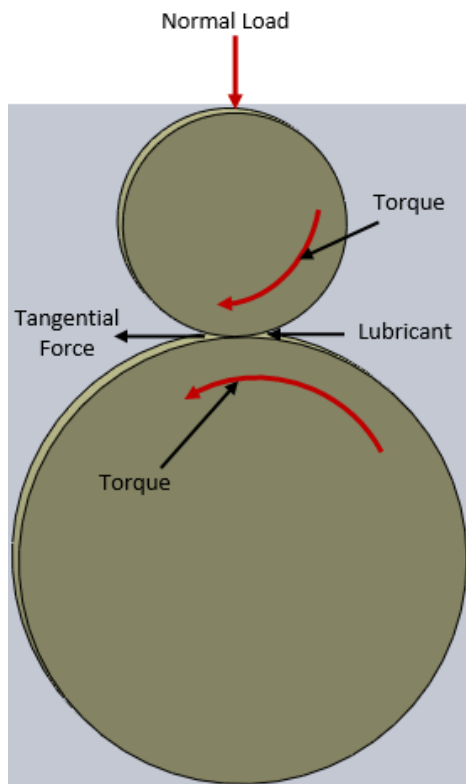
$$Traction\ Coefficient = \frac{Tangential\ Force}{Normal\ Load}$$

Equation 6.1
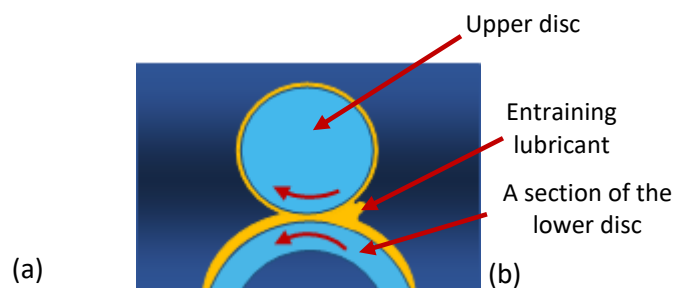
Figure 6.4: Schematics of (a) the discs held in contact by normal load uniformly distributed along their contact length and (b) a depiction of ideal EHD lubrication condition for the contacting discs

The process of loading is through a servo-controlled pneumatic bellows actuator incorporated with force transducer feedback. The test chamber where the specimens are accommodated is provided with a cover having a sight-glass to observe the level of the lubricant. There are also electrical resistance heaters within the chamber for high temperature testing with two thermocouples, one to measure the chamber temperature and the other for the temperature of the lubricant. Practically, valvetrain's cam lobe/roller follower contact encompasses both rolling and sliding motions.

6.1.1 Slide/roll ratio

The traction measuring transducer is normally designed to operate with the link to the upper disc shaft in tension, as shown in Figure 6.5; and the occurrence of this is guaranteed with the surface velocity of the upper disc being always greater than the surface velocity of the lower disc, that is, $U_{upper} > U_{lower}$ [172]. The rolling velocity is analogous to entrainment velocity, since the contacts are lubricated [164]. Equations 6.2 to 6.6 highlight how the relevant parameters, such as: slide/roll ratio, sliding and rolling velocities, and speeds of upper and lower discs, are determined.
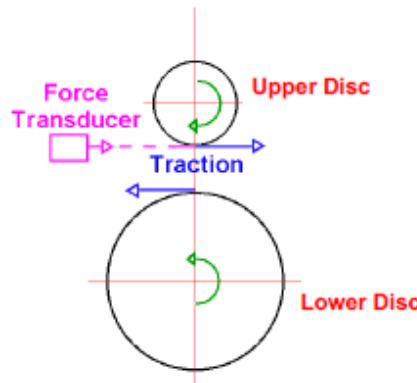
Figure 6.5: The operation of the force transducer with the link to the upper disc [172]

Conventionally, Slide/Roll Ratio is defined [172] as:

$$\frac{Slide}{Roll} Ratio = \frac{Sliding\ Velocity}{2\ x\ Rolling\ Velocity} \qquad \text{Equation 6.2}$$

where:

Sliding Velocity = $U_{upper} - U_{lower}$ Equation 6.3

Rolling Velocity = ½ ($U_{upper} + U_{lower}$)   Equation 6.4

and:

$$U_{upper} = \frac{\pi\ x\ D_U\ x\ N_U}{60}\ ms^{-1} \qquad \text{Equation 6.5}$$

$$U_{lower} = \frac{\pi\ x\ D_L\ x\ N_L}{60}\ ms^{-1} \qquad \text{Equation 6.6}$$

where:

D_U and D_L are the diameters of the upper and lower discs respectively

and N_U and N_L are the rotations (in rpm) of the upper and lower discs respectively

6.2   Test specimens

Any alteration to the geometric profile of cam lobes due to wear can retard valve timing; this is detrimental to internal combustion engine power and performance [173]. Consequently, cam lobe are generally made of high performance steel due to the requirements of hardness, strength and high resistance to wear. Chrome steel fits these requirements because it gives suitable permissible compressive stresses [174].

Accordingly, the material selected for the upper and lower ring specimens is chrome steel (EN31) which contains high carbon and about 1.5% chrome. Table 6.2 gives the chemical composition and mechanical properties of the material. With this composition, chrome steel offers high degree of hardness with compressive strength and abrasion resistance and used in automobiles for ball and roller bearings. While Figure 6.6 presents the orthographic drawings of the upper and lower discs with specified dimensions.

Table 6.2: Chemical composition and mechanical properties of chrome steel

Chemical composition	
Element	**Weight (%)**
Carbon	0.90 – 1.20
Manganese	0.30 – 0.75
Silicon	0.10 – 0.35
Sulphur	0.40
Phosphorus	0.40
Chromium	1.00 – 1.60
Mechanical properties	
Tensile Strength (MPa)	750
Yield Strength (MPa)	450
Average Hardness (HRC)	63
Young's Modulus, E (GPa)	215
Poisson's Ratio, υ	0.3
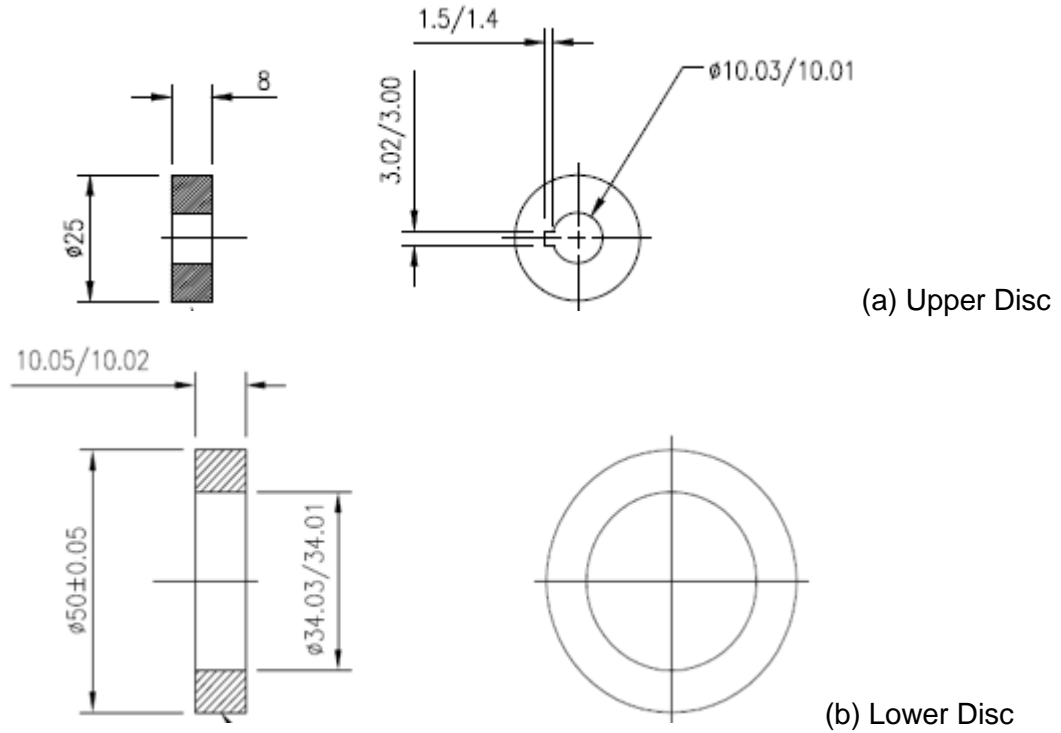
Figure 6.6: Upper and lower rings with specified dimensions

The specimens were produced by KTL Designs Ltd/WA Carr (Dena) with a 25 mm diameter and an 8 mm width for the upper disc and a 50 mm diameter and 10 mm width for the lower disc, thus resulting in an 8 mm wide line contact. The surface roughness of the specimens were measured using Mitutoyo's Surftest SJ-500 profilometer; the average values of upper and lower specimens were 0.130 µm and 0.133 µm respectively.

6.3 Calculation of contact parameters

Theoretically, the contact area for two parallel cylinders is a non-conformal line contact. The contact parameters can be estimated using the following formulae obtained from Stachowiak and Batchelor [40].

6.3.1 Contact pressure

The maximum contact pressure, p_o, was estimated using Hertzian's contact formula:

$$p_o = \frac{P}{\pi b l} \qquad \text{Equation 6.7}$$

Average contact pressure, p_m is:

$$p_m = \frac{P}{4bl} \qquad \text{Equation 6.8}$$

Maximum shear stress, τ_{max} is:

$$\tau_{max} = 0.304 p_o \qquad \text{Equation 6.9}$$

Contact area dimensions, b, is given by:

$$b = \left(\frac{4PR'}{\pi l E'}\right)^{1/2} \qquad \text{Equation 6.10}$$

Depth at which τ_{max} occurs, z is:

$$z = 0.786b \qquad\qquad \text{Equation 6.11}$$

b is the half width of the contact rectangle and other parameters are as defined in the preceding chapter.

Figure 6.7 presents a schematic diagram of the two parallel cylinders contact (a) along with the contact pressure distribution (b). The contact area is rectangular with semi-elliptical pressure distribution.

(a)   (b)
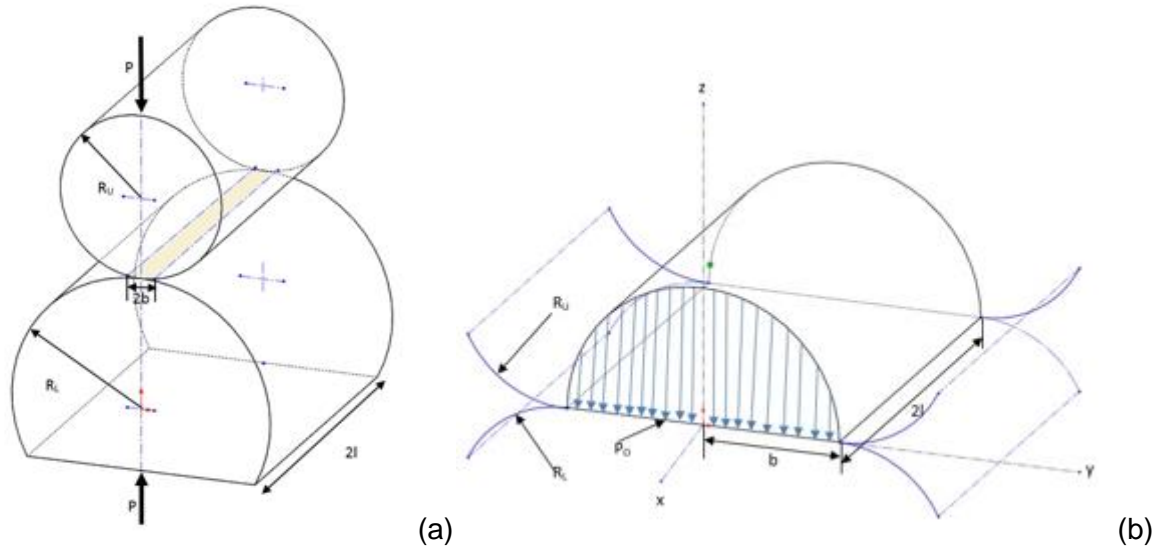
Figure 6.7: Schematic diagrams of (a) the two parallel cylinders contact [40] and (b) semi-elliptical pressure distribution [173]

6.3.1.1 Hertzian contact conditions

The Hertzian contact pressures along with maximum shear stresses, the depth at which they will occur and the contact area dimensions were estimated (using Equations 6.7 to 6.11) for the proposed tests at varying normal loads with an entrainment speed of 1 m/s and 10% slip. The results are presented in Table 6.3 and detailed spreadsheet calculations are included in Appendix VII.

Table 6.3: Contact pressures at various nominal loads

Nominal Load, P (N)	p_o (MPa)	p_m (MPa)	τ_{max} (MPa)	2b (mm)	z (mm)
50	167.93	131.90	51.05	0.047	0.019
100	237.49	186.53	72.20	0.067	0.026
150	290.87	228.45	88.42	0.082	0.032
200	335.87	263.79	102.10	0.095	0.037
250	375.51	294.93	114.15	0.106	0.042
300	411.35	323.08	125.05	0.116	0.046
350	444.31	348.96	135.07	0.125	0.049
400	474.99	373.06	144.40	0.134	0.053

Maximum Contact Pressure, p_o (MPa),

Mean Contact Pressure, p_m (MPa),

Maximum shear stress, τ_{max} (MPa),

Contact area dimensions, 2b (mm),

Depth at which τ_{max} occurs, z (mm)

6.3.2 Film thickness

To determine the lubrication regime under which the rings will operate, theoretical estimation of the film thickness was done using the central film thickness formula, Equation 6.12, which is similar to the previous formula used in Chapter 5.

$$\frac{h_c}{R'} = 2.69U^{0.67}G^{0.53}W^{-0.067}\left(1 - 0.61e^{-0.73k}\right)$$ Equation 6.12

h_c is the central film thickness, other parameters are as defined in the preceding chapter.

The central film thickness was adopted for this estimation because an EHD or mixed lubrication regime is proposed [150]. In elastohydrodynamically lubricated contacts, the contacting bodies in relative motion are separated by a film of approximately constant thickness that may be well represented by the central value over the Hertzian contact zone.

The theory is that if the mean film thickness is less than three times the composite surface roughness of the contacting bodies, the surface asperities will experience EHD and some level of asperity contacts concurrently leading to mixed EHD [49].

6.3.2.1 Film thickness and Lambda ratio

The theoretical central film thickness at 100°C was estimated using Equation 6.12 while the Lambda ratio was determined from Equation 5.14. The values obtained for various carbon black compositions at the minimum load of 50 N are presented in Table 6.4 while Figure 6.8 shows the film thickness at higher loads for various sooty oils. As expectedly, there is progressive increase in film thickness with increasing carbon black content. The detailed spreadsheet analysis is included in Appendix VIII.

Table 6.4: Central film thickness and Lambda ratio of each CB composition at 50 N

Sooty oils	Central Film Thickness (μm)	Lambda Ratio, λ
0wt%CB	0.122	0.525
3wt%CB	0.198	0.853
5wt%CB	0.208	0.897
7wt%CB	0.216	0.927
10wt%CB	0.284	1.221
12wt%CB	0.372	1.601
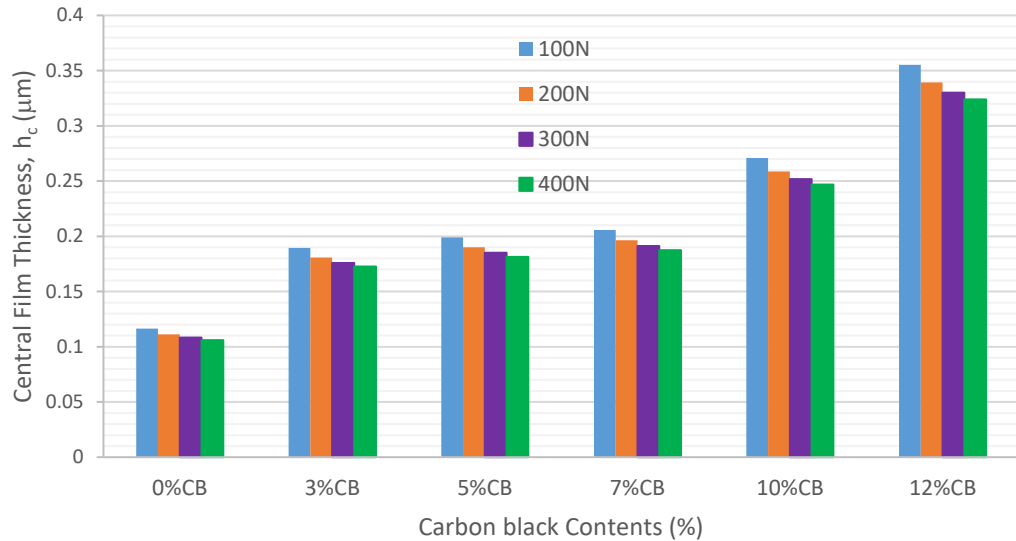
Figure 6.8: Theoretical film thickness estimations at different loads for various carbon black contents

6.4　Experimental procedures

A pair of chrome steel rings (upper and lower) was used for each carbon black composition for the three sets of test details of which will be given below. The discs are fitted to their carriers using appropriate tools and each composition of carbon black-mixed oil are, in turn, fed in through the filler plug until the indicated minimum level is reached (approximately 30ml). While the first set of tests (increasing contact load) ran for 16 minutes, each of the other two (increasing percentage slip and mean speed) ran for 12 minutes. This implies that each of the pair undergoes 40 minutes of continues running. This process was repeated three times to determine levels of repeatability. The summary of the conditions for each of the tests are shown in Table 6.5.

The justification for the relatively short period of test was because the major focus of the test was to study the frictional behaviour of the sooty-oil as each of these parameters (load, slip and speed) changes.

The first set of tests involved maintaining a constant entrainment speed of 1 m/s at 10% percentage slip while increasing the load progressively from 50 to 400 N in steps of 50 N. In the second set, the percentage slip was increased from 2% to 10% at constant entrainment speed of 1 m/s and constant load of 400 N. For the third set, the speed of the upper disc was increased from 504 rpm to 3025 rpm at constant normal load of 400 N and 10% percentage slip. For each set, the test step duration was 120 seconds. The acquired data were stored for post-test analysis using Microsoft Excel.

For the load range set (50-400 N), the contact pressure is between 168-475 MPa. The percentage slip was set at a maximum of about 10% to minimize surface wear and thermal effect at low and high speeds respectively. For speed varying tests, the entrainment (surface) speed was gradually increased from 0.63 m/s to 3.78 m/s. It should be noted here that the programme was sequenced to reduce the speed from the maximum value (3025 rpm) gradually, running each speed backwards for 5 seconds. This is to prevent sudden stoppage which may increase the stress on the specimens.

92

Khurram et al. [175] reported that the percentage slip at the cam-roller interface ranges between 1.6% and 11.4% at the camshaft speeds of 800 rpm and 2000 rpm respectively.

As mentioned earlier, there are two lower specimen holders that were supplied with the machine; fixed for ball-on-ring point contact and self-aligning for ring-on-ring line contact. Although, the upper and lower specimens in this test are discs, both holders were used to observe the effects.

Table 6.5: TE 54 mini traction machine (MTM) test conditions

Set	Test No	Formulated Oil + %Carbon Black (All @ 100°C)				
		0wt%	3wt%	5wt%	7wt%	10wt%
A (Increasing contact load@1m/s & 10% slip)	1	50 N-400 N				
	2					
	3					
	4					
	5					
B (Increasing level of slip@1m/s & 400 N)	1	2% - 10% Slip				
	2					
	3					
	4					
	5					
C (Increasing mean speed@400 N & 10% slip)	1	500 rpm – 3000 rpm				
	2					
	3					
	4					
	5					
Parameter		Tolerances				
Load (N)		± 1				
Lubricant temperature (°C)		± 2				
Peak mean speed (m/s)		± 0.01				

These tests were repeated for selected compositions of carbon black (0wt%CB, 5wt%CB and 10wt%CB) using grey cast iron, whose composition is similar to EN1561 used in the preceding chapter. The purpose was to determine the consistency of the test method and observe how the measured frictional parameter would react when a material of lower strength and hardness is used.

6.4.1 Data acquisition system

TE 54 is operated through a sequenced programme to be prepared for each test as dictated by specific requirements with COMPEDIM 2000 software installed on the attached PC serving as the data acquisition system. Table 6.6 presents the test operational sequence for the test at varying speeds.

Table 6.6: Test operational sequence showing steps for increasing mean speed
(@400N, 100°C & 10% slip)

Step No.	Operation	Step Time (s)	Lower Disc Speed (rpm)	Upper Disc Speed (rpm)
1	Start	2	0	0
2	Oil Temp to 100°C	C Stp+	0	0
3	Load to 400N	C Stp+	OR	OR
4	Run Motor@0.63m/s	C Stp+	229	504
5	Hold @ 10% Slip	120	OR	OR
6	Speed-2@1.26m/s	120	458	1008
7	Speed-3@1.89m/s	120	688	1513
8	Speed-4@2.52m/s	120	917	2017
9	Speed-5@3.15m/s	120	1146	2521
10	Speed-6@3.78m/s	120	1375	3025
11	Speed-5@3.15m/s	5	1146	2521
12	Speed-4@2.52m/s	5	917	2017
13	Speed-3@1.89m/s	5	688	1513
14	Speed-2@1.26m/s	5	458	1008
15	Speed-1@0.63m/s	5	229	504
16	End		OR	OR

C Stp+ is a Conditional step which means move to the next step when the set condition is satisfied

OR means Operate Relative to the previous set condition

6.5   Results

The tests involved progressive variations of load, slip and speed from low level to high level. These variations are therefore expected to influence the results obtainable across the tests.

6.5.1 Friction measurement

6.5.1.1 Traction coefficient

The data obtained from the test is presented in Figures 6.9 to 6.26. Figure 6.9 shows the variation in traction coefficient with time for various carbon black contents at different loads using self-aligning holder, while Figure 6.10 is the graph obtained using the fixed holder. Table 6.7 presents the average values of traction coefficient from these graphs where it can be seen that the value of traction coefficient decreases with increasing carbon black content in both cases, but the values obtained from the self-aligning specimen holder are lower when compared with those from the fixed specimen holder.

To determine how traction coefficient changes with load, Figure 6.11 was extracted from Figure 6.9 and Figure 6.12 from Figure 6.10. The results indicate that traction coefficient remains relatively constant under different loads for each carbon black content.
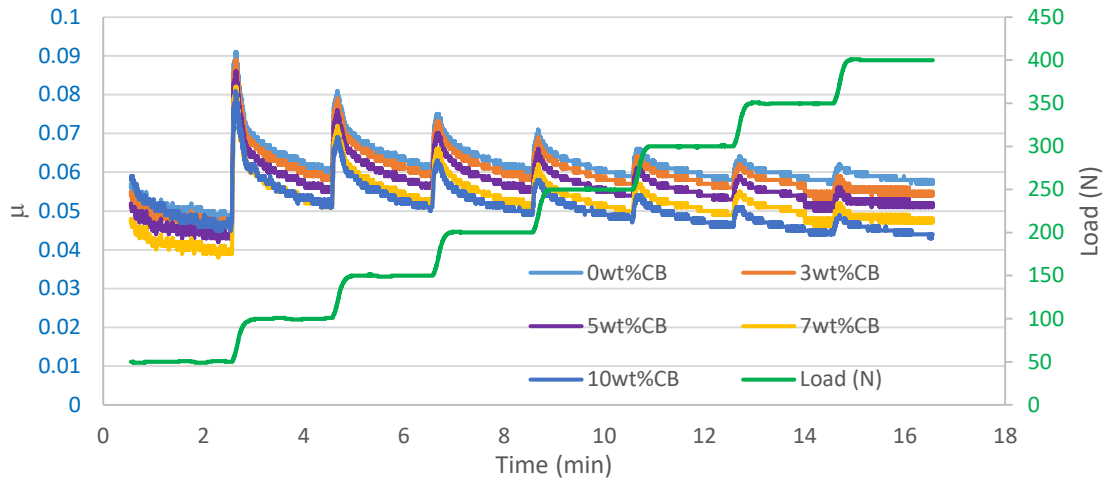
Figure 6.9: Traction coefficient versus time under different loads@1m/s, 10% slip and 100ºC for various carbon black composition using a self-aligning specimen holder
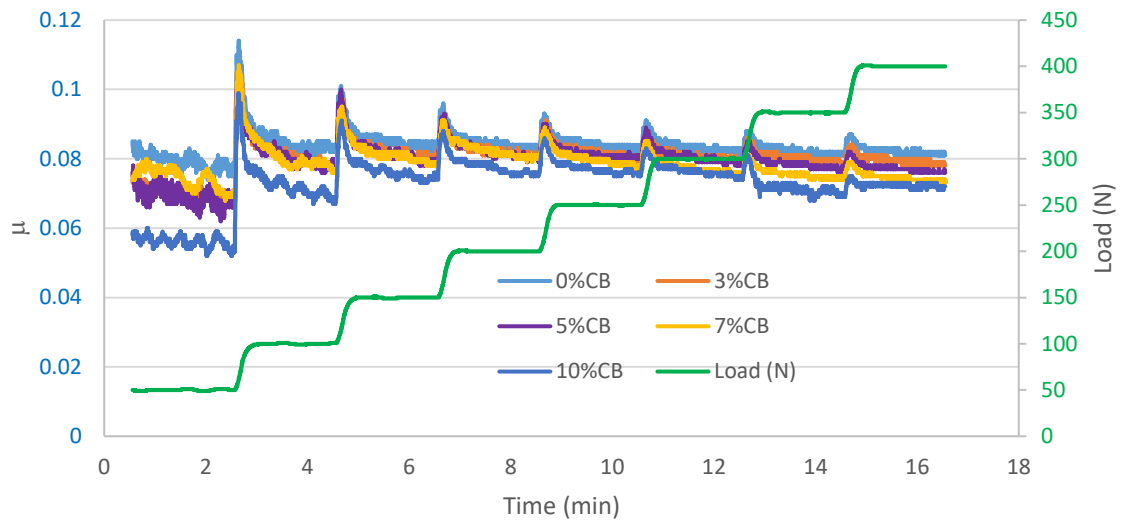
Figure 6.10: Traction coefficient versus time under different loads@1m/s, 10% slip and 100ºC for various carbon black composition using a fixed specimen holder

Table 6.7: Comparison of traction coefficient values for different disc holders (From Figures 6.9 and 6.10)

Sooty oils	Traction coefficients	
	Self-aligning disc holder	Fixed disc holder
0wt%CB	0.061	0.083
3wt%CB	0.059	0.0805
5wt%CB	0.056	0.0795
7wt%CB	0.052	0.079
10wt%CB	0.051	0.073
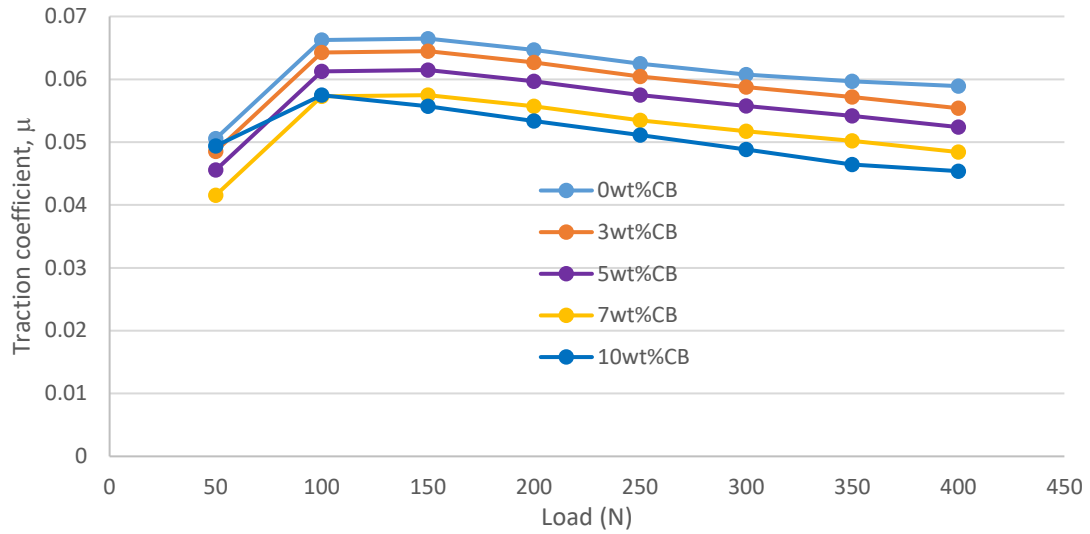
Figure 6.11: Traction coefficient at various loads for different carbon black compositions using a self-aligning specimen holder
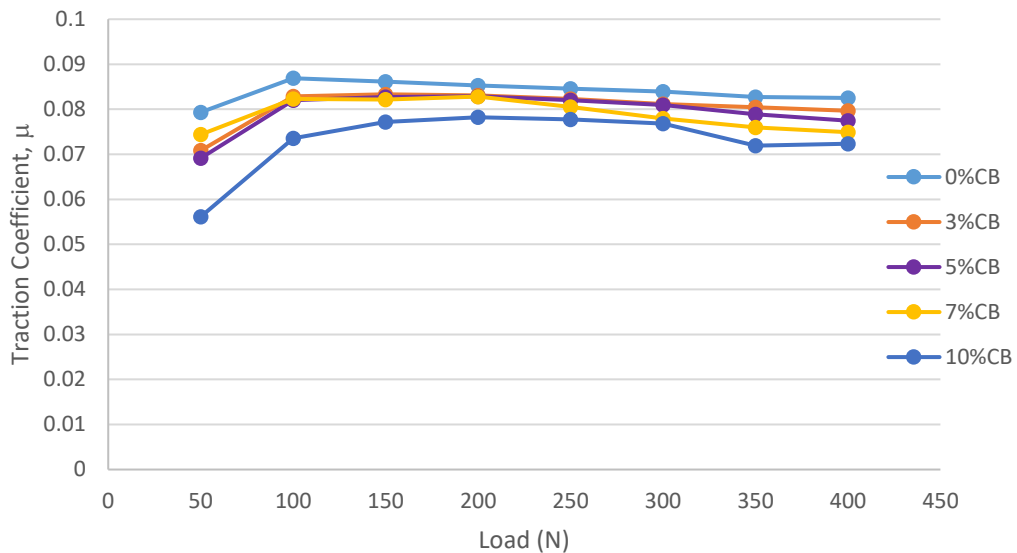
Figure 6.12: Traction coefficient at various loads for different carbon black compositions using a fixed specimen holder

Figures 6.13 and 6.14 present the variation in traction coefficient with time for various carbon black contents at different percentage slips for self-aligning and fixed specimen holders respectively. Table 6.8 presents the ranges of traction coefficient, as the percentage slip varied, for different disc holders. The observed trend of decreasing traction coefficient with increasing carbon black content for varying loads was replicated here too. In addition, the average values of traction coefficient for the self-aligning holder are still lower than those for the fixed holder. The variation of traction coefficient with percentage slip was also determined from each of the figures. Figure 6.15 and Figure 6.16, extracted from Figures 6.13 and 6.14 respectively, show that traction coefficient increases with percentage slip.

96
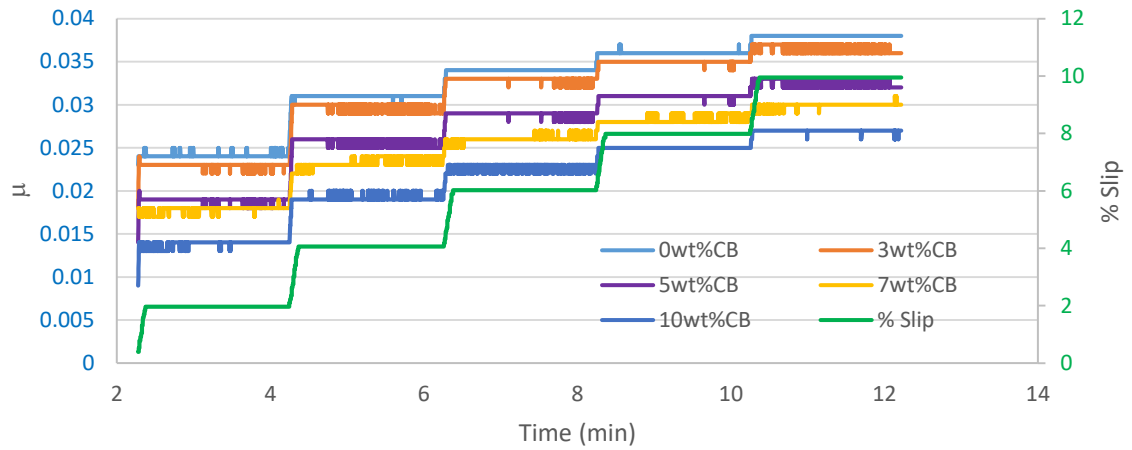
Figure 6.13: Traction coefficient versus time under different slips@1m/s, 400N and 100ºC for various carbon black composition using a self-aligning specimen holder
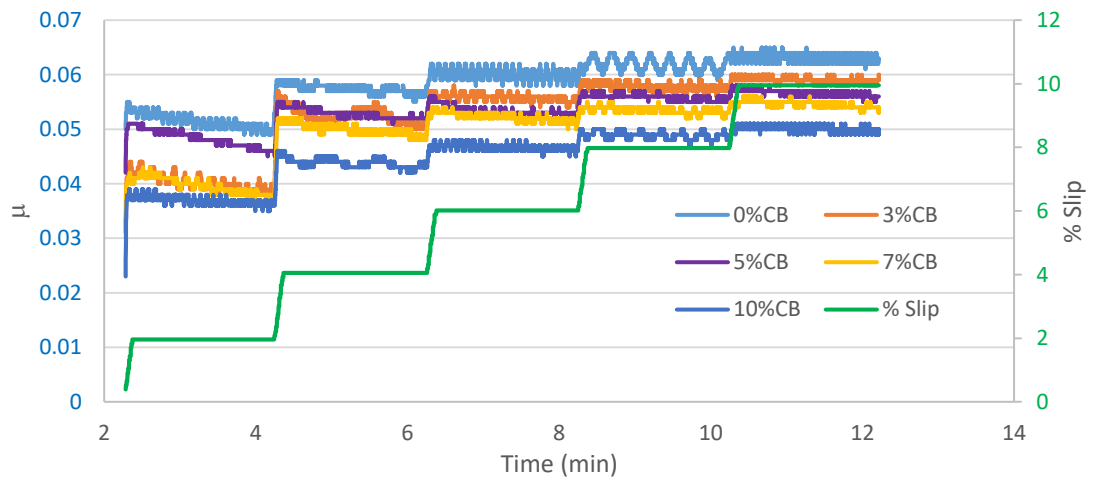
Figure 6.14: Traction coefficient versus time under different slips@1m/s, 400N and 100ºC for various carbon black composition using a fixed specimen holder

Table 6.8: Comparison of traction coefficient ranges for different disc holders (From Figures 6.13 and 6.14)

Sooty oils	Range of traction coefficients	
	Self-aligning disc holder	Fixed disc holder
0wt%CB	0.023-0.038	0.050-0.063
3wt%CB	0.022-0.036	0.039-0.059
5wt%CB	0.018-0.032	0.046-0.056
7wt%CB	0.017-0.030	0.038-0.054
10wt%CB	0.013-0.027	0.036-0.050
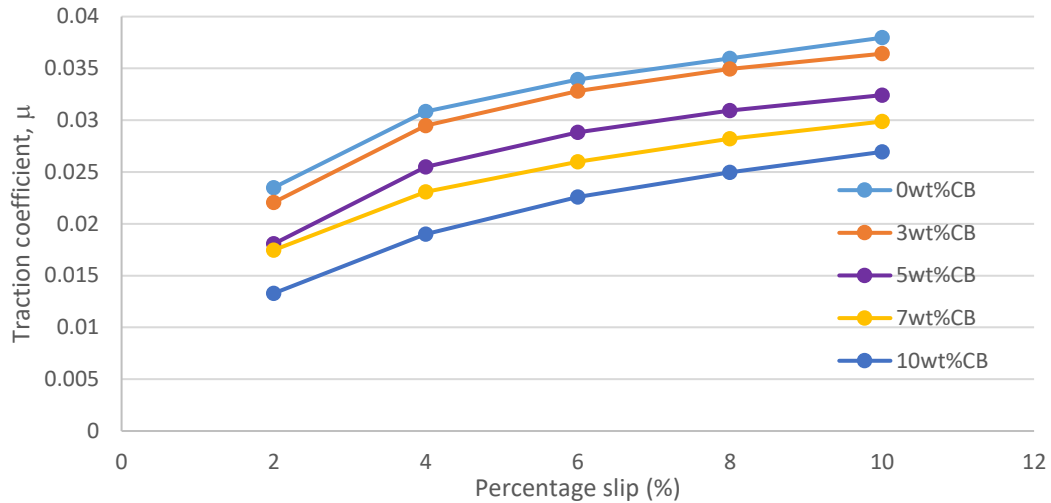
Figure 6.15: Traction coefficient at various % slips for different carbon black compositions using a self-aligning specimen holder
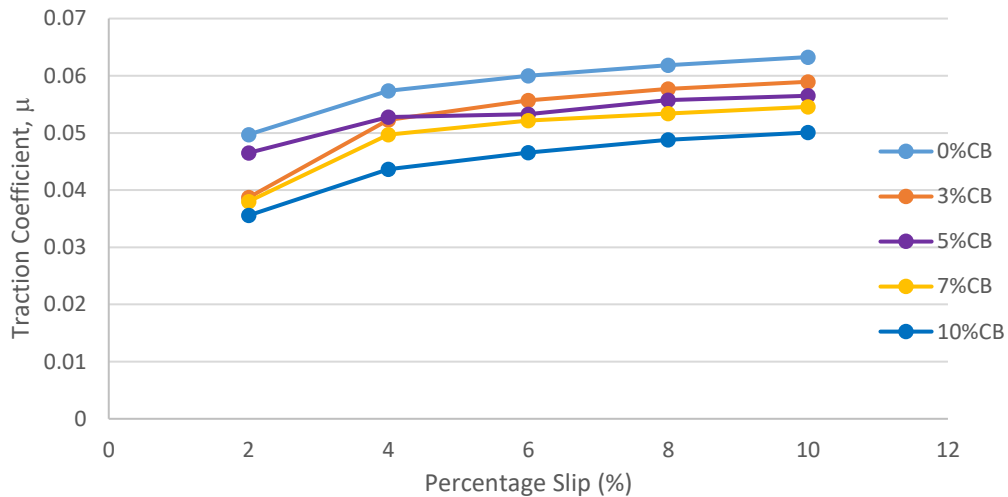
Figure 6.16: Traction coefficient at various % slips for different carbon black compositions using a fixed specimen holder

The variation in traction coefficient with time for various carbon black contents at different entrainment speeds are shown in Figure 6.17 for the self-aligning holder and Figure 6.18 for the fixed holder. Table 6.9 presents the ranges of traction coefficient, as the speed increased, for different disc holders. The traction coefficient is still observed to decrease with increasing carbon black content for varying entrainment speed, thus replicating previous trend. The trend was also maintained in the average values of traction coefficient as those obtained for self-aligning holder are still lower when compared with fixed holder values. The variation of traction coefficient with entrainment speed extracted from Figure 6.17 and 6.18 are presented as Figure 6.19 and 6.20 respectively. The figures indicate that traction coefficient decreases with increasing entrainment speed.
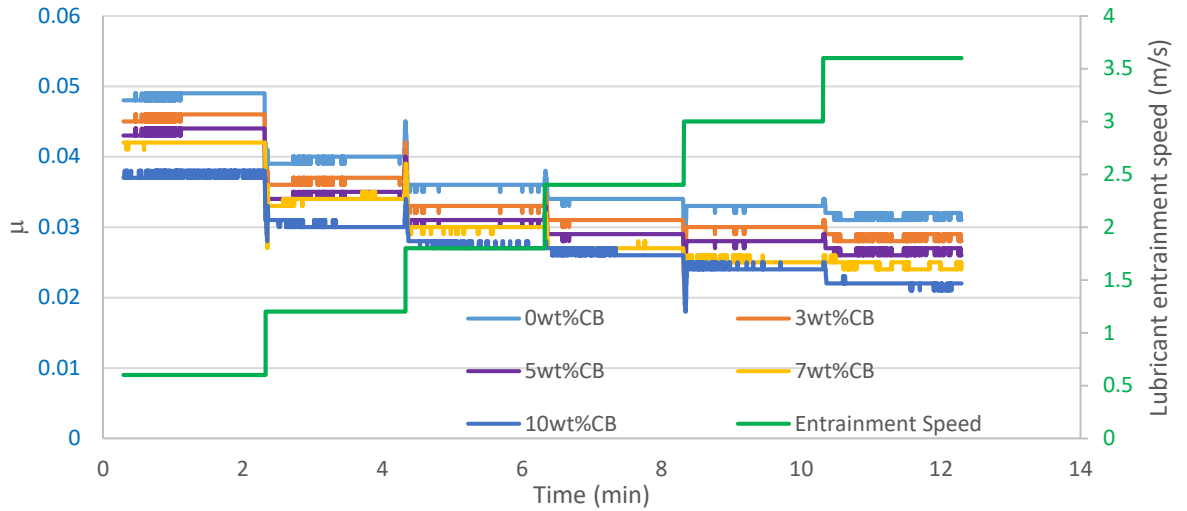
Figure 6.17: Traction coefficient versus time under different entrainment speeds @400N, 10% slip and 100°C for various carbon black composition using a self-aligning specimen holder
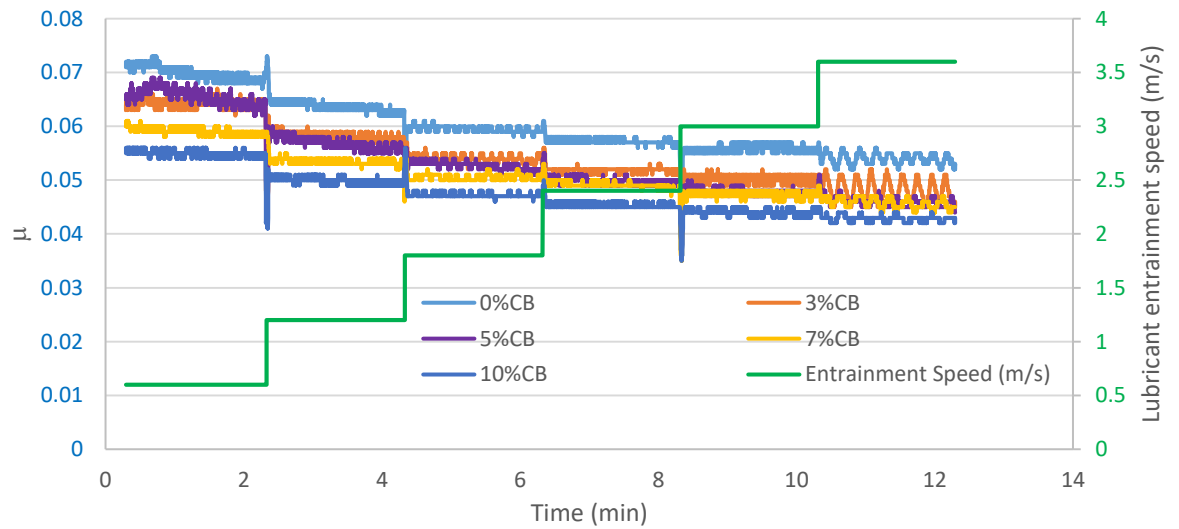
Figure 6.18: Traction coefficient versus time under different entrainment speeds @400N, 10% slip and 100°C for various carbon black composition using a fixed specimen holder

Table 6.9: Comparison of traction coefficient ranges for different disc holders (From Figures 6.17 and 6.18)

Sooty oils	Range of traction coefficients	
	Self-aligning disc holder	Fixed disc holder
0wt%CB	0.049-0.032	0.070-0.054
3wt%CB	0.046-0.028	0.064-0.048
5wt%CB	0.044-0.026	0.066-0.046
7wt%CB	0.042-0.024	0.059-0.046
10wt%CB	0.038-0.022	0.055-0.043
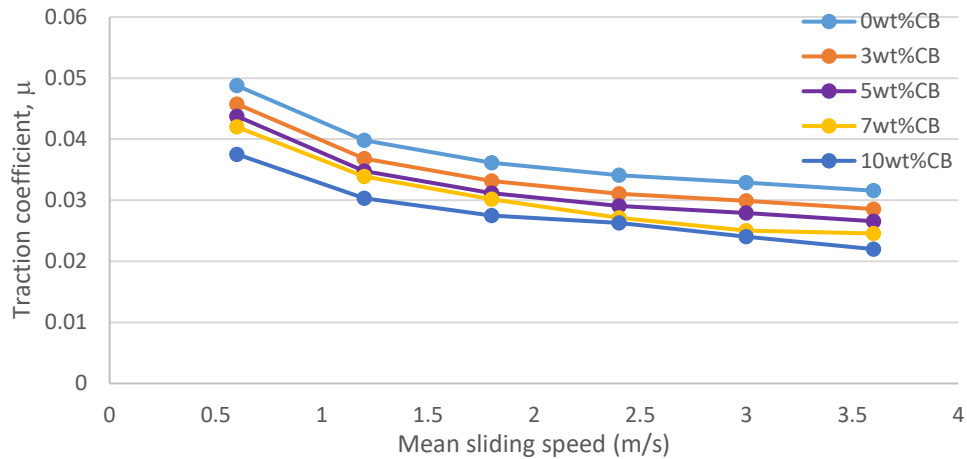
Figure 6.19: Traction coefficient at various mean sliding speeds for different carbon black compositions using a self-aligning specimen holder
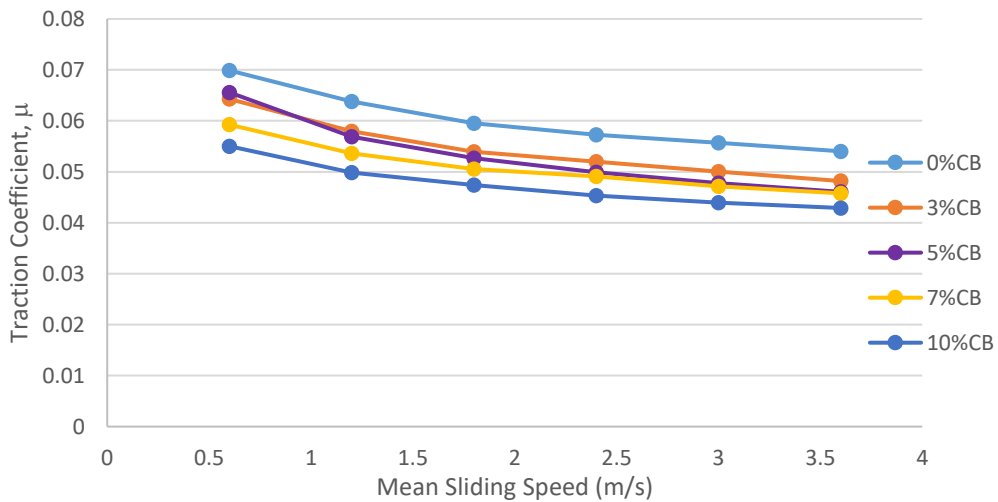
Figure 6.20: Traction coefficient at various mean sliding speeds for different carbon black compositions using a fixed specimen holder

6.5.1.2 Grey cast iron

The analysis of data obtained from the grey cast iron test for selected compositions of carbon black (0wt%CB, 5wt%CB and 10wt%CB) using the self-aligning specimen holder only are presented in Figures 6.21 to 6.23. Figure 6.21 shows the graph of traction coefficient against time for different loads, while Figure 6.22 and Figure 6.23 present traction coefficient versus time for different percentage slips and different entrainment speeds, respectively.

It is obvious that the figures are consistent with the trends observed with earlier tests using chrome steel. That is, the traction coefficient decreases with increasing carbon black content on one hand and on the other, marginally decreasing with increasing load, increasing with percentage slip and decreasing with increasing entrainment speeds. The only difference is that the values of traction coefficient are much lower than those obtained for chrome steel tests. This is clearly shown in Figure 6.24, where the mean traction coefficients obtained at varying loads for chrome steel (EN31) and grey cast iron were plotted together for easy comparison.

100
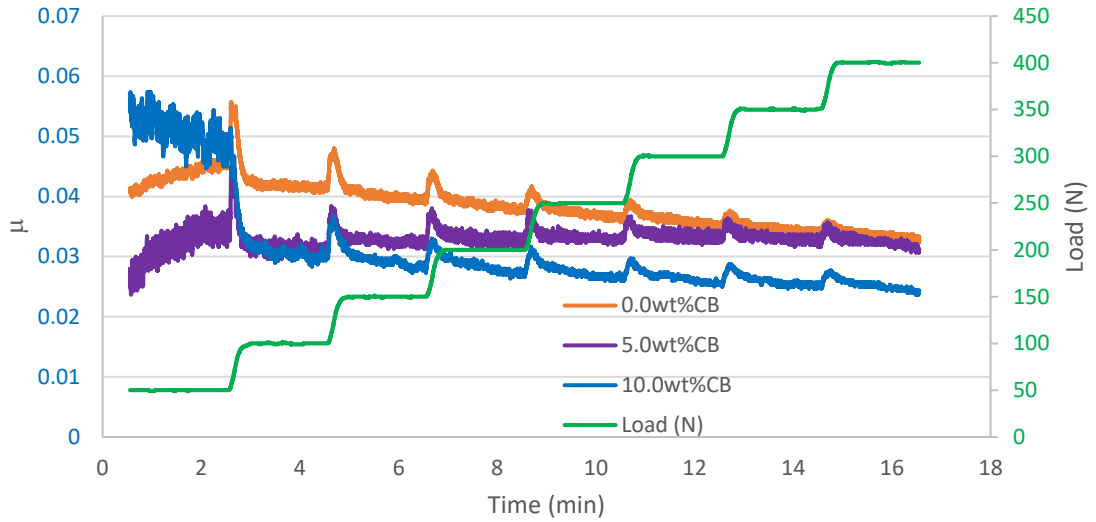
Figure 6.21: Traction coefficient versus time under different loads for 0wt%CB,
5wt%CB and 10wt%CB contents using GCI
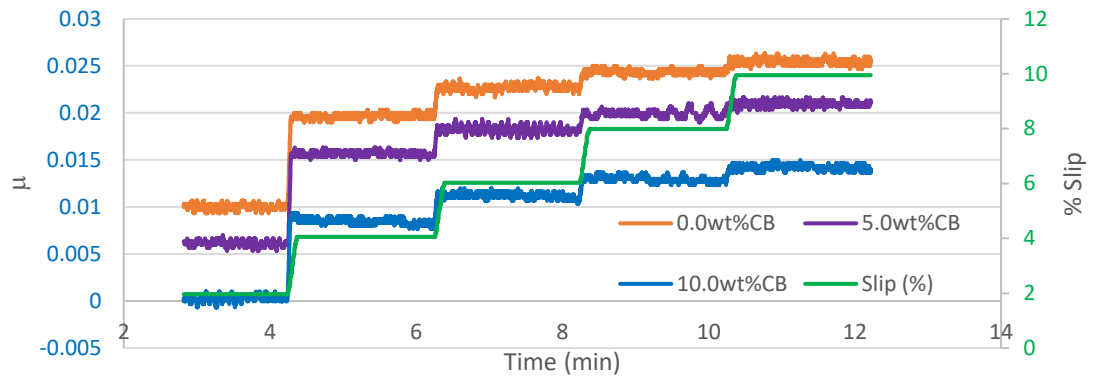
Figure 6.22: Traction coefficient versus time under different % slips for 0wt%CB,
5wt%CB and 10wt%CB contents using GCI
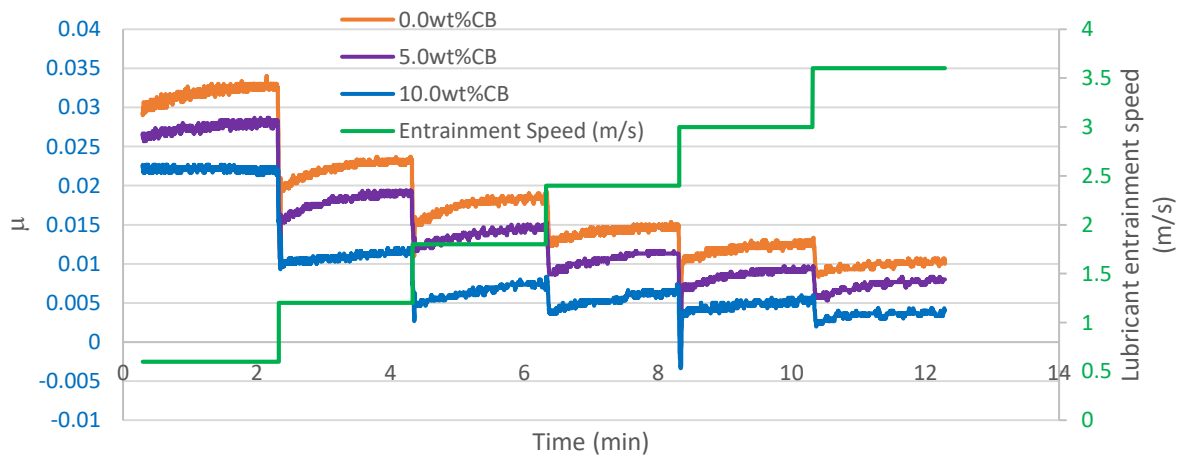
Figure 6.23: Traction coefficient versus time under different entrainment speeds for
0wt%CB, 5wt%CB and 10wt%CB contents using GCI

101
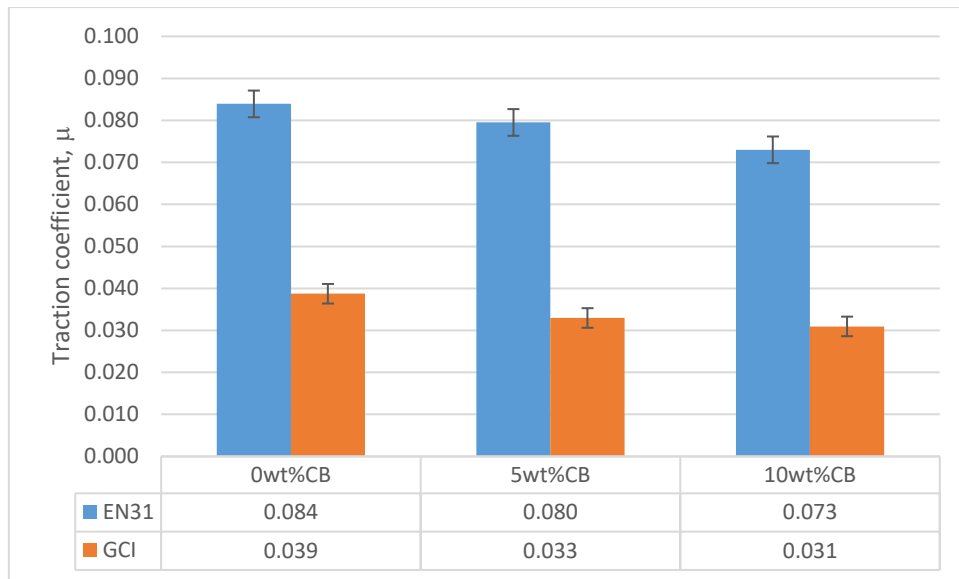
Figure 6.24: Comparison of the varying load average traction coefficients for EN31 and GCI with standard error bars

	0wt%CB	5wt%CB	10wt%CB
EN31	0.084	0.080	0.073
GCI	0.039	0.033	0.031

6.5.1.3 Stribeck curve

In order to know how the frictional behaviour fits into the standard Stribeck curve, appropriate data were also extracted from varying load and varying entrainment speed tests. The data were used to obtain the relationship between the traction coefficient and the dimensionless Sommerfeld number for different carbon black contents. Figure 6.25 presents the results obtained when varying loads were used to compute the Sommerfeld number while Figure 6.26 presents the results when varying mean sliding speeds were used.

The plots are presented in a scatter diagram because the range of values of Sommerfeld number varies for different compositions of carbon black. In spite of this, each of the composition exhibits a similar trend and fits appropriately into the mixed lubrication regime of the standard Stribeck curve, shown in Figure 2.4. This can be seen from the indicated trend lines.
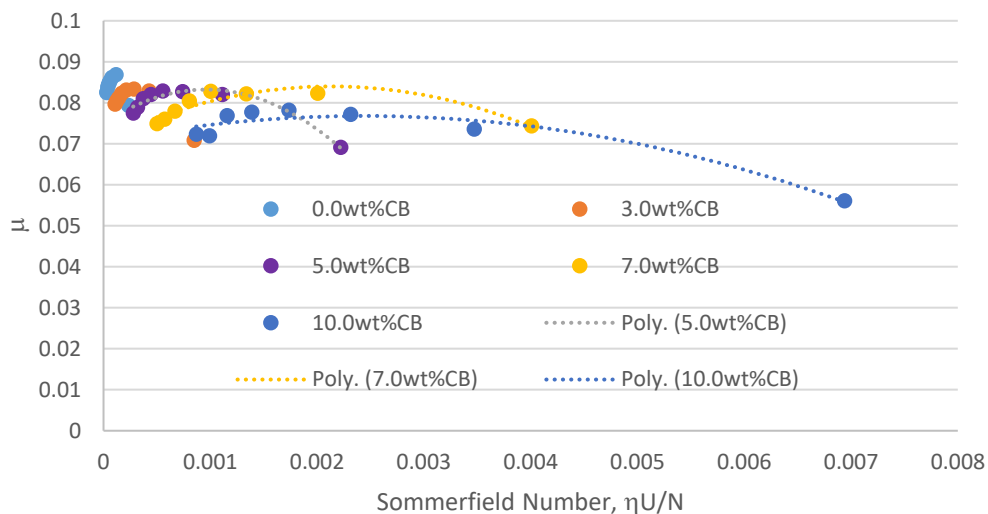
Figure 6.25: Stribeck curve obtained for different carbon black compositions with varying loads

102
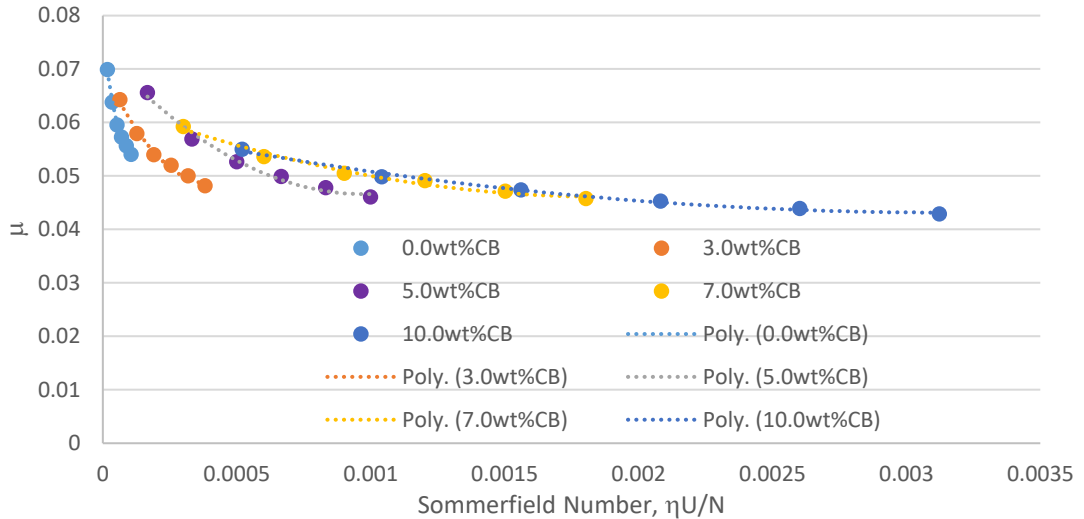
Figure 6.26: Stribeck curve obtained for different carbon black compositions with varying entrainment speeds

6.5.2 Wear analysis

The specimens were cleaned through sonication in acetone for 2 minutes after which they were air-dried, in preparation for post-test wear imaging.

6.5.2.1 Optical microscope images

Microscopic images of the surfaces (upper and lower rings) were taken round each specimen using a Zeiss Imager A2.M optical microscope which was manufactured by Carl Zeiss Microimaging GmbH, Germany. Selected images of the upper disc when the self-aligning specimen holder was used are presented in Figures 6.27 and 6.28 for pre-test and various carbon black compositions. There is conspicuous evidence of abrasive wear which started with the removal of substantial portion of the original grinding marks with uncontaminated oil (0wt%CB) which were completely removed with 3wt% carbon black content. With 5wt%CB content, the surface appeared polished with some pits which become elongated with 7wt% carbon black content. The abrasive wear becomes more severe with 10wt%CB content characterised by roughened surfaces and transfer of fragments of the materials in some sort of galling.

Images obtained from the fixed specimen holder test are presented in Figures 6.29 and 6.30 showing similar behaviours. For uncontaminated oil (0wt%CB), some remnants of the grinding marks can still be seen; these marks have all been abraded with 3wt% carbon black content with some patches of pits. Evidence of the polishing effect of carbon black can be seen with 5wt%CB content accompanied by some level of galling, ostensibly caused by some trapped carbon black particles. Images of 7wt% carbon black content also show progressive level of abrasion with patches of scuffing; and with 10wt%CB content, the surfaces are severely damaged with pronounced galling covering virtually all area of contact. It is obvious that the level of abrasion increases with increase in carbon black content.

The effect of uneven contact between the discs when using the self-aligning and fixed specimen holders is obvious in the resultant wear obtained as presented in the two sets of figures.
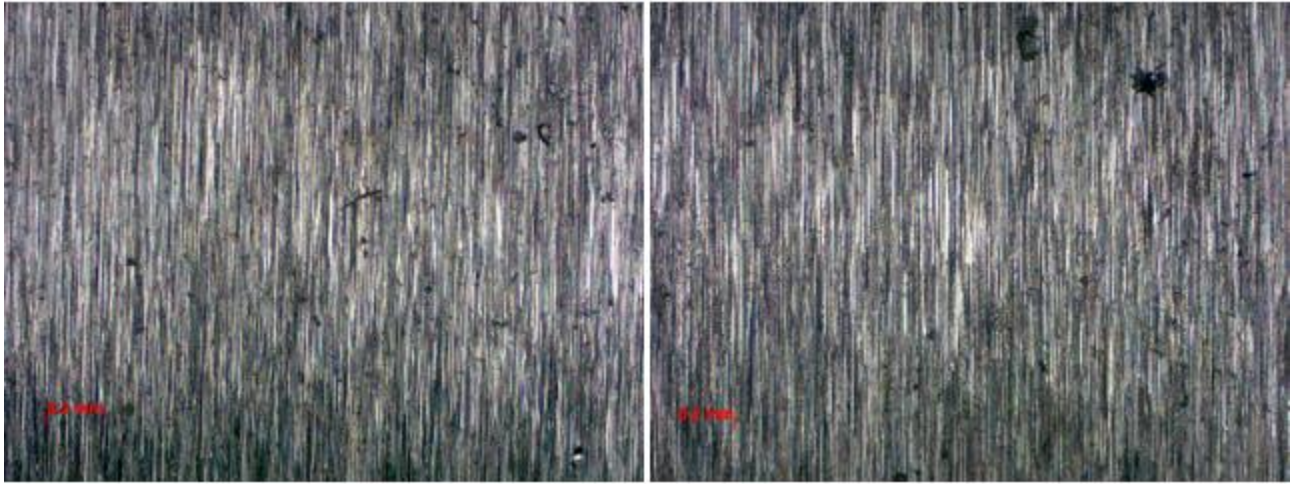
Pre-test specimen with the original grinding marks
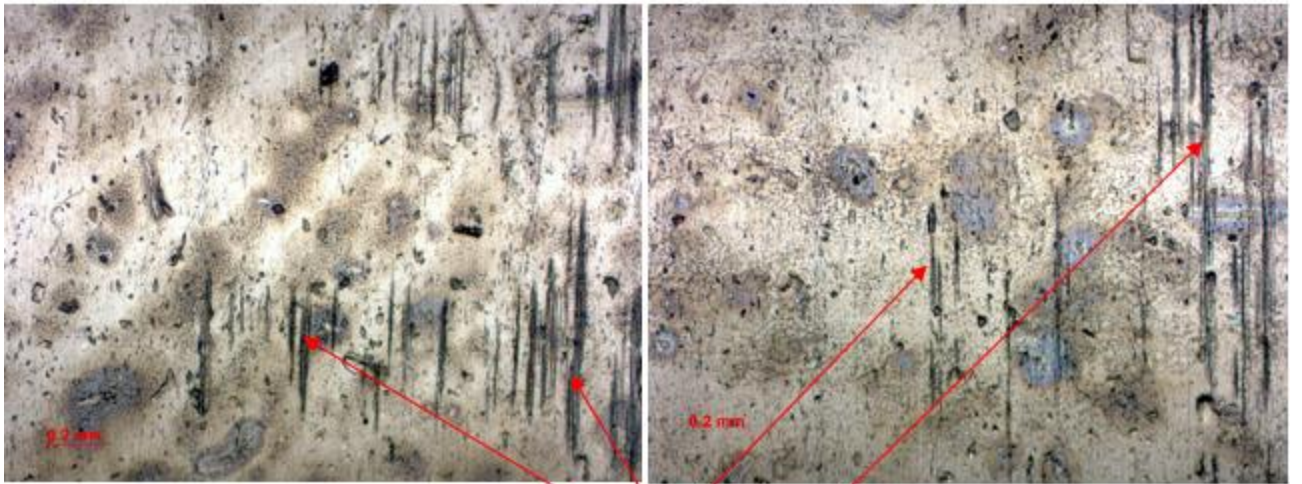
Remnants of original grinding marks

0wt%CB – Mild abrasive wear with the presence of remnants of grinding marks
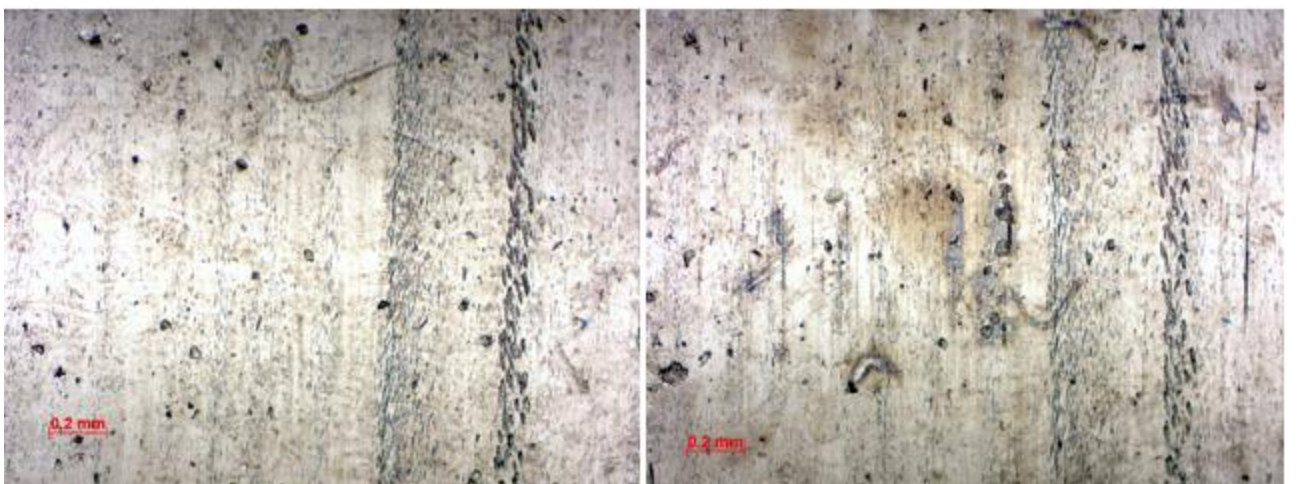
3wt%CB – Abrasive wear with the grinding marks completely worn out

Figure 6.27: Optical microscopic images of upper disc showing untested,
0wt%CB and 3wt%CB contents for a self-aligning specimen holder

104
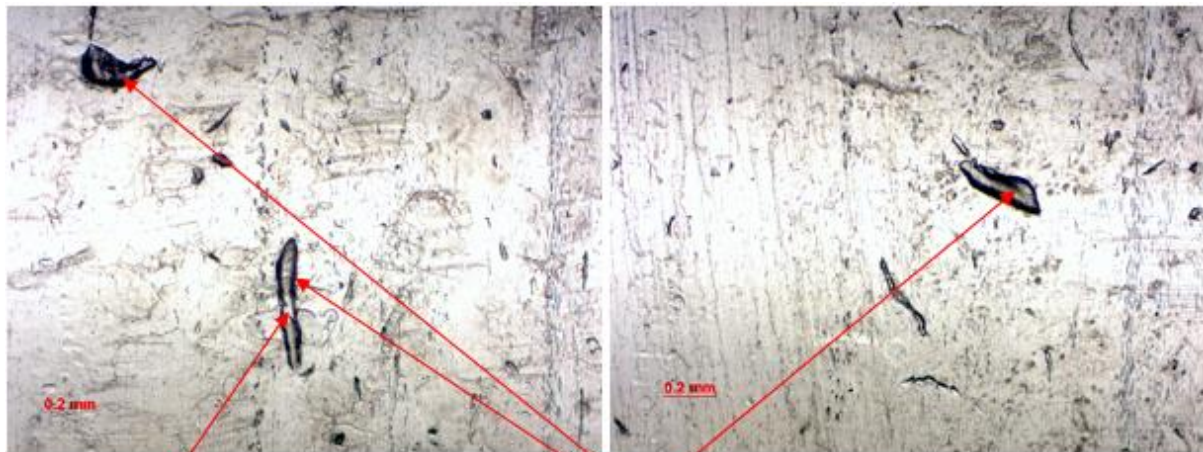
Evidences of three-body abrasion   Patches of pits

5wt%CB – Polishing and abrasive wear with some pits
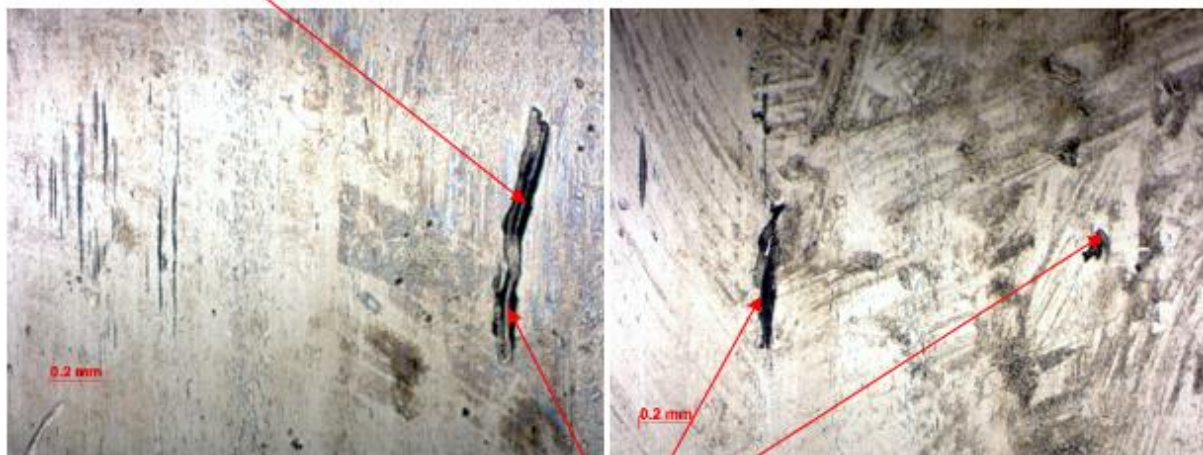
Patches of elongated pits

7wt%CB – Abrasive wear with some elongated pits due to three-body abrasion
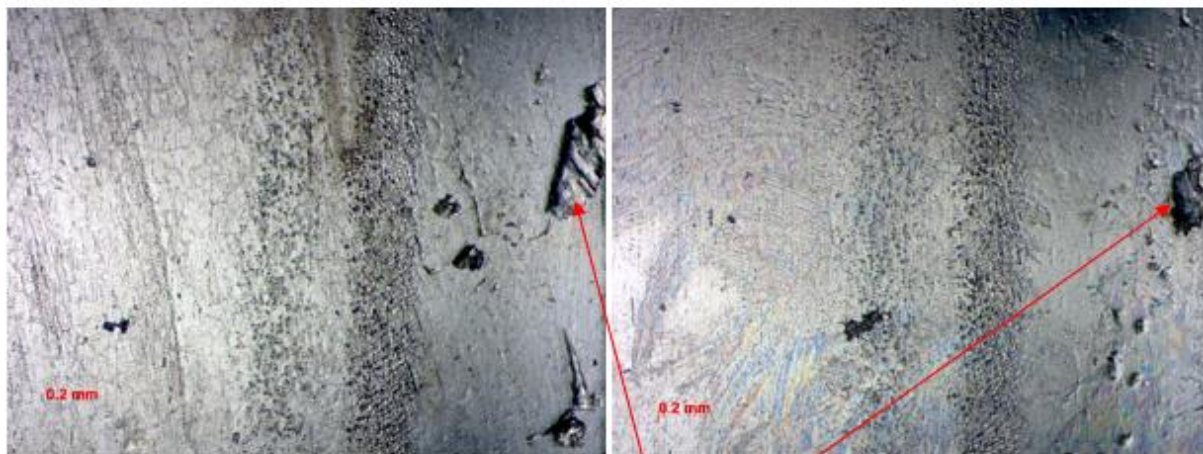
Severe surface damage resulting in material transfer

10wt%CB – Abrasive wear with pronounced surface damage due to surface contact fatigue

Figure 6.28: Optical microscopic images of upper disc with 5-10wt%CB contents for a self-aligning specimen holder
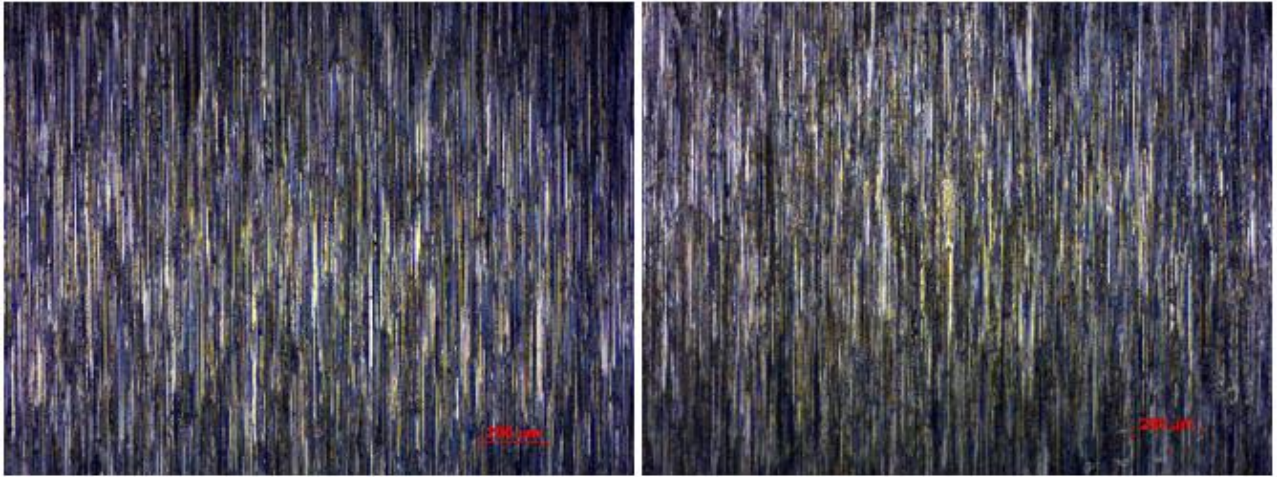
Pre-test specimen with the original grinding marks
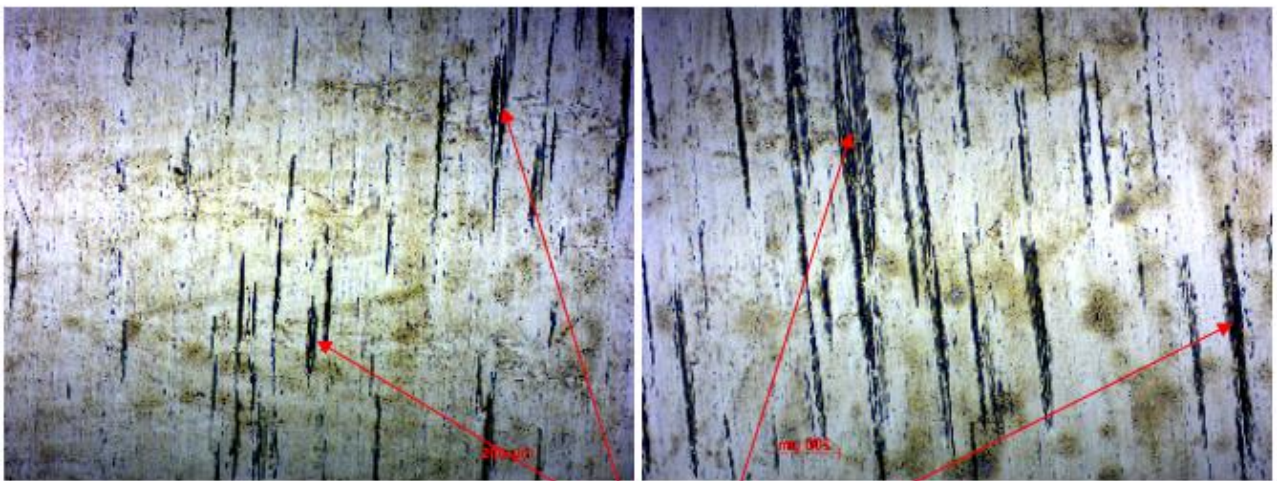
0wt%CB – Mild abrasive wear with the presence of remnants of grinding marks

Remnants of original grinding marks
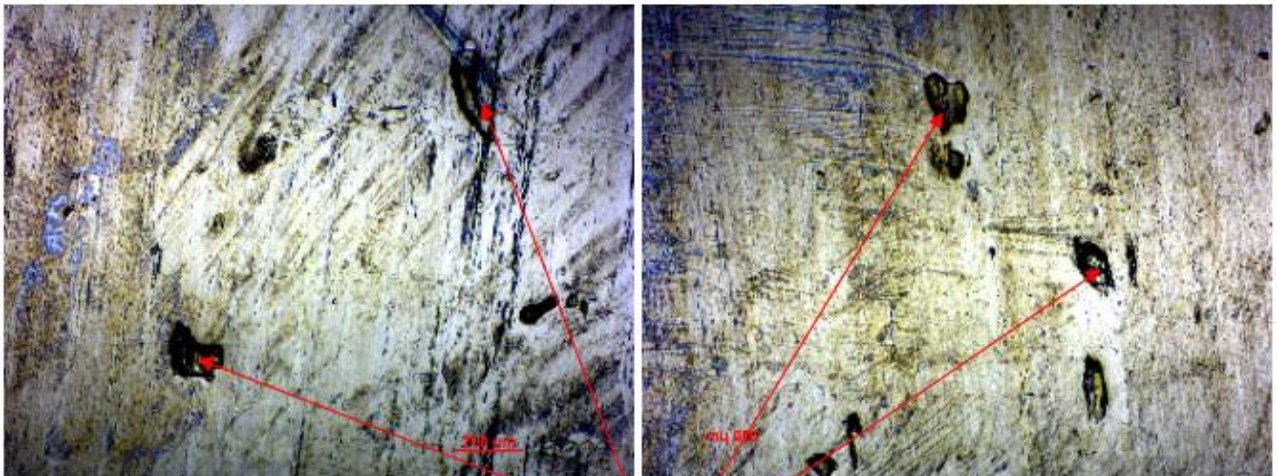
Patches of pits

3wt%CB – Abrasive wear with patches of pits

Figure 6.29: Optical microscopic images of upper disc showing untested, 0wt%CB and 3wt%CB contents for a fixed specimen holder

Patches of scuffing   Polished surface
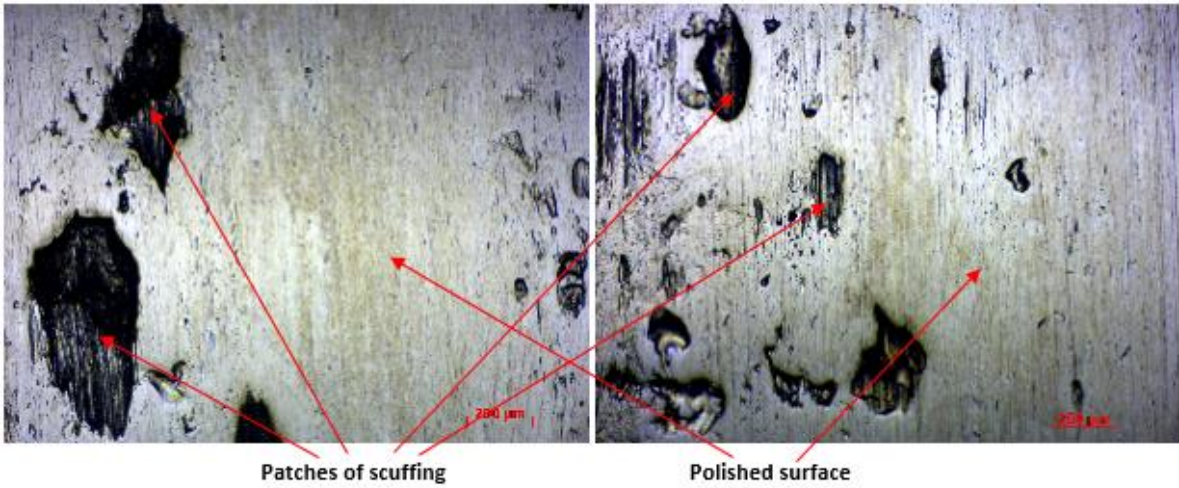
5wt%CB – Polishing and abrasive wear with scuffing

Patches of scuffing

7wt%CB – Abrasive wear with patches of scuffing
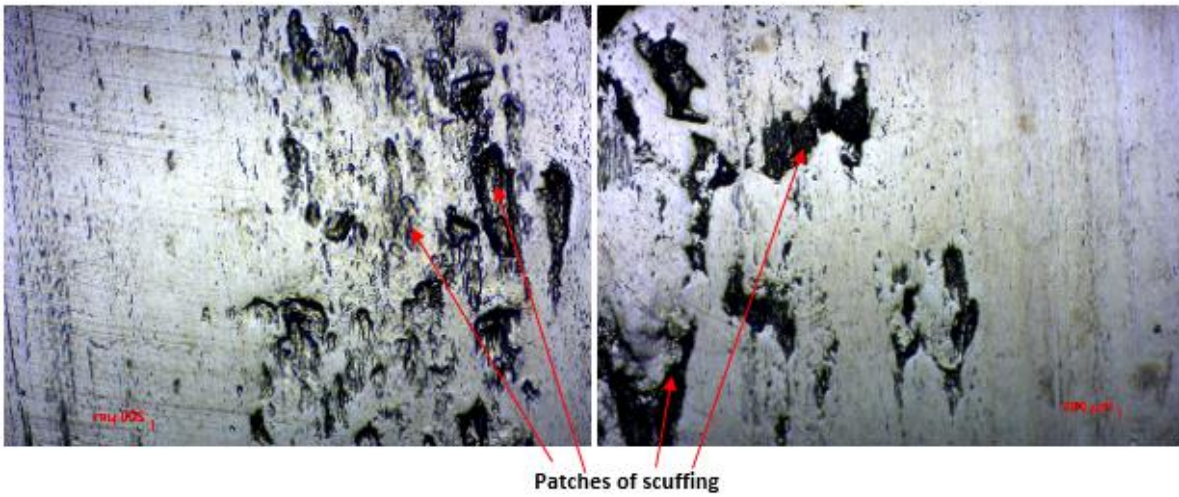
Severe surface damage resulting in pronounced galling
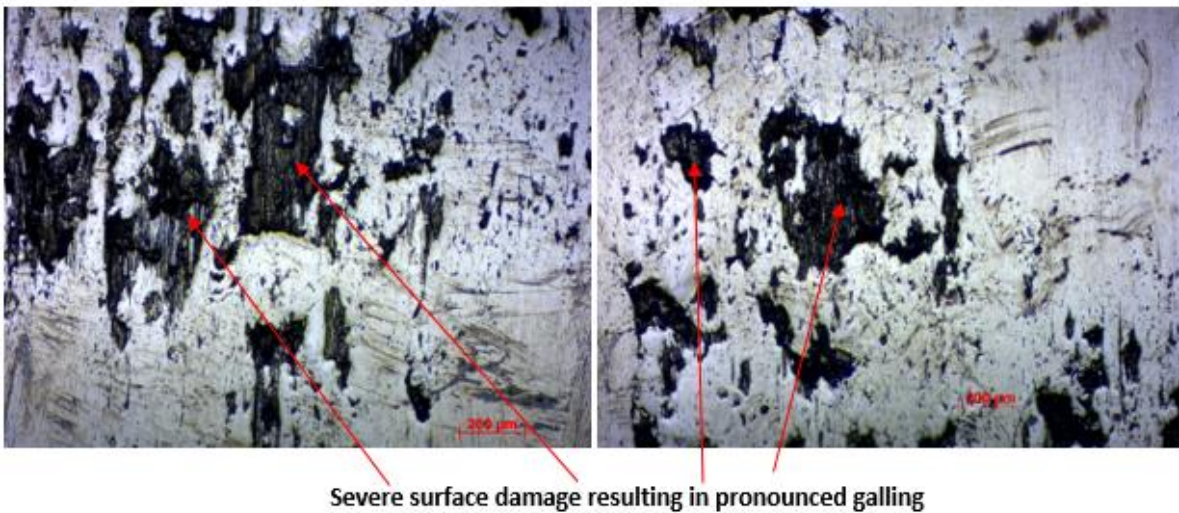
10wt%CB – Abrasive wear with highly pronounced surface damage induced by surface contact fatigue and break-down of lubrication due to starvation

Figure 6.30: Optical microscopic images of upper disc with 5-10wt%CB contents for a fixed specimen holder

6.5.2.2 Microstructural study of surface fatigue

It has been discovered that sliding and rolling contacts between two bodies produce much more damage to the materials beneath the contacting surfaces than the surface themselves [40, 166].

To further study the trend of deformation from the surface to subsurface level in relation to the carbon black contamination, a microstructural study of selected post-test specimens (0wt%CB, 5wt%CB and 10wt%CB) was undertaken. Each of the upper discs was sectioned into two equal parts using the Buehler Isomet 5000 precision cutter; the sectioned parts were then mounted on the Bakelite (PhenoCure Resin) using a Buehler SimpliMet 1000 Automatic Mounting Press. They were then taken through grinding and polishing using a Buehler EcoMet 250 Pro with Silicon Carbide Abrasive Paper Discs (P400, P800 and P1200) for grinding, followed by polishing with Monocrstalline Diamond Suspension (9 μm) on a complimentary rotating disc with a UltraPad polishing cloth and finished with a Colloidal Silica Polishing Suspension on contra rotating disc with ChemoMet polishing cloth. The samples were then etched with 2% Nital (Nitric Acid and Ethanol), rinsed in water and dried in air. The etched samples were then observed under a Scanning Electron Microscope (TM3030Plus Tabletop SEM), manufactured by Hitachi High-Technologies Corporation, Japan.

The microstructural features of each of the samples for 0wt%CB, 5wt%CB and 10wt%CB contents are presented in Figures 6.31, 6.32 and 6.33 respectively. It should be noted that the 0wt%CB content sample was etched for 10 seconds, hence the darker appearance, while subsequent etchings were done for only 5 seconds. There is no evidence of surface fatigue for 0wt%CB content as opposed to 5wt%CB content where there are minor signs indicating surface fatigue which becomes more pronounced with 10wt%CB content. Generally, the microstructure comprises of plate-like fine grains connected by a network of partially parallel needles dispersed at various angles [176, 177].
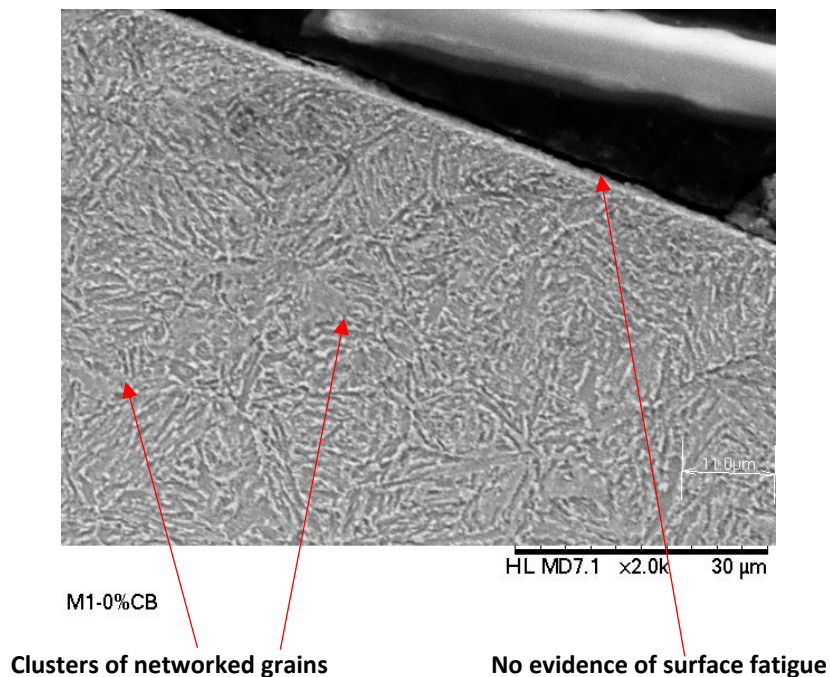
Figure 6.31: Photomicrograph of sectioned EN31 disc for 0wt%CB (etched for 10 secs) content showing a network of grains structure with no evidence of surface fatigue. Etchant: 2% Nital (Magnification: x2000)

A network of needle-shaped microstructure   **Minor surface fatigue**

M3-5%CB
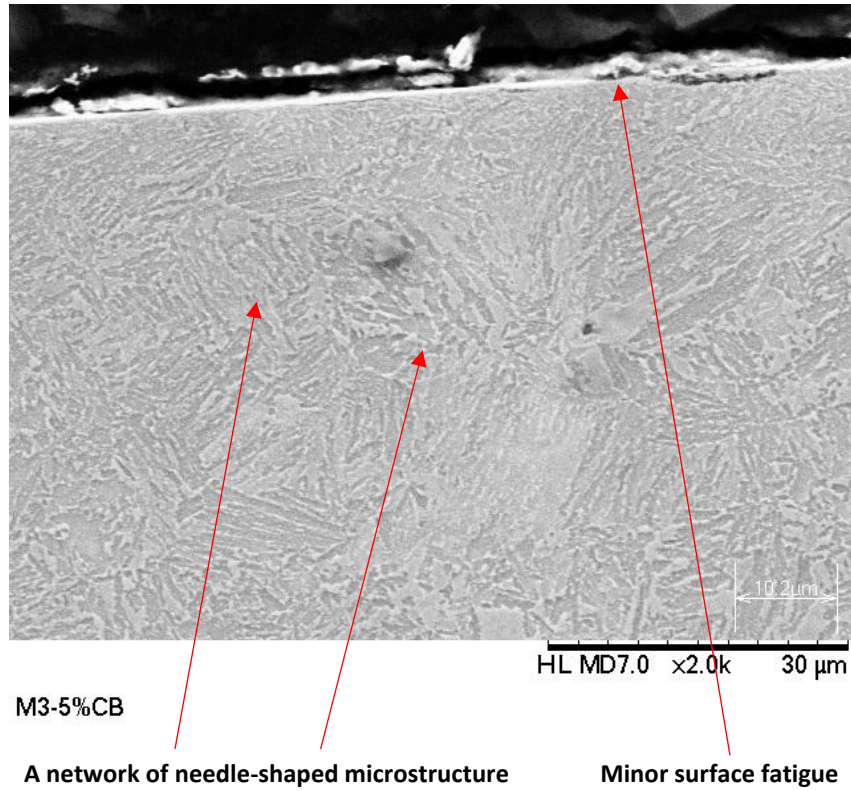
Figure 6.32: Photomicrograph of sectioned EN31 disc for 5wt%CB (etched for 5 secs) content showing a network of grains structure with minor surface fatigue. Etchant: 2% Nital (Magnification: x2000)

A network of fine-grained microstructure   **Pronounced surface fatigue**

M5-10%CB
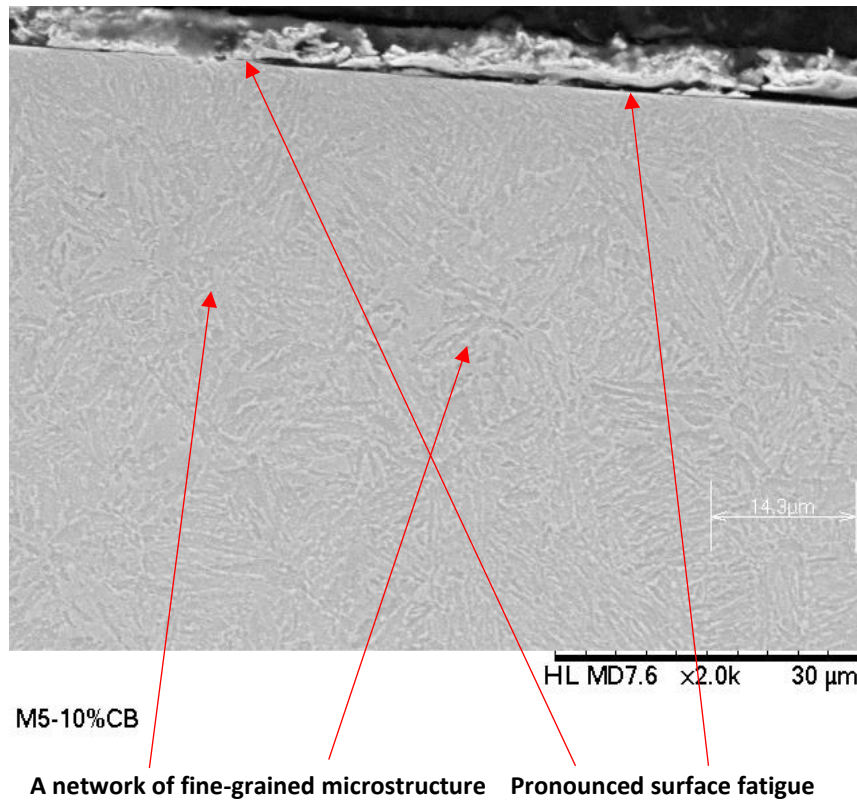
Figure 6.33: Photomicrograph of sectioned EN31 disc for 10wt%CB (etched for 5 secs) content showing a network of grains structure with pronounced surface fatigue. Etchant: 2% Nital (Magnification: x2000)

6.5.2.3 Microstructural study of subsurface fatigue

The effect of subsurface fatigue due to high-stress and repeated cyclic loading can be seen in Figure 6.34 showing the sectioned SEM image of the EN31 disc used for the 10wt% carbon black content. Further evidences of surface and subsurface fatigues are presented in Figures 6.35 where one of the distinctive features of rolling contact fatigue, multiple cracking, is shown. Various dimensions of these deformations are taken to enable comparison with the estimated values. Figure 6.36 also presents another dimensioned micrograph of the subsurface damages.

The expected region of crack propagation is normally along the plane of maximum shear stress; the theoretically estimated maximum shear stress (τ_{max}) value for the normal load of 50N to 400N ranges from 51 to 144MPa occurring at the depth of 18.6 to 52.7 μm. From Figures 6.35 and 6.36, it can be seen that the subsurface microcracks appear between a minimum of 16.2 to a maximum of 25.7 μm within the limited areas the images were taken. This is an indication that the maximum shear stresses occur within the estimated range.

Severe surface fatigue   **Occurrence of subsurface micro cracks**
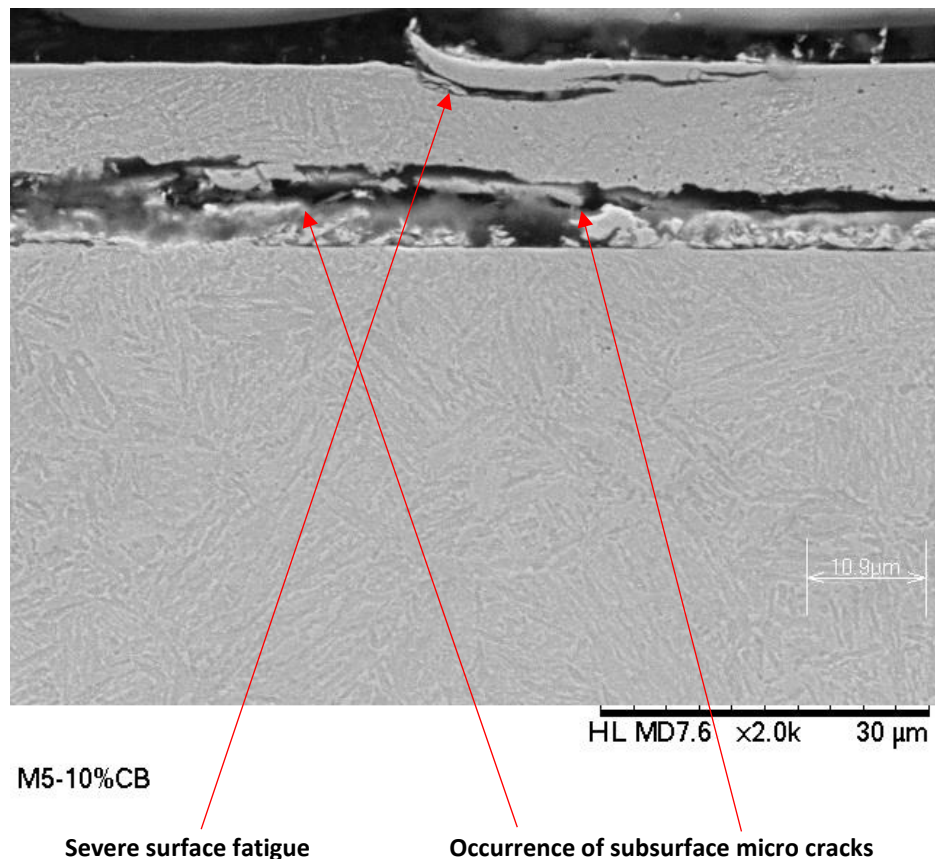
Figure 6.34: Photomicrograph of sectioned EN31 disc for 10wt%CB content showing severe surface fatigue and occurrence of subsurface shear stress. Etchant: 2% Nital (Magnification: x2000)
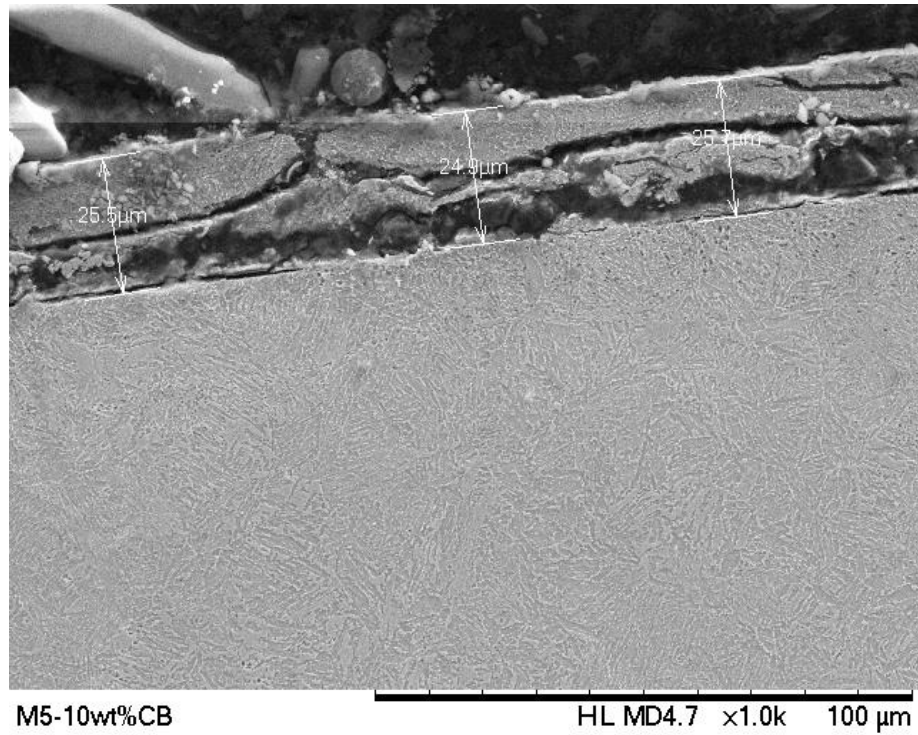
Figure 6.35: Photomicrograph of sectioned EN31 disc for 10wt%CB content showing severe surface fatigue and subsurface damages with various dimensions. Etchant: 2% Nital (Magnification: x2000)
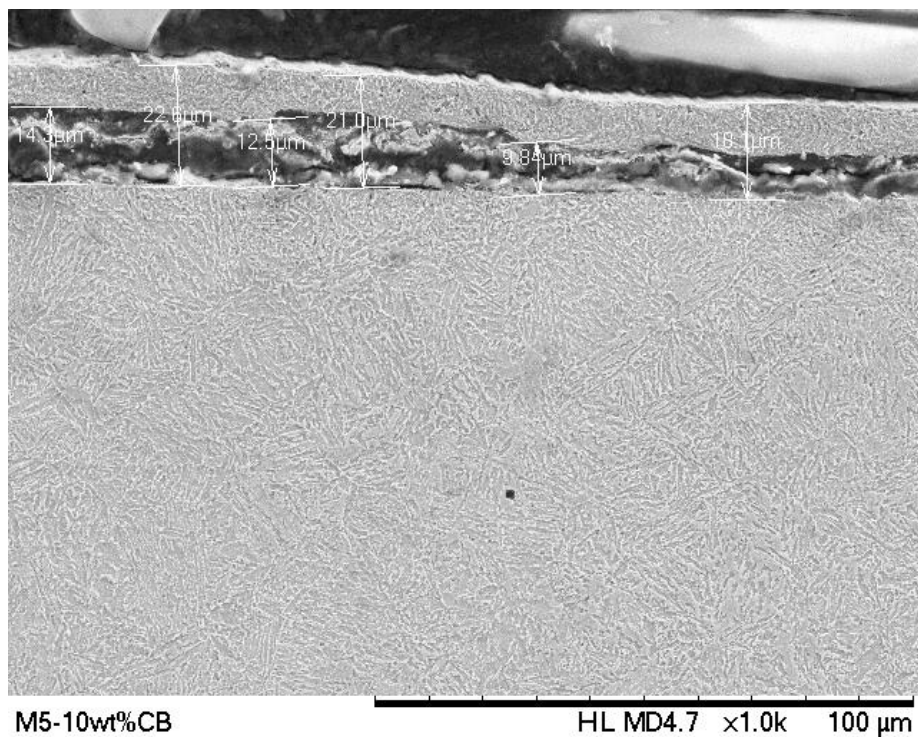
Figure 6.36: Photomicrograph of sectioned EN31 disc for 10wt%CB content showing various dimensions of subsurface damages. Etchant: 2% Nital (Magnification: x2000)

6.5.2.4 Surface roughness

The post-test roughness was measured using a Mitutoyo Surftest SJ-500 profilometer and the average values of root mean square (Rq) for the upper disc for different carbon black contents are shown in Figure 6.37 with standard error bars derived from standard deviations. From the original average value of Ra, 0.130 μm and Rq, 0.173 μm, the surfaces attained different level of roughness as dictated by the lubricating oils. The values are obviously lower than the pre-test average values, showing the polishing effect of carbon black.
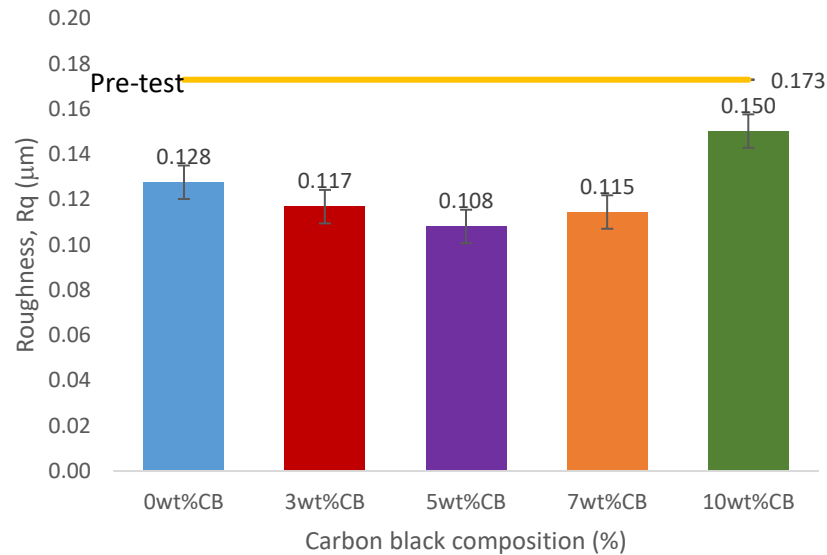
Figure 6.37: Post-test surface roughness, Rq of the upper disc for various carbon black contents with standard error bars

6.6 Discussion

6.6.1 Contact parameters

The estimated theoretical contact parameters comprising Hertzian contact pressures along with maximum shear stresses, the depth at which they will occur and the contact area dimensions give some insight into what is to be expected as each of the tests progresses. For instance, the Hertzian contact pressure for the load range of 50N to 400N gives values ranging from 168 MPa to 475 MPa. This range of the contact pressure falls in the realm of the mixed lubrication regime.

The estimated theoretical central film thickness for various carbon black contents reveals that none of the values is less than 0.1 μm, which means the operating film thickness will be able to sustain the desired regime of lubrication. Secondly, there is progressive increase in film thickness with increasing carbon black content. This is obviously due to the thickening effect of carbon black [178]. The estimated values of the lambda ratio range between 0.525 and 1.601 for different compositions of sooty-oil surrogates.

The operating regime of lubrication proposed for the tests was EHD which Hamrock et al. [128] classifies as "hard elastohydrodynamic" for metallic materials of high elastic modulus, where the film thickness exceeds 0.1 μm and maximum contact pressure between 0.5 to 3 GPa. However, lambda ratio for EHD lubrication regimes ranges between 1 and 3. There is therefore the possibility of the contact operating under EHD and boundary lubrications intermittently.

6.6.2 Friction measurement

6.6.2.1 Traction coefficient

For each sooty-oil surrogate, there seems to be a steady and smooth increase in the traction coefficient as dictated by percentage slip variations. This transition was not so smooth for tests involving variations of load and speed as their traction coefficient graphs are characterised by intermittent spikes seen as momentary sudden jumps in response to stepwise change in load and speed after every 120 seconds. This is an indication that frictional response is influenced by contact pressure and surface speed [45].

The observed general trend is that there is progressive and consistent reduction in traction coefficient with increasing carbon black content for each type of test; namely: varying loads, varying slips and varying entrainment speeds. Antusch et al. [73] also observed a similar trend in their tests with engine soot, carbon black-contaminated oil and fresh oil using pin-on-disc tribometer. This observed trend is obviously due to the fact that at a mixed lubrication regime, properties of the lubricating medium have more effect. And since lubricity and film thickness increase with carbon black content, the logical consequent is decreasing traction coefficient [179]. Green and Lewis [6] also observed the tendency of formulated oil mixed with various percentage of carbon black to reduction in traction coefficient in their MTM ball-on-disc tests. The slippery nature of agglomerated carbon black particles, like soot, is taking effect; thus, they behave like solid lubricants.

The slight, but progressive, decrease in traction coefficient with increasing load may be due to phase transformation or tribochemical reaction at the interface during sliding as the load increases. Extreme pressure additives in the formulated lubricant have the tendency to react with the sliding surface and form tribofilm, especially at higher contact pressures.

One notable observation in the original tests plotted figures are the spikes as the sequence of the test changes from one level to another, especially for load and speed variations tests. This is an indication of the change in contact condition as these changes take place. It must also be mentioned that the level of carbon black contents (hence the lubricant contamination) plays a major role in the resultant frictional behaviour of the lubricating medium [48]. This is indicated by the progressive and consistent reduction in the coefficient of friction with increasing carbon black content levels, in respective of the changes in other parameters.

The self-aligning specimen holder was able to achieve the desired line contact resulting in lower traction coefficients. This is because with perfect line contact, the frictional force generated by the normal load was evenly distributed along the line of contact. This is assumed to be responsible for the relatively low traction coefficient when compared with values obtained for the fixed specimen holder where the line contact cannot be achieved between the discs as they are misaligned. They would rather have an uneven contact or possibly point contact. The effect of this is that only a part along the line of contact is carrying the normal load, hence the higher values of traction coefficient.

It was also observed that for each level of carbon black content, the traction coefficient marginally decreases with load for self-aligning specimen holder but relatively consistent at varying loads with fixed holder. While the trends for both holders were the same for slip and speed, increasing and decreasing at increasing percentage slip

and entrainment speed respectively. Though, these relations cannot be numerically correlated.

At high velocities and pressures, the elastohydrodynamic effects build up a fluid layer of lubricant along the line of contact [48]. This explains the reason for the decrease with increasing speed because at higher entrainment speed, as the thickness of oil film increases [180], thus resulting in a decrease in the real contact area. Kano [181] made the same observation in his pin-on-disc tests with a specific report on the increase in the film thickness with increasing speed. The film thickness equation, equation 5.12, also supports this observation.

In addition, these trends were replicated even when grey cast iron was used in place of chrome steel. The difference being with the values of traction coefficient which are lower for grey cast iron. This may be due to the fact that the grey cast iron possesses self-lubricating properties [182-184] resulting mainly from its graphite constituents which is a good solid lubricant [185].

The obtained Stribeck curves show that each sooty-oil surrogate displays a similar trend and both can be represented by Figure 6.38(a); with the upper and lower curves illustrating the Stribeck curves for varying loads and varying speeds respectively. The curves, when combined, as shown in Figure 6.38(a) fits into the mixed lubrication regime of Figure 2.4. This is a clear manifestation that the friction level of a lubricant influences its regime of operation [186].

(a)   (b)
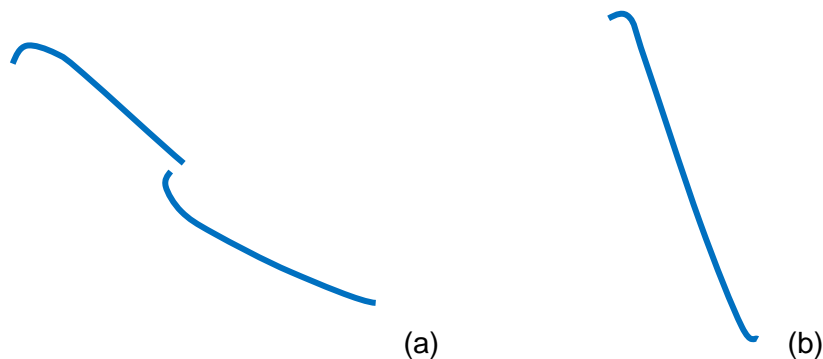
Figure 6.38: Depictions of the (a) obtained Stribeck curves and (b) combined

6.6.3 Wear images

The implication of achieving perfect line contact with self-aligning specimen holder in contrast to misaligned contact with fixed specimen holder is that while the contact pressure is evenly distributed along the line of contact in the former, it would only concentrate on the limited area of contact provided by misaligned contact in the latter. The clear manifestation of this effect is evidenced in the microscopic images obtained from both holders as explained below.

The effect of misalignment between two contacting bodies, leading to irregular contact area and contact pressure, can be seen from the observed results on fixed specimen holder. Figure 6.39(a) shows a schematic of misaligned discs.

The worn surface spread across the whole contact width of the discs for self-aligning specimen holder tests; this was however not so for the fixed specimen holder tests where the worn surface skewed to a narrow portion of the disc contact width, Figure 6.39(b&c). Obviously, this was responsible for the higher levels of damage observed

for fixed holder tests since the contact pressure will be higher as a result of narrower contact width between the contacting discs. Therefore, the self-aligning holder was beneficial from tribological point of view.
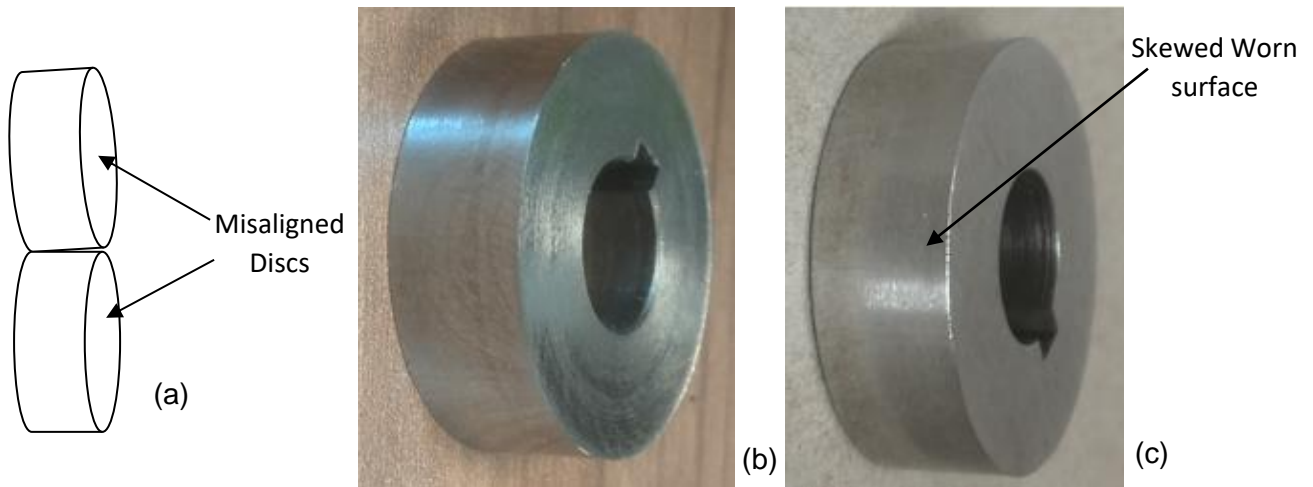
Figure 6.39: (a) Schematic of misaligned discs with pictorial views of the disc showing (b) uniform wear across the surface for the self-aligning holder and (c) skewed wear on the surface for fixed holder

The optical microscopic images show obvious evidence of increasing level of abrasion with increasing carbon black content; and this tendency is presented by both the self-aligning and the fixed specimen holders. The difference being that while images from the self-aligning holder are evenly abraded, those from fixed holder are not; revealing the effect of misalignment. The progression of abrasive wear also unveils this effect further. With uncontaminated lubricant (0wt%CB), the level of removal of original grinding marks is higher with a self-aligning holder and while patches of pits heralded abrasion with 3wt%CB content for fixed specimen holder, self-aligning holder has no such pits. This is due to the misalignment between the discs for fixed holder and can be seen when Figure 6.27 and 6.29 are compared.

Carbon black manifests its polishing effect with 5wt% carbon black content for both types of specimen holders but while this is accompanied by few pits for self-aligning holder, it is accompanied by patches of scuffing for fixed holder. The level of abrasion also gets more severe with 10wt%CB resulting in displacement of fragments of the materials, which is more pronounced with fixed specimen holder tests. The occurrence of this level of surface defect may be due to break down of lubricant film [140] at this level of carbon black content coupled with high load (up to 400N), leading to the possibility of trapped carbon black particles just rolling between the contacting discs in a form of third-body particles as the discs rotate [187].

6.6.3.1 Wear mechanisms

At 0wt%CB content, the lubricant minimizes the direct contact of the discs' asperities, Figure 6.40(a). However, the applied normal load and sliding/rolling actions result in gradual removal of the high points of the surface asperities; especially when the load and speed are increasing stepwise. This removal process may eventually aggravate to lubricated sliding/rolling wear of the contacting discs. Abrasive wear sets in when the carbon black-mixed lubricant is introduced into the contact. At moderate concentration levels (3-5wt%CB), the well-dispersed carbon black particles penetrate

into the contacting zone of the rotating discs along with the entraining lubricant, thereby causing three-body mild abrasion which may even polish the surfaces as observed with 5wt%CB content. Figure 6.40(b) depicts this mechanism. At higher levels of concentration (7-10wt%CB), the carbon black particles agglomerated and prevented the lubricant from getting to the contact zone resulting in two-body abrasion, Figure 6.40(c). The continuous rotation of the discs might eventually drag some of these hard particles into the contact zone of the discs where they become squeezed thereby aggravating the contact conditions and causing severe damage to the surfaces.
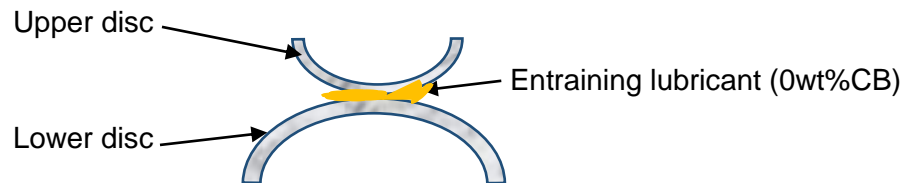
(a) Entraining lubricant minimizes the direct contact between the asperities of the contacting discs resulting in lubricated sliding/rolling wear
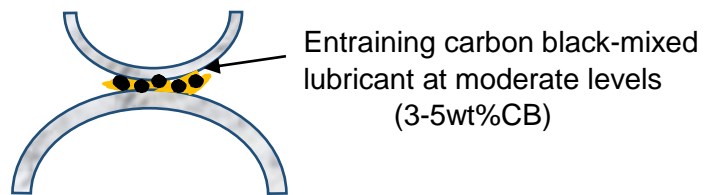
(b) At moderate concentration levels, carbon black particles within the lubricant infiltrate into the contact zone causing mild abrasive wear, essentially three-body
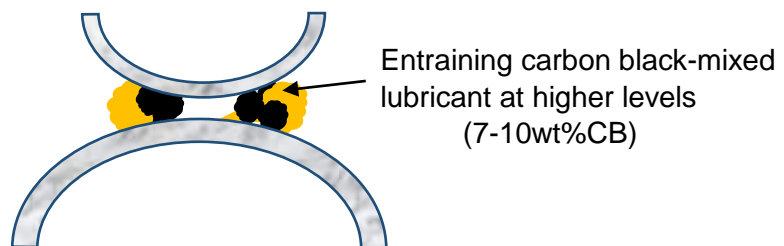
(c) At higher levels of concentration levels, carbon black agglomerates hinder the lubricant from getting into the contact zone thereby causing severe metal-to-metal wear (mostly, two-body abrasion)

Figure 6.40: A schematic of the wear mechanisms expected from various level of carbon black concentrations showing entraining lubricant with (a) no carbon black particle, (b) moderate levels of concentration and (c) higher levels of concentration

6.6.3.2 Surface and subsurface fatigues

It is evident from the presented photomicrographs that surface contact fatigue gradually occurred when carbon black-mixed lubricant was introduced into the contact between the discs; and its level became significant with the increase in carbon black

content. At higher content level where agglomeration restricts in flow of lubricant into the contact zone, it may be only the carbon black particles that are mainly present within the region of contact. The combined effects of high contact pressure resulting from Hertzian line contact and high load lead to the surface fatigue and subsurface damages [188].

The occurrence of fatigue-induced incipient damage in the subsurface, along the plane of maximum shear stress, observed for the sectioned disc used for 10wt%CB content test was due to the fact that at higher carbon black agglomeration. Carbon black particles in the oil infiltrated the high-load rolling contact region between the discs, created a reduced lubrication regime through starvation leading to deformation of the metal which manifests as microcracks at a point, below the metal surface, where contact stress is concentrated [39].

Under these harsh contact conditions, the near surface materials are subjected to plastic deformation depicted by various cracking mechanisms [189]. These subsurface cracks are essentially horizontal with both leading and trailing tips propagating towards the surface [190]; subsequently resulting in the delamination of the surface material in form of peeling as shown in Figure 6.34. This means that even under mixed EHD lubrication conditions where surfaces are expected to be relatively separated, the carbon black agglomeration can behave as oversized debris infiltrating the contact and causing severe damages to the contacting surfaces [40].

6.6.3.3 Surface roughness

For the measured post-test roughness, the average value for 10wt%CB content was the highest as expected. Though, the surfaces are relatively smoother at moderate carbon black content: 3wt%CB (0.117 μm), 5wt%CB (0.108 μm) and 7wt%CB (0.114 μm) with 5wt%CB content recording the lowest value. This means 5wt% carbon black appears to be a critical threshold for there to be enough carbon black particles to cause appreciable polishing through three-body abrasion. Nonetheless, this is a further manifestation of polishing effect of carbon black as observed with reciprocating wear test.

6.7   Conclusions

The MTM experimental test involves a combination of rolling and sliding contacts under a non-conformal condition which implies that the contacting discs are subjected to both normal and tangential surface tractions. The cumulative effects of all these are that contact stresses are very high, repetitive and concentrated along the line of contact. Consequently, the nature of the materials in contact and operating conditions would play a major role in the resultant wear mechanisms.

The effect of cyclic stress variations may also come in, the influence of this can be felt in all the three types of tests. For the variation of load test, normal load is applied from 50N to 400N in 50N steps after every 2 minutes, while the speed of the upper disc continuously varies from 764 rpm to 840 rpm to achieve variation of slip, the speeds of both upper and lower discs are simultaneously steadily adjusted for varying speed test. All these variations can be seen in the plotted traction coefficient curves for all the tests; and their resultant consequence is induced imbalance of the cyclic stress.

The values of traction coefficient varied from test to test; nonetheless, similar trend was maintained for each composition of carbon black and both materials (chrome steel and grey cast iron).

The progressive and consistent decrease in traction coefficient for mixed lubrication regime points in the direction of improved fuel efficiency. This is an indication that carbon black, just like soot, may though have a negative effect on the contacting surfaces in terms of wear, it has the tendency to reduce friction between them. Consequently, sooty oil potential to achieve this may be harnessed positively, especially at moderate content levels.

It must however be noted that the relative change in the traction coefficient is minimal for the test at different loads, this is an indication that if the contact condition between the surfaces are similar, the resultant traction coefficient may not produce significant difference at various loads. This is because coefficient of friction is supposed to be a ratio of frictional force to the normal load.

In spite of high testing loads (up to 400N), the severity of wear is not so pronounced in the mini traction machine (MTM) tests as compared to the reciprocating (TE 77) tests. This is due to the fact that the contact pressure in line contact was smaller because the sooty-oil surrogates were able to distribute the normal load over a wider surface area as against what happens with point contact, where a small area of contact carries the full load. Secondly and more importantly, the motion of the contacting rings dragged the lubricant into the contacting surfaces and thus eased its entrainment in MTM tests, being a rolling-sliding contact; unlike sliding contact, which pushes away the lubricant from the contacting surfaces in reciprocating tests.

The wear analysis clearly shows that the level of abrasion and severity of surface damage is influenced by the level of carbon black contamination.

Chapter 7

Conformal Contact Test with Pin-in-Bush Set-up

In Chapters 5 and 6, detailed discussions of the specimen tests involving non-conformal point and line contacts are presented. In this chapter, conformal contacts using a pin-in-bush arrangement is described.

The pin-in-bush test was designed, as part of this research, to simulate chain link articulation under load; a similar approach was used in some previous work [114]. The approach suits the study of soot wear in conforming contacts using a reciprocating sliding arrangement.

The designed pin-in-bush experiment is intended to be a fundamental study to give a basic insight and understanding on how soot content causes wear in conformal contacts.

Under constant load, the conformal contact test has the advantages of sustaining the same area of contact and hence, contact pressure, relatively uniform pressure distribution and constant lubricant film thickness [45].

7.1   The pin-in-bush (PIB) rig

The pin-in-bush (PIB) rig, Figure 7.1, was specifically designed to meet the peculiarity of the proposed test, in terms of simulation of chain link articulation and fitting perfectly with the existing reciprocating rig dedicated to drive it. The rig was statically loaded with a mass of 5466 g (53.62 N) resulting in average contact pressure of 36.63 MPa. The sliding rod of the prime mover (existing reciprocating rig) is attached to the oil bath of the PIB rig, this rolls the bush specimen which, under the static loads, rests in the lubricant-flooded oil bath. The pin specimen, which is firmly held by the lower arm of the connecting rod that transmits load to the contact, passes through the internal bore of the bush is thus fully encircled resulting in conformal contact between the pin and the bush. There is a flexible coupling between the rod transmitting motion and the oil bath, this enhances the self-aligning contact between the pin and the bush; and, consequently, eliminates the challenge of alignment usually associated with a conformal contact [45].
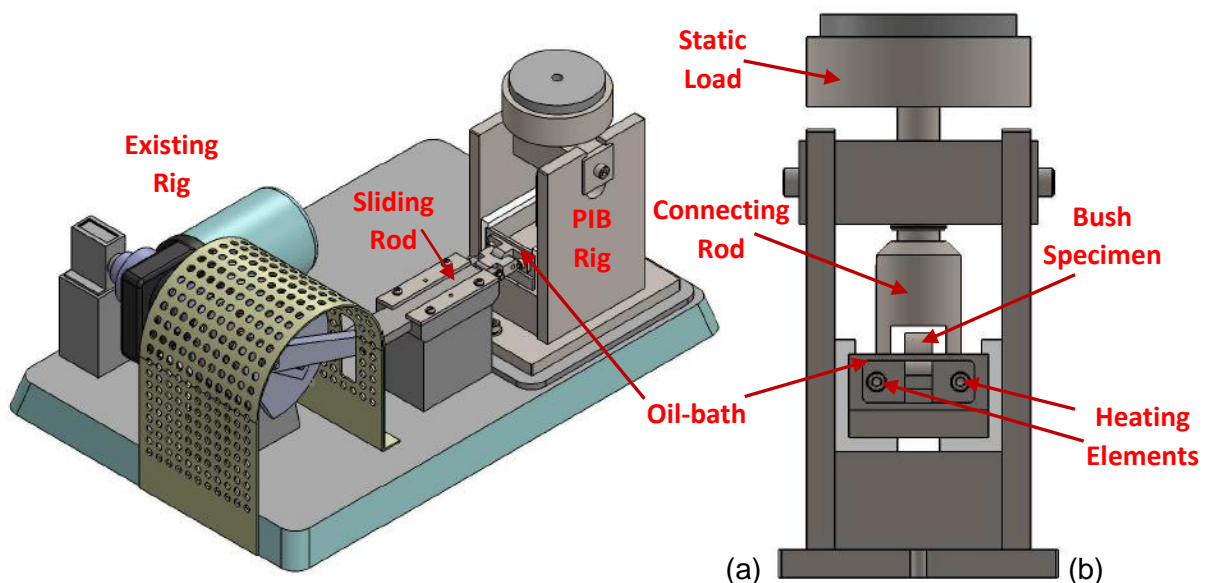
Figure 7.1: Schematic diagrams of pin-in-bush rig showing (a) coupled with the existing rig (b) standing alone

The lubricant is heated with the aid of two cartridge heating elements which are inserted to the base of the oil bath. Detailed specifications of the heating elements are highlighted in Table 7.1. While the PID (proportional-integral-derivative) controller is used to control and regulate the temperature during the testing; the feedback is through the attached K-type thermocouple wire which is fixedly positioned to sense the temperature of the lubricating oil.

Table 7.1: Specifications of the heating element

Product	Cartridge heater
Diameter (mm)	8
Inserted length (mm)	40
Current (watts)	100
Voltage (volts)	220
Type	G
Leads	42" f/g leads

7.2   Test specimens

The material selected for the pin and bush specimens was high carbon bright steel, normally referred to as "Silver Steel" (BS 1407:1970 grade steel). The choice is based on the fact that silver steel has a modest automotive application in the production of shafts, axles, pinions, pins, etc.

Table 7.2 highlights the chemical and mechanical properties of the material. With high carbon content, silver steel can be hardened to deliver high wear resistance and chromium content increases the strength and hardness. Chromium is also responsible for its bright "silver-like" finish from which it derives that traditional description, in spite having no silver content. Additional qualities of silver steel include: simple heat treatment, bright ground and polished, good machinability and toughness properties. These properties have made silver steel a versatile material for many applications, including axles and shafts, pinions and pins, small tools and structural parts in precision mechanics, milling cutters, toothed drills, gear cutters and metal cutting saws among others.

Table 7.2: Chemical and mechanical properties of silver steel (BS1407:1970)

Chemical Composition:		
Element	Range (%)	Typical (%)
Carbon	0.95 – 1.25	1.13
Manganese	0.25 – 0.45	0.37
Silicon	0.40 Max	0.22
Sulphur	0.045 Max	0.018
Phosphorus	0.045 Max	0.014
Chromium	0.35 – 0.45	0.43
Mechanical Properties:		
Tensile Strength (Pa/ N/mm^2)		700/850
Typical Hardness (HB)		207 – 237 with 285 Maximum
Young's Modulus, E (GPa)		210
Poisson's Ratio, υ		0.3

Figure 7.2(a) gives the pictorial views of both specimen and the connecting rod into which they are assembled before been coupled to the rig, Figure 7.2(b). Two views of the assembly drawing are presented in Figure 7.3 to clearly show the engagement of the pin and the bush.
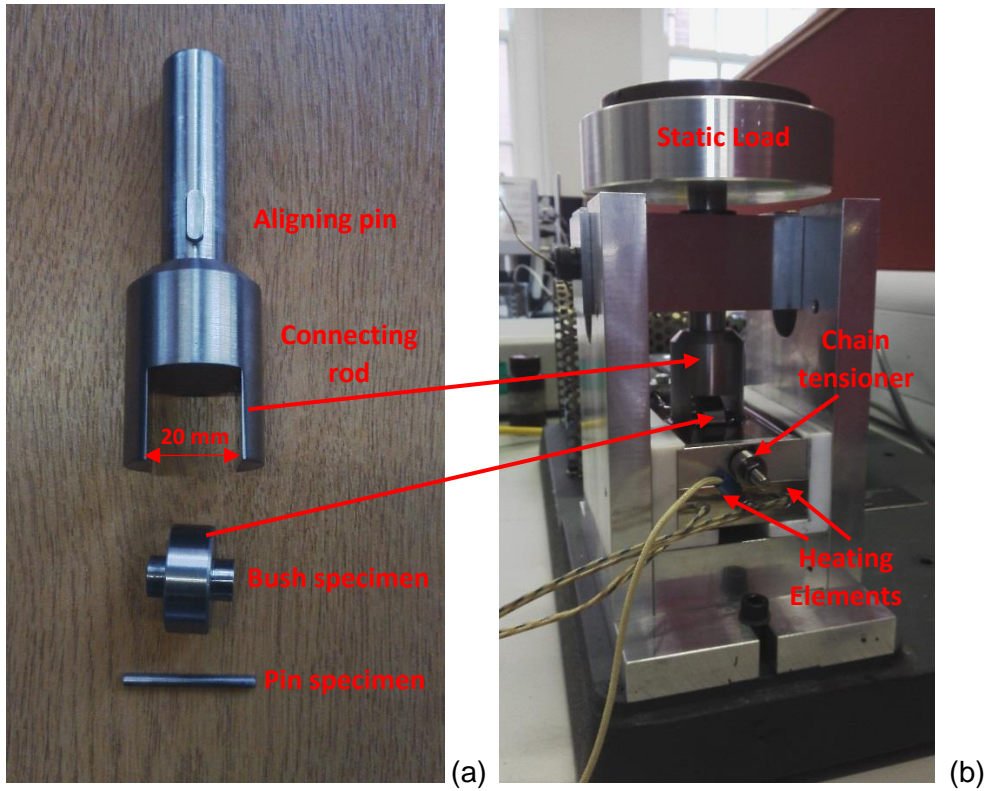
Figure 7.2: Pictorial views of the specimens (a) before being coupled and (b) as mounted on the rig
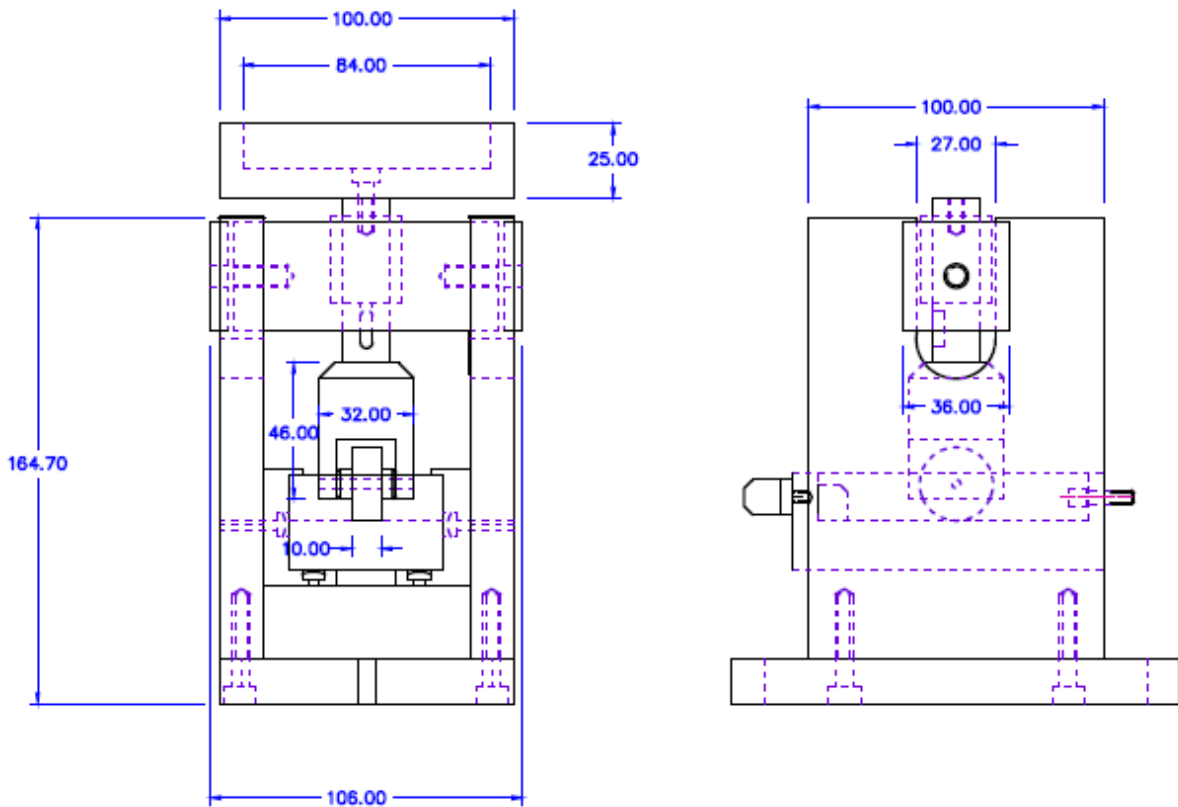
Figure 7.3: Front and side views of the PIB rig assembly drawing

7.3　Calculation of contact parameters

Hertzian contact theory has been used to estimate the contact parameters in the preceding tests because contact is basically non-conformal; which implies the contact area is small compared to the geometric dimensions of the contacting bodies [191, 192]. Hertzian theory is, however, inappropriate when the geometric dimensions of the contacting bodies are comparable to the contact area [193, 194]; such a contact is considered conformal. For spherical conformal contact, this is numerically estimated to be when the diametric ratio of ball socket to sphere is less than 1.072 [195].

Nonetheless, if the loads are small or the clearance is large, the pressure distribution approaches that of Hertz [192] and the contact stresses over the major part of the cylinder length are predicted accurately by the Hertz theory. Since the load is relatively small ($\cong$54N) in this case, Hertzian pressure distribution will therefore be assumed to be acting on a rectangular contact area of width 2*b* and length 2*l*, where *l>>b*. Hence, the estimations, similar to disc-on-disc's treated in the last chapter will suffice for the computations of the required contact parameters; except that the pin-in-bush configuration is like a cylinder in a cylindrical groove and a cylindrical groove is a cylinder with a negative radius, being a concave surface.

7.3.1　Contact pressure

The maximum contact pressure, p_o, was estimated using Herzian's contact formula [40]:

$$p_o = \frac{P}{\pi b l}$$

Equation 7.1

Average contact pressure, p_m is:

$$p_m = \frac{P}{4bl}$$

Equation 7.2

Maximum shear stress, τ_{max} is:

$$\tau_{max} = 0.304 p_o$$

Equation 7.3

Contact area dimensions, b, is given by:

$$b = \left(\frac{4PR\prime}{\pi l E\prime}\right)^{1/2}$$

Equation 7.4

b is the half width of the contact rectangle and other parameters are as defined in the preceding chapter.

Figure 7.4(a) presents the three-dimensional schematic diagram of the conformal contact between the pin and bush with the normal load and pressure distribution in three dimensions, while Figure 7.4(b) shows the contact in 2D and Figure 7.4(c) is the depiction of the pin and bush moving with a reciprocating sliding action on the lubricant film at the interface. The contact area is rectangular with a semi-elliptical pressure distribution.
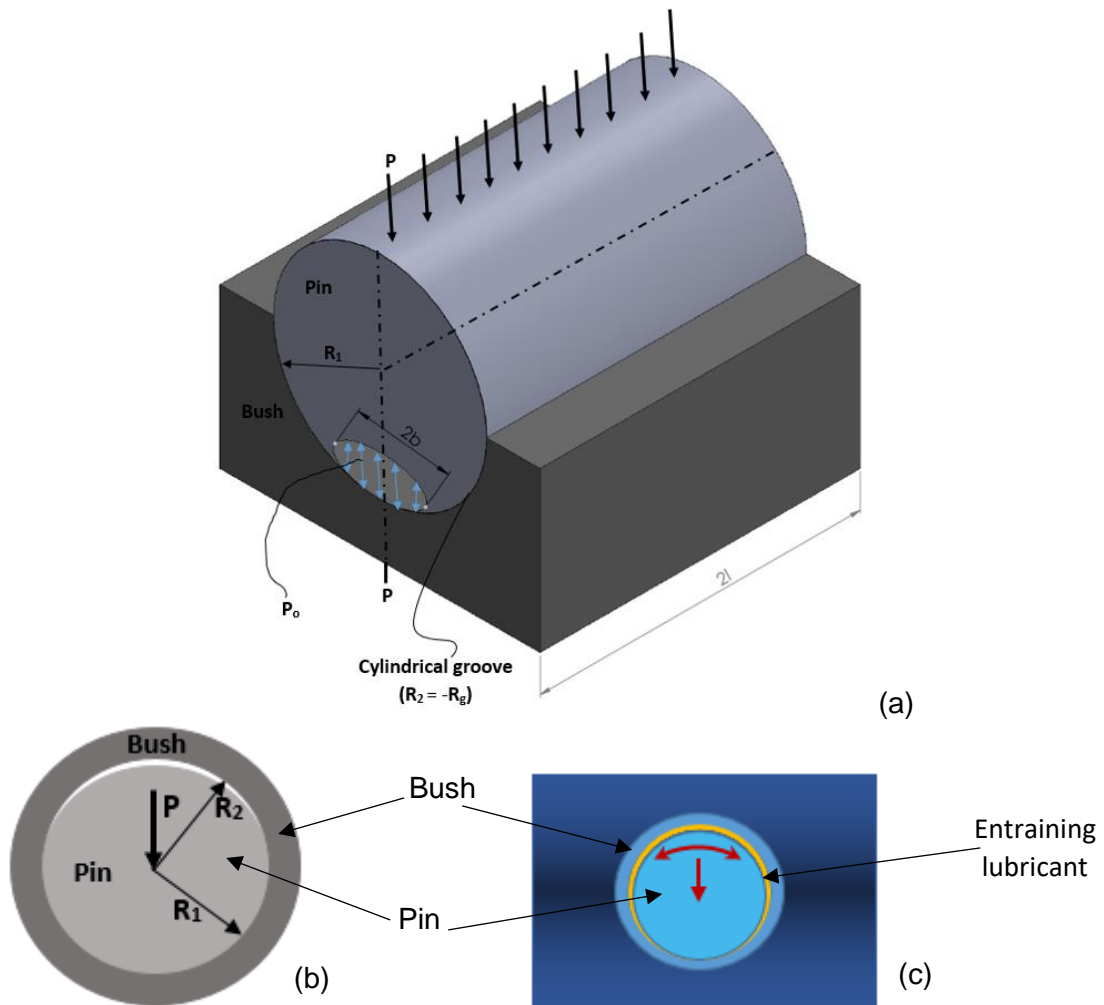
Figure 7.4: (a) 3D schematics of the conformal contact between the bush and pin with the normal load, (b) 2D representations of the contact and (c) depiction of the ideal lubrication between the specimens

The pin is closely fitted into the bush, but runs freely with a tolerance of 20-70 μm. This free running tolerance is suitable for the tests considering the various levels of carbon black compositions and the temperature under which the tests will be conducted.

With the normal load of 53.62 N, the results of these estimations are:

Maximum contact pressure, p_o = 46.63 MPa;

Average contact pressure, p_m = 36.63 MPa;

Maximum shear stress, τ_{max} = 14.18 MPa and

Contact area dimensions, 2b = 0.163 mm

7.3.2 Film thickness

A conformal contact generally favours hydrodynamic lubrication [128]; but with the estimated contact pressure being greater than 5 MPa, the contacting surfaces will most likely undergo significant elastic deformation. Consequently, elastohydrodynamic lubrication is proposed for the estimation of the film thickness operational between the pin and bush in the tests. This can be determined using a central film thickness formula, Equation 7.5 [40].

$$\frac{h_c}{R'} = 2.69U^{0.67}G^{0.53}W^{-0.067}\left(1 - 0.61e^{-0.73k}\right) \qquad \text{Equation 7.5}$$

where,

h_c is the central film thickness, other parameters are as defined in chapter 5.

The geometric conformity of the contact means the load is carried over a relatively large area [128]. This load-carrying surface area is essentially maintained even when the load is increased. The outcome of the film thickness estimation as presented in Table 7.3 indicated a values ranging from 36 to 84 nm.

Table 7.3: Minimum film thickness of sooty-oil surrogates

Sooty oils	Minimum Film Thickness (nm)
0%CB	36.03
3%CB	58.60
5%CB	61.62
7%CB	63.70
10%CB	83.88

7.4   Experimental procedures

The specimens were ultrasonically cleaned with acetone and dried, after which each pin specimen was (in turn) inserted into the bush through the carrying arm. This assembly was carefully placed in the oil bath and the upper rod inserted into the aligning arm before being bolted into the supporting stands. The basin that carries the dead-weight load was then bolted atop the upper rod. The carbon black-mixed oil was thoroughly shaken and poured into the oil bath until the pin specimen was fully submerged, taking 25ml approximately. The procedures were repeated for each of the carbon black compositions using different specimen pairs.

The PIB rig was programmed, through the PID controller, to heat to a temperature of 100°C and retain that temperature for 420 minutes; each test ran for 12 hours in two days (6 hours/day). The operating temperature was monitored through the attached thermocouple. However, the outcome was a ramping to 115°C in 50 minutes and soaking at that stabilized temperature for the set period of 420 minutes. Each test commenced 15 minutes after the stabilized temperature was reached. Figure 7.5 shows the entire experimental set-up of the rig and the PID with its accessories. The summary of the test conditions is highlighted in Table 7.4 below.

Prior to the beginning of the test, each pin specimen was weighed using the weighing balance, Sartorius Electronic Analytical Balance (Basic[Plus] BP210D). At the end of the test, they were only rinsed in acetone without wiping or ultrasonic sonication. This is to guide against removal of any embedded carbon black particles during the test [114].
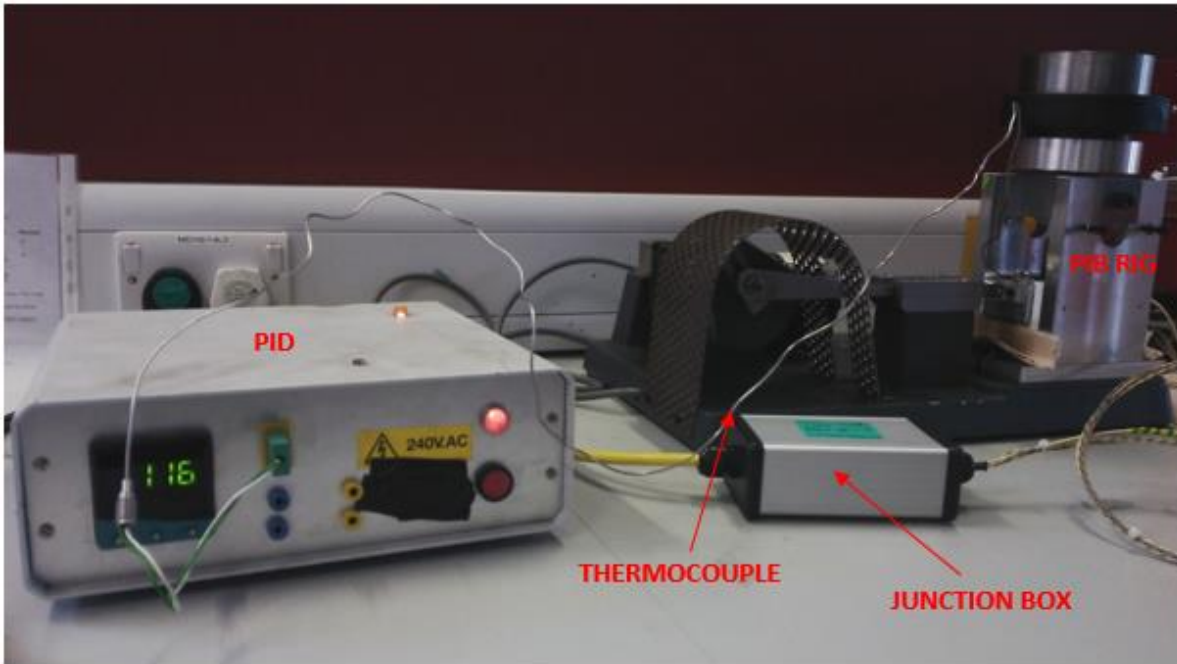
Figure 7.5: The experimental set-up showing the rig with PID instrumentations

Table 7.4: Test conditions for pin-in-bush experiment

Parameter	Value
Lubricant	Sooty-oil surrogates (0wt% - 10wt%)
Lubricant quantity (ml)	$\cong 30$
Lubricant temperature (°C)	115±1
Normal Load, P (N)	53.62 constant
Contact pressure, P_o (MPa)	26.02 constant
Contact area dimension, b (mm)	0.146
Reciprocating frequency (Hz)	0.86
Rotation (rpm)	51.5
Stroke length (mm)	8
Linear speed (m/s)	0.0137
Test duration (hours)	12
Cycles	37080
Bush specimen specification	Silver steel (BS 1407) 20 mm with 3 mm D9 hole
Pin specimen specification	Silver steel (BS 1407) 3 mm h9 – stationary
Tolerance (mm)	0.02-0.07 (Free running clearance fit)

Figure 7.6(a&b) presents schematics of the pin and bush specimens, while Figure 7.6(c) shows the front view of their assembly with the clearance indicated. Figure 7.7 shows the schematic representation of fit.

(a)

(b)

Bush specimen
(reciprocating)

Pin specimen
(stationary)
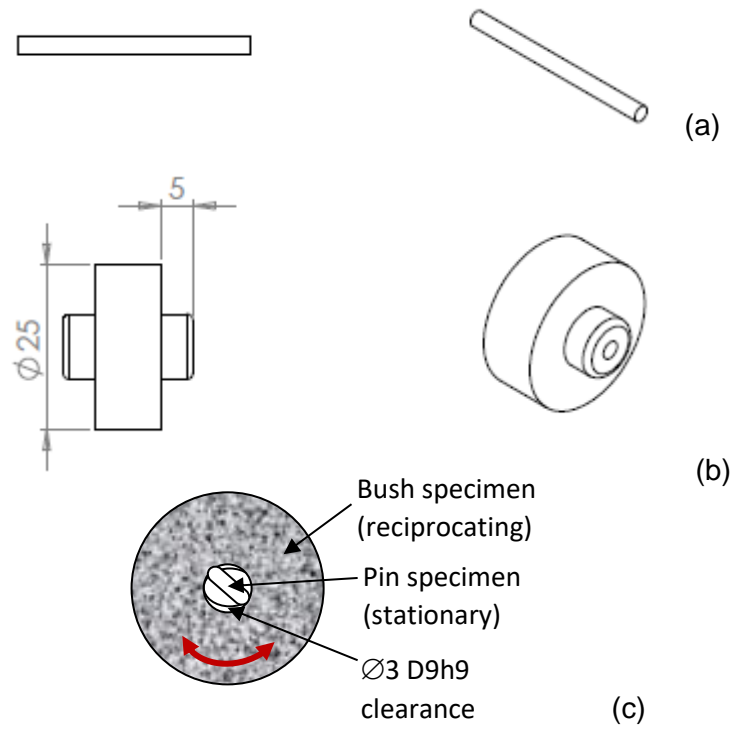
⌀3 D9h9
clearance   (c)

So, the clearance between the pin and the hole of the bush is essentially ⌀3 D9h9.

Figure 7.6: Schematics of (a) pin specimen, (b) bush specimen and (c) assembled
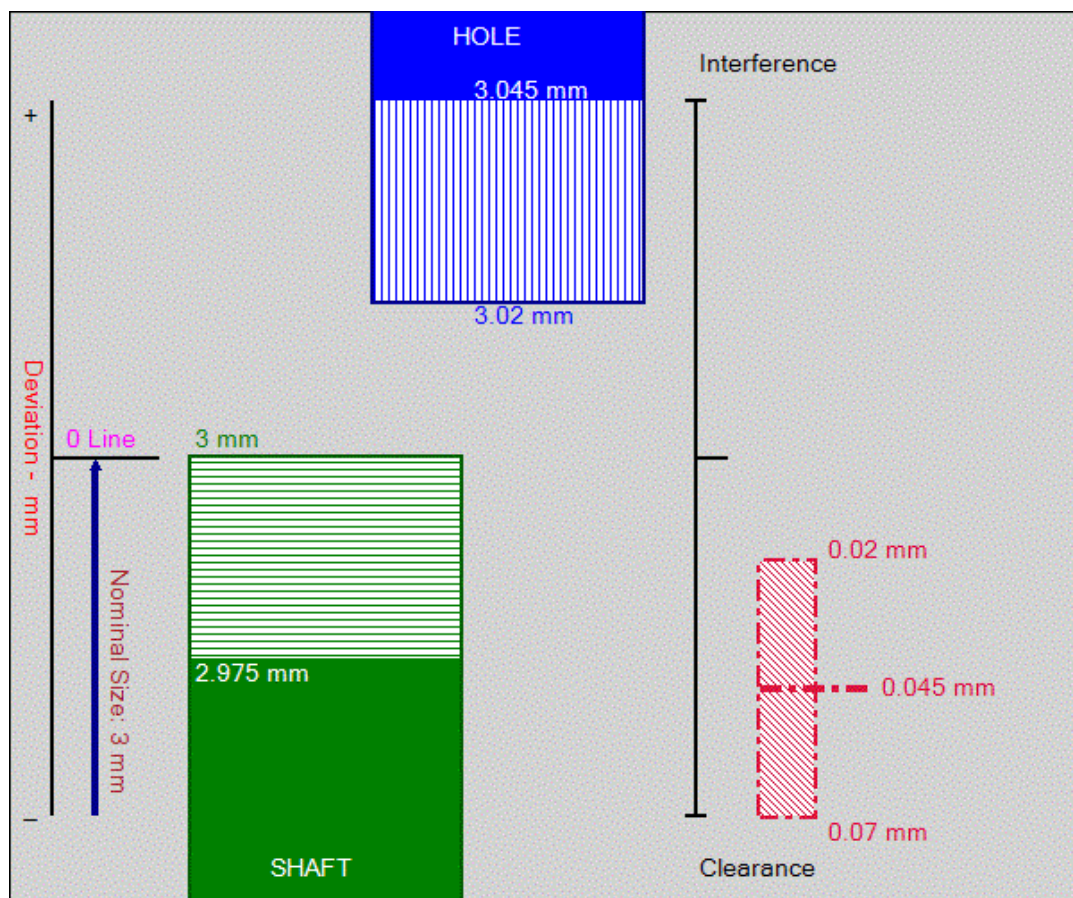
Figure 7.7: Schematic representation of fit

7.5   Results

As shown in Table 7.4, the tests were conducted under the same conditions for each composition of the lubricants. Apart from the recorded masses of the pin specimen before and after the test, the results are mainly post-test analysis of the wear induced on the pin specimen surfaces by each composition of carbon black.

7.5.1   Pre-test and post-test recorded masses of the pin specimen

Pin specimen assigned to each carbon black content was weighed prior to the test and afterwards using Sartorius BP 210 D precision scale, with an accuracy of 0.1 mg. The results of the recorded masses are presented in Table 7.5.

Table 7.5: Pre-test and post-test masses of the pin specimen

Pin specimen assigned to each lubricant	Pre-test mass (g) ±0.0001	Post-test mass (g) ±0.0001
0%CB	1.7370	1.7372
3%CB	1.7392	1.7398
5%CB	1.7368	1.7370
7%CB	1.7346	1.7355
10%CB	1.7385	1.7397

The result shows a marginal increase in each of the pin, this may have arisen from surface-bound carbon black particles or possibly due to material transfer between the test specimens.

The gravimetric (mass loss) analysis becomes suitable here because the mass of the pin specimen is quite very small unlike the mass of the flat specimen in the ball-on-flat test which is very large when compared with the generated wear scar.

7.5.2   Wear analysis

The specimens were rinsed in acetone for about 20 seconds after which they were air-dried in preparation for post-test wear imaging. This is to guide against tampering with the carbon black particles that were envisaged would be embedded.

7.5.2.1 SEM images

Scanning electron microscopic images of the pin specimen were taken for each carbon black content. Figure 7.8(a) presents the SEM micrographs of pin specimen prior to the commencement of the test, the tiny dark spots visible on the images may be ignored as they may have emanated from machining and polishing processes. Figure 7.8(b) and Figure 7.8(c) show the micrographs for 0wt%CB content and magnified image of the wear track for a closer observation, respectively. There appears to be some level of surface scratching emanating from asperity contacts here and there and evidence of this can be seen in the dispersed lubricated wear with some level of abrasion along the length of the pin. The level of abrasion becomes more conspicuous and continuous with 3wt%CB content as presented in Figure 7.9. The magnified micrograph of a selected wear track, Figure 7.9(b), shows tiny, but lengthy surface scratches along the sliding direction. These are possibly caused by well-dispersed carbon black particles within the lubricant in the contact zone. The concentrated black spot on the image, Figure 7.9(a), is not given any prominence as a windowed image does not present it as having anything to do with the wear track. Therefore, it could not have been a collection of carbon black particles.

As the content of carbon black increases, the effect of carbon black particles becomes obvious in the formation of wear on the surface of the pin specimen and along the sliding direction.

Consequently, scuffing and carbon black particles embedment are observed at higher CB contents. Figure 7.10 presents the micrographs for 5wt%CB content with pronounced abrasive wear as evident by the wear track with embedded carbon black particles. The particles are hard enough to create a well-defined wear track with significant depth; though, there is just a small patch of this at this level of carbon black content. At 7wt% carbon black content, the abrasive wear is more severe, Figure 7.11(a); the evidence of this is seen on the magnified micrographs as shown in Figure 7.11(b). The wear tracks appear in form of grooves formed by ploughing along the length of the pin by the entraining hard carbon black particles [40]. Figure 7.12 presents further evidence of severe abrasive wear at 7wt%CB content with embedded carbon black particles along the wear track.

There is an enormous level of surface damage across the entire length of the pin for 10wt%CB content as shown in Figure 7.13(a). A close-up view of the image, Figure 7.13(b), shows the extent of colossal damage that trapped hard carbon black particles can cause at that level of contamination. This is further corroborated by additional micrographs, Figure 7.14, taken at two other spots along the length of the same pin.
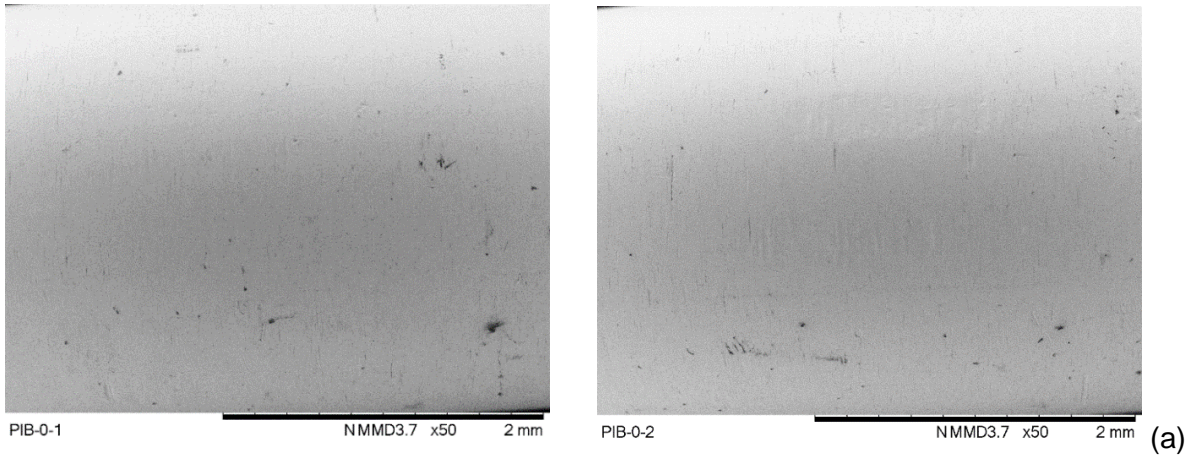
Pre-test specimens
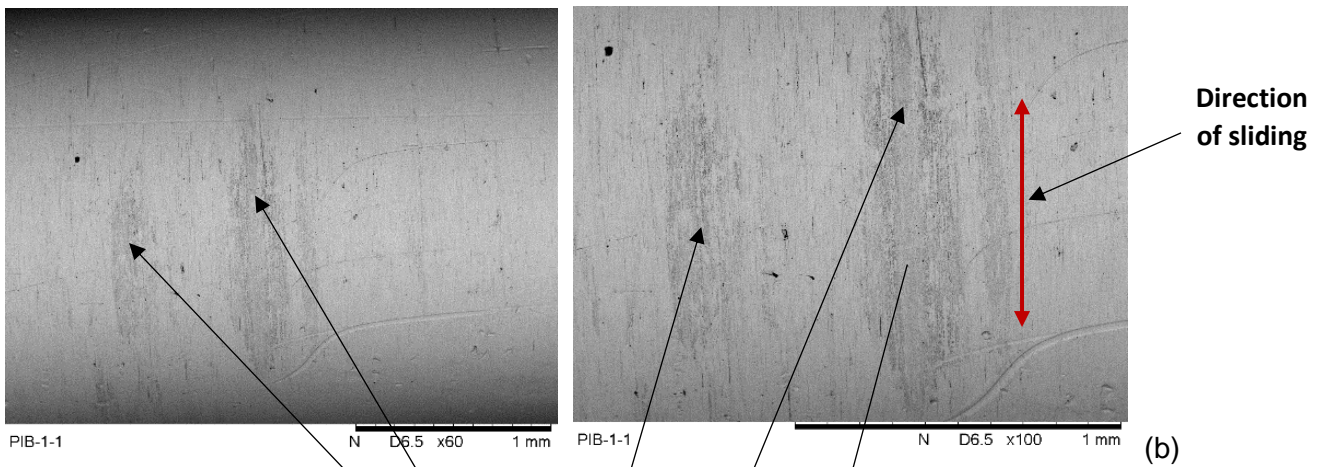
Evidences of lubricated wear scattered along the pin length

Direction of sliding

0wt%CB – Lubricated wear with some level of abrasion appearing here and there along the pin length

Two-body (metal-to-metal) abrasion
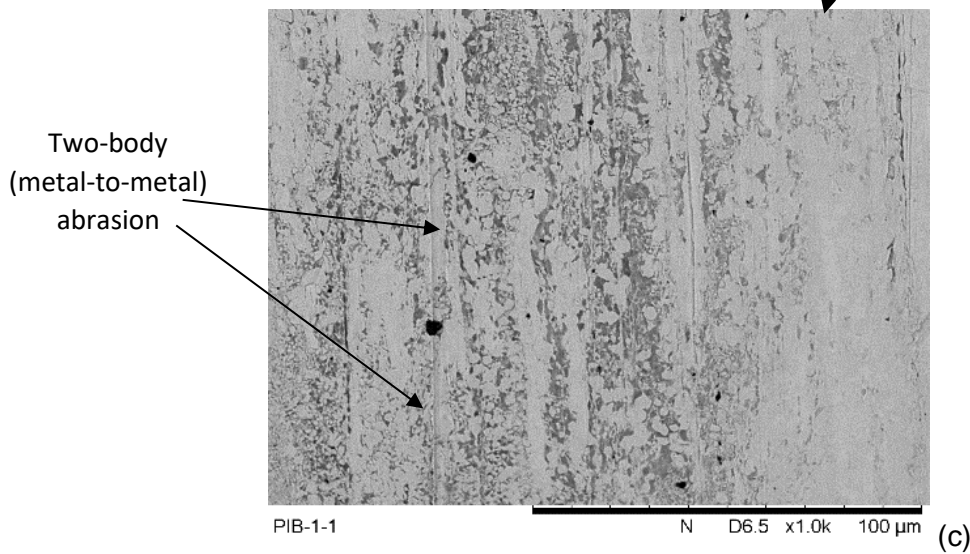
A closer look at the wear track showing evidence of mild abrasive wear

Figure 7.8: Photomicrographs of (a) the pre-test pin specimen, (b) 0wt%CB content with evidence of abrasive wear along the pin length and (c) a further magnification (x1000) of the wear track

Direction of sliding
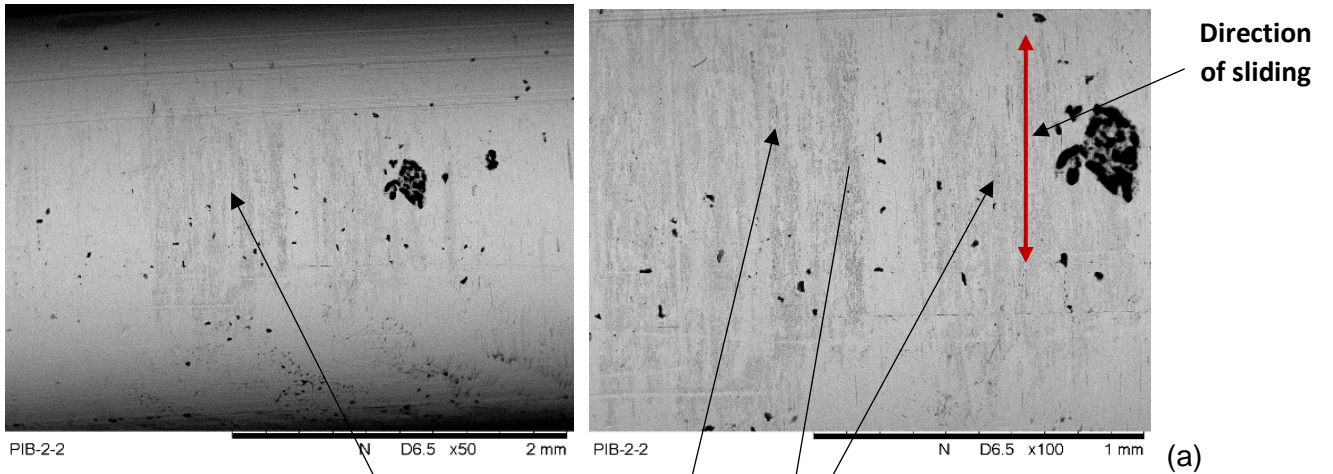
The abrasive wear is continuous along the pin length

3wt%CB – Abrasive wear is conspicuous and continuous along the pin length

(a)

Evidences of well-dispersed CB particle scratches on the pin surface

(b)
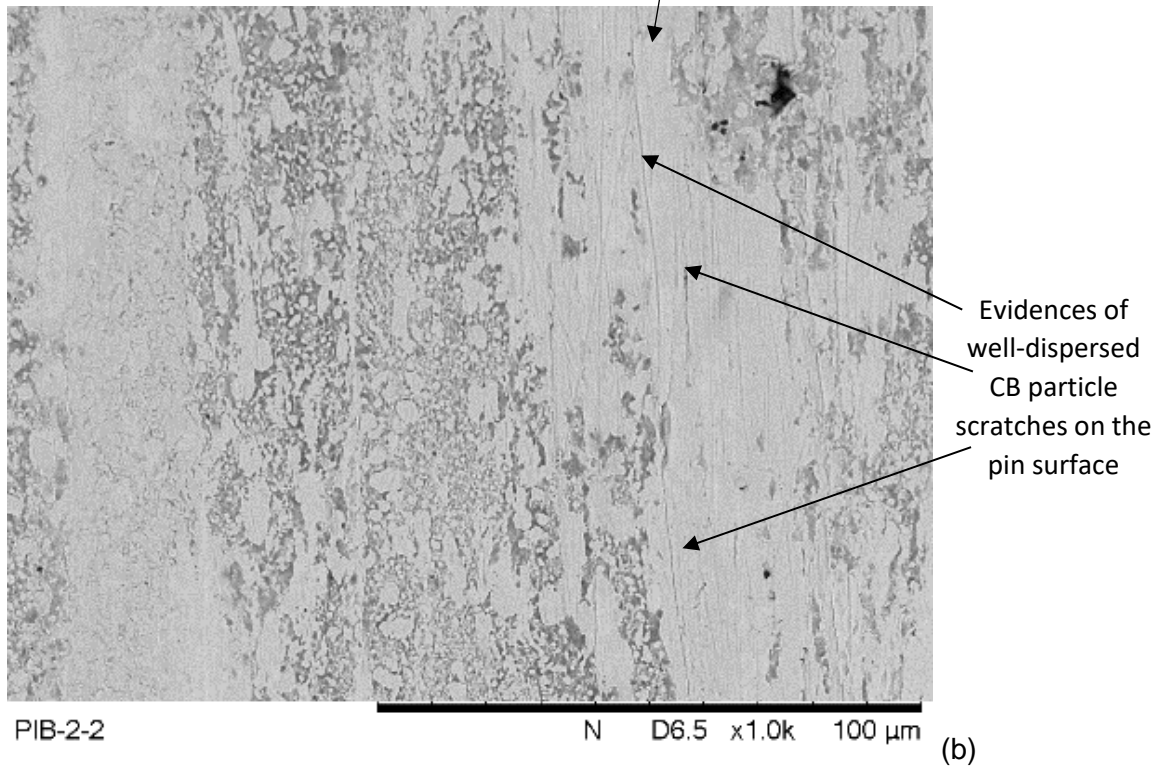
Higher magnification of the image showing pronounced abrasive wear

Figure 7.9: Photomicrographs of (a) 3wt%CB content showing continuous abrasive wear along the pin length and (b) a closer look (x1000) at the wear track

More pronounced abrasive wear

Embedded particles along the wear track

Direction of sliding

(a)

5wt%CB – Abrasive wear is more pronounced with embedded particles along the wear track
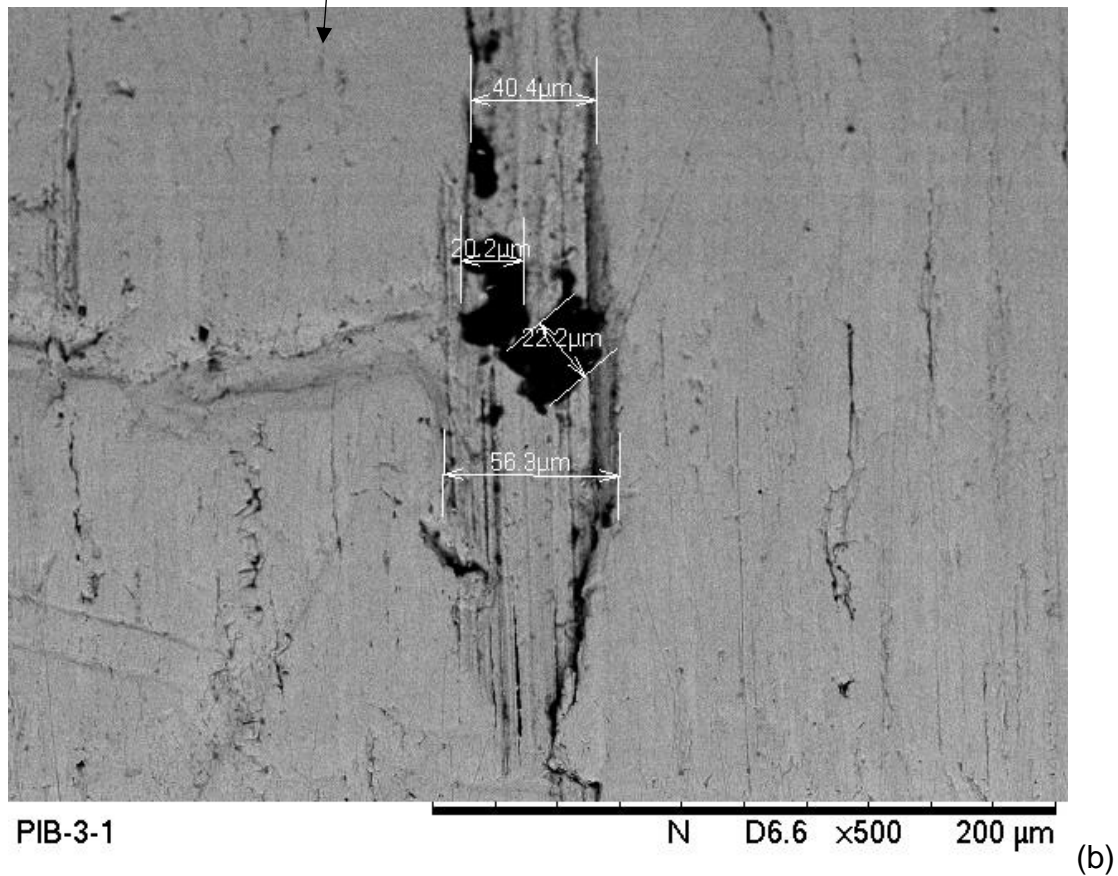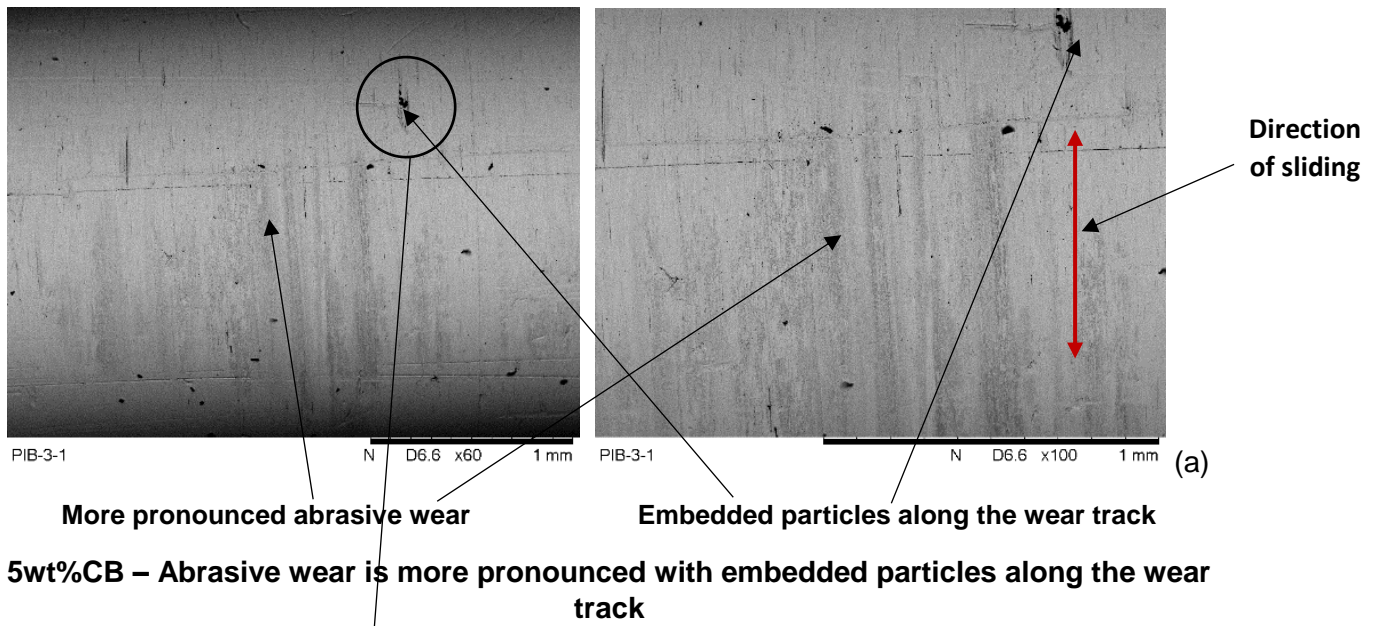
Higher magnification of the image showing the carbon black particle-induced wear with dimensions

(b)

Figure 7.10: Photomicrographs of (a) 5wt%CB content with pronounced abrasive wear along the pin length and (b) windowed wear track with embedded carbon black particles
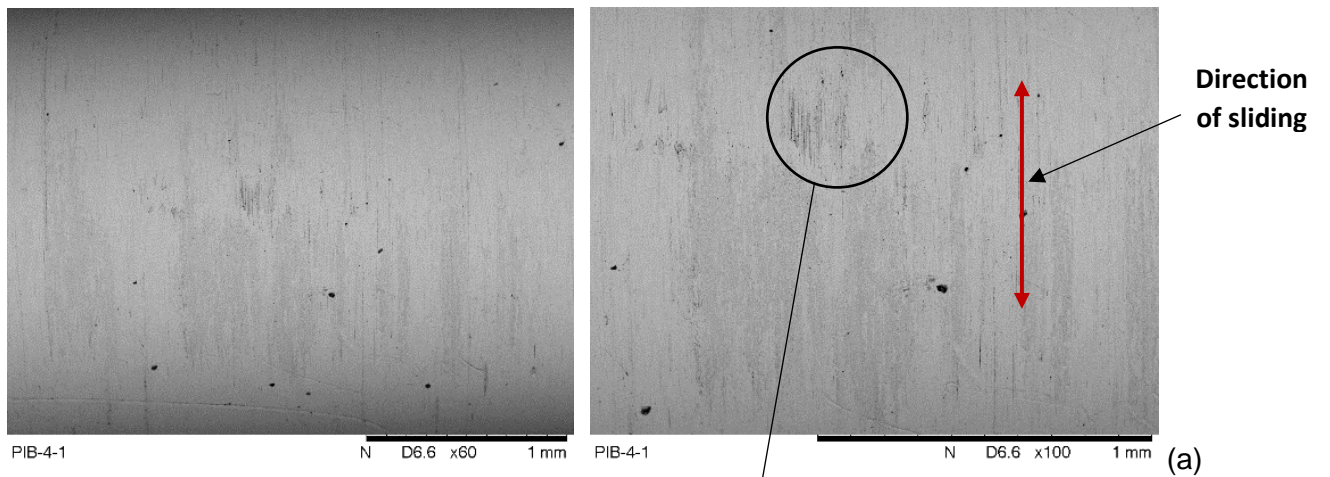
7wt%CB – Severe abrasive wear with deep-cut wear track as evident on the magnified window
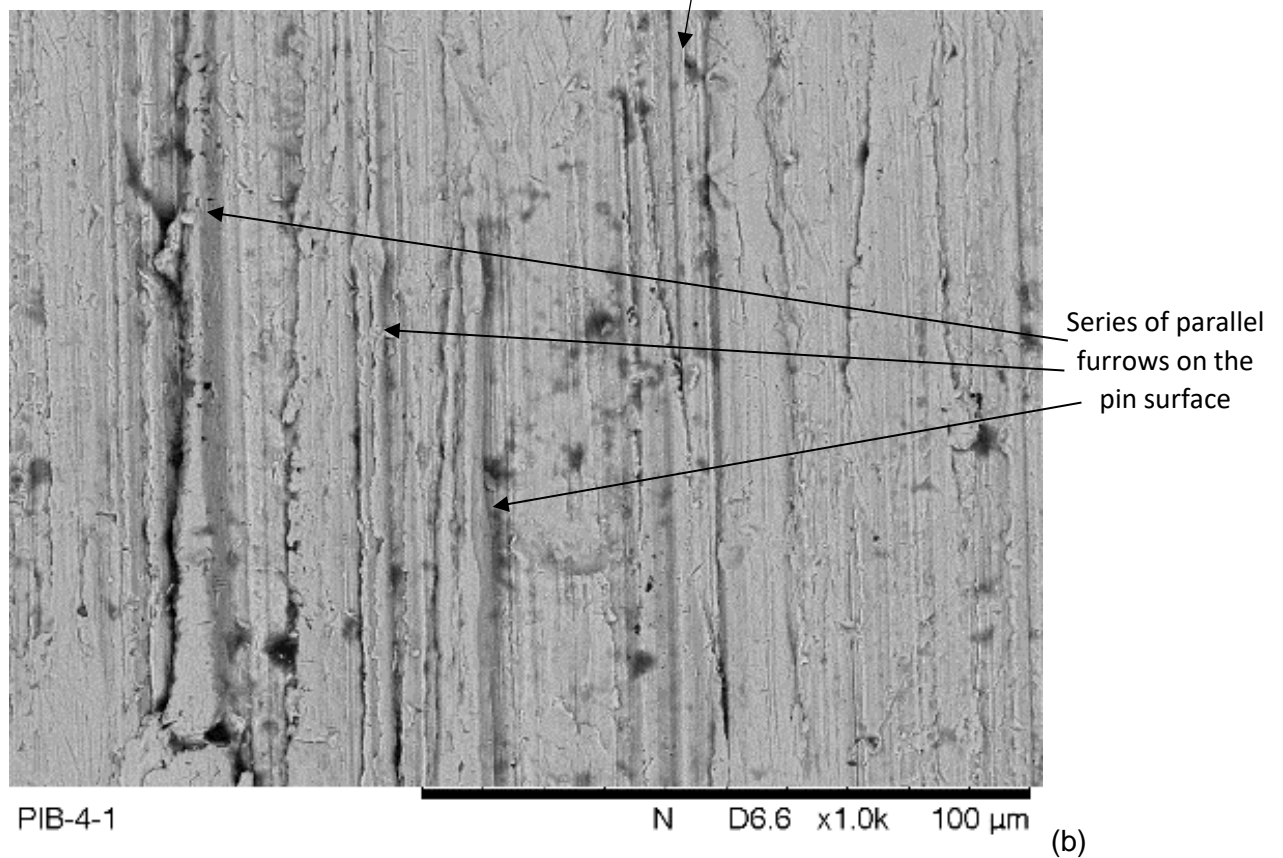
A close-up view of the severely abraded wear track induced by carbon black particles

Figure 7.11: Photomicrographs of (a) 7wt%CB content showing severe abrasive wear along the pin length and (b) windowed deep-cut wear track as evidence of severe abrasion
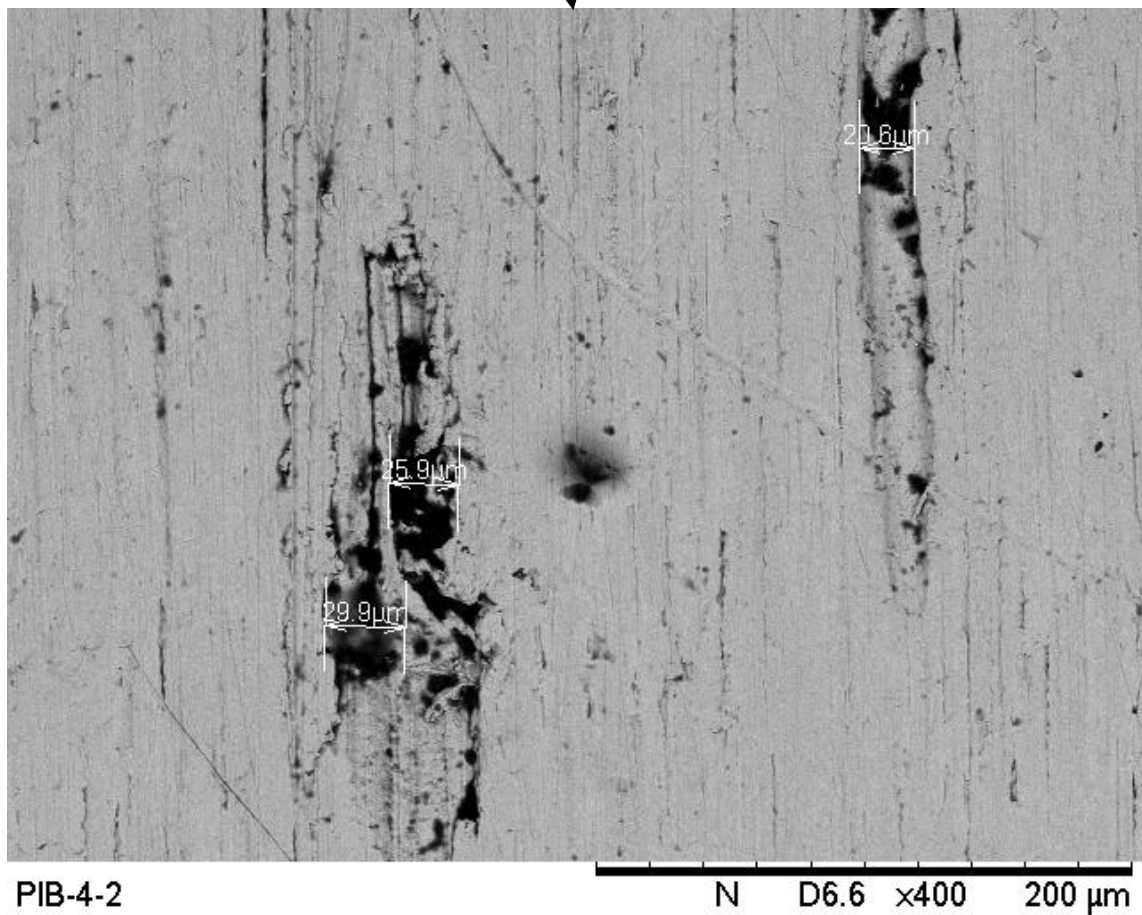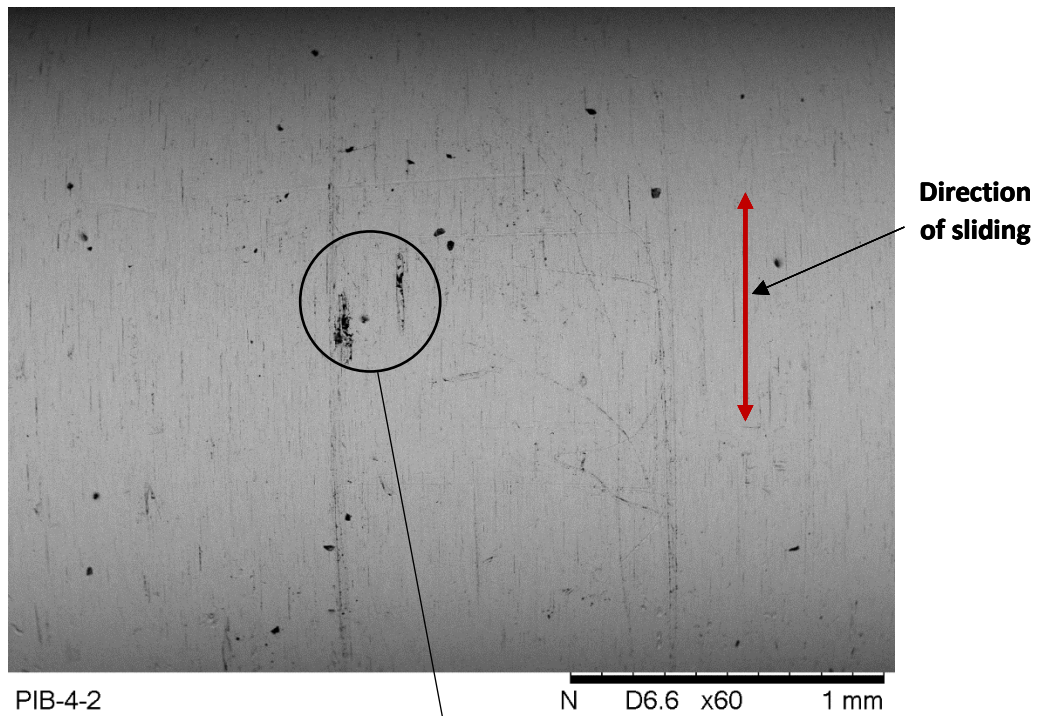
7wt%CB – Severe abrasive wear with embedded particles

Figure 7.12: Photomicrographs of 7wt%CB content presenting further evidence of severe abrasive wear with embedded CB particles along the wear track, dimensioned at higher magnification

Direction of sliding
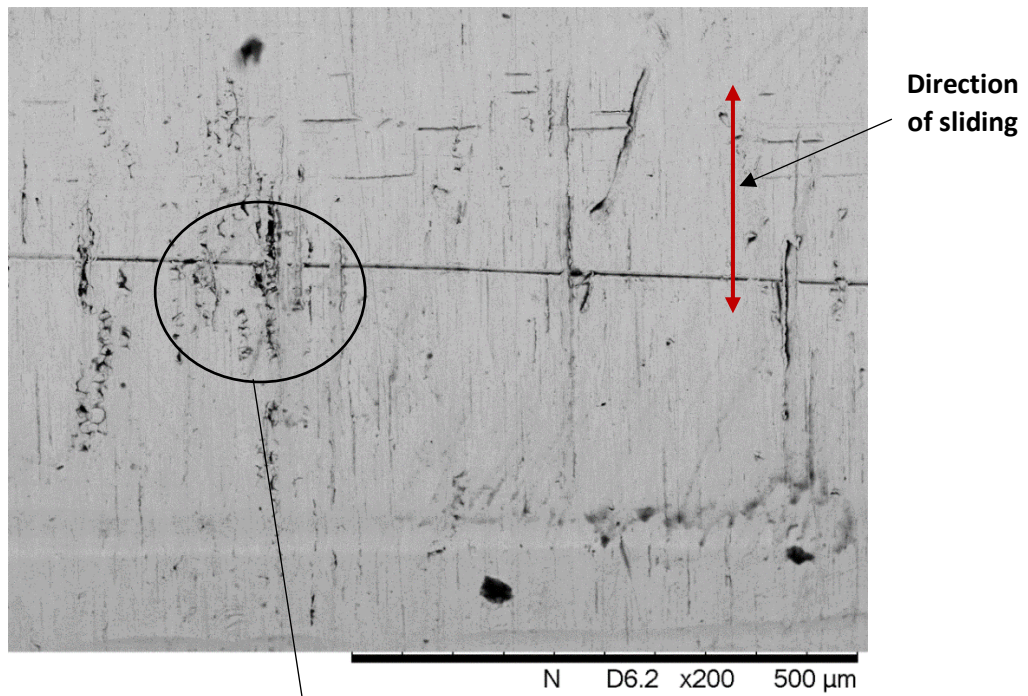
PIB-5-3

(a)

10wt%CB – Severe surface damage across the pin length as evident on the magnified window
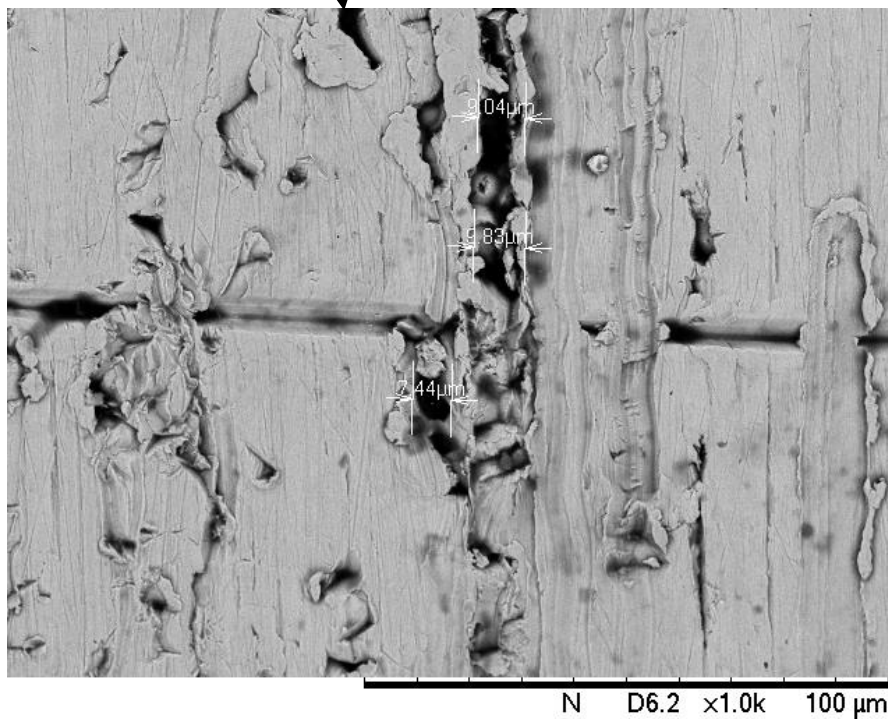
PIB-5-3

(b)

The magnified window showing severely damaged surface induced by trapped hard carbon black particles

Figure 7.13: Photomicrographs of (a) 10wt%CB content with evidence of severe surface damage along the pin length and (b) windowed image of the extent of severity caused by trapped hard CB particles

134

Direction of sliding

PIB-5-1

N   D5.9 x100   1 mm

N   D9.3 x100   1 mm

Trapped carbon black agglomerates resulting in scuffing
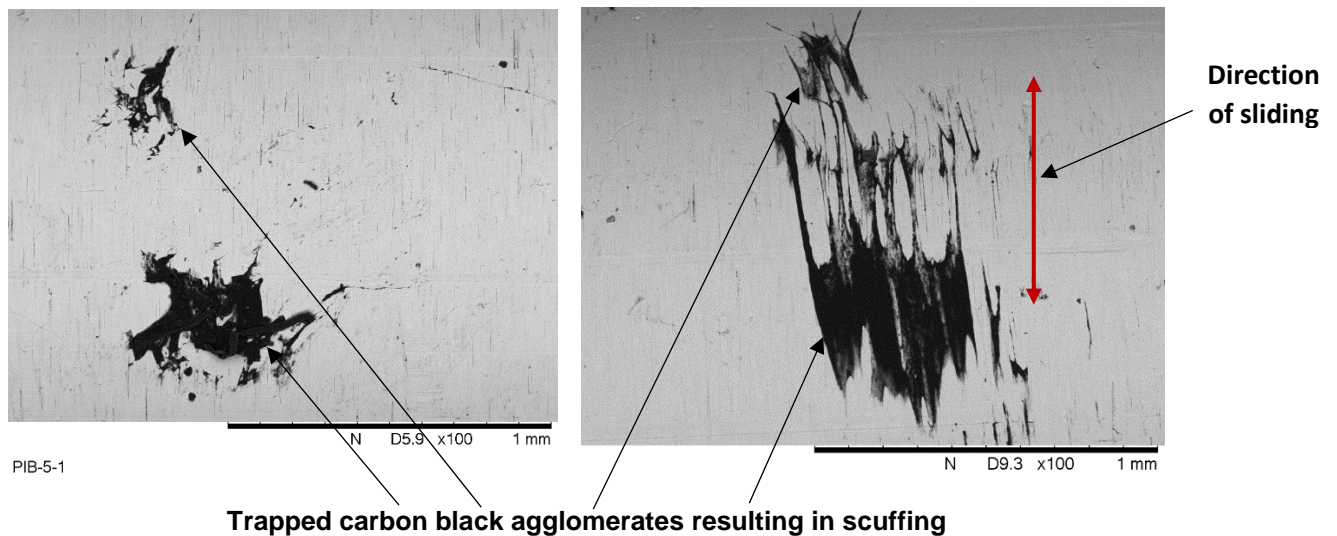
10wt%CB – Further evidences of severe surface damage due to scuffing caused by trapped carbon black agglomerates

Figure 7.14: Photomicrographs of 10wt%CB content presenting further evidence of severe abrasive wear with embedded CB particles along the wear track

7.5.2.2 Surface profile images

Three-dimensional surface images of the pin specimens prior to the commencement of testing and post-test for various carbon black contents were taken using a non-contact Veeco's ContourGT-K1 scanning white light interferometry (SWLI) operated with Vision64 operation and analysis software. The same set-up was maintained for all the images taken in terms of magnification (10x, to cover a reasonable portion of the pin for each imaging), measurement type (vertical scanning interferometry, VSI) and sampling length ($\cong$1.3 mm). The middle portion of the wear track for each of the pins were imaged, avoiding both ends of the pin where each pin was firmly held by the lower arm of the rod transmitting load to the contact; three to five positions were imaged on each pin. The ContourGT-K1 was manufactured by Veeco Instruments Inc., USA.

The ContourGT imaging was expected to provide quantitative surface profile, in terms of roughness values. The selected topographic images obtained from the pre-test pin specimen and various carbon black contents post-test pin specimens are presented in Figures 7.15 to 7.22.

Figure 7.15 presents the image for the pre-test pin specimen with a root mean square (rms) roughness, R_q, value of 0.132 μm. The surface profile for the uncontaminated lubricant (0wt%CB), Figure 7.16, shows some scratches along the sliding direction with roughness value of 0.170 μm.

P₀ – Pre-test

Surface Stats:

Ra: 0.106 μm

Rq: 0.132 μm

Measurement Info:

Magnification: 10x

Measurement Mode: VSI
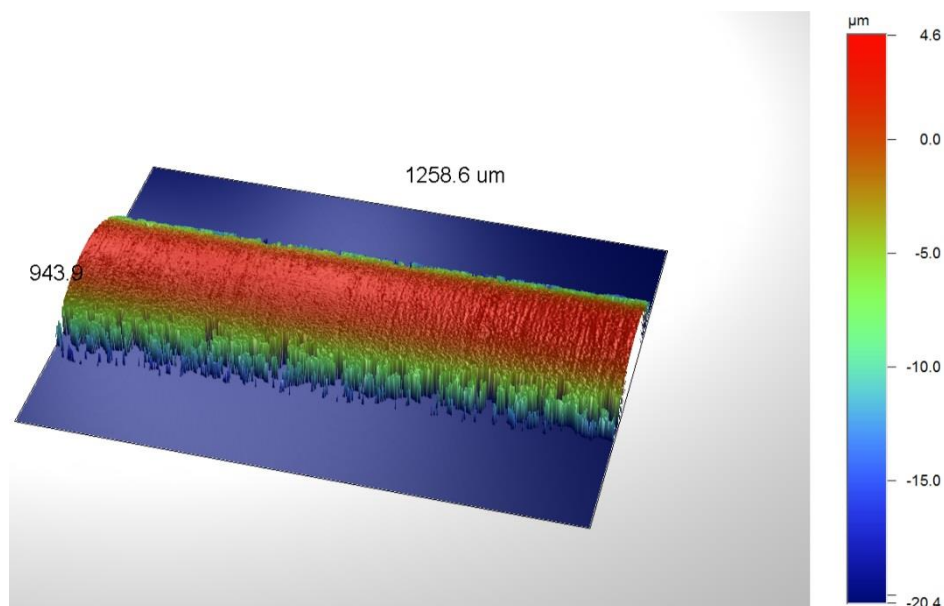
Sampling: 1258.6 μm

Figure 7.15: Three dimensional surface plot of the pre-test pin specimen; Ra = 0.106 μm

P₁ – 0wt%CB

Surface Stats:

Ra: 0.141 μm

Rq: 0.170 μm

Measurement Info:

Magnification: 10x

Measurement Mode: VSI

Sampling: 1258.6 μm
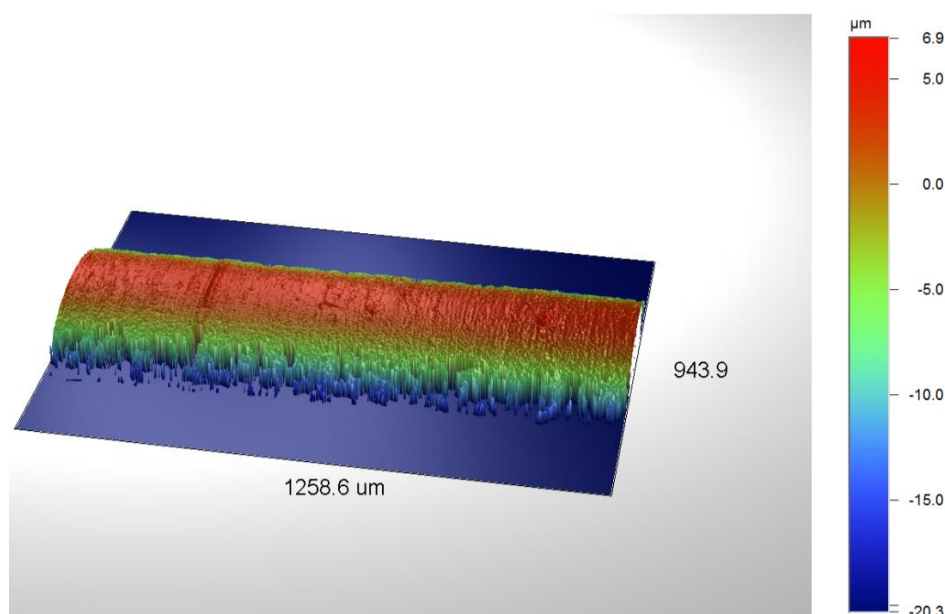
Figure 7.16: Three dimensional surface plot of the 0wt%CB content; Ra = 0.141 μm

Figure 7.17 and Figure 7.18 show the topographic images for the 3wt%CB and 5wt%CB contents respectively. The average roughness value for the 3wt%CB content, 0.168 μm, is surprisingly higher than that of 5wt%CB, which is 0.161 μm; in spite of higher level of wear tracks visible on 5wt%CB image when compared with those on 3wt%CB image. However, their rms roughness, Rq, values are: 0.184 μm and 0.198 μm respectively.

P₂ – 3wt%CB

Surface Stats:

Ra: 0.168 μm

Rq: 0.184 μm

Measurement Info:

Magnification: 10x

Measurement Mode: VSI
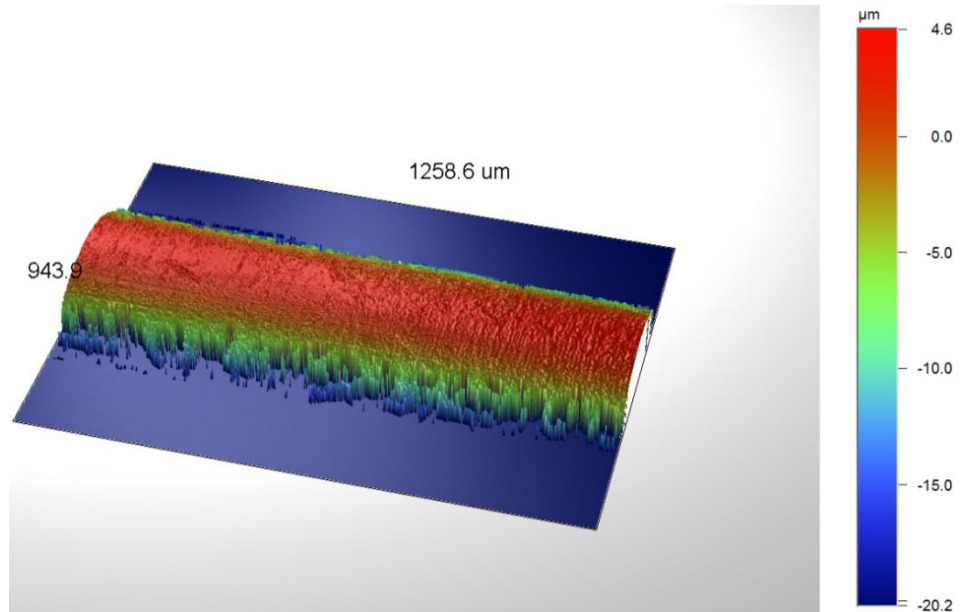
Sampling: 1258.6 μm

Figure 7.17: Three dimensional surface plot of the 3wt%CB content; Ra = 0.168 μm

P₃ – 5wt%CB

Surface Stats:

Ra: 0.161 μm

Rq: 0.198 μm

Measurement Info:

Magnification: 10x

Measurement Mode: VSI

Sampling: 1258.6 μm
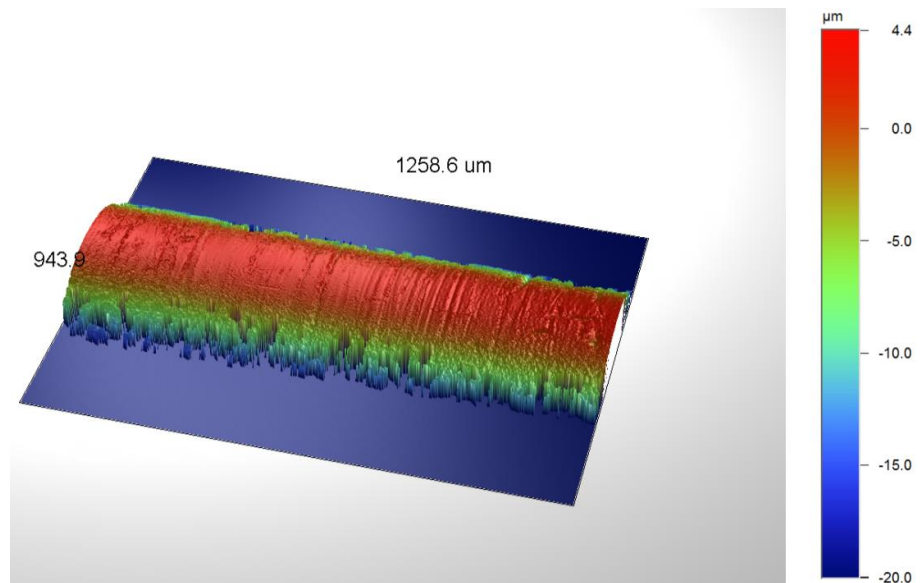
Figure 7.18: Three dimensional surface plot of the 5wt%CB content; Ra = 0.161 μm

The topographic image obtained for 7wt%CB content indicates a portion along the pin with significant level of wear, Figures 7.19. This may possibly be an area where embedded carbon black particles caused severe wear on the pin specimen as earlier highlighted on the SEM images. The surface profile gives a roughness value, Rq of 0.217 μm.

Virtually every portion of the 10wt%CB content pin specimen shows measurable wear topography. Three of the images taken at different portions along the length of the pin specimen are presented here, Figures 7.20-7.22. Each of the images presents evidence of severely roughened surface emanating from carbon black particles that are trapped within the tolerable gap between the pin and the bush resulting in third body abrasion. The roughness, Rq value for each of the images are: 0.357 μm, 0.331 μm and 0.321 μm respectively.

137

P4 – 7wt%CB

Surface Stats:

Ra: 0.175 μm

Rq: 0.217 μm

Measurement Info:

Magnification: 10x

Measurement Mode: VSI
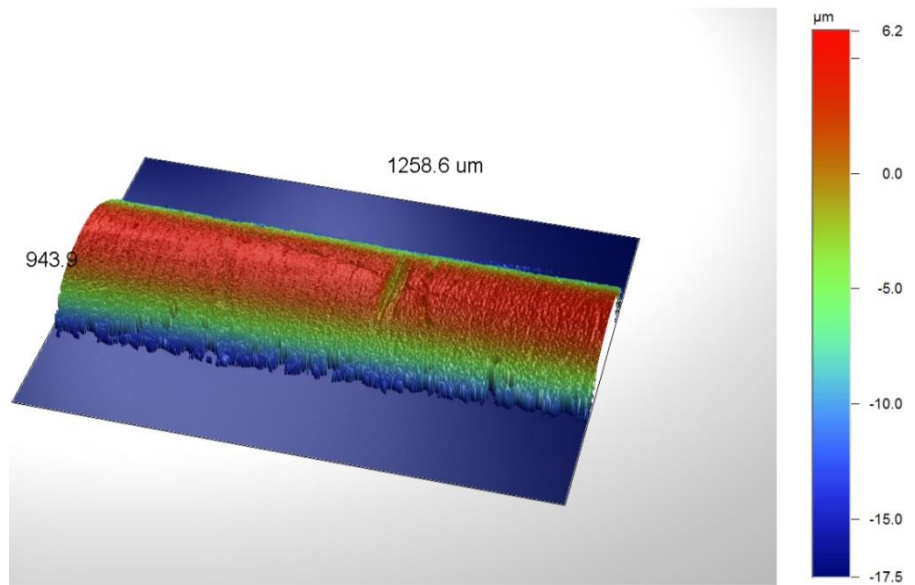
Sampling: 1258.6 μm

Figure 7.19: Three dimensional surface plot of the 7wt%CB content; Ra = 0.175 μm

P5 – 10wt%CB

Surface Stats:

Ra: 0.284 μm

Rq: 0.357 μm

Measurement Info:

Magnification: 10x

Measurement Mode: VSI
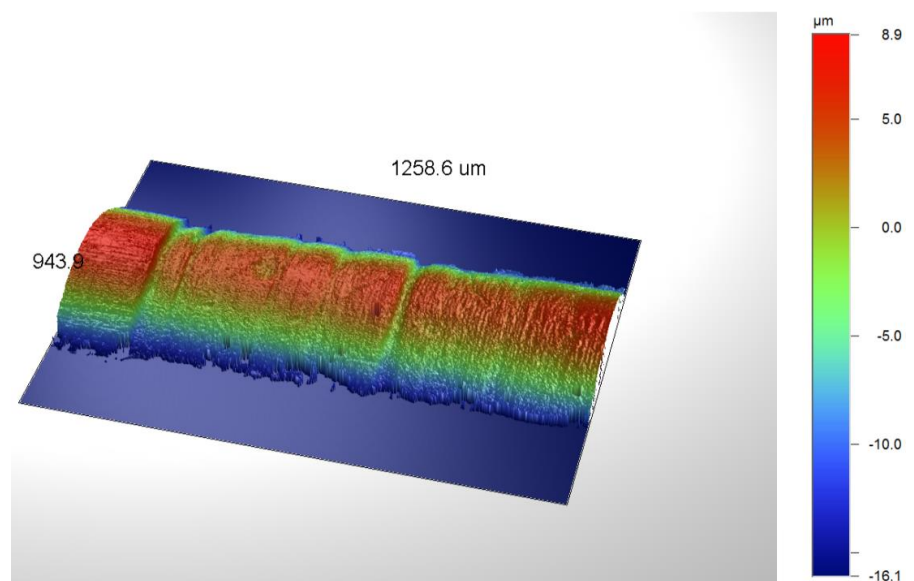
Sampling: 1258.6 μm

Figure 7.20: Three dimensional surface plot of the 10wt%CB content; Ra = 0.284 μm

P$_5$ – 10wt%CB

Surface Stats:

Ra: 0.262 μm

Rq: 0.331 μm

Measurement Info:

Magnification: 10x

Measurement Mode:
VSI
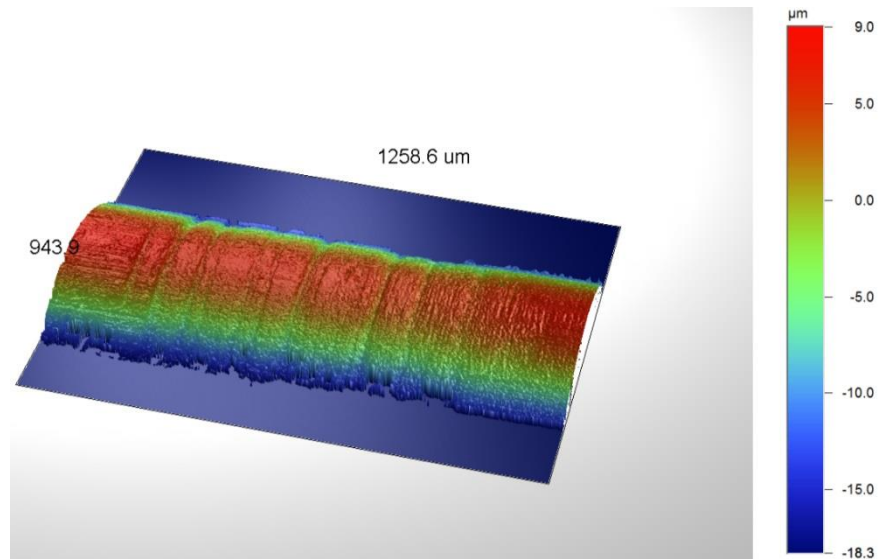
Sampling: 1258.6 μm

Figure 7.21: Three dimensional surface plot of the 10wt%CB content; Ra = 0.262 μm

P$_5$ – 10wt%CB

Surface Stats:

Ra: 0.269 μm

Rq: 0.321 μm

Measurement Info:

Magnification: 10x

Measurement Mode:
VSI

Sampling: 1258.6 μm
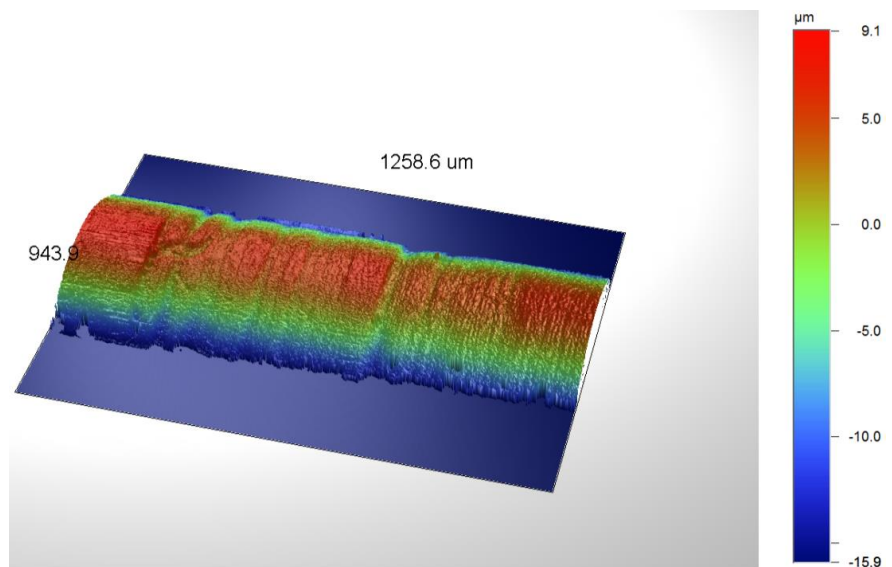
Figure 7.22: Three dimensional surface plot of the 10wt%CB content; Ra = 0.269 μm

The quantified surface roughness of the pin specimens for the pre-test and each of the sooty-oil surrogates were combined to have a summarized comparative view of their values. Figure 7.23 presents the outcome obtained through a plot of the average of three values of the root mean square (rms), Rq of each of the pin specimens.
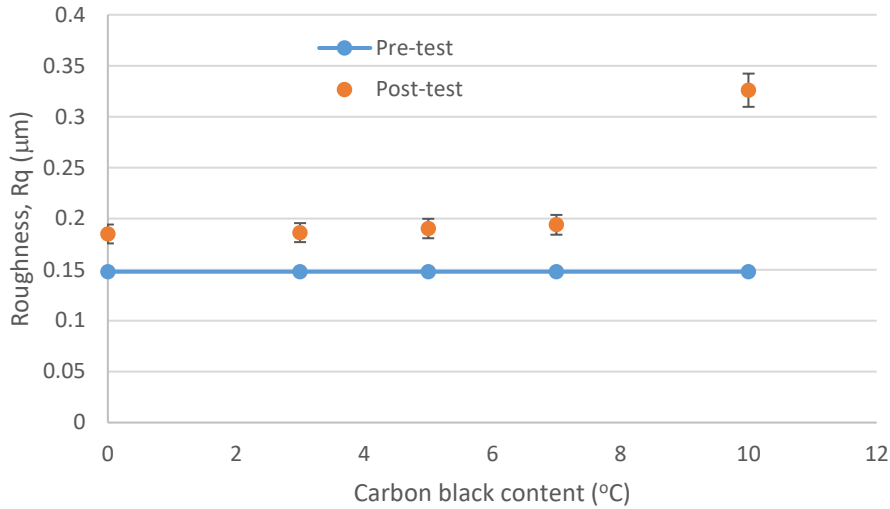
Figure 7.23: The surface roughness, Rq along the pin for various carbon black contents with percentage error bars

The average of three readings of the pin surface roughness profiles were plotted against the distance along the pin for various composition of sooty-oil surrogates, Figure 7.24. The figure is aimed at comparing only the regularity of the surface profiles for various compositions and not the numerical values of the resultant roughness. From the figure, it is obvious that the pre-test and 5wt%CB pins are relatively smoother than the rest. There is some level of deviation with 0wt%CB and 3wt%CB; while higher carbon black content, especially 10wt%CB presents high level of waviness characterised by hills and valleys.
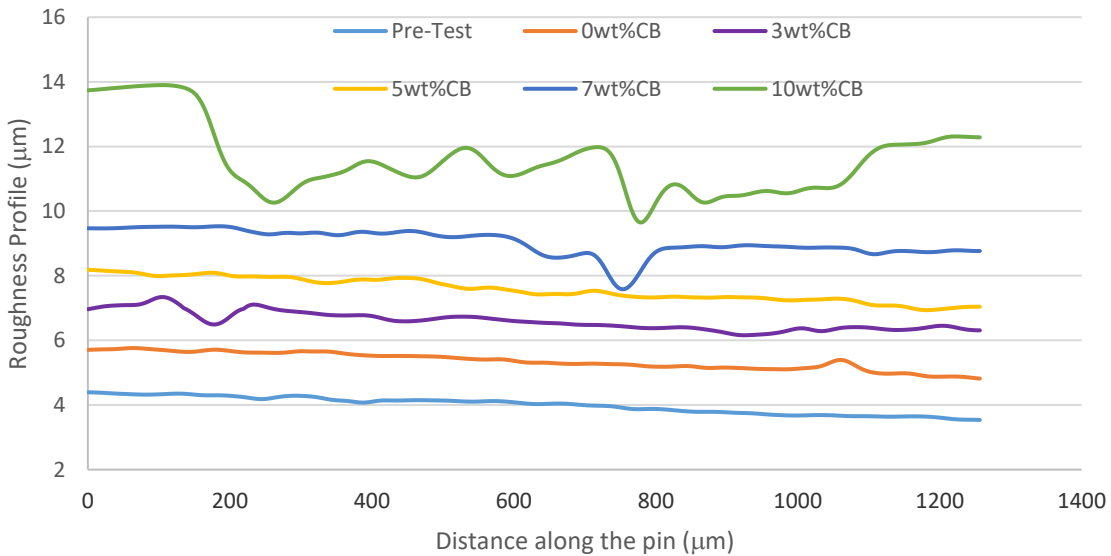
Figure 7.24: The waviness of the pin surface profile for each composition of the lubricant

7.6   Discussion

7.6.1 Contact parameters

It is worth noting that despite the fact that the diameters of the contacting discs in disc-on-disc (25 mm on 50 mm) are about ten times those of pin-in-bush (3 mm in 3 mm), the contact area dimension under a normal load of about 50 N is significantly different for the two contacts. While this is estimated to be 0.163 mm for the pin-in-bush (conformal contact), it is

approximately 0.047 mm for the disc-on-disc (non-conformal contact). This numerical difference in contact area dimension is a clear indication of extent of contacting bodies' surface interaction when operating under different contact conditions.

7.6.2 Post-test recorded masses

The marginal increase in post-test mass recorded for each of the pins may have been caused by embedded carbon black particles. This also indicates that the observed abrasive wear seen in each of the specimen are more of material flow or displacement rather than material removal.

7.6.3 Wear images and wear mechanisms

The non-continuous nature of the observed wear scars along the length of the pin specimen, especially for the moderate carbon black contents (0wt%CB-5wt%CB), may be due to the fact that the clearance between the contacting specimens creates enough space for the lubricant to form a significant film thickness. With the free running tolerance adopted for the contacting pin and bush, the entraining lubricant film is expected to be continuous in the non-contacting regions, thus preventing asperity contact; while contact may occur at point where film thickness is thin or where the carbon black particles assert their presence.

For the uncontaminated oil test, 0wt%CB, the direct contact between the asperities of the pin and bush are prevented by the presence of the lubricant, this minimizes the level of abrasion; hence, the resultant lubricated wear. While, the presence of the carbon black particles may have been responsible for the significant abrasive wear observed at 3wt%CB content. This assertion is further corroborated by more pronounced abrasion with some level of particle embedment observed at 5wt%CB content. The logical explanations for this is that at moderate content levels, the lubricant gets into the contact zone along with the suspended carbon black particles causing some level of abrasive wear in third-body version [187].

The micrographs for higher carbon black contents, 7wt%CB and 10wt%CB, depict severe alteration of the pin surface features in form of scuffing [196]. This, obviously, may be due to the fact that lubricant entrainment into the contact zone is restrained and the minima agglomerates of the carbon blacked-mixed lubricant that gets in are squeezed within the contact and get embedded into the surfaces; causing severe two-body abrasion in form of ploughing. Schematic depiction of the mechanism of ploughing as evident in Figure 7.11(b) is presented below, Figure 7.25. The measured wear groves also matched the reported ranges of carbon black particle sizes.

In spite of the fact that the embedded particle causing the ploughing is a "foreign body", it is still seen as part of the surface into which it is embedded and considered as two-body abrasion [40, 163].
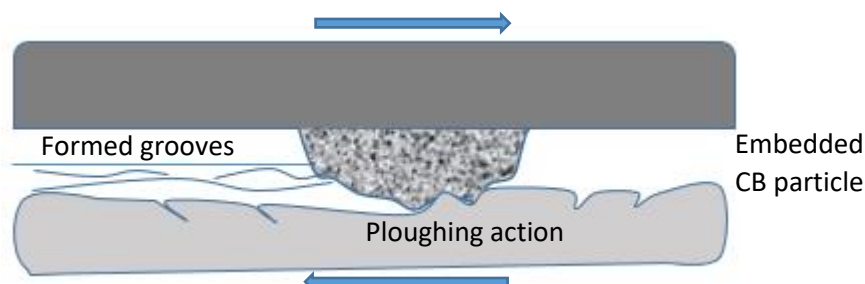
Figure 7.25: Ploughing action by the embedded carbon black particles resulting in groove formation

It appears, particularly for the 10wt%CB content, that the carbon black agglomerates get clogged into some sections along the surface of the pin specimen, causing colossal damages. The carbon black particles affirmed how hard they can be here, Figure 7.13(b), by piercing through the pin specimen surface with traceable wear tracks.

The estimated film thickness values also corroborated the observation as the carbon black particles influenced the amount of wear between the contacting bodies especially at higher contents where the sizes of the agglomerated sooty-oil surrogates, expected to be between 200 and 800 nm [53], which is obviously greater than the maximum film thickness obtainable from the estimations.

7.6.4 Surface profile

ContourGT profilometry achieved dual roles of rendering three-dimensional images and quantifying the surface roughness profile of the pin specimen using the traditional surface metrology parameters, Ra and Rq. The results are indicative of the influence of each lubricant composition on the pin specimens; revealing that while there is increase in the roughness values for all the pin specimens from pre-test value, there is marginal difference for the roughness values for 0wt%-7wt%CB with increment ranging from 25%-30% from the pre-test value. The roughness value for 10wt%CB content was, however, very significant; up to 120% from the pre-test value.

The root mean square (Rq), being a better discriminator for surface deviations, was used as the basis for comparing the pre-test and post-test pin specimen surface roughness values shown in Figure 7.23. Average roughness (Ra) cannot adequately differentiate between large groups of fine asperities and small numbers of severe asperities [197]. This assertion is evidently corroborated with roughness values for 3wt%CB content (Ra = 0.168 μm; Rq = 0.184 μm), Figure 7.17 and 5wt%CB content (Ra = 0.161 μm; Rq = 0.198 μm), Figure 7.18; despite conspicuous difference in their images.

Also, there seems to be noticeable increase in waviness of the pin surface roughness profiles with increasing level of carbon black content; except for 5wt%CB which shows similar pattern with pre-test pin. Ostensibly, due to polishing effects of carbon black at moderate content.

7.7 Conclusions

The conformal contact test, using the designed pin-in-bush rig, was carried out to give a basic understanding on how carbon black, and hence soot content causes wear in conformal contact. In addition, it also serves to simulate chain link articulation under load. The following conclusions can be drawn from this test:

a. The wear mechanism varies from lubricated wear at no contamination to a gradual increase in the level of abrasion with carbon black content. At moderate content (3-5wt%CB), third-body abrasion was observed caused by carbon black particles suspended in the entraining lubricant. At higher content, however, either or both lubricant starvation or/and particle embedment can occur.
b. The surface profile analysis also demonstrates an increasing trend in roughness with carbon black content.

Chapter 8

Automotive Engine Real Component Test (Chain Rig)

This chapter details work on a real engine component test using internal combustion engine (ICE) components, solely isolated, to evaluate the wear effects of soot. This aspect of the research is designed to be multipurpose. Firstly, it is expected to reveal the effects increasing soot contents can have on the wear of the real ICE components; secondly, it serves the purpose of bridging some of the gaps caused by lack of adequate real engine component tests. In addition, the results obtained from one of the components will be compared with a similar component that has undergone several thousand miles in a real engine.

An engine chain drive is generally known to be very sensitive to lubrication contaminants; thus making soot the main catalyst for chain wear through its abrasion of the interface between the chain bushes and pins [101]. The chain drive system was modelled to study the effects of increasing lubricant soot content on the wear of sections of chain and sprocket components of Mercedes Benz M271 engine. The pin-in-bush arrangement used in the last chapter was adapted for this test, with a few modifications. This approach helped a great deal in minimizing the cost and time of building a new rig.

A chain drive is often the most suitable option for timing drive systems because it satisfies many of the durability and lifetime requirements [198], but often at the expense of increasing engine noise. The timing drive system basically comprises the timing chain which transmits, with a constant ratio of 1:2, the rotational motion from engine's crankshaft to the camshaft(s) [199] operating the valves in synchronized manner with the piston strokes. This operation is facilitated by the chain meshing with the sprockets mounted on the crankshaft and camshaft(s).

The timing chain is thus a critical part of an internal combustion engine (ICE) because of the roles it plays in the ignition process. In the timing drive system, a common failure criterion is chain elongation resulting from wear. High chain wear can cause uneven load distribution between the sprocket and chain. Chain-drive system must, therefore, be properly lubricated to prevent sprocket wear, chain elongation and power loss. For automotive timing chains, any of these defects will distort the synchronization process between the crankshaft and camshaft, the effect of which is detrimental to ignition/combustion process. The bushed chain, whose schematic is shown in Figure 8.1, comprises conventional pins, rollers, side plates, links and bushes. It is normally used for transmission applications.
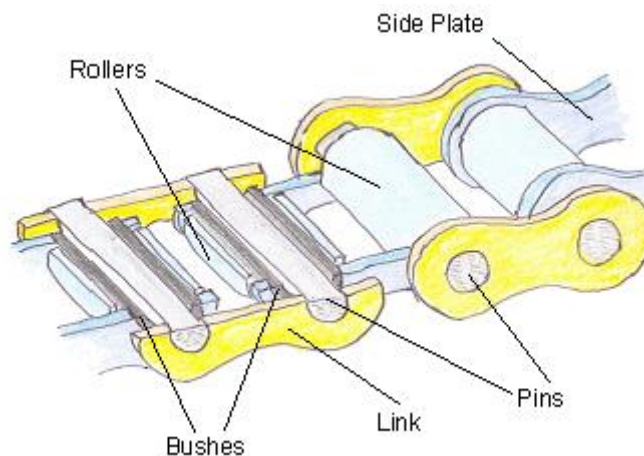
Figure 8.1: Schematics of the bushed chain [113]

The timing-chain operation is usually accompanied by a whining noise due mainly to the meshing impact of the chain with the sprocket [200-202]. The severity of this chain-sprocket meshing impact is dictated by the relative velocity between the chain link and the sprocket tooth at their meshing point and the effective mass of the chain [203]. Ridges are built into sprocket tooth face as part of its surface texturing; these ridges serve as oil pockets ensuring friction reduction [204]. Notably, a chain-sprocket contact is effectively conformal.

The test is aimed at observing the chain-roller and sprocket wear trend with carbon black contents. Various post-test analyses are designed to achieve this.

Some of the advantages of this test are:

i. The ability to solely evaluate the effects of a parameter, soot in this case, which is practically impossible in an internal combustion engine,
ii. Real ICE components are used,
iii. It is easy to control and repeat the tests as desired.

8.1 The chain rig

The chain rig, Figure 8.2, was adapted from the PIB rig with a few modifications to suit the components for the test. It comprises a chain and sprocket arrangement where a section of the chain attached to the oil-bath meshes with a segment of the sprocket held in position by two uprights. Appropriate holes were made on the shaft to align with the pin holes in the sprocket through which screws to tightly hold them together were passed. The chain, on the other hand, is attached to a fixed end within the oil-bath while the other end is adjustable with a tensioner incorporated. This simplifies fitting and removal of the chain specimen for each test. Figure 8.3 presents the pictures of each component as assembled before being coupled to the rig. The oil-bath is driven back and forth by the reciprocating rig, thus oscillating the sprocket which meshes with the chain. There is a flexible coupling, Figure 8.4 (a), between the slider and the oil-bath which ensures self-aligning contact between the chain and the sprocket. The contact between the chain and sprocket, Figure 8.4 (b) was fully submerged in the lubricant. Table 8.1 presents the parameters of the existing reciprocating rig.
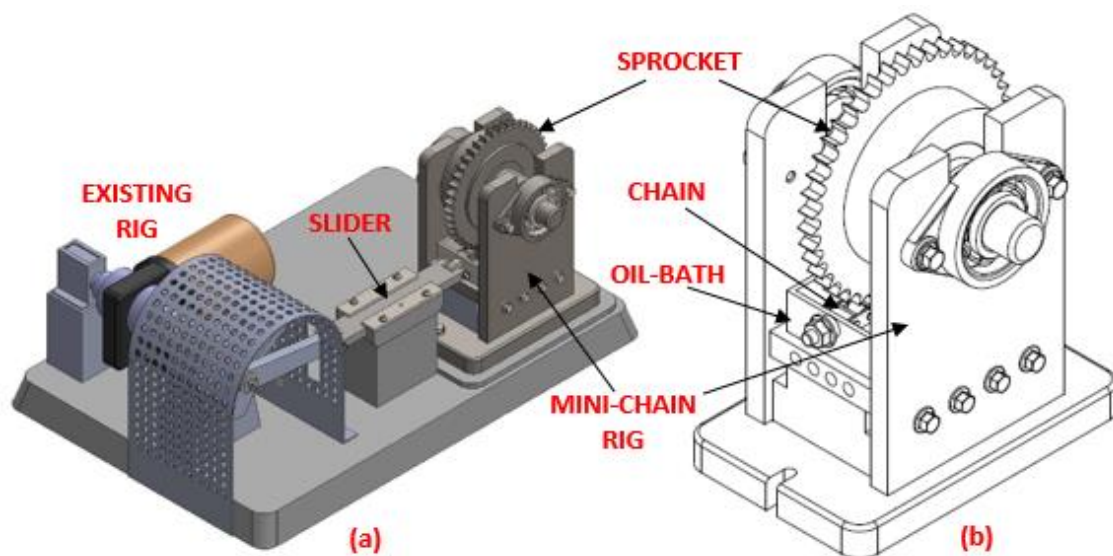
Figure 8.2: Schematic diagrams of chain rig showing the rig (a) connected to the existing rig and (b) standing alone

Table 8.1: Parameters of the existing reciprocating rig

The Parameters of the Existing Reciprocating Rig	
Torque (N-mm)	1422
Motor Speed (rpm)	48
Voltage (V)	240

NB: Torque indicated on the motor is 14.5 Kg-cm = 1422 N-mm
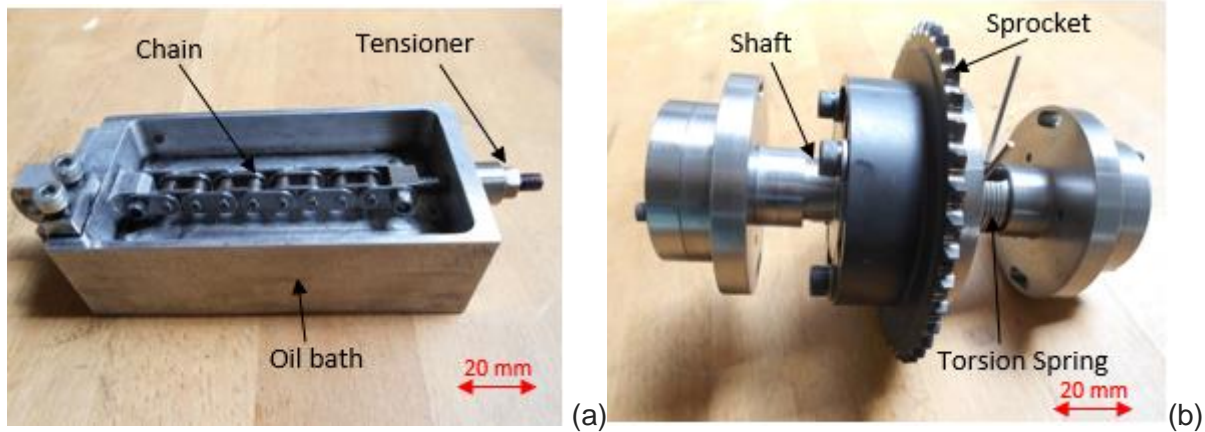
Figure 8.3: The pictures of assembled components (a) chain as positioned in the oil bath and (b) the sprocket as mounted on the shaft
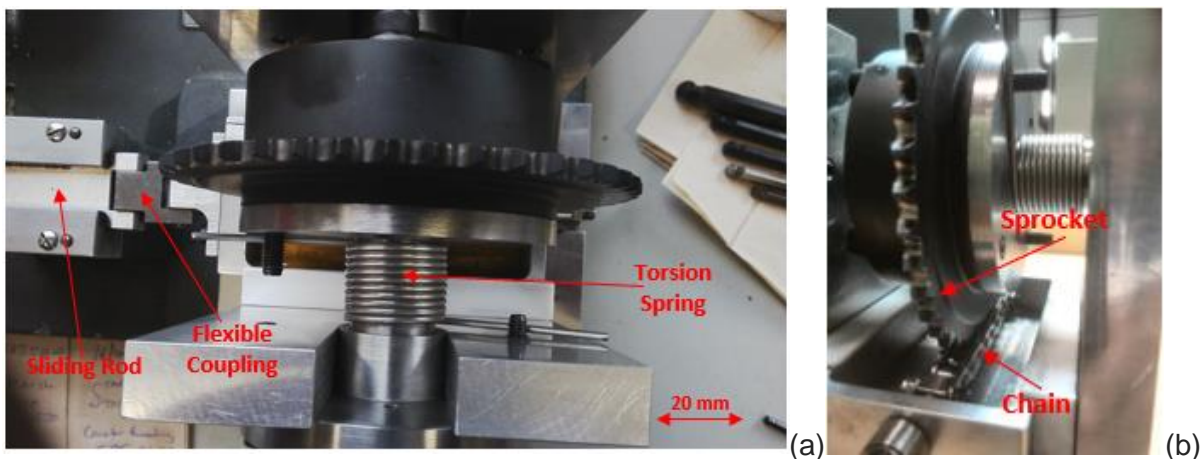
Figure 8.4: (a) Overhead view of the rig showing the sliding rod, flexible coupling and the torsion spring as anchored in the set-up and (b) contact between the chain and the sprocket

The torsion spring was incorporated to resist motion which induces load to the contact; thereby enhancing generation of wear between the contacting components. Two of the screws holding the sprocket to the shaft protruded out to anchor both arms of the torsion spring.

The lubricant is heated with the aid of two cartridge heating elements which are inserted to the base of the oil bath. Detailed specifications of the heating elements are highlighted on Table 8.2; while its schematics are presented in Figures 8.5. A PID (proportional-integral-derivative) controller is used to control and regulate the temperature during the testing; the feedback is through the attached K-type thermocouple wire which is fixedly positioned to sense the temperature of the lubricating oil. It should be mentioned that new set of heating elements and thermocouple were used for this test.

Table 8.2: Specifications of the heating element [205]

Diameter (mm)	8
Inserted Length (mm)	40
Wattage (W)	150
Voltage (V)	220
Type	G
Leads	42" fibre glass leads
Maximum Temperature (^{o}C)	250
Resistance Tolerance (%)	+10 – 5
Wattage Tolerance (%)	+5 – 10
Sheath material	S/S 304
Spirals	Nickel – Chrome
Insulation	Magnesium Oxide – Powder
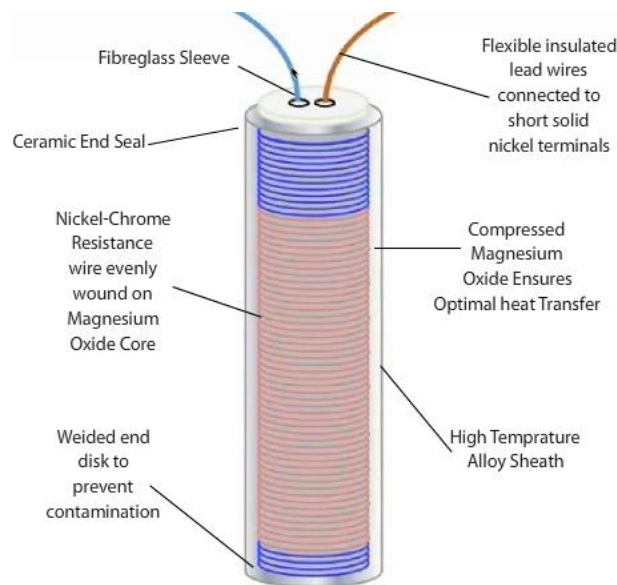
Figure 8.5: The schematics of the heating element [205]

8.1.1 Selection of the torsion spring

To estimate the maximum force, *F*, to be exerted on the sprocket from the motor:

Torque from the motor = 1422 Nmm (from Table 8.1),

The sprocket pitch circular diameter = 111 mm (r = 55.5 mm)

$$T = Fr$$ Equation 8.1

Therefore, $F = \frac{T}{r}$ = 1422 Nmm/55.5 mm = 25.6 N

The average timing chain load is between 1,500 N to 2,000 N at 4000 rpm engine speed [125]; 25 N, is therefore, proportionately appropriate for 51.5 rpm rig.

The requirement now is to design appropriate torsion spring, fixed at longer arm of the shaft, to resist the oscillatory motion of the sprocket with a resisting force of, at least, 30N.

To translate the torque values to the direct load,

$$P = \frac{T}{R}$$
<div align="right">Equation 8.2</div>

where:

P is the Load applied at Radius ("R")

T is the Torque

R is the half the leg length, in all cases (½ L)

For the selected torsion spring, therefore:

P = 970.502 Nmm/25.4 mm = 38.21 N

This implies that the torsion spring can safely resist the force being transmitted to the sprocket from the motor.

Table 8.3 highlights the specifications of the selected torsion spring, while Figure 8.6 shows its pictorial and schematics views.

<div align="center">Table 8.3: Specifications of the torsion spring [206]</div>

Outside diameter (mm)	25.019
Wire diameter (mm)	1.904
Free positions of Ends (°)	360.000
Torque (Nmm)	970.502
Radius (mm)	25.400
Length of leg (mm)	50.800
Body Length (mm)	22.352
Total Coils	10.5
Material	SS (Type 302 Stainless Steel)
Finish	Passive per ASTM A967
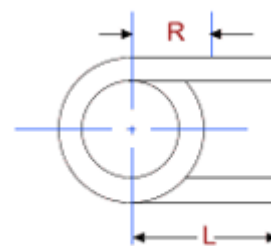
(a)   360° Deflection   (b)

Figure 8.6: Torsion spring views: (a) pictorial and (b) schematics

8.1.2 Calibration and alignment of the chain test rig

The speed rating on the electric motor driving the existing rig is 48 rpm. The calibration of the chain test rig was therefore necessary to determine its actual speed in rpm; and this was achieved through a painstaking measurements carried out for several tests using the counter connected to the output shaft, Figure 8.7. These measurements yielded an average of 3088 rotations for every hour. This implies the actually delivered speed is 51.5 revolutions per minute. This is because the electric motor is not directly connected to the slider-crank mechanism, but rather its motion is transmitted through a pair of bevel gear arrangement. The alignment of the connection between the existing rig and the chain rig was ensured through a

flexible coupling, shown in Figure 8.4 (a), which links the slider and the oil-bath; this arrangement also ensures self-aligning contact between the chain and the sprocket.

It must be pointed out that the reciprocating motion does not necessarily represent the actual application in the real engine where the motion is unidirectional. Both flanks of the sprocket teeth experience about the same load impact and hence wear occurrence in this chain test rig; while in the real engine, there is significant difference in the level of wear between the active and non-active flanks on the sprocket teeth.
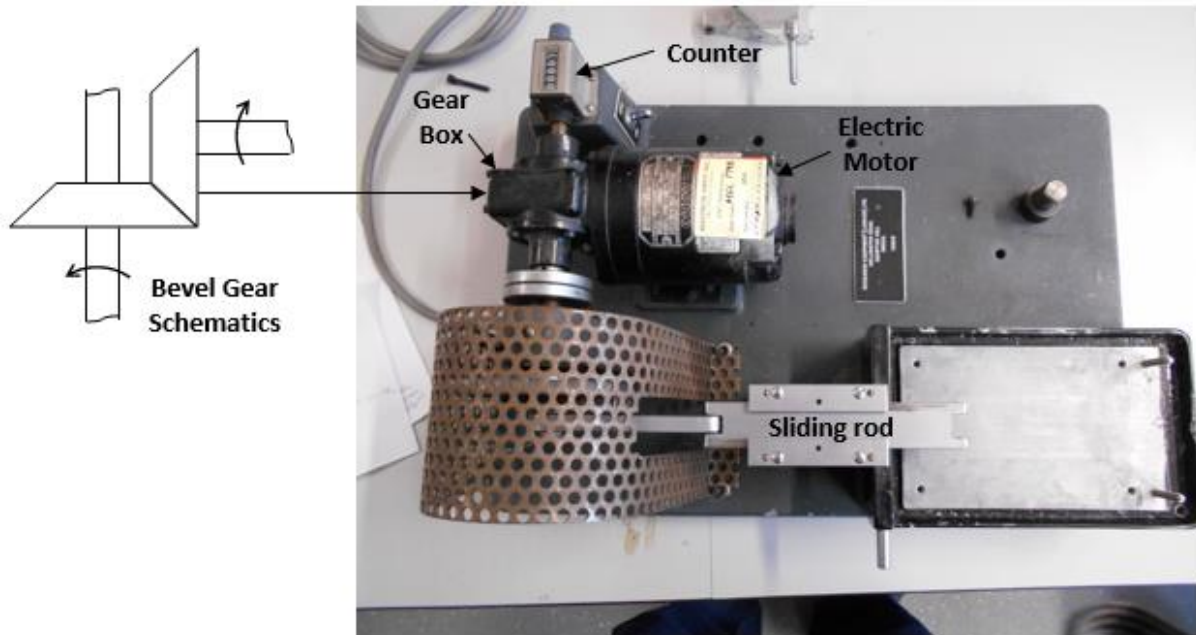
Figure 8.7: Top view of the reciprocating rig showing the electric motor and the gear box with the output shaft connected to the counter

8.2   Test specimens

The specimens used for this test are timing chain and sprocket components of Mercedes Benz M271 engine. The engine, which is a single-stage cam drive system with a 6.35 mm pitch silent chain, was designed to facilitate engine compactness in terms of size and weight. Other advantages of this design are reduced noise and less friction in the system. Wear elongation is, however, the main drawback of silent chain [207]. The sprocket consisted of 44 teeth (pitch circle diameter of 111 mm) and the chain full length is approximately 1135 mm comprising 71 links; for each test, however, only a segment of the sprocket can be in contact with a specified length of the chain. Two opposing segments ($\cong 180°$ apart) of each sprocket are appropriately marked for 12-hour and 24-hour tests, allowing a sprocket to be used for both tests. With this, the chain specimen was replaced after a test while the sprocket is just turned through an angle of 180°. Each test has a chain length of 80 mm (5 links) and a sprocket segment of 6 teeth. Figure 8.8 shows the pictorial view of the components with a mark on the sprocket indicating a segment for 24-hour test.
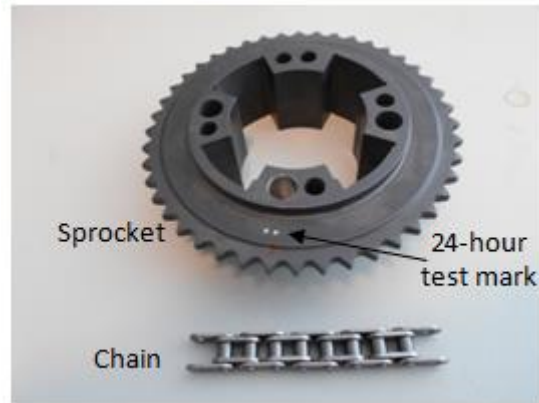
Figure 8.8: Pictorial view of the chain and sprocket (with a segment marked for 24-hour test) components

8.3 Experimental procedures

The components were thoroughly cleaned with acetone and dried, after which the chain was attached to the oil-bath and the sprocket mounted on the shaft, as shown in Figure 8.3, before being assembled with other parts of the rig and finally coupled to the existing rig. Each lubricant composition was shaken thoroughly before being carefully poured into the oil-bath, fully submerging the contact between the chain and sprocket; this takes approximately 25ml of the lubricant.

The same procedure was repeated for each test under similar conditions. Each lubricant was tested for two varying times, that is, 12 hours and 24 hours; approximately equivalent to 0.371 km and 0.742 km respectively (see section 8.3.1 for details). At the end of each test, both components were removed, cleaned with acetone, dried and stored for post-test analysis.

The PID controller was programmed to ramp from room temperature to 100°C and retained that temperature for 420 minutes (6 hours/day). The operating temperature was monitored through the attached thermocouple. An approximate time of 20-30 minutes was allowed for the temperature to stabilize before the commencement of each test. Figure 8.9 shows two views of the experimental set-up of the mini-chain rig with the PID accessories and heating elements connections. The summary of the test conditions are given in Table 8.4, while Table 8.5 presents the test plan.

Before the commencement of the test, each of the chain specimen assigned to each lubricant composition was weighed using the weighing balance, Sartorius Electronic Analytical Balance (Basic[Plus] BP210D); the average of this for the six chain specimens were recorded for comparison with the post-test measurement. At the end of the test, they were gently rinsed in acetone without wiping or sonication to prevent dislodgement of any carbon black particle that might have been embedded during the test [114]. The specimens were then delinked using a chain pin extractor to separate the chain rollers for post-test analysis.

149
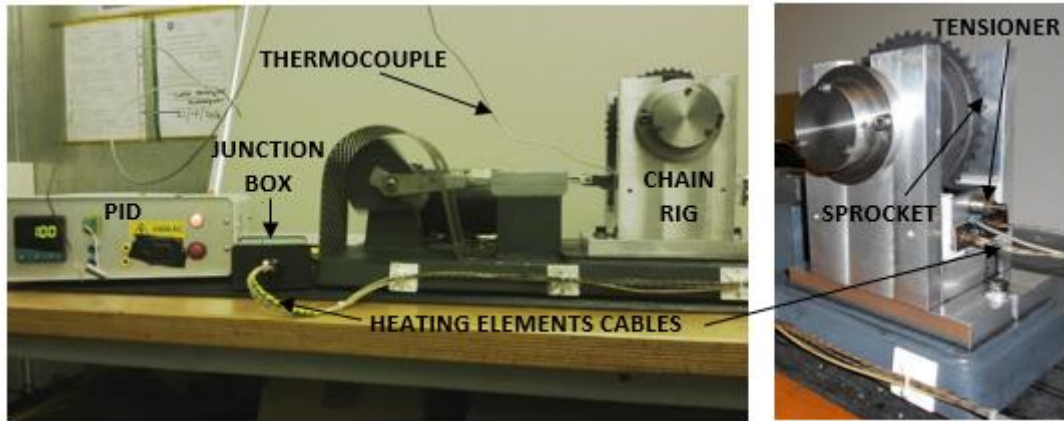
Figure 8.9: The experimental set-up showing the mini-chain rig with PID instrumentations

Table 8.4: Test conditions for chain-rig test

Parameter	Value
Lubricant	Sooty-oil surrogates (0wt% - 12wt%)
Lubricant quantity (ml)	$\cong 25$
Lubricant temperature (°C)	100±1
Reciprocating frequency (Hz)	0.86
Rotation (rpm)	51.5
Stroke length (mm)	8
Linear speed (m/s)	0.0137
Test duration (hours)	12 and 24
No of Cycles	37080 and 74160

Table 8.5: Chain-rig test plan

Test	12-hour	24-hour
C1 – 0wt%CB	C1-1	C1-2
C2 – 3wt%CB	C2-1	C2-2
C3 – 5wt%CB	C3-1	C3-2
C4 – 7wt%CB	C4-1	C4-2
C5 – 10wt%CB	C5-1	C5-2
C6 – 12wt%CB	C6-1	C6-2

8.3.1 Determination of the distance covered

The calibration of the chain test rig, as discussed earlier (section 8.1.2), indicated that the actually speed of the chain rig is 51.5 revolutions per minute. For every complete revolution of the prime mover, the slider moves 8x2 mm and the sprocket oscillates through a distance of approximately 5x2 mm.

Therefore, for every 12-hour test, the sprocket moves through an approximate distance of 10 mm x 51.5 x 60 x 12 = 370,800 mm. This implies a 24-hour test covers a distance of 0.742 km. Though, this may be a relatively short distance in the real world; but looking at it from laboratory-test point of view where it took three days (at 8-hour/day) to cover this, it is quite a long distance.

8.4   Results

The results are basically the post-test analysis of the sprocket and chain specimens from various carbon black compositions. While six images of chain rollers were taken for pre-test and used chain from 'L' vehicle, four images of the rollers from the central portion of the chain and corresponding teeth from the sprocket were taken for various carbon black compositions.

8.4.1   Pre-test and post-test recorded masses of the chain specimen

Sartorius BP 210 D precision scale was used to measure the masses of the chain specimens assigned to sooty-oil surrogates prior to the commencement of the test and the average of these masses were recorded; this was repeated for the two testing times, 12-hour and 24-hour, at the end of the tests. The results are presented in Figure 8.10. The result shows a progressive decrease in masses with increasing carbon black content and marginal decrease with longer time of test within same content.

8.4.2   Diameter of the chain rollers

The diameter of all the rollers (pre-test, used and from each carbon black content tests) were taken using a pair of Moore and Wright Digitronic Vernier callipers. The average of six measurements was recorded for pre-test and used samples, while the average of four measurements was computed for each of the carbon black contents. The results are presented in Figure 8.11.

	0wt%CB	3wt%CB	5wt%CB	7wt%CB	10wt%CB	12wt%CB
12-hour	22.772	21.967	21.656	21.296	20.872	20.574
24-hour	22.568	21.764	21.312	20.974	20.581	20.452
Pre-test	23.353	23.353	23.353	23.353	23.353	23.353
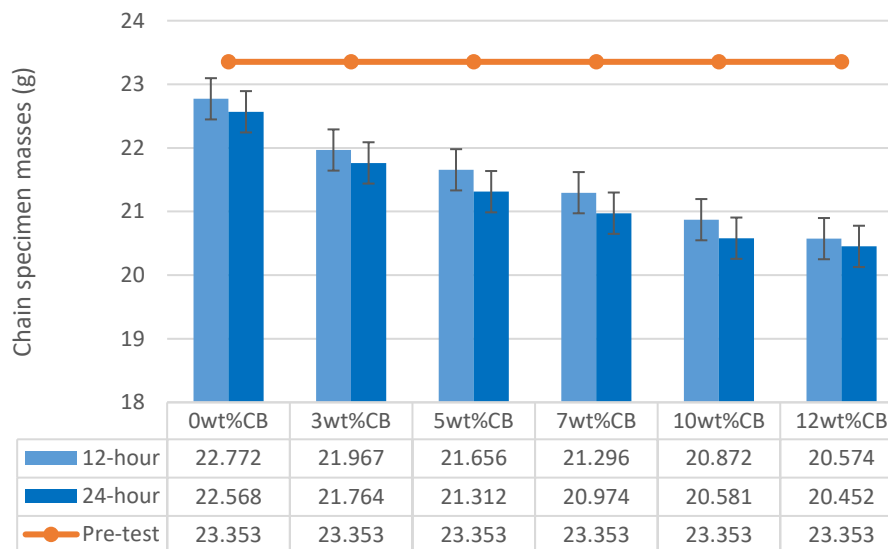
Figure 8.10: Pre-test and post-test masses of the chain specimen with standard error bars

	0wt%CB	3wt%CB	5wt%CB	7wt%CB	10wt%CB	12wt%CB
12-hour	4.90	4.86	4.85	4.85	4.84	4.83
24-hour	4.89	4.85	4.84	4.84	4.83	4.82
Pre-test	4.91	4.91	4.91	4.91	4.91	4.91
Used	4.82	4.82	4.82	4.82	4.82	4.82

Figure 8.11: Average diameter of the chain roller for the used chain, pre-test and various carbon black contents with standard error bars

The value of chain roller diameter ranges between 4.90 to 4.92 mm for the pre-test rollers while it ranges between 4.76 to 4.86 mm for the used rollers. This indicates a significant reduction in the diameter of the used rollers which is not unconnected with the fact that they would have undergone varying levels of abrasion while in operation.

8.4.3 Scanning electron microscope (SEM) images

Photomicrographs of the chain rollers were also obtained using the Scanning Electron Microscope (Hitachi TM3030Plus Tabletop SEM). Figures 8.12(a), (b) and (c) show the images obtained for pre-test, 0wt%CB 12-hour test and 0wt%CB 24-hour test respectively. There is obvious difference between the 12-hour test and 24-hour test with the latter leaving some scratching impression on the roller surface. For the 3wt%CB content test, one can see the abrasive wear marks left on the roller surface by the carbon particles, Figure 8.13(a), these marks are, however, less conspicuous for the 24-hour test, Figure 8.13(b) and (c).
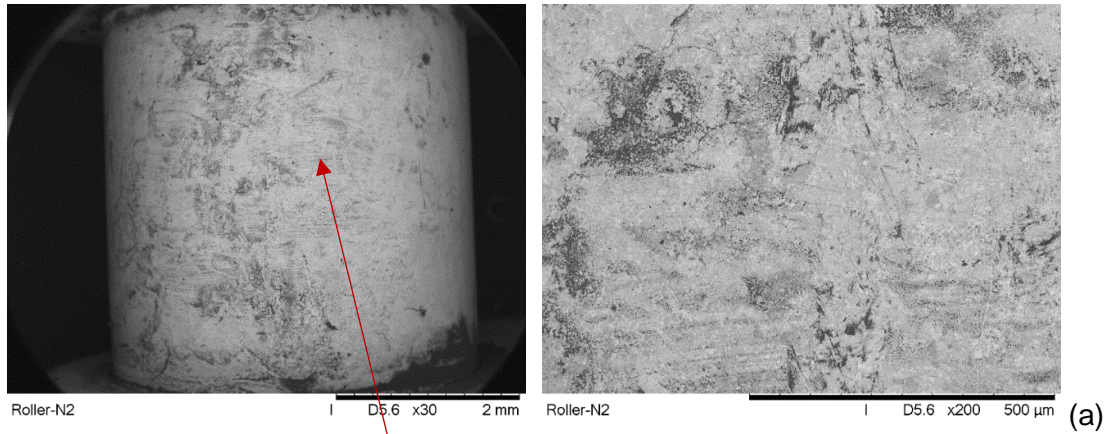
No significant difference between pre-test and 12-hour test with no CB
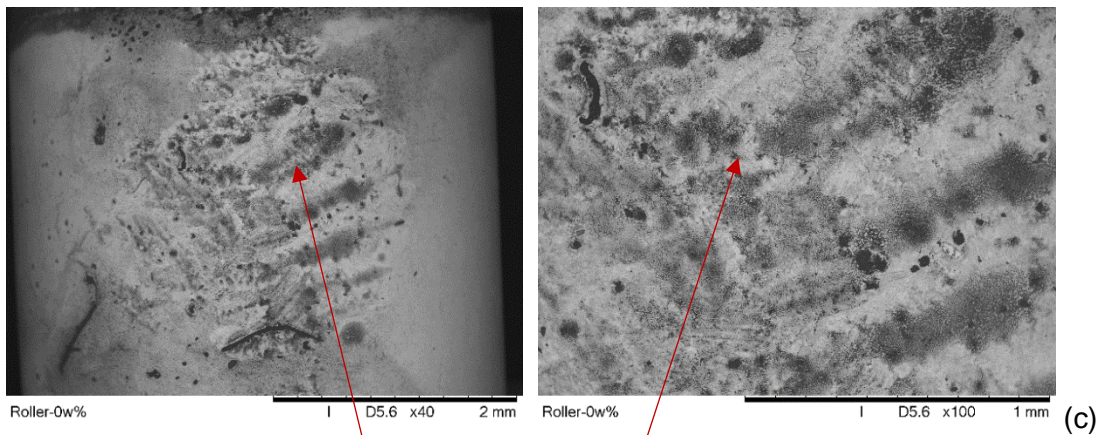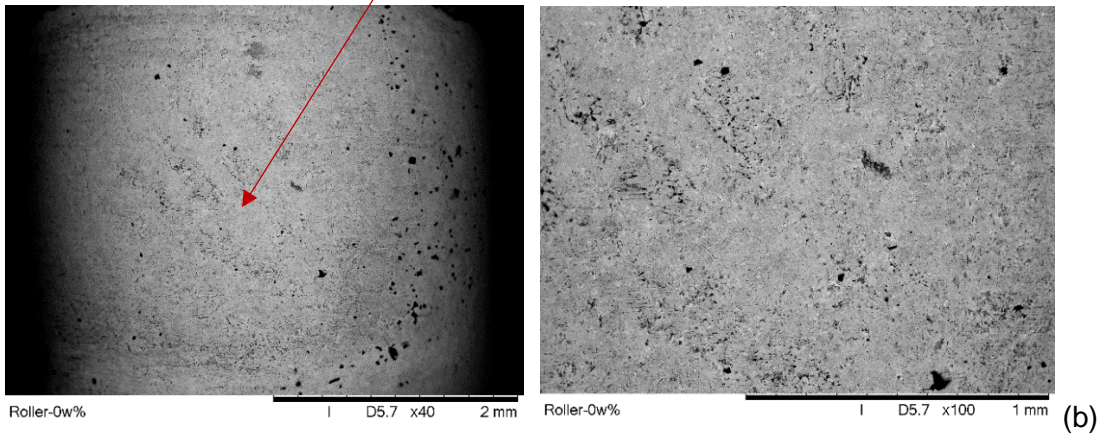
24-hour test with 0wt%CB leaving some scratching impressions on the roller surface

Figure 8.12: Photomicrographs of the chain roller specimen (a) pre-test, (b) 0wt%CB content 12-hour test and (c) 0wt%CB content 24-hour test

Sliding marks left on the roller surface by the carbon black particles
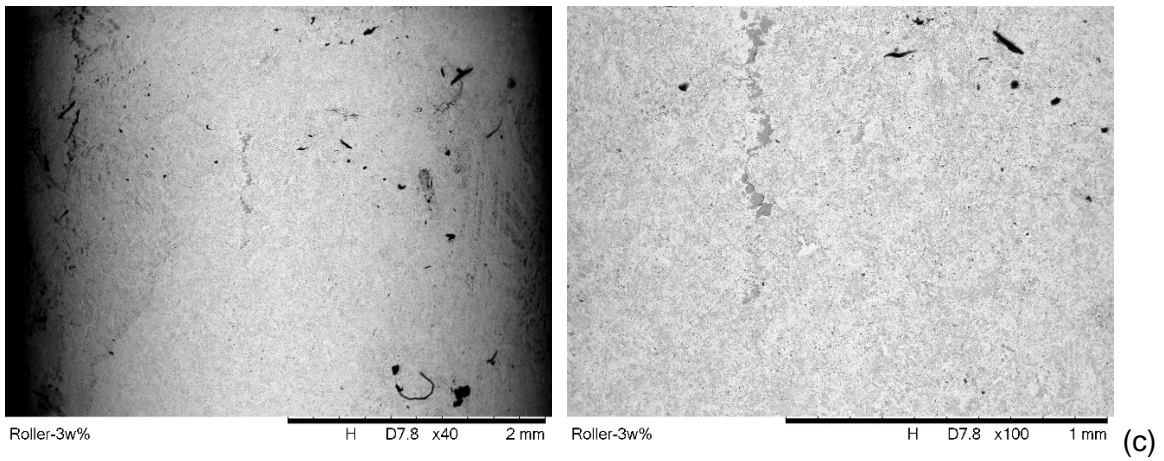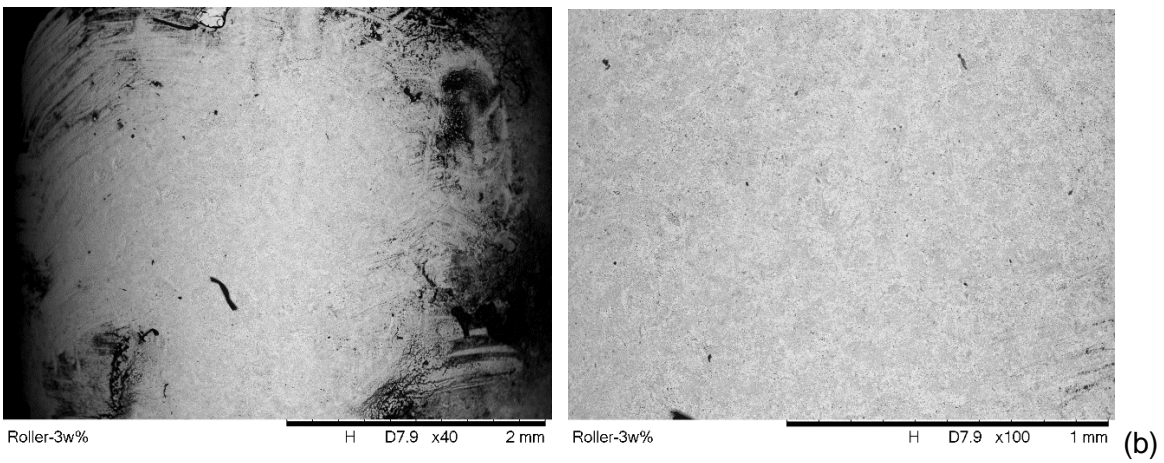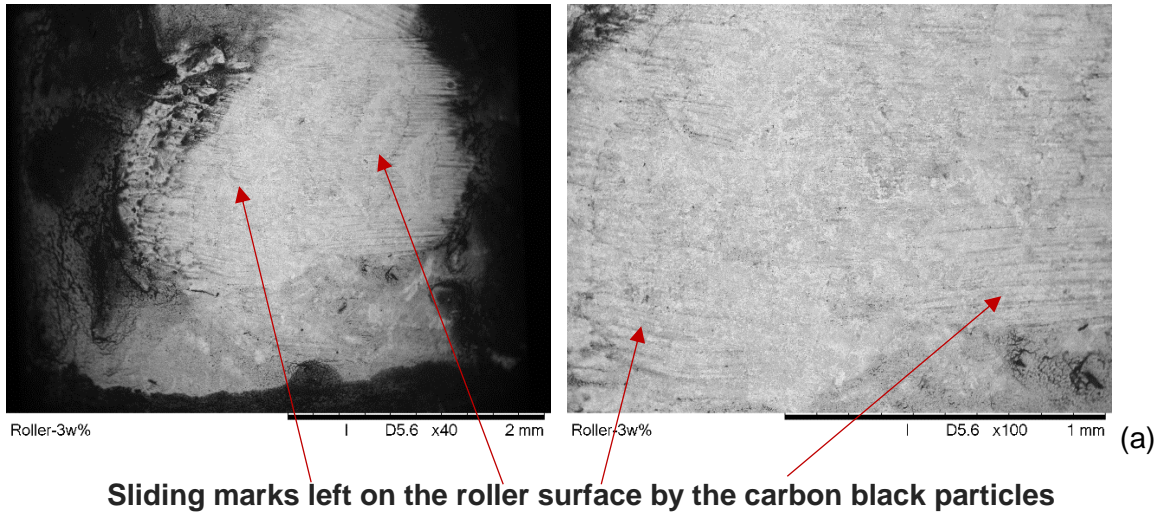
Figure 8.13: Photomicrographs of the chain roller specimen (a) 3wt%CB content 12-hour, (b) 3wt%CB content 24-hour test and (c) 3wt%CB content 24-hour test

Similar marks with patches of black dots can be seen on the roller surface for 12-hour 5wt%CB content, Figure 8.14(a); while the marks eventually faded away for 24-hour test, the black patches were still visible, Figure 8.14(b). The presence of the black patches can therefore be seen as an indication of higher carbon content.

Abrasive wear marks left on the roller surface by the carbon black particles

Patches of black dots
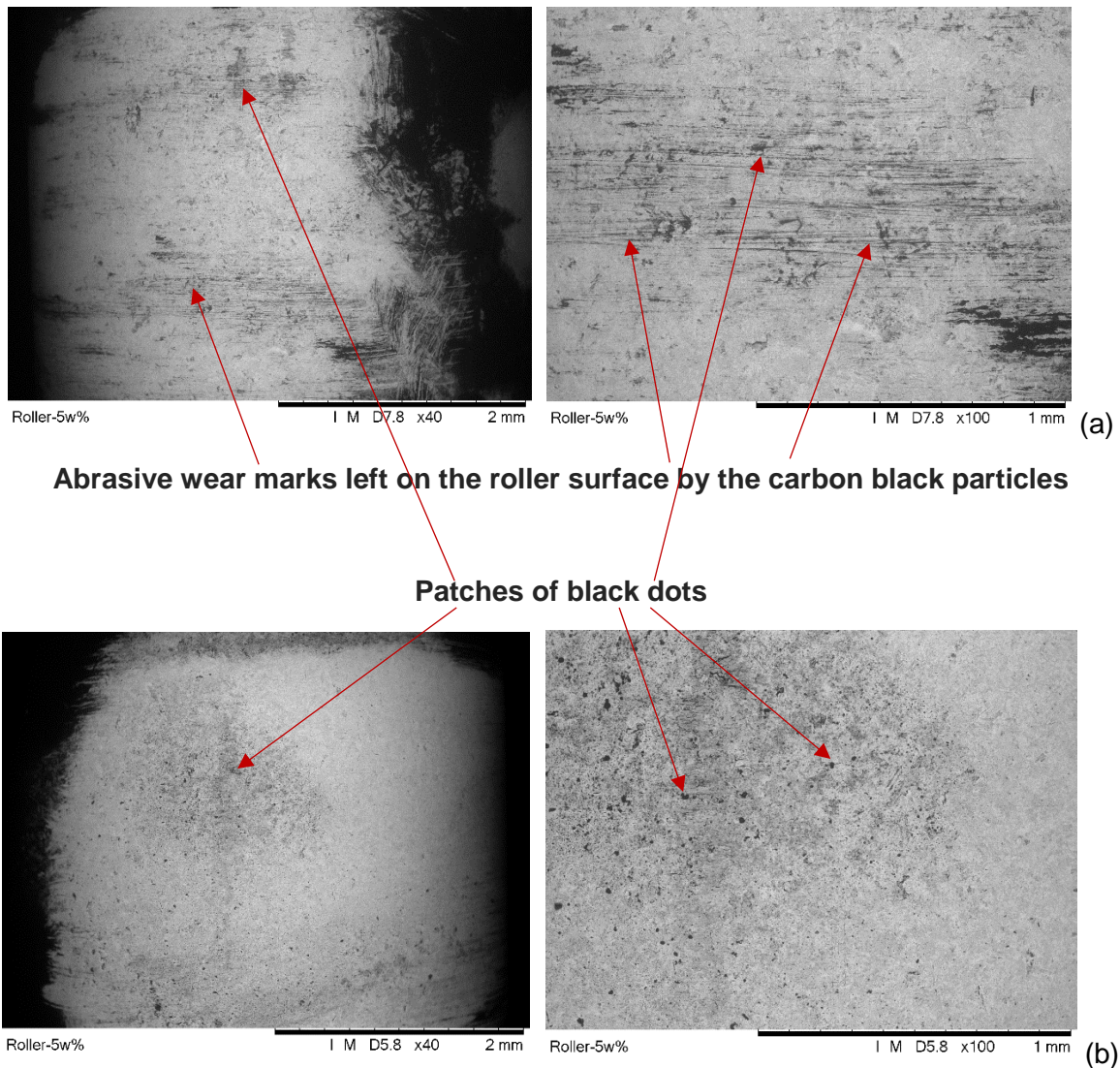
Figure 8.14: Photomicrographs of the chain roller specimen (a) 5wt%CB content 12-hour and (b) 5wt%CB content 24-hour test

Figure 8.15 presents the images of the roller surfaces for 7wt%CB content. Patches of embedded carbon black particles can be seen on the roller surface which sizes are indicated on the enlarged image, Figure 8.15(b). Figure 8.16(a) shows the photomicrographs for 12-hour 10wt%CB content with ploughing on the roller surface emanating from the impact stresses which are induced by the meshing impact between the chain and the sprocket; Figure 8.16(b) is the enlarged image showing the clusters of carbon black particles. Figure 8.17 presents the images obtained from 24-hour test for the same composition, that is, 10wt%CB content with Figure 8.17(b) showing the clusters of carbon black particles in an the enlarged image.

For 12wt%CB content, Figure 8.18 and Figure 8.19 present the photomicrographs for 12-hour and 24-hour tests respectively; each of the figures is accompanied with corresponding enlarged images to show the embedded carbon black particles with varying dimensions.
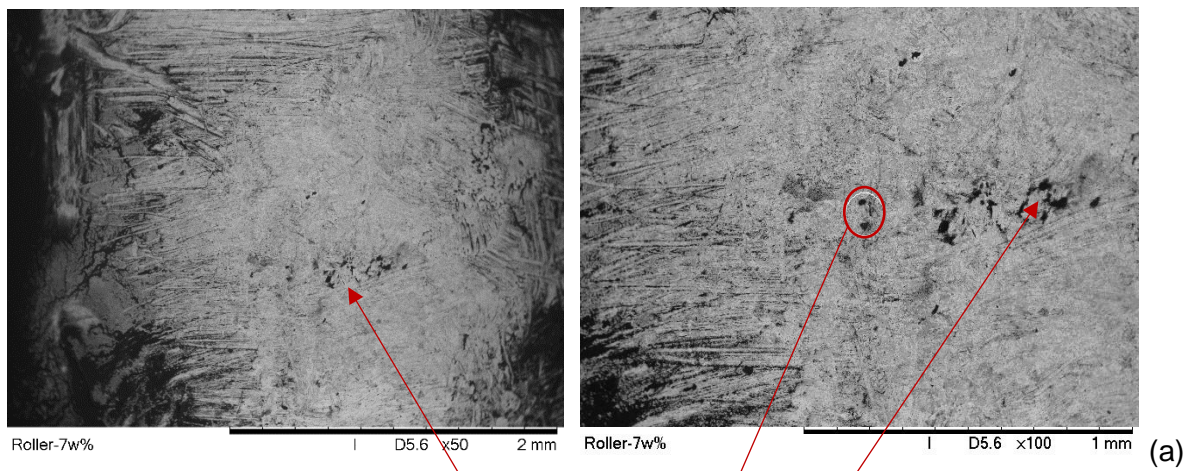
Embedded carbon black particles on the chain roller surface
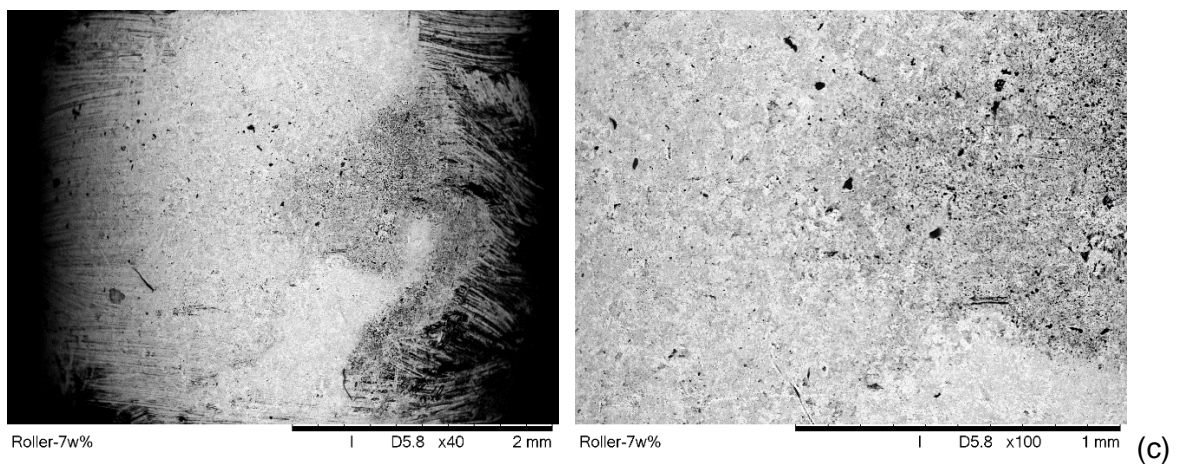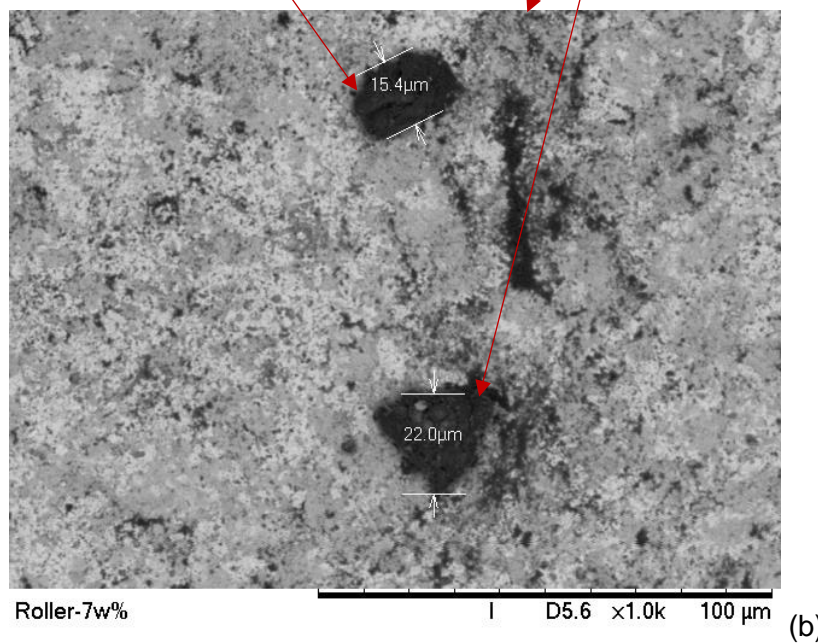
Figure 8.15: Photomicrographs of the chain roller specimen (a) 7wt%CB content 12-hour, (b) enlarged image (x1000) showing the trapped carbon black particle (with sizes) on the roller surface and (c) 7wt%CB content 24-hour test

156

Ploughing due to the effect of impact stresses
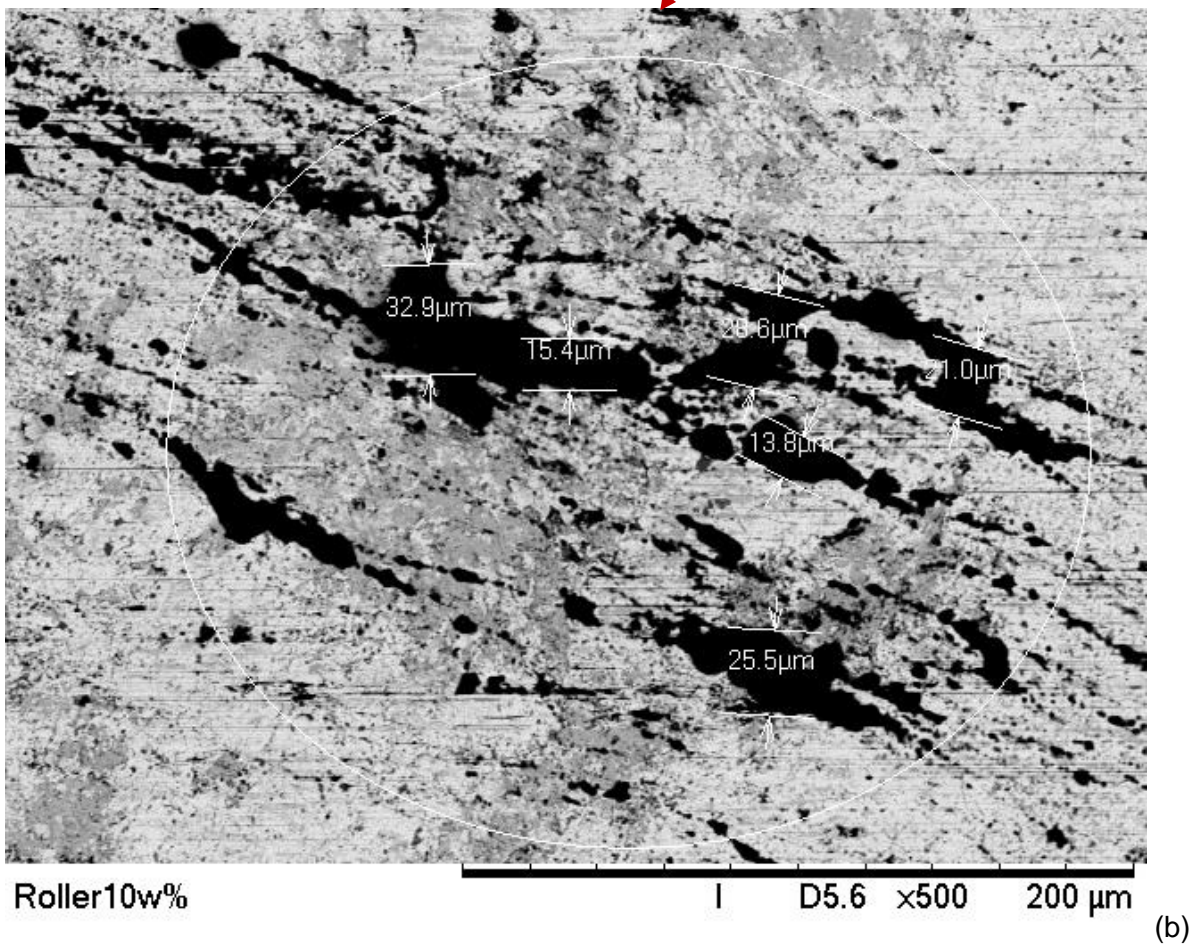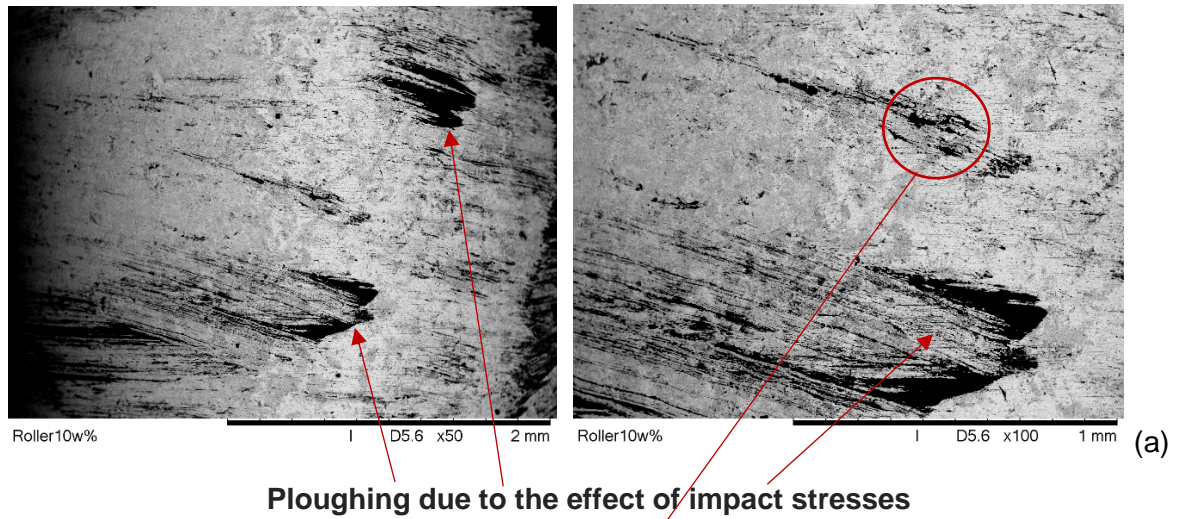
Figure 8.16: Photomicrographs of the chain roller specimen (a) 10wt%CB content 12-hour (b) enlarged image (x500) showing clusters of carbon black particle on the roller surface
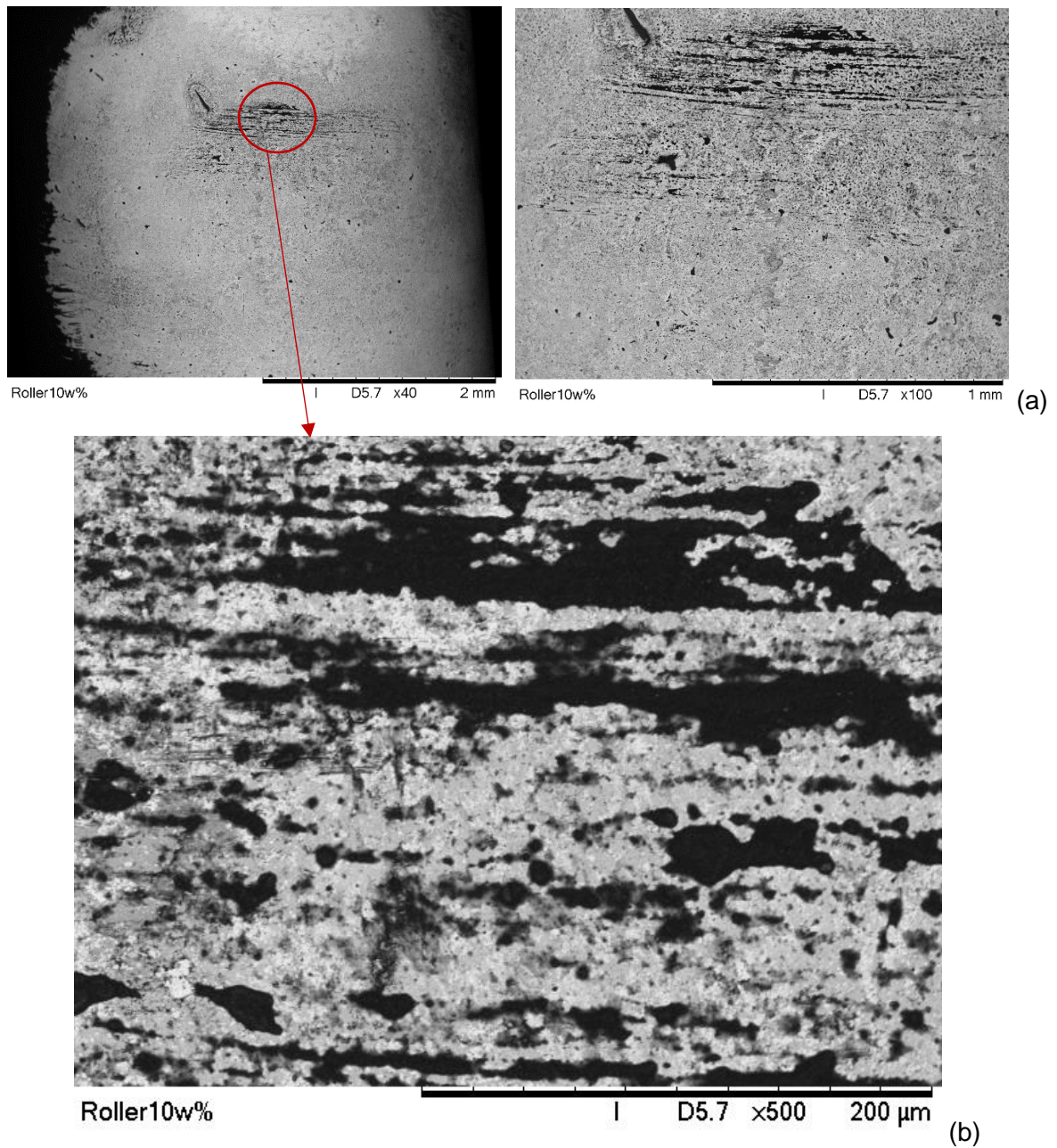
Figure 8.17: Photomicrographs of the chain roller specimen (a) 10wt%CB content 24-hour (b) enlarged image (x500) showing clusters of carbon black particle on the roller surface
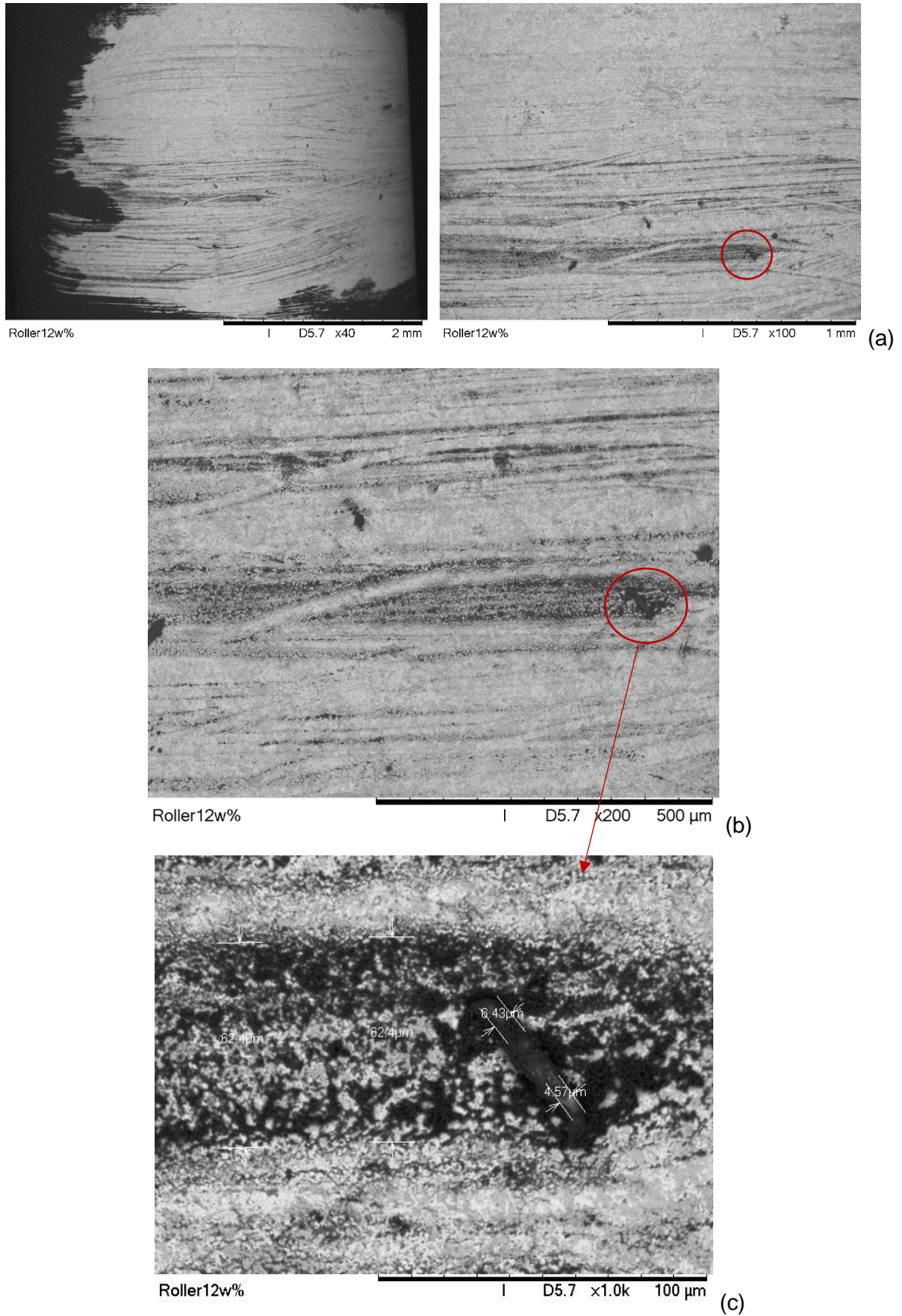
Figure 8.18: Photomicrographs of the chain roller specimen (a) 12wt%CB content for 12-hour test (b & c) enlarged image (x200 & x1000) showing clusters of carbon black particle on the roller surface
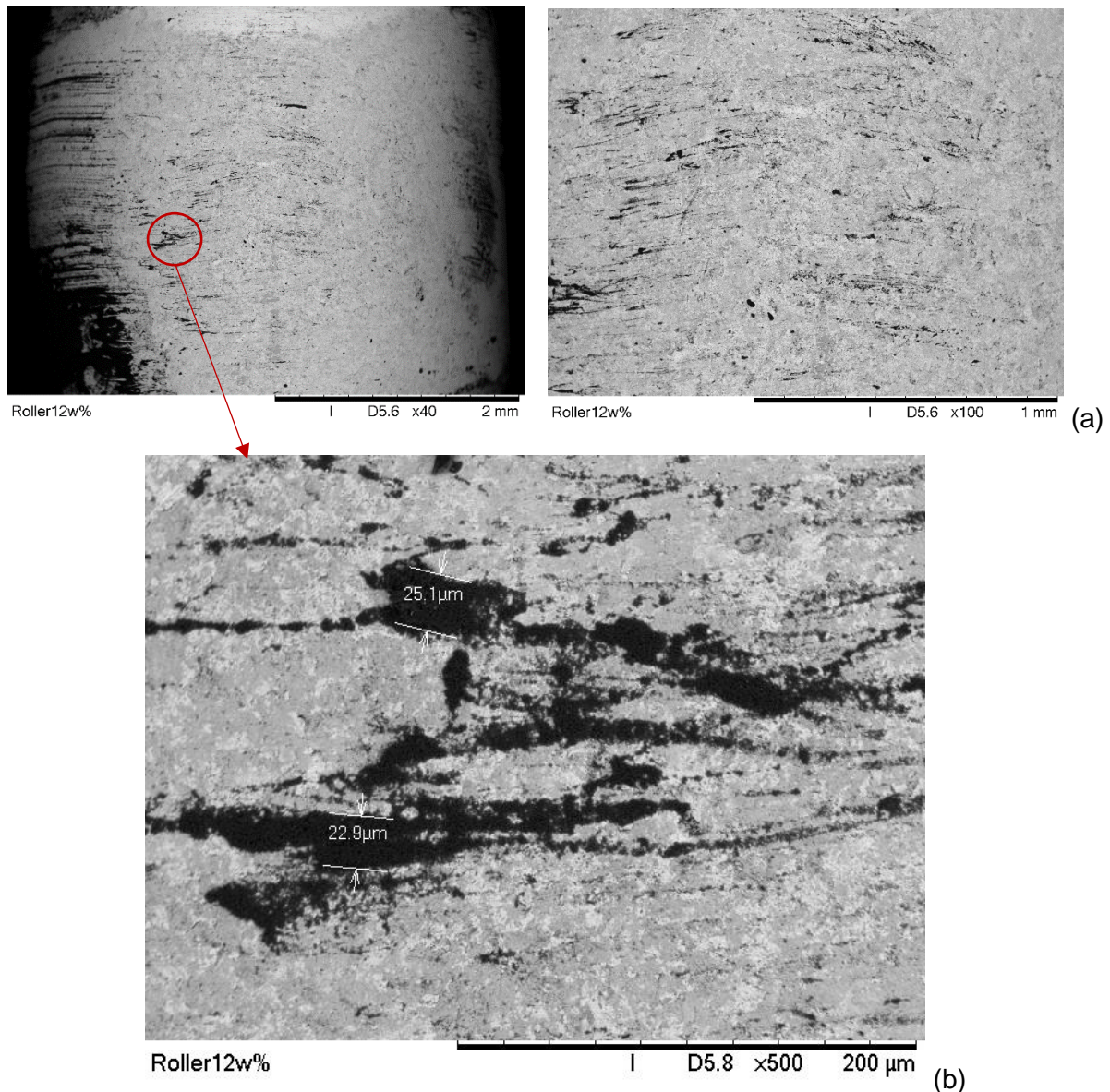
Figure 8.19: Photomicrographs of the chain roller specimen (a) 12wt%CB content for 24-hour test (b) enlarged image (x500) showing clusters of carbon black particle on the roller surface

8.4.4 Alicona-optical metrology

Alicona InfiniteFocusSL, manufactured by Alicona Imaging Inc., Austria and supplied by Optimax, was used to quantify and evaluate the surface damage resulting from carbon black effects through the acquisition of two-dimensional and three-dimensional images of the chain rollers and sprocket teeth. This instrument also measures the roughness profile along with the form of the specimens. Other advantages of this instrument are presentation of the obtained images in their natural colour and indication of the line along which the roughness values been presented are measured.

8.4.4.1 Three-dimensional images of the sprocket teeth

Three-dimensional images were acquired for the sprocket teeth before the test and afterwards. Figure 8.20 presents selected 3D images of the sprocket specimen teeth for the pre-test and 24-hour test for various carbon black compositions. The pre-test image, Figure 8.20(a) shows the presence of the ridges which were intended to trap the lubricant [113] and carry it along

160

as the sprocket rotates and comes into contact with the chain. The ridges are incorporated as part of surface texturing to derive from their tribological benefits in terms of friction reduction, particularly in a conformal contact [204]. The vividness of these ridges gradually fades out with an increase in carbon black content and prolonged time of test.
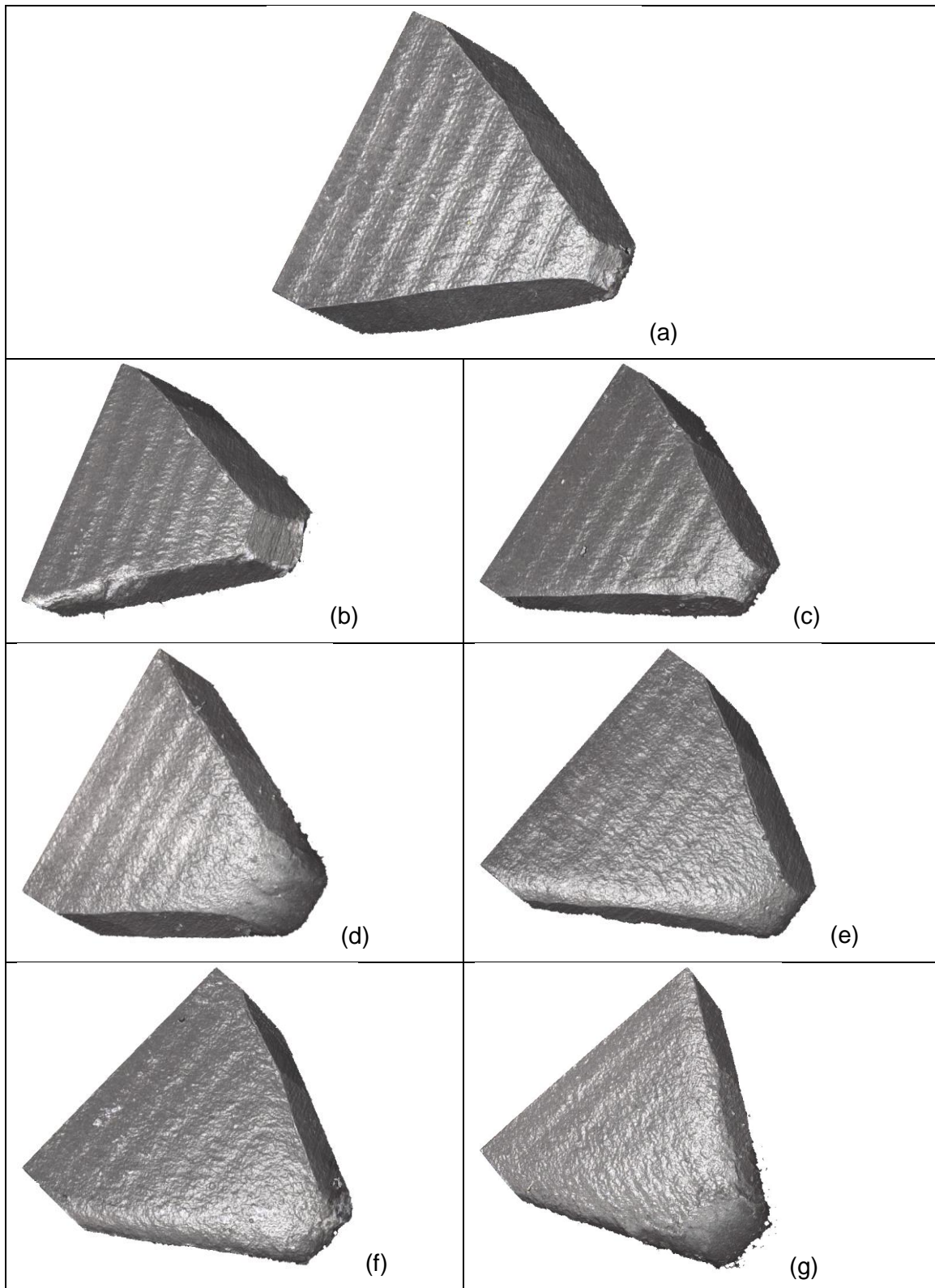
Figure 8.20: 3D images of the sprocket teeth showing (a) the pre-test sprocket specimen tooth with the original ridges and 24-hour test teeth for various carbon black compositions: (b) 0wt%CB, (c) 3wt%CB, (d) 5wt%CB, (e) 7wt%CB, (f) 10wt%CB and (g) 12wt%CB.

8.4.4.2 Two-dimensional images of the chain rollers

In addition, the two-dimensional images of the chain rollers were obtained and some of these images are presented, Figures 8.21 to 8.26, for pre-test and each lubricant composition for the two testing times, that is, 12-hour and 24-hour. While there is virtually little difference between the pre-test images, Figure 8.21(a) and images for 0wt%CB content for 12-hour, Figure 8.21(b), the images for 0wt%CB content for 24-hour test have obvious scratches all over the surface of the rollers resulting from sprocket teeth contact with the chain rollers. Similarly, images from various carbon black compositions show varying levels of abrasion.

(a)

Pre-test chain roller images

(b)

Surface scratches resulting from contact between the sprocket teeth and the chain roller

(c)
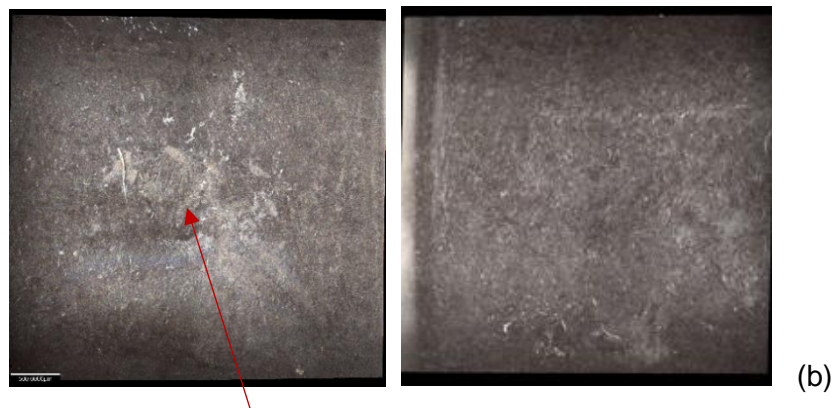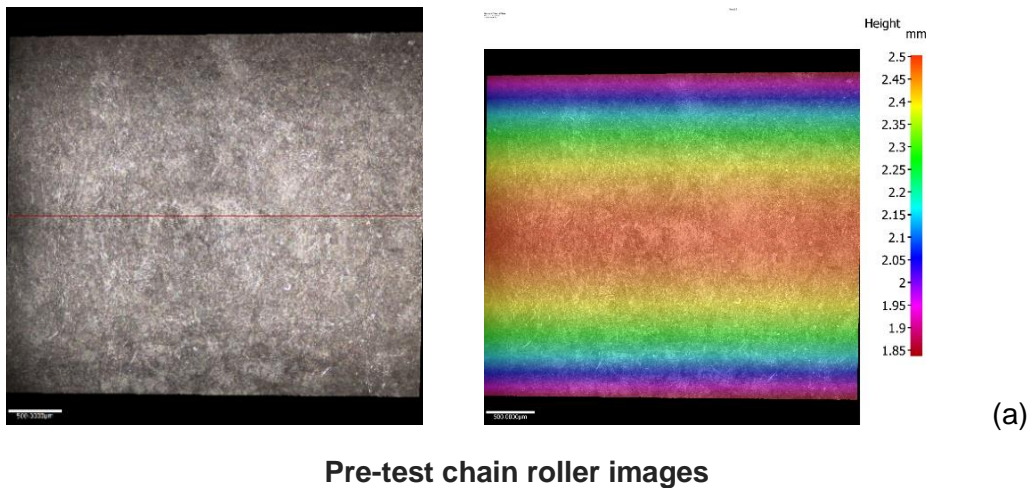
Figure 8.21: 2D surface images of the chain roller specimen (a) pre-test in its true and pseudo colour of the surface with height differences, (b) 0wt%CB content 12-hour test and (c) 0wt%CB content 24-hour test

Inscribed abrasive wear marks on the surface of the chain roller
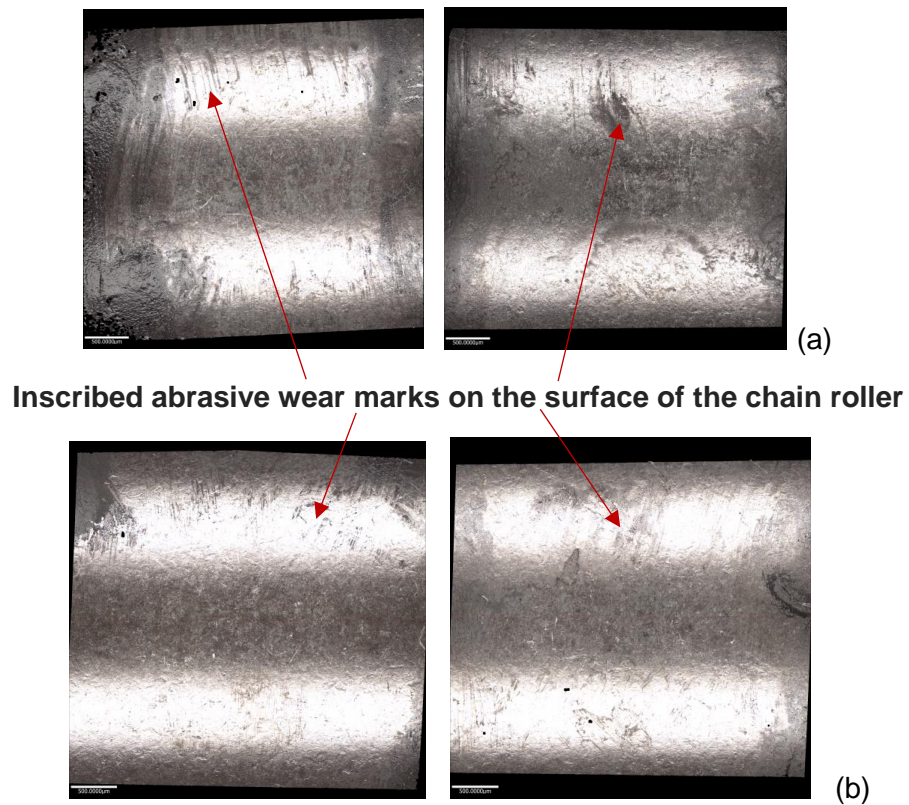
Figure 8.22: 2D surface images of the chain roller specimen (a) 3wt%CB content 12-hour test and (b) 3wt%CB content 24-hour test

CB particles induced abrasive wear marks on the surface of the chain roller, decreasing with increasing testing time
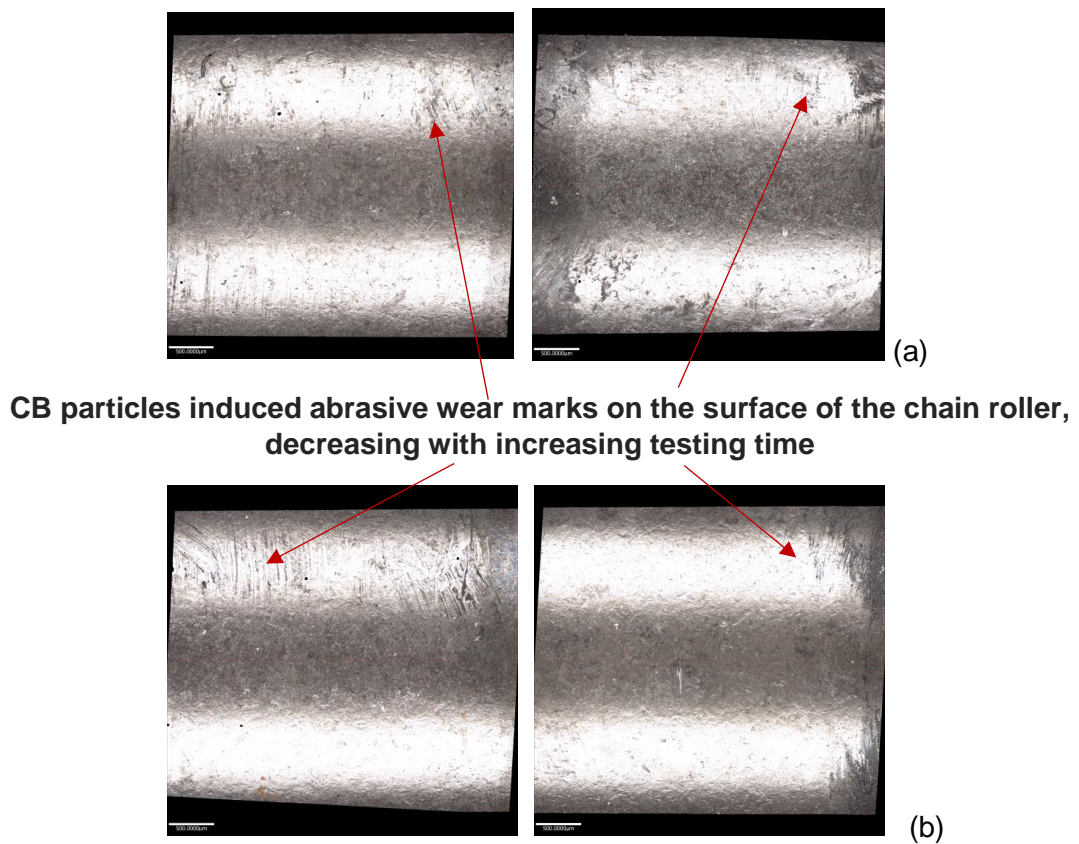
Figure 8.23: 2D surface images of the chain roller specimen (a) 5wt%CB content 12-hour test and (b) 5wt%CB content 24-hour test
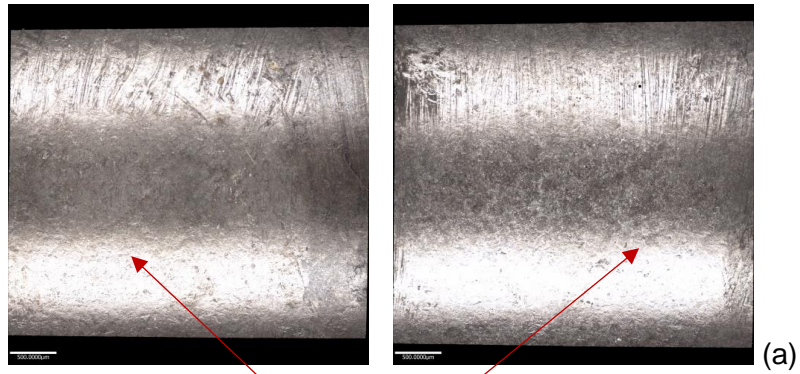
Chain roller surfaces appeared smoother for prolonged testing time
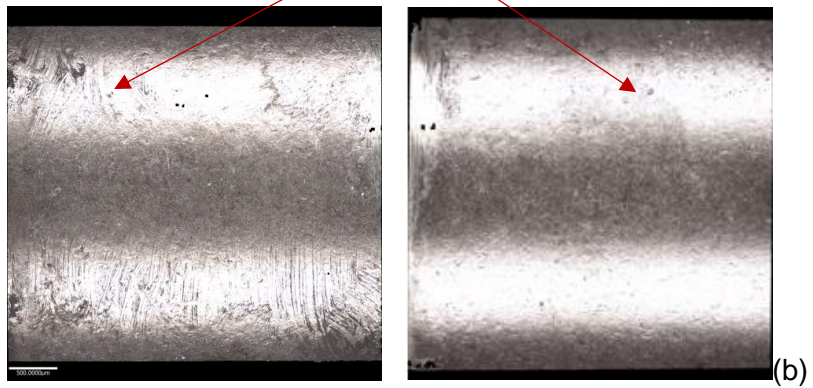
Figure 8.24: 2D surface images of the chain roller specimen (a) 7wt%CB content 12-hour test and (b) 7wt%CB content 24-hour test
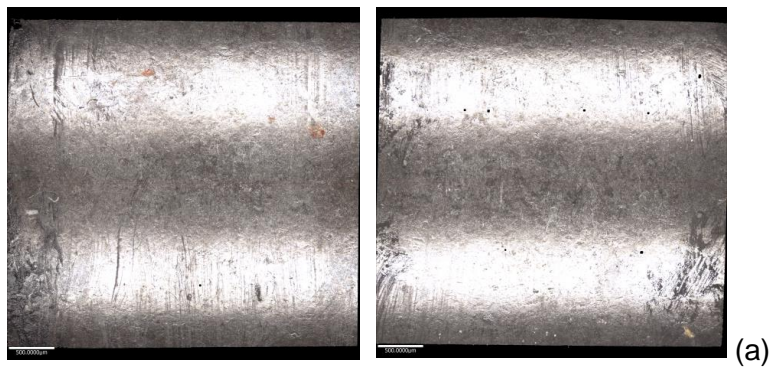
CB particles induced abrasion higher on 24-hour test chain roller surface
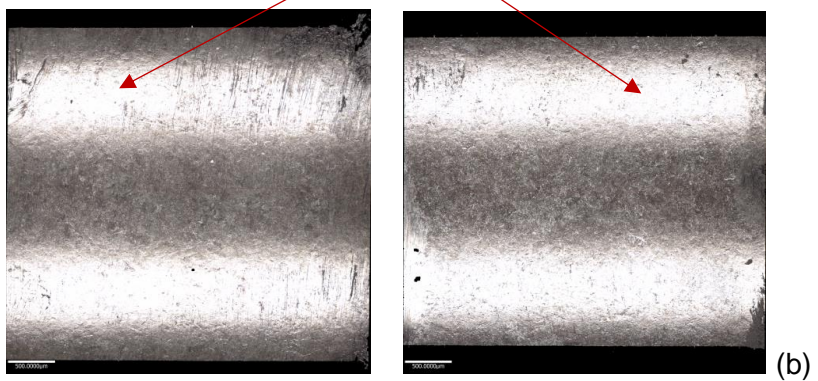
Figure 8.25: 2D surface images of the chain roller specimen (a) 10wt%CB content 12-hour test and (b) 10wt%CB content 24-hour test

164
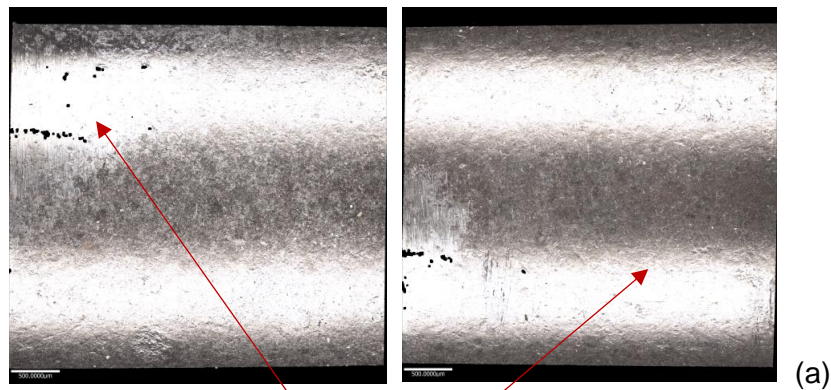
Pronounced abrasion due to higher CB content for both 12-hour and 24-hour tests
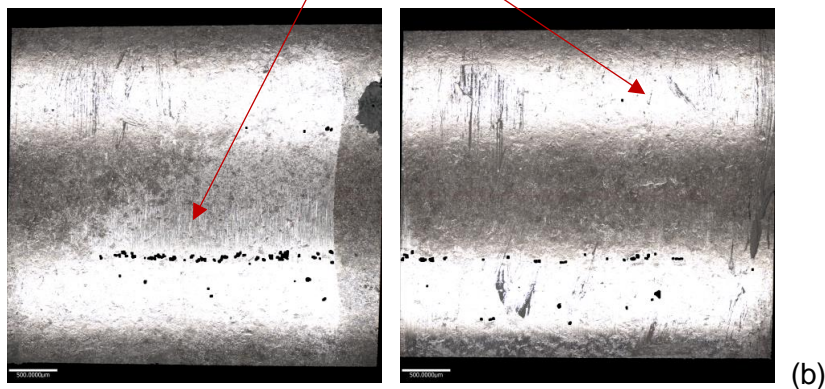
Figure 8.26: 2D surface images of the chain roller specimen (a) 12wt%CB content 12-hour test and (b) 12wt%CB content 24-hour test

8.4.4.3 Roughness profiles

The surface roughness profiles of the chain rollers and sprocket teeth were measured and recorded. The average of three measurements was computed and plotted for each of the lubricant composition. Figure 8.27 presents a sample of the measurement for the pre-test chain roller with the sampling length. Each roughness parameter is defined within a sampling length that is indicated. The profile form measurement is also presented in Figure 8.28 along with its graphical form, indicating a well-rounded cylinder. Similar images are presented for the pre-test sprocket tooth surface in Figure 8.29; while Figure 8.30 shows the pre-test and post-test profiles of the sprocket teeth from selected images.

The average of the surface root mean square (rms) roughness, Rq, of the chain roller and sprocket teeth was measured and computed for the pre-test and various carbon black contents; the same was done for the used chain from the real engine that has undergone several thousands of miles. The results of these computations are presented in Figures 8.31 and 8.32 for the chain rollers and sprocket teeth respectively. While trend of reduction in surface roughness with increasing carbon black content is progressive with sprocket teeth, the same cannot be said of the chain rollers. This is highlighted in Table 8.6, where the average surface roughness values are presented in tabular form for easy comparison.

Table 8.6: Comparison of average surface roughness of the sprocket teeth and chain roller (From Figures 8.31 and 8.32)

Sooty oils	Surface roughness (μm)		
	Sprocket teeth	Chain roller	
Pre-test	1.263	0.255	
		12-hour	24-hour
0wt%CB	1.123	0.313	0.349
3wt%CB	0.963	0.306	0.266
5wt%CB	0.906	0.278	0.266
7wt%CB	0.728	0.281	0.256
10wt%CB	0.676	0.299	0.264
12wt%CB	0.461	0.303	0.264

From these values, it is obvious that the surface of the chain roller gets roughened with each of the tests while the sprocket teeth surface gets smoother. The trend of change in the surface roughness of the chain roller with increasing carbon black content is, however, not sequential; the lowest value of 0.278 μm (5wt%CB content) was recorded for 12-hour test, while 24-hour test recorded the lowest value of 0.256 μm (7wt%CB). The results also indicate that the surface roughness decreases with the longer time of test, the only exception here is the test with no carbon black (0wt%CB) where the roughness value increased from 0.313 μm to 0.349 μm for 12-hour and 24-hour tests respectively.

Ra=0.1955 μm; Rq=0.2479 μm
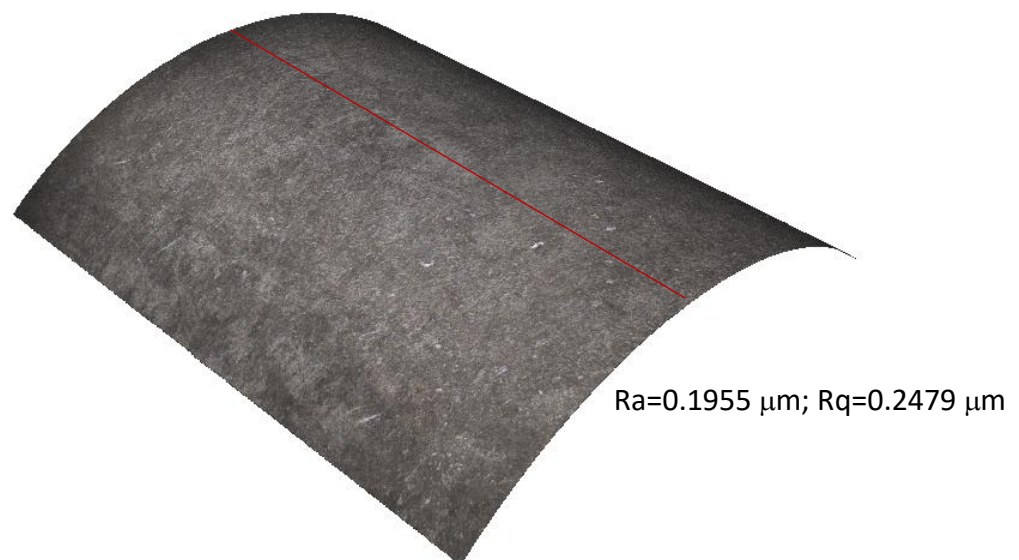
Figure 8.27: Roughness profile of a pre-test chain roller surface image showing the sampling length

(a)

(b)
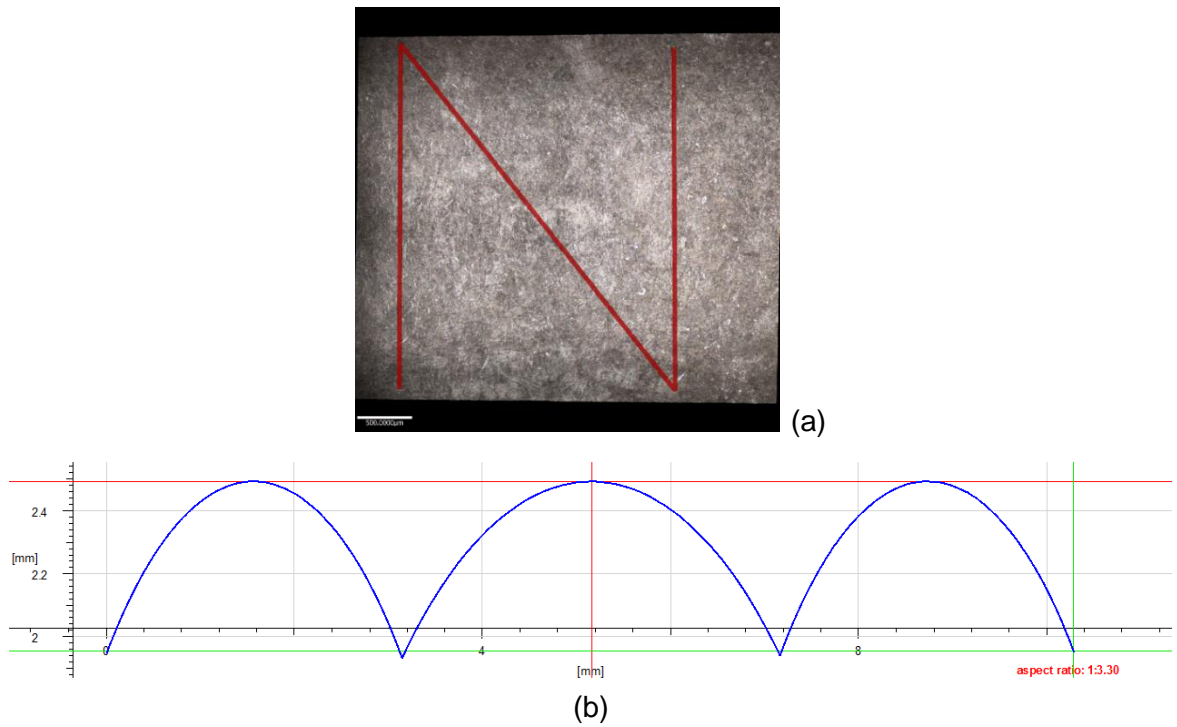
Figure 8.28: Profile form measurement of the chain roller showing (a) the measurement line and (b) graphical form (presenting the object as a well-rounded cylinder)

Ra=1.0346 um; Rq=1.1853 um

(a)

(b)

(c)
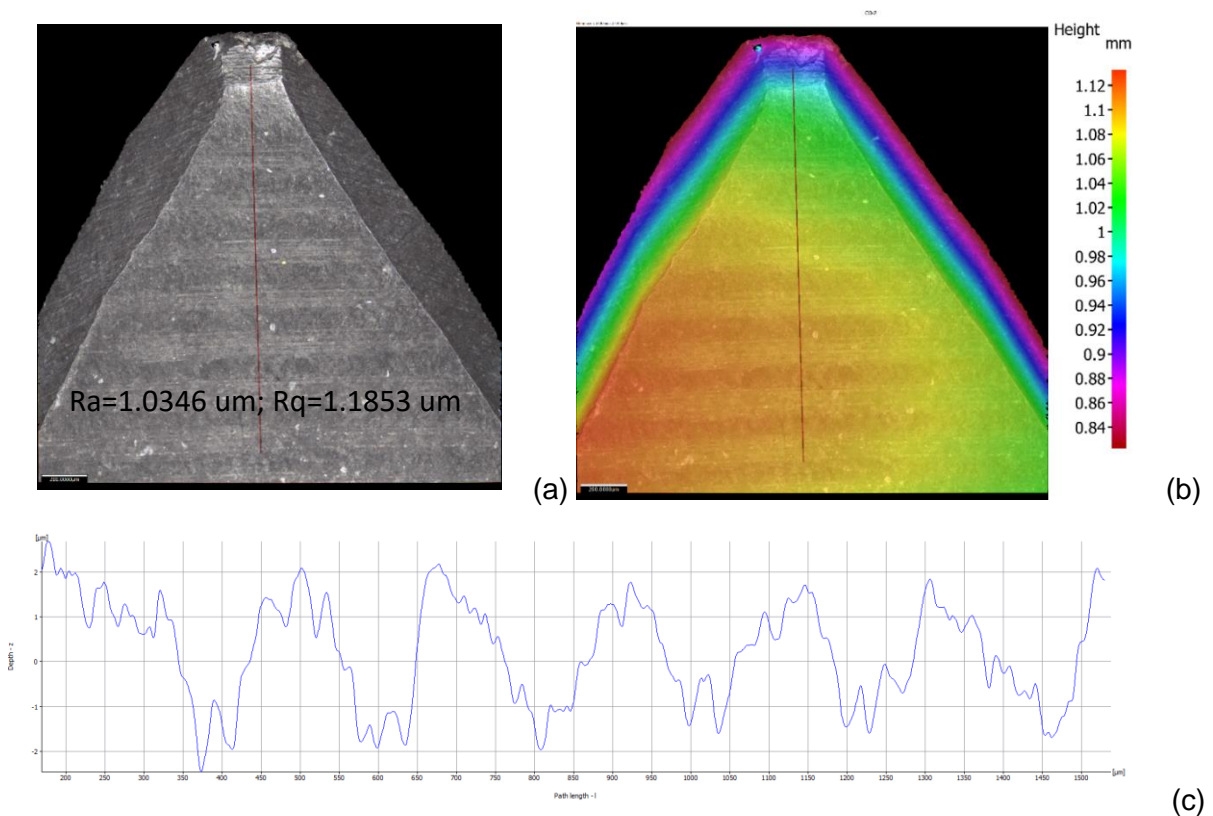
Figure 8.29: Roughness profile of a pre-test sprocket tooth surface (a) image showing the sampling length and (b) pseudo colour indicating height (c) graphical form
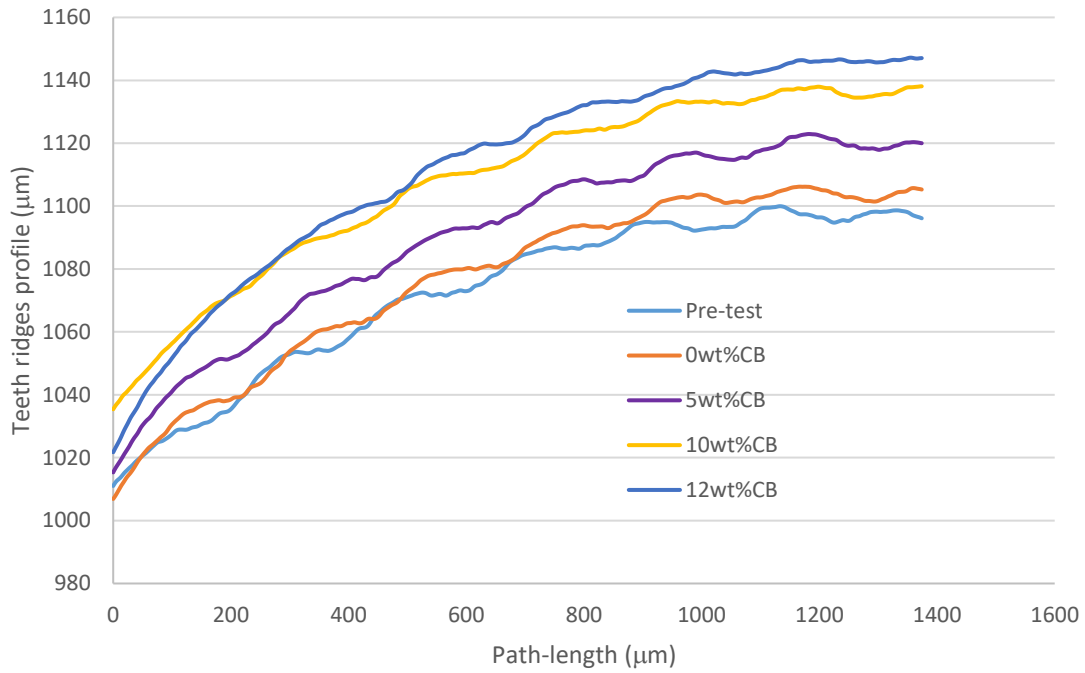
Figure 8.30: Pre- and post-test profiles of the sprocket teeth from selected images

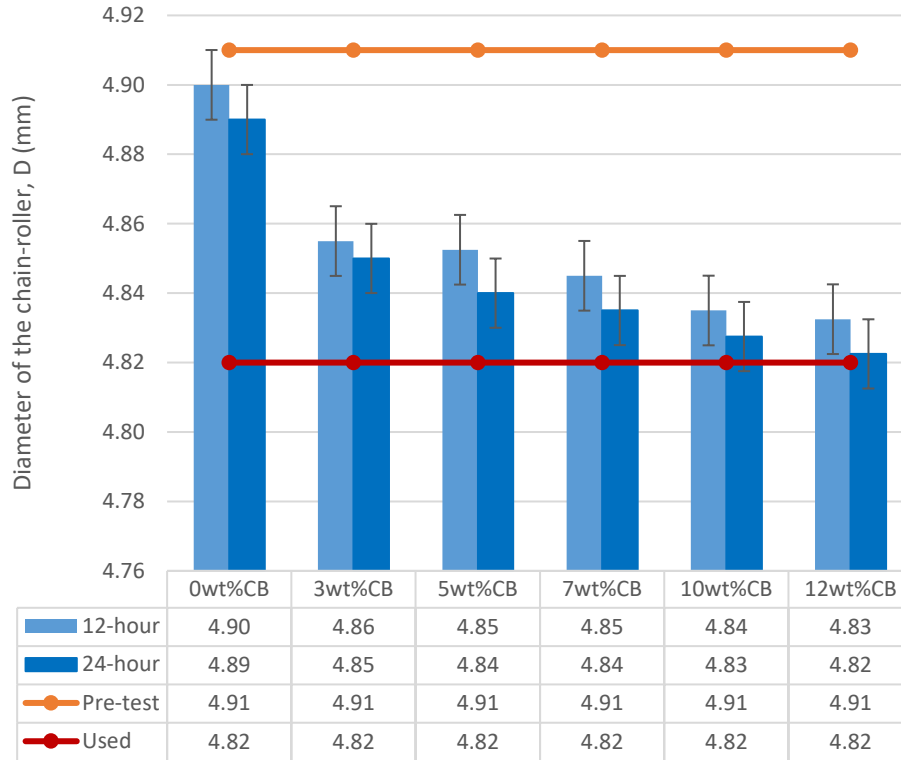|	0wt%CB	3wt%CB	5wt%CB	7wt%CB	10wt%CB	12wt%CB
12-hour	0.313	0.306	0.278	0.281	0.299	0.303
24-hour	0.349	0.266	0.266	0.256	0.264	0.264
Pre-test	0.255	0.255	0.255	0.255	0.255	0.255
Used	0.322	0.322	0.322	0.322	0.322	0.322
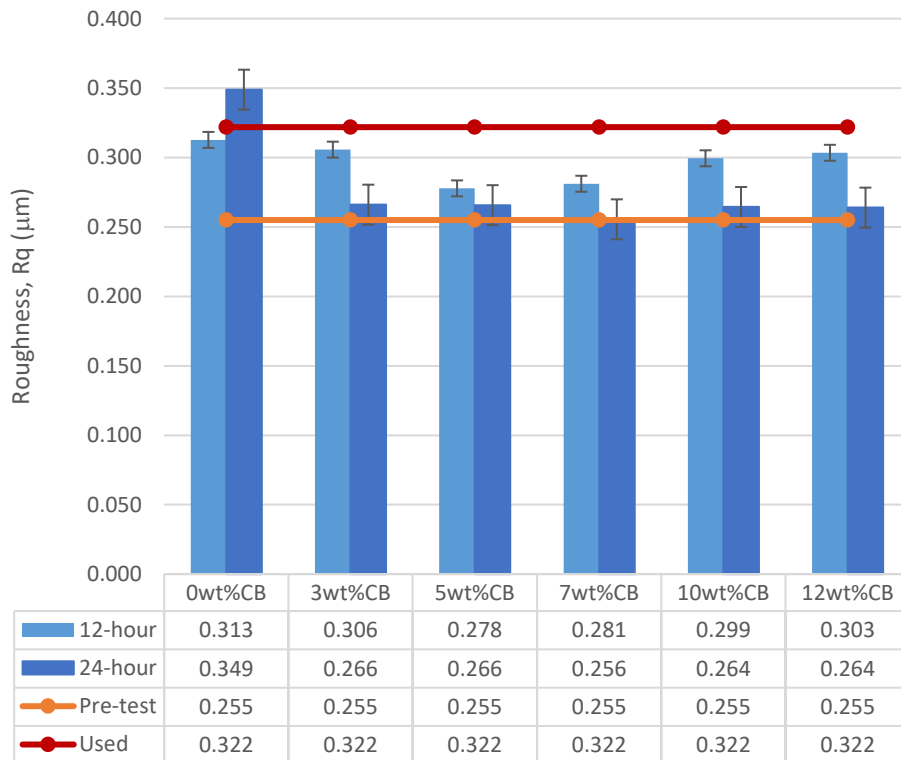
Figure 8.31: The average surface roughness of the chain roller for the used chain, pre-test and various carbon black contents with standard error bars
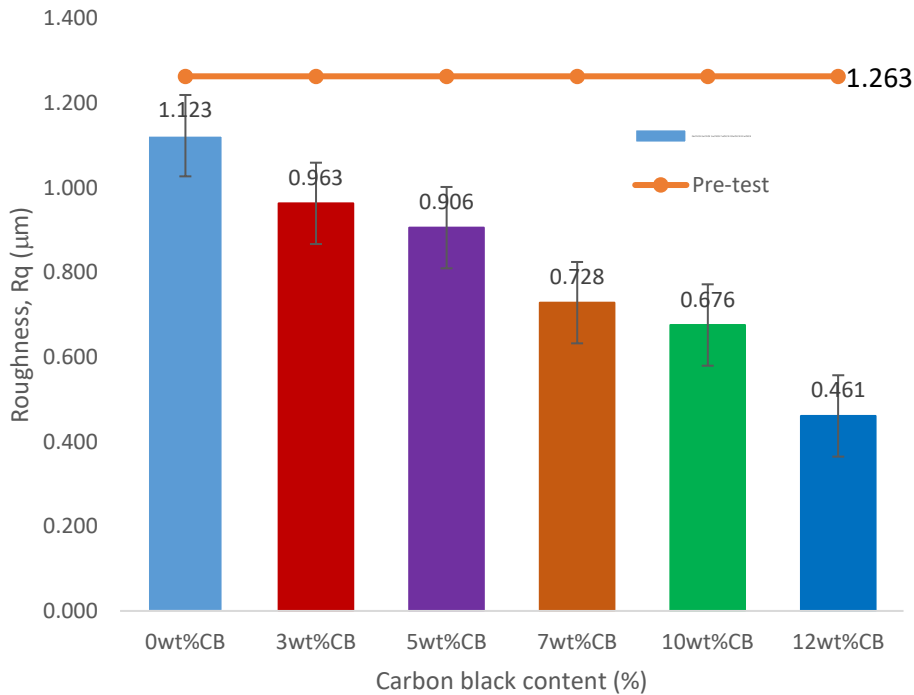
Figure 8.32: The average surface roughness of the sprocket teeth for various carbon black contents with standard error bars

8.5 Analysis of the images of components from 'L' Vehicle (LV)

This section highlights the analysis of the chain that has undergone about 206,000 kilometres on real engine; specifically, Mercedes-Benz M271 engine, C-Class (W203), 2005 C180 Kompressor model. This is one of the unique aspects of this research work as it is not common to have a similar component comparison between laboratory and real-life situation, especially with that long mileage coverage.

The vehicle, which is coded 'L' Vehicle (LV), is a 4-door saloon car with a front-mounted engine driving the rear wheels through a 6-speed manual gearbox. The Mercedes-Benz C180 Kompressor belongs to the W203 family of cars from Mercedes-Benz. Powered by supercharged 1.8-litre with double overhead camshaft and 4-cylinder engine that produces 141 hp (105 kW) of power at 5200 rpm and maximum torque of 220 Nm (22.4 kgm) at 2500-4200 rpm. At the top speed of 223 km/h, its fuel consumption is 11.4/5.9/7.9 l/100km urban/extra urban/combined and carbon dioxide emissions are 190.0 g/km. The pictorial view of the timing chain system arrangement in the engine is shown in Figure 8.33, while the detailed technical specifications of the vehicle is presented in Appendix IX.

Only the chain was replaced as the sprocket was still very good and performing well. However, at the point of the replacement of the used chain, pictures of the sprockets that has been in service with the chain were taken for examinations. And from some of the pictures as presented in Figure 8.34, a critical examination of the sprocket tooth faces gives clear indication that some level of wear had occurred. This is evident as a polished worn segment about the pitch circle diameter of the sprocket teeth.

The chain and the drained oil from the engine were collected for various laboratory analysis. After a thorough cleaning of the chain, it was dried and stored; its image and that of the new

chain are presented in Figure 8.35; where used chain shows evidence of discolouration, apparently due to prolonged service. The analysis commenced with the measurement of the whole length of the chain along with that of the new chain, this is to determine the extent of elongation the chain would have experienced. The outcome of this, Figure 8.36, gives an estimate of 1135 mm for the new chain and 1140 mm for the used chain, indicating that the latter has stretched by approximately 5 mm. This may not be big enough to cause jumping of the sprocket teeth but it is enough to cause timing offset by some degrees. The masses of the used and new chains were also measured and the result gives the values of 385 g and 387 g for the used and new chains respectively. Some portions of the chains (used and new) were then disassembled, delinking some rollers for further observations.
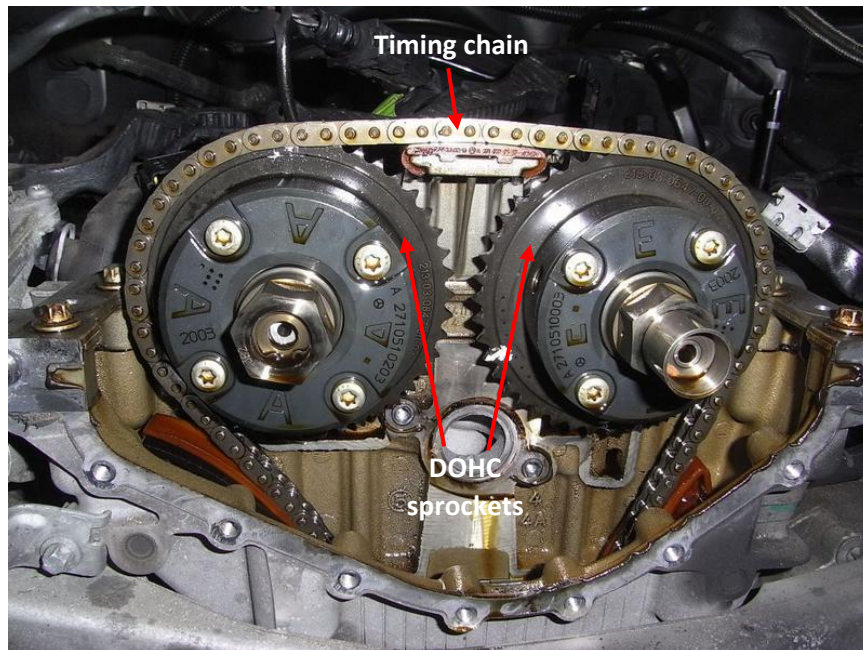
Figure 8.33: Pictorial view of the timing chain arrangement in Benz M271 engine [208]
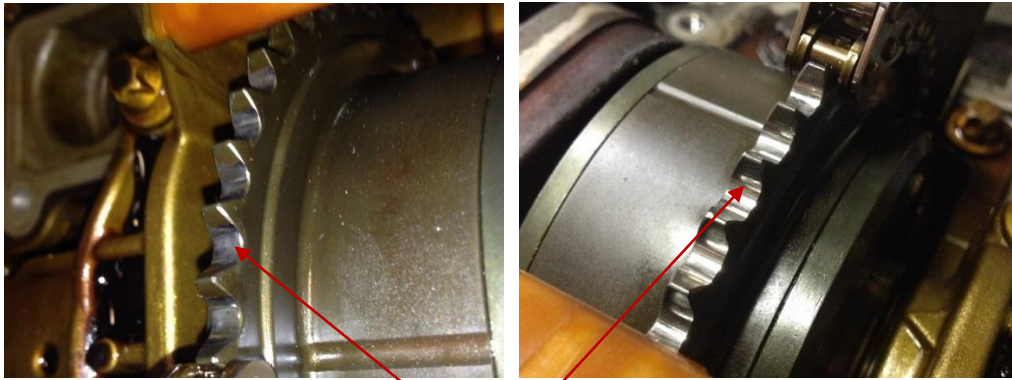
Evidences of abrasion on the point of contact between the sprocket teeth and chain rollers
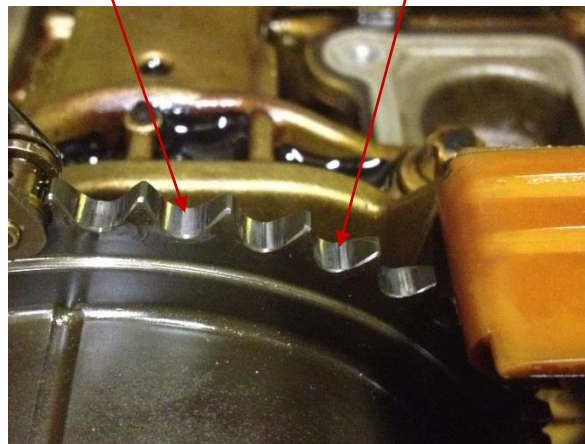
Figure 8.34: Pictorial views of the sprocket that has been in service with the used chain showing evidence of abrasion on its teeth faces

 (a)   (b)

Figure 8.35: Pictorial view of the chains (a) New and (b) Used
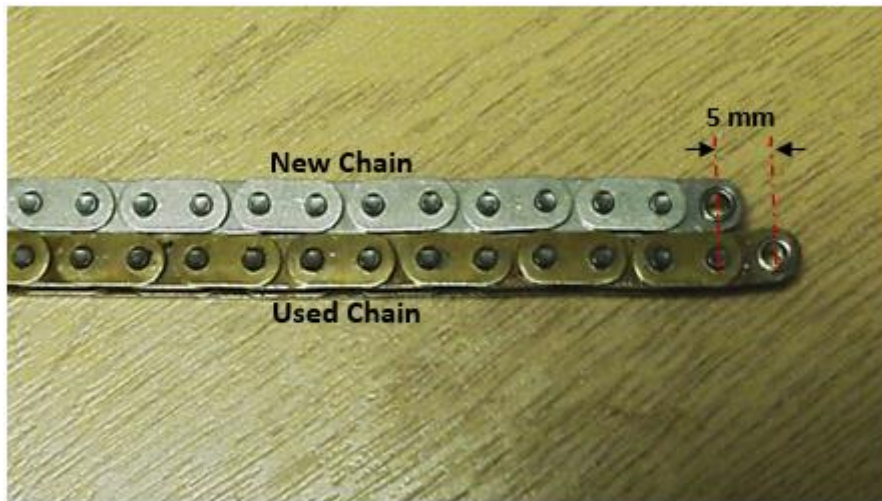
Figure 8.36: Comparison of the lengths of the new and used chains with used chain showing an elongation of 5 mm

8.5.1 Chain-link

The chain links from the new and used chains were examined under the scanning electron microscope (Hitachi TM3030Plus Tabletop SEM) with interesting images from the used chain surfaces. The photomicrographs for the new and used chain link surfaces are presented in Figure 8.37 showing carbon deposits on the used chain link surfaces, Figure 8.37(b). Figure 8.38 shows additional images from the link surfaces, while Figure 8.39 shows a semblance of a crater-like damage found on the surface of one of the links.

8.5.2 Chain-roller

The rollers were similarly observed under the same microscope. The photomicrographs obtained from these rollers are presented in Figures 8.40 and 8.41. In addition, these rollers were also subjected to Alicona analysis. Some of the images, 3D and 2D are shown in Figure 8.42. The roller surfaces show conspicuous signs of prolonged combustion action they have been exposed to for that long mileage.
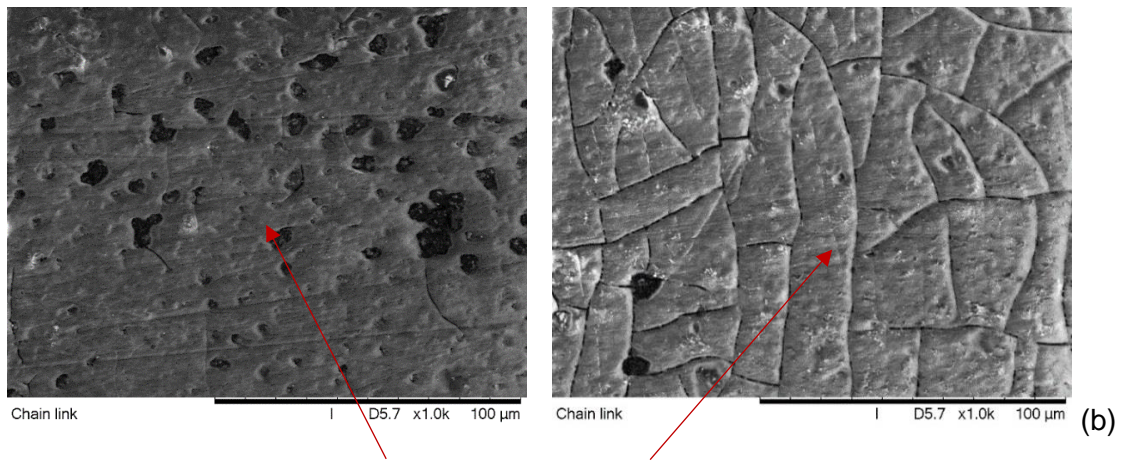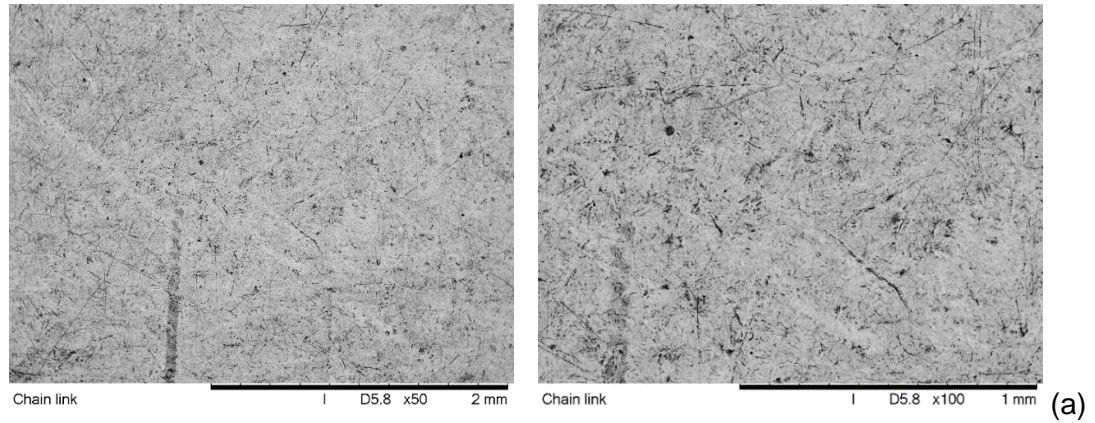
Carbon deposit on chain link surfaces

Figure 8.37: Photomicrographs obtained from chain link surfaces (a) New chain (b) Used chain with massive carbon deposit
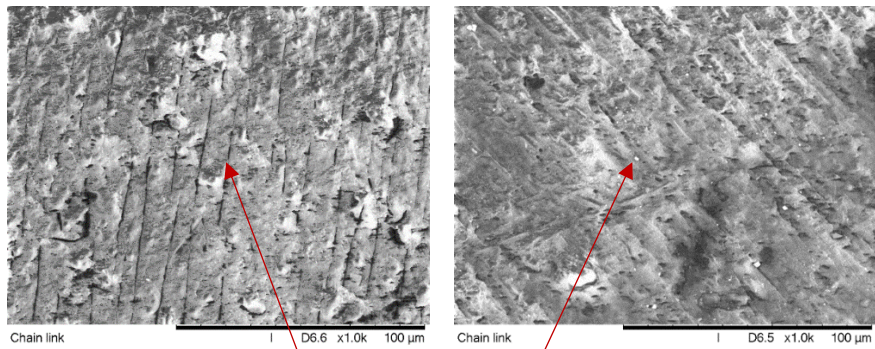
Carbon deposit on chain link surfaces
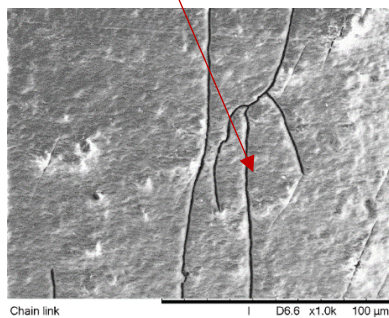
Figure 8.38: Photomicrographs from other chain link surfaces
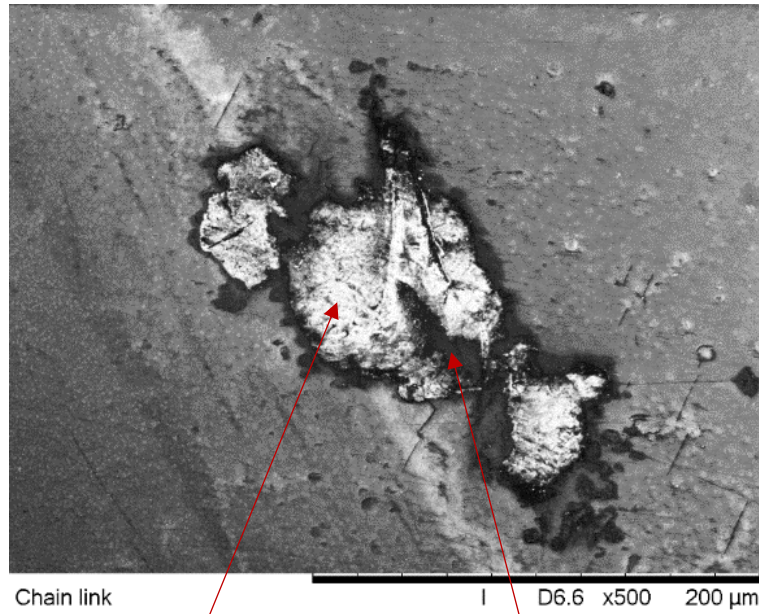
A crater-like damage found on the surface of one of the links

Figure 8.39: Photomicrographs from one of the chain links with excessive crater-like damage
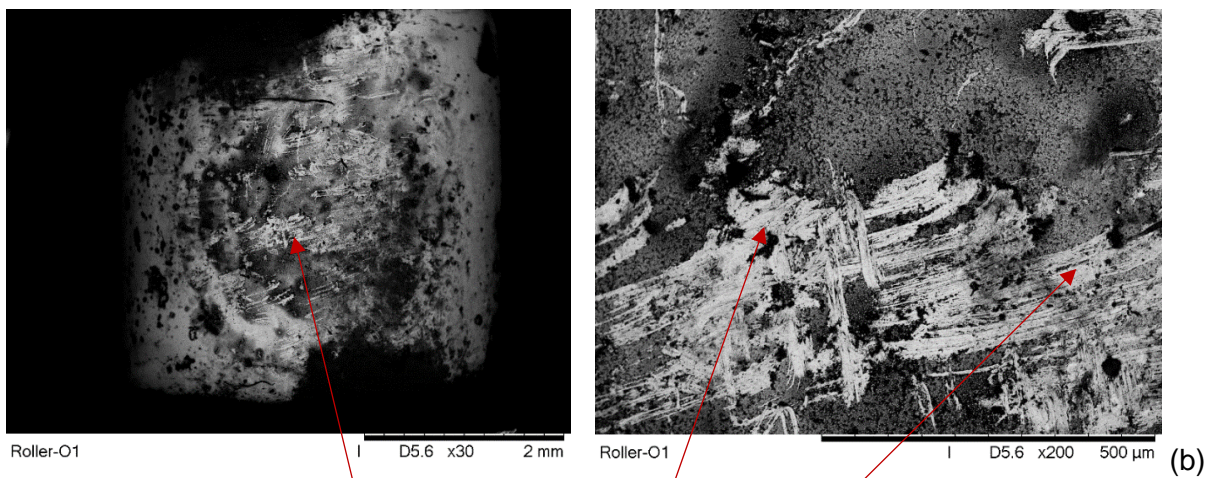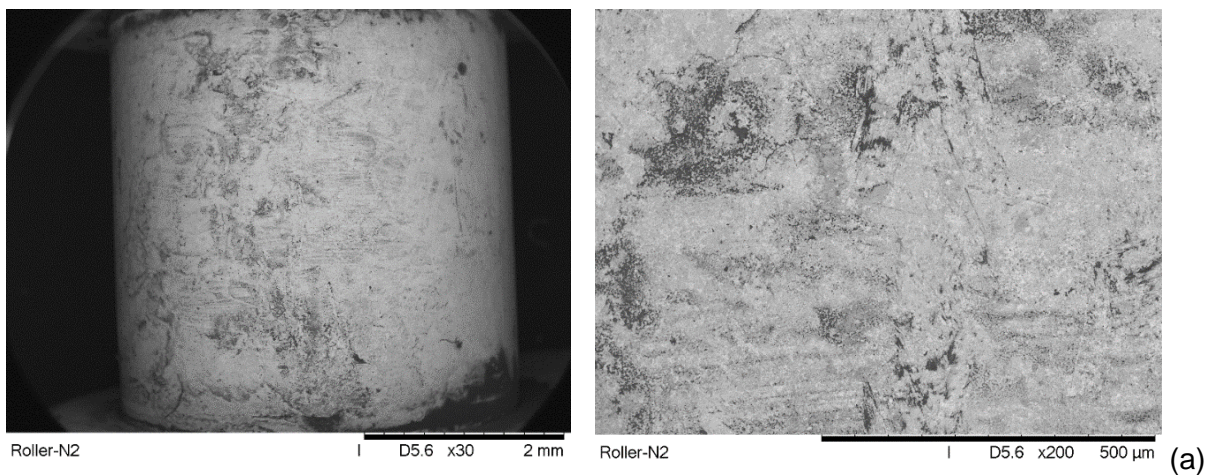
Surfaces scratches apparently from sprocket-roller contact

Figure 8.40: Photomicrographs of the chain roller surfaces (a) New chain (b) Used chain
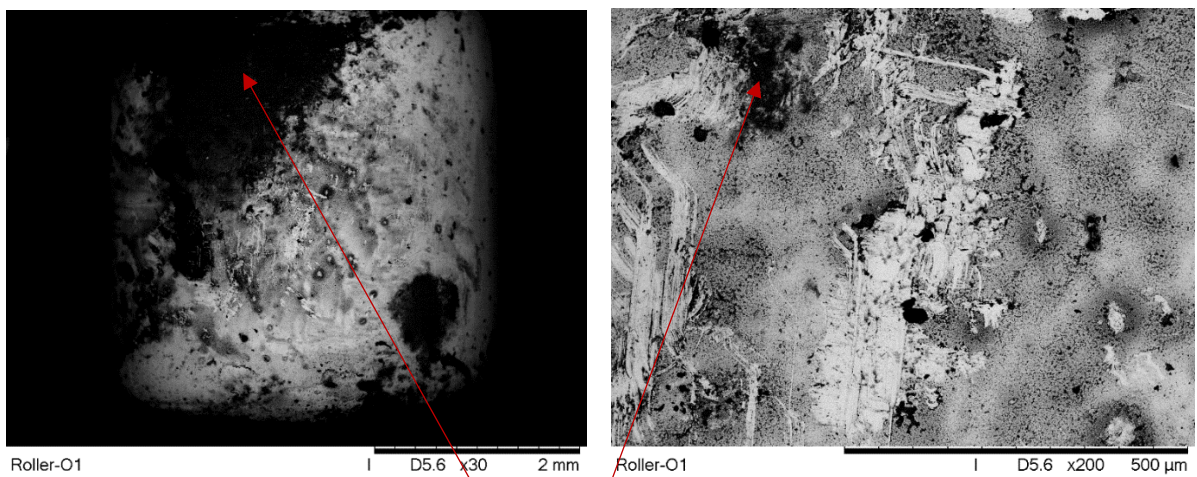
Excessively burnt surfaces of the used chain rollers
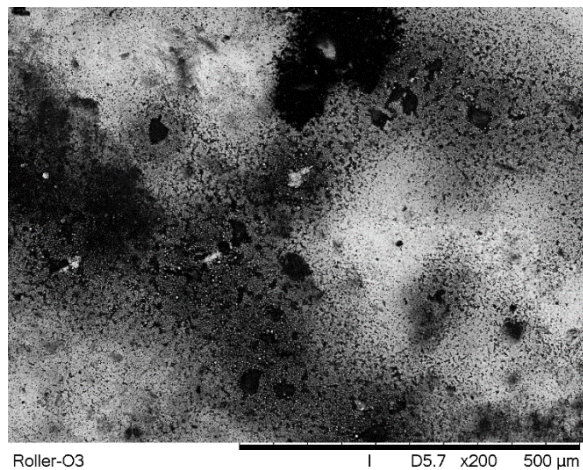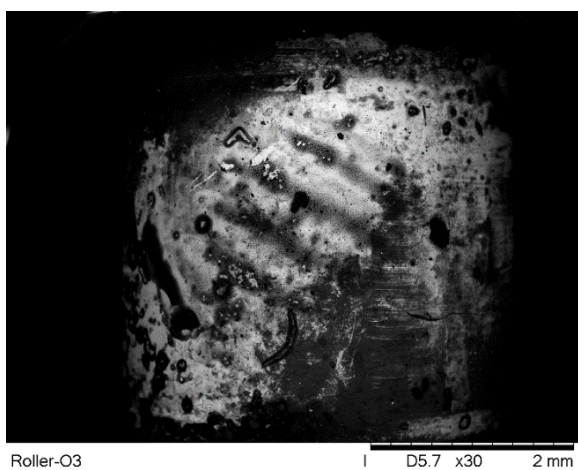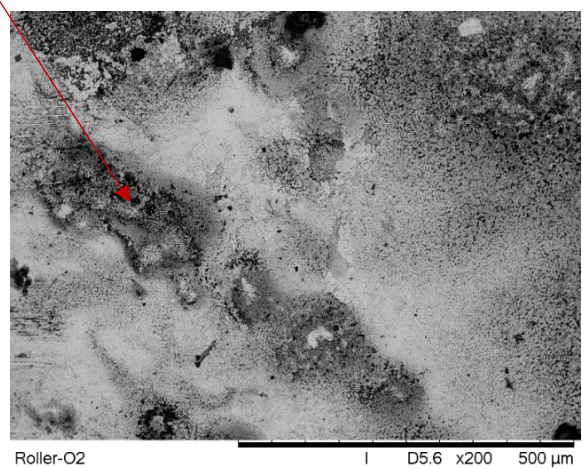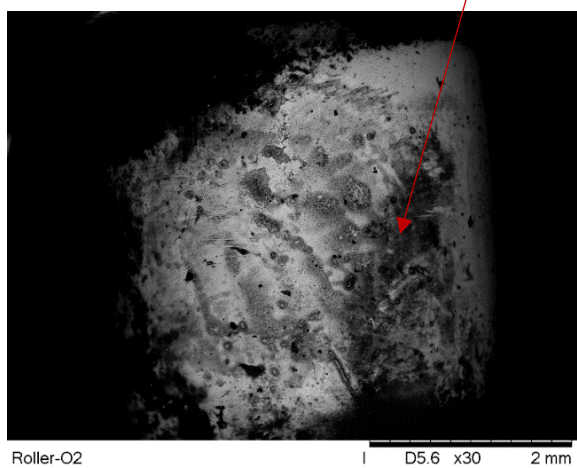
Figure 8.41: Photomicrographs of chain roller surfaces showing signs of excessively burnt surfaces
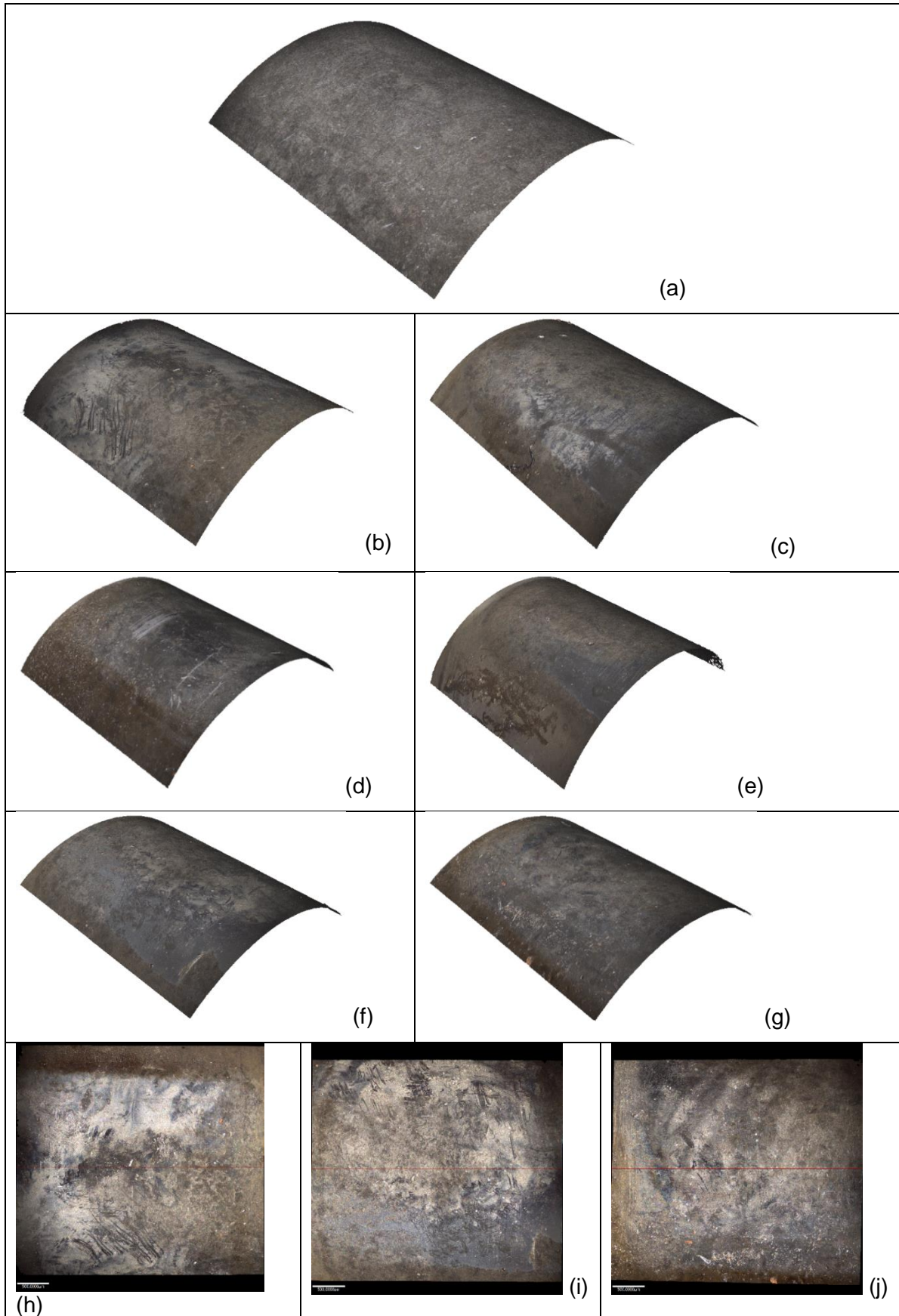
Figure 8.42: Alicona images of the chain roller showing (a) New chain roller in 3D (b-g) Used chain roller in 3D (h-j) Used chain roller in 2D

8.5.3 Oil Analysis

The oil drained from the vehicle engine sump (LVO) when changing the chain and the uncontaminated oil used for 12-hour and 24-hour tests on the designed chain rig (CTO) were sent to the laboratory for analysis. Figure 8.43 shows spectrochemical analysis while Table 8.7 presents the physical properties of the analysed oils.

	Fe	Cr	Al	Mo	Cu	Pb	Sn	Ni	Si	Na	B	V	Ca	P	Zn	Mg	Ba
LVO (ppm)	34	1	6	75	19	1	0	1	10	4	90	0	2975	895	1091	46	0
CTO (ppm)	7	1	23	182	1	1	0	1	2	9	44	0	3102	698	817	10	1
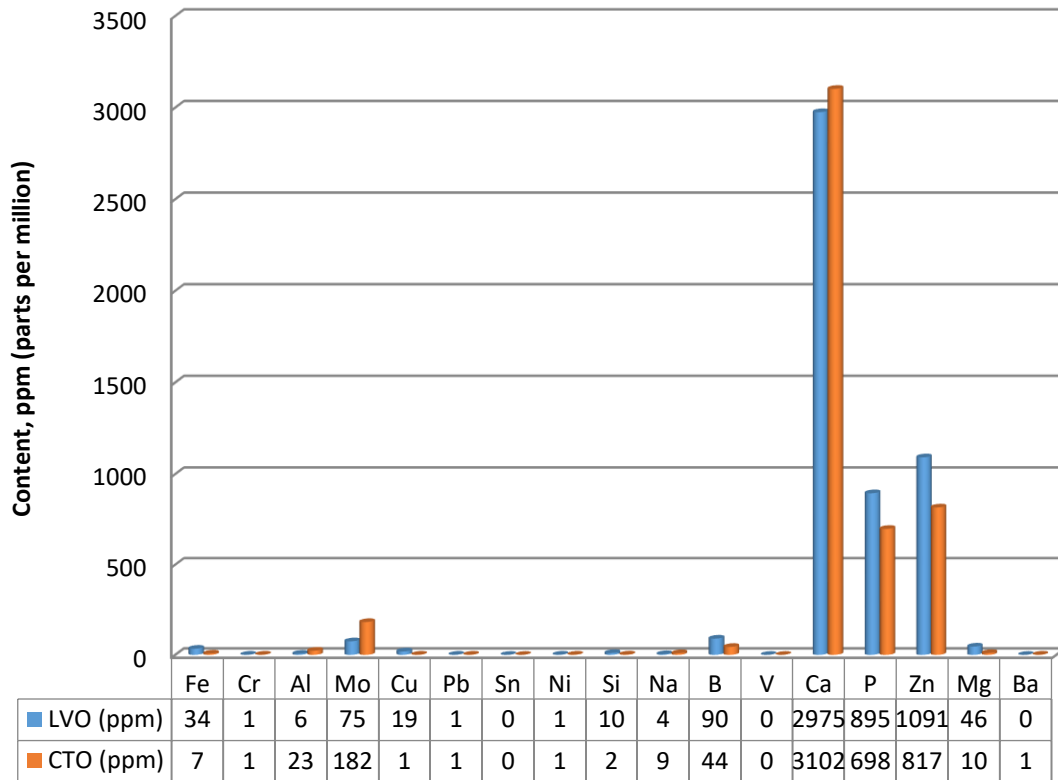
Figure 8.43: Spectrochemical analysis of the oils drained from Les' vehicle (LVO) and Chain-test rig (CTO) running uncontaminated oil for 36-hour.

Table 8.7: Physical properties of the analysed oils

Oil ID	LVO	CTO
Oil in Use	SAE 10w40	SAE 15w40
Viscosity@40°C (cSt)	70	111.7
Water Content (%wt)	0.0	0.0
Fuel Dilution	Negative	n/a
Total Insoluble Matter (%wt)	0.5	0.1
TBN (mgKOH/g)	2.9	n/a
STATUS	NORMAL	CAUTION

The results of the analysis from the laboratory were returned with remarks of NORMAL for the LVO and CAUTION for the CTO, with an explanation that the caution status of CTO emanates from the level of Aluminium (23 ppm) as any value from 20 ppm and above is not good for the engine.

Further explanations of the analysis are highlighted thus:

Total Insoluble Matter (TIM): Principally carbon/soot generated by combustion (2.5% max).

Iron (Fe): Generally from ring, bore, cam, tappet or crankshaft wear; permissible maximum is 100 ppm.

Chromium ((Cr): Usually from piston rings or plated bores; 30 ppm maximum.

Aluminium (Al): Caused by piston or bearing wear; warning from 20 ppm and above.

Copper (Cu): May originate from copper/lead bearings, oil coolers and pipework erosion or synchromesh's in gear boxes; tolerable maximum level is 50 ppm.

Lead (Pb): Usually derived from lead/tin bearings or copper/lead big end bearings; over 50 ppm indicates a problem.

Tin (Sn): From lead/tin or aluminium/tin bearings; levels above 25 ppm need investigation.

Nickel (Ni): Used as an alloy in steel components and will rise as a function of component wear.

Silicon (Si): Normally derived from sand/clay, that is, dust; over 20 ppm calls for attention to air intake filter/trunking to prevent component wear. Other possible sources of silicon are antifoam additives, silicon sealant or coolant leaks.

Sodium (Na): Indicates water ingress most commonly due to coolant leaking in to the oil; usually caused by faulty head gasket, liner seals or perforated liner. Level above 100 ppm calls for concern.

Boron (B): Used either as an additive in antifreeze or as an extreme pressure additive in some oil blends. If they come from antifreeze additive, levels above 50 ppm indicate a problem.

Vanadium (V): Contained in surface coatings and valves; it is also a trace element derived from base oil or fuel. It is, however, not of concern in normal applications.

Calcium (Ca), Molybdenum (Mo), Phosphorus (P), Zinc (Zn), Magnesium (Mg) and Barium (Ba): Are additives used by oil formulators in the manufacture of their lubricants.

8.6 Discussion

8.6.1 Impact stresses

The back and forth sliding of the oil-bath carrying the chain specimen which actuates the oscillatory motion of the meshing sprocket induces impact stresses on the contacting bodies. These stresses are partially responsible for the level of surface damage and wear observed on the components [209].

These impact stresses, complemented by the presence of carbon black particles, have the tendency to burrow the contacting surfaces through either two-body or three-body abrasion; a semblance of this can be seen in Figures 8.16(a) and 8.18 where the repeated impacts of the sprocket teeth ploughed into the chain roller surface.

8.6.2 Masses of the chain specimen

The progressive decrease in the recorded masses of the chain specimen with increasing carbon black content is an indication that the material removal resulting from the effects of sprocket-chain contact action and carbon black plays a more significant role in the post-test masses than the particle embedment shown on the micrographs from scanning electron microscope (SEM) for higher carbon black contents.

8.6.3   Scanning electron microscope (SEM) images

SEM investigations revealed that the carbon black particles inscribed abrasive wear marks on the chain roller surfaces. These marks are conspicuously seen for each tested lubricant composition, especially with 12-hour tests; and they increase with carbon black contents. However, these abrasive wear marks disappear or are less visible with elongated time of testing as seen on 24-hour test images for each of the carbon black contents. The disappearance of these marks is likely caused by hard carbon black particles grinding the contact surfaces with prolonged testing time. Similar abrasive marks were observed on chain bushes and pins by Polat [101] in his performance evaluation of different oils (mineral-based, semi-synthetic and fully-synthetic) on a timing chain wear using an accelerated dynamometer.

Expectedly, the influences of carbon black agglomeration at higher contents are obvious with 10wt%CB and 12wt%CB contents. Images obtained for these tests present cluster of embedded carbon black on the chain roller surfaces.

8.6.4   3D and 2D optical images

The surface profiles of the sprocket teeth change with carbon black content. This is obviously due to the rolling contact it undergoes with the chain rollers on one hand and the sliding contact it encounters with the chain side plates, particularly in the presence of carbon black particles as observed in this work. The most notable of this profile change is observed with the ridges; they wear out progressively with increasing carbon black contents.

Impressions created by contact between the sprocket teeth and the chain can be seen even with uncontaminated oil (0wt%CB), especially for 24-hour test. Signs of abrasion begin to manifest with 3wt%CB, and this gradually progresses with extended time of test and increase in carbon black content; thus suggesting that the abrasion is caused by the presence of carbon black particles.

8.6.5   Roughness profile

The progressive reduction in the sprocket teeth surface roughness values with increasing carbon black content is mainly due to the fact that the undulating ridges on the teeth are gradually reduced by the dual effects of the carbon black particles and the rolling and sliding actions between the contacting bodies (chain and sprocket).

For the chain roller, the rolling and sliding actions of the contacting bodies has the tendency to roughen the surface as manifested in the Alicona images and the roughness values for 12-hour and 24-hour tests when no carbon black was used (0wt%CB). However, the effect of the carbon black particles points in the direction of abrasion and polishing especially at moderate content levels (5-7wt%CB). This assumption is further vindicated by the smoother roughness values recorded for all the carbon black compositions with prolonged time of testing (24 hours).

8.6.6   'L' Vehicle

The results obtained from the analysis of 'L' vehicle chain cannot be exclusively attributed to any particular parameter; it is rather the cumulative effects of several actions within the engine including some environmental factors also due to the long period the chain was in operation.

The elongation of 5 mm observed on the used chain suggests some level of tensile failure resulting from repeated dynamic, mainly impact, loads that the chain has experienced. Possibly, these impact loads may have been above its elastic limit at one time or another. Having undergone such a long distance, it is not unexpected to have overstretched side plates, expanded plate holes and worn rollers. The cumulative effect of these is the resultant elongation of the entire chain component.

The reason for the excessive carbon deposits on the chain link is possibly due to the fact that the link is not in direct contact with the sprocket; it just links (as its name implies) the rollers which the sprocket rolls on. This massive carbon deposit may have contributed to the closeness of the total measured masses of the used and new chain. The crater-like damage found on the surface of one of the detached links is an indication that the chain may have sustained fatigue cracking that will eventually cause failure. This is suspected to have been as a result of repeated impact loads and combustion actions that the chains have been subjected to.

For the chain rollers, there are conspicuous evidences of excessive surfaces burnt resulting from prolonged exposure to the combustion actions. In addition, there are also evidences of surface scratches ostensibly from the combination of impact and sliding actions between the sprocket teeth and the chain rollers. These may have been responsible for the higher surface roughness values recorded for the used chain rollers, as shown in Figure 8.31.

The high level of aluminium content discovered from the laboratory analysis of the CB-free oil used for 12-hour and 24-hour chain rig tests clearly reveals the level of abrasion resulting from the contact action between the sprocket teeth and the chain rollers. Expectedly, the addition of carbon black will increase this level of abrasion.

While the remaining elements are within the tolerable limits, it is worth noting that the level of Phosphorus is approximately 0.07% and 0.09% for CTO and LVO respectively; this level satisfies the new specification of Phosphorus limit aimed at ensuring exhaust catalyst compatibility [32].

8.7 Conclusions

The outcomes from the tests highlighted in this chapter have shown that there are multiple effects on the contacting specimens. The sliding and rolling actions between the sprocket teeth and the chain rollers on one hand and the carbon black particles on the other; the impact stresses induced by the collision of chain with the sprocket teeth during engagement also has its own effects. The emerging results from various post-test analysis have also revealed the damaging effects any particle infiltration into the contact between various moving parts of the timing chain system can cause. This ranges from mild abrasion at low level (0-3wt%CB), more significant abrasive polishing at moderate level (5-7wt%CB) and particle embedment leading to more damaging two-body abrasion at higher level (10-12wt%CB). The abrasive removal of the ridges on the sprocket teeth which neutralizes their tribological benefits is, notably, one of the major negative effect of carbon black, hence soot, particles into these contacts.

Though, the analysis of the 'L' vehicle components may not be attributable to particle infiltration specifically, it nonetheless gives some valuable and instructive indications of possible damages that prolonged usage can cause to a component, particularly timing drive components which constitute parts of the most durable and lifetime components in an internal combustion engine (ICE).

The timing chain, therefore, needs to be properly and adequately lubricated because of the consequences of its poor performance or failure. Indicators of its failure are sequential; starting with strange sound which eventually graduates to noise. With further deteriorations, it can jump, skip a tooth and potentially snap. The unpleasant implication of a snapped chain or one that jumps a tooth is that the valves can come into contact with the piston, resulting in catastrophic engine failure.

In conclusion, this test has been carried out as a modest attempt at bridging some of the gaps caused by lack of real engine components tests, particularly in the study of soot-related wears. However, this is not a perfect representation of the actual engine test.

Generally, laboratory simulated tests have good control and repeatability and can easily be used to evaluate the effect of varying parameters, such as load, speed, temperature, contact geometry, lubrication, etc, on the level of wear and resultant wear mechanism. While the real engine tests are not easy to control and produce less repeatability, their test conditions are more appropriate and produce good representation of the real world occurrence.

Chapter 9

General Discussion, Conclusions and Recommendations

This chapter presents the summary of the discussion and conclusions drawn from this research work along with the recommendations for future work.

9.1 General discussion

9.1.1 Soot build-up

Contemporary automotive technology development is often dictated by the need to comply with stringent emission legislations that continue to be periodically regularly reviewed, as well as the need for improved fuel economy; the development that has also engineered paradigm shift in the formulation of engine lubricants. This state of affairs has particular consequences on the tribological performance of the automotive engines due to resultant soot build-up.

A more compact engine to minimize fuel consumption implies increase in specific power accompanied by higher cylinder pressures and oil temperatures; while emission reduction through the use of EGR results in soot build-up with consequent increase in lubricating oil viscosity which in-turn may lead to pumpability problems and increase fuel consumption.

There is yet to be a consensus on the mechanism responsible for high wear in soot-contaminated lubricant; thus, necessitating further fundamental studies on the underlying wear mechanisms.

9.1.2 Contact profile

Automotive components operate in various forms of contact (sliding, rolling and reciprocating) under mixed friction conditions causing abrasive, adhesive and fatigue wear processes. These wear mechanisms often result into the failure of many vital components in dynamic contacts. Some of the parameters that have effects on wear are [210].

  i.   Material (material pairing, heat treatment, coating)
  ii.   Contact geometry (type of contact, geometric accuracy, roughness)
  iii. Load (forces, moments, Hertzian pressure)
  iv.   Kinematic design (relative speed, hydrodynamic speed, contact pressure)
  v.   Lubrication (oil, viscosity, quantity, additives, contamination, aging)

The performance of a tribological system is largely influenced by the condition under which it operates [27].This formed the basis for the evaluation and variation of these parameters in this research work.

To provide a practical basis for this research work, the specimen tests were designed to simulate specific contact conditions in an internal combustion engine (ICE); while real engine components were used for the component test, the results of which were compared with a similar components that had undergone a real-life situation.

While previous research works were limited to 7wt% carbon black content, this study investigated higher contents (10wt% and 12wt%CB). With the extensive damage observed at these higher concentration, there is the need to ensure that these levels of soot contamination are avoided as much as possible. The use of bypass filter with finer grade filtering elements and deep bed filters comes to the rescue and they have been very effective.

The carbon black particles were well-dispersed in the prepared sooty-oil surrogates, especially for 0-7wt%CB; for the higher contents levels, 10-12wt%CB, presence of agglomerates could

be seen. However, all the mixtures remained quite stable throughout the period of testing, spanning 15-18 months.

9.1.3 Surface roughness

The post-test surface roughness of the specimens for each of the tests were determined and they exhibited varying trends; Figure 9.1 shows a free-hand illustration of these trends. While the ball-on-flat and pin-in-bush test display increasing surface roughness with increasing carbon black content, chain and sprocket from the chain test display a reversing trend; that is, decreasing roughness with increasing carbon black content. For the ring-on-ring test, however, the surface roughness values was steadily decreasing from 0.128 um for 0wt%CB to the minimum value of 0.108 for 5wt%CB and then increased to 0.150 for 10wt%CB. Nonetheless, the polishing effect of carbon black was manifested in each of the tests; especially, at moderate carbon black contents (3wt%-5wt%CB), when the particles were well-dispersed.
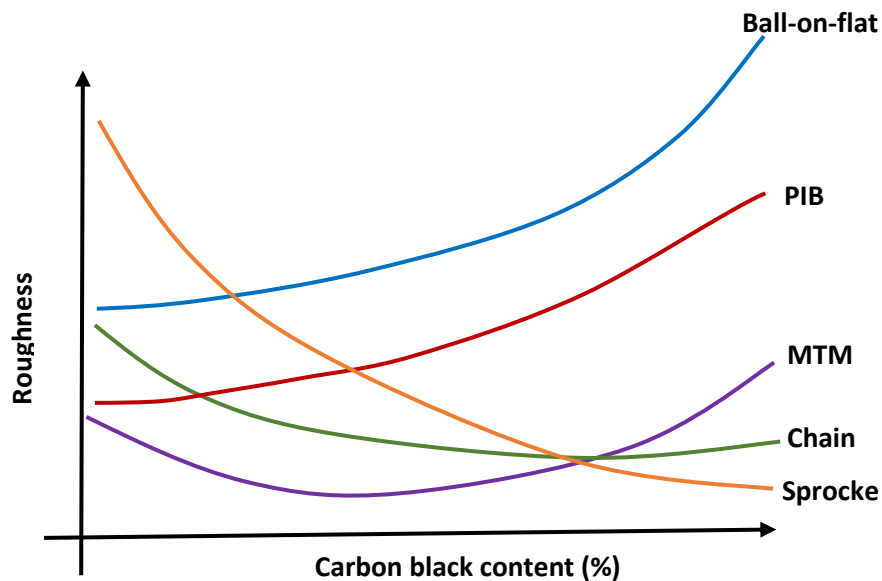
Figure 9.1: A free-hand illustration of the post-test surface roughness trends for various tests

9.1.4 Contact geometry

The contact geometry and the mode of the interacting motion between the contacting surfaces determined the thickness of the lubricating film, and therefore, influenced the observed level of wear and the resultant wear mechanism manifested by each of the tests. For the ball-on-flat test, apart from the fact that the contact width is limited due to its non-conformal point contact, the sliding motion of the ball on the flat specimen also shoved the entraining lubricant away from their contact point, as shown in Figure 9.2(a); thereby increasing metal-to-metal contact. For the non-conformal line contact, ring-on-ring test, the rolling motion of the discs against each other draw the entraining lubricant into their line of contact, thus enhancing significant separation due to increased film thickness. This is depicted in Figure 9.2(b).

For the pin-in-bush test, though the contact is conformal, there was a limited clearance between the contacting specimens which restricted the access of the entraining lubricant into their contact, especially at higher carbon black contents; this is displayed in Figure 9.2(c). Conversely, the entraining lubricant had an unrestricted access to the contact between the chain and the sprocket teeth in the chain rig test, Figure 9.2(d).

The lubricant film is expected to be continuous in the non-contacting regions while asperity contact will occur at points where the film thickness is thin. This observation was particularly

significant for the chain-sprocket contact test where the sprocket original surface texture (crests and troughs) forming ridges manifested increasing obliteration with increasing carbon black content.
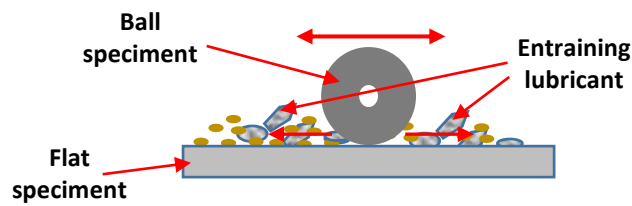
(a) Ball-on-flat contact with the entraining lubricant being pushed away by the reciprocating motion of the ball specimen.
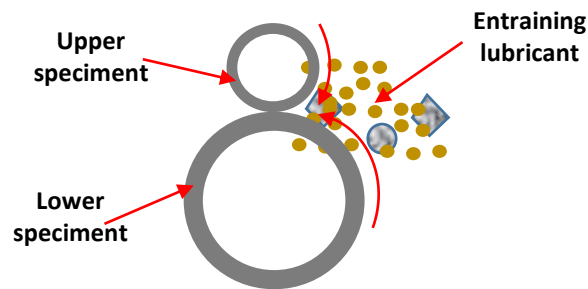
(b) Ring-on-ring contact with the entraining lubricant being easily drawn into the contact.
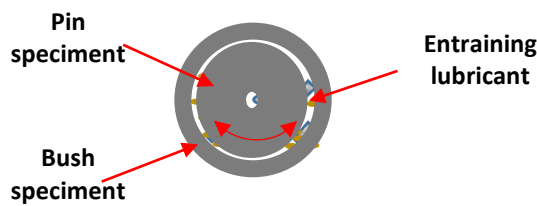
(c) Pin-in-bush with the entraining lubricant restricted by the small clearance between the contacting specimens.
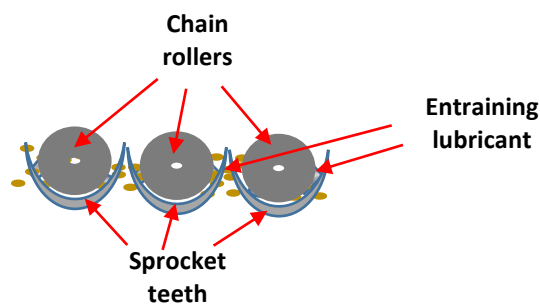
(d) Chain-sprocket contact with the entraining lubricant having an unrestricted access to the contacting surface.

Figure 9.2: Schematics of the contact geometry and lubricant entrainment modes for (a) ball-on-flat, (b) ring-on-ring, (c) pin-in-bush and (d) chain rig tests

9.1.5 Wear mechanisms

Various forms of wear mechanisms were observed from the tests in this research work; ranging from abrasive wear, some level of adhesive wear, surface and subsurface fatigue wears. However, the dominating wear that was common to all the tests is the progressive abrasive wear as dictated by the carbon black contents and operating contact conditions.

For the 0wt%CB content, the wear mechanism was mild abrasion where the asperities of the contacting specimens were sparingly touching one another, Figure 9.3(a). For moderate compositions (3-5wt%CB), the observed wear was three-body abrasion where the hard, but well-dispersed carbon black particles penetrate the gap between the specimens along with the entraining lubricant as they slide/roll against each other. This is diagrammatically illustrated in Figure 9.3(b). At the higher contents (7-12wt%CB), either or both of the following explanations are possible. The carbon black particles agglomerate and prevent the lubricant from getting into the contact zone or some of these hard particles get into the contact zone where they become squeezed and get embedded into the surfaces. The embedded hard particles plough through the contacting surfaces and form extensive grooves along the sliding direction, as observed with pin-in-bush test. The second explanation is that starved lubrication, caused by agglomeration, may occur; resulting in metal-to-metal contact as the asperities of the specimens come more into direct interaction, Figure 9.3(c). Both of these explanations result in two-body abrasion.
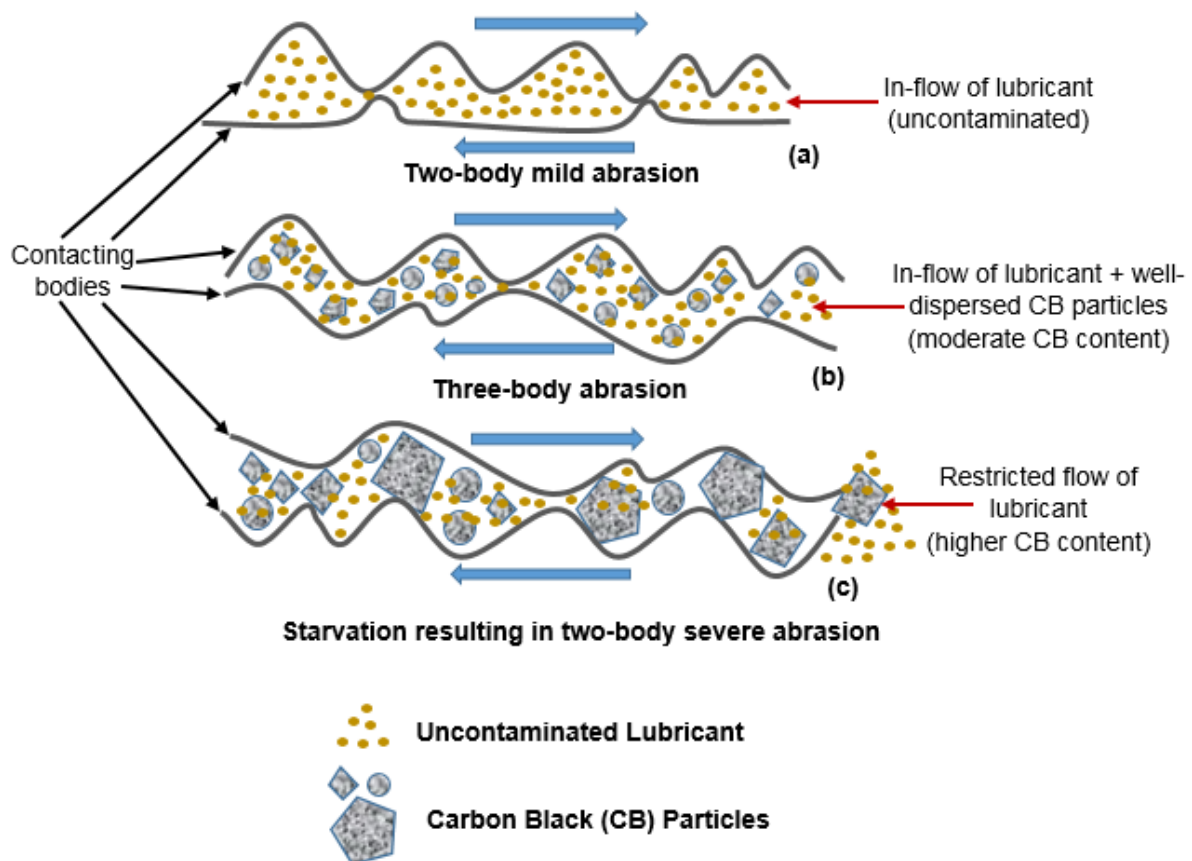
Figure 9.3: Illustration of different wear mechanisms emanating from different CB contents (a) two-body abrasion, (b) three-body abrasion and (c) starvation-induced two-body abrasion

9.2　General conclusions

9.2.1　Viscosity

The viscosity of the sooty-oil surrogates increased with increasing carbon black contents and decreased with increasing temperature. This is an exhibition of inverse viscosity-temperature relation which is common to most lubricants. Increased viscosity is expected to reduce friction coefficient between the contacting bodies and this was observed with ring-on-ring test operating under mixed lubrication regime. For the boundary lubrication test, however, friction coefficient increased with carbon black content, especially at higher compositions (7wt%-12wt%CB).

The fact that the increasing viscosity at higher content level was not manifested in the resultant frictional effect for the boundary lubrication is an indication that the regime of lubrication takes precedence over the viscosity of the lubricating medium.

9.2.2　Wear analysis

For the ball-on-flat tests, the volume of the wear scar increased steadily with increasing temperature and carbon black content but very sharply at higher contents, especially 10wt%CB and 12wt%CB. Increasing load at the same carbon content also caused increase in wear scar. This is a manifestation of a direct relationship between wear and carbon black content, load and temperature. A similar increase in the level of wear with increasing carbon content was observed for the ring-on-ring, pin-in-bush and chain tests. The dominant form of wear exhibited by the carbon black in all the tests was abrasive wear.

9.2.3　Coefficient of friction

The specimen tests (ball-on-flat and ring-on-ring) showed a clear correlation between the regime of lubrication and the variation of coefficient of friction. At moderate carbon black content (3wt%-5wt%CB), coefficient of friction remained relatively similar; even at higher loads for the ball-on-flat test, operating under boundary lubrication. Remarkably, 3wt%CB delivered a value lower than that of the uncontaminated oil; ostensibly due to the additives-assisted dispersion of carbon black uniformly. The significant increase at higher contents (10wt%-12wt%CB) is likely due to agglomeration and thickening. For the ring-on-ring test, operating under mixed lubrication regime, the value of the coefficient of friction decreased with increasing carbon black content. The value remained relatively constant under different load, increased with percentage slip and decreased with speed.

In spite of the decreasing trend of the coefficient of friction with increasing carbon black content in the ring-on-ring test, there was significant increase in the level of wear with increasing carbon black content. The implication of this is that the abrasive characteristic of carbon black particles is not inhibited by their slippery interaction between neighbouring particles when agglomerated. Another possible explanation for this is that the increasing wear results in smoother surface which will help reduce the coefficient of friction.

The study has tackled soot-contaminated issues with pragmatic approach, in terms of simulating realistic engine contacts and test conditions, using standardised testing methodologies that are capable of producing reliable and repeatable data. All the tests are laboratory-based; however, realistic automotive engine contacts were simulated using appropriate materials. Furthermore, real engine components were also tested along with the analysis of a similar component that has undergone several thousands of miles on a real engine which provided a basis for comparison. From the results and analysis carried out, it can be concluded that the contact geometry and regime of lubrication under which the

automotive components operate will influence the level of wear they are likely going to experience .from soot contamination.

9.2.4 Ultrasonic film thickness measurement

The use of the ultrasonic technique in the instantaneous measurement of the film thickness of selected sooty-oil surrogates can be said to be very effective. The experimental results produced the same trends with the analytical prediction; and the numerical values of the film thickness obtained experimentally also indicated closeness to the analytical results. Being a novel approach in the measurement of the real-time film thickness of the soot-contaminated lubricant, the results look promising and demonstrate the potentials for harnessing this approach in real application.

9.3 Recommendations for future work

9.3.1 Soot surrogates

This work has used a single type of carbon black as soot surrogate; other types may be further tested to compare their results. In the same vein, the possibility of testing with real engine soot may also be considered.

9.3.2 Test materials

Metallic materials, particularly ferrous metals, have been widely tested for soot-related wear study. Non-ferrous metals, especially aluminium and its alloys, are now gaining grounds as alternative materials in automotive applications because of the need to increase efficiency by reducing weight. Also, various types of elastomers are widely used as seals in internal combustion engine (ICE). There is therefore the need to consider other materials apart from ferrous metals for soot-related wear study.

9.3.3 Modelling of soot wear mechanisms

Numerical simulation and modelling of soot have been limited to its formation, oxidation and particle size distribution. An area of automotive soot study that has not received any attention is modelling of soot wear mechanisms, ostensibly because they are still not fully understood; and also due to the fact that the complexity of soot wear mechanism makes the task of accurately simulating and predicting soot wear behaviour very difficult. Nonetheless, work in this direction is overdue.

9.3.4 Improvement on PIB rig

The pin-in-bush (PIB) rig designed in this work can be improved on by incorporating a variable motor into the present design; this may facilitate measurement of power variation for each lubricant.

9.3.5 A follow-up to the chain rig

It should be noted that the chain arrangement in this design is perfectly horizontal, while it is always inclined in the real engine; this is one of the limitations of this design. Another limitation is that both flanks of the sprocket teeth are subjected to relatively the same load impact due to reciprocating motion of this design. Consequently, both active and non-active flanks are likely going to experience the same level of wear which is not the case in real engine where the motion is unidirectional.

A follow-up to this study is, therefore, recommended with the rig upgraded to a design that can accommodate full chain and the accompanying sprockets; thus simulating the real engine arrangement.

9.3.6 A follow-up on the use of ultrasonic technique

With the significant level of success recorded on the use of ultrasonic for real-time measurement of film thickness, there is a need for further studies in order to ascertain its veracity.

References

1.	McGuire, N., *Seeing the Interface: How Realistic is the Picture?* Tribology & Lubrication Technology, 2015. **71**(4): p. 36.

2.	Green, D. and R. Lewis, *The effects of soot-contaminated engine oil on wear and friction: a review.* Proceedings of the Institution of Mechanical Engineers, Part D: Journal of Automobile Engineering, 2008. **222**(9): p. 1669-1689.

3.	Green, D. and R. Lewis, *Investigation of soot contaminated lubricant wear mechanisms*. 2007, SAE Technical Paper.

4.	Green, D., R. Lewis, and R. Dwyer-Joyce, *Wear effects and mechanisms of soot-contaminated automotive lubricants.* Proceedings of the Institution of Mechanical Engineers, Part J: Journal of Engineering Tribology, 2006. **220**(3): p. 159-169.

5.	Rudnick, L.R., *Synthetics, mineral oils, and bio-based lubricants: chemistry and technology*. 2013: CRC press.

6.	Green, D. and R. Lewis, *Effect of soot on oil properties and wear of engine components.* Journal of Physics D: Applied Physics, 2007. **40**(18): p. 5488.

7.	Green, D.A., R. Lewis, and R. Dwyer-Joyce, *Wear of valve train components due to soot contaminated lubricant*. 2006, SAE Technical Paper.

8.	Green, D., R. Lewis, and R. Dwyer-Joyce, *The wear effects and mechanisms of soot contaminated automotive lubricants, IMechE.* Part J. Journal of Engineering Tribology, 2005. **220**: p. 159-169.

9.	Aldajah, S., O.O. Ajayi, G.R. Fenske, and I.L. Goldblatt, *Effect of exhaust gas recirculation (EGR) contamination of diesel engine oil on wear.* Wear, 2007. **263**(1): p. 93-98.

10.	Singh, S.K., A.K. Agarwal, and M. Sharma, *Experimental investigations of heavy metal addition in lubricating oil and soot deposition in an EGR operated engine.* Applied thermal engineering, 2006. **26**(2): p. 259-266.

11.	Duvvuri, P.P., and N. Deshpande, *Lube Oil Soot Reduction Using Combustion Simulation for CPCB2 Compliant Cummins N14 Engine*. in *ASME 2014 Internal Combustion Engine Division Fall Technical Conference*. 2014: American Society of Mechanical Engineers.

12.	Daido, S., Kodama, Y., Inohara, T., Ohyama, N., and Sugiyama, T., *Analysis of soot accumulation inside diesel engines.* JSAE Review, 2000. **21**: p. 303-308.

13.	Clague, A.D.H., J.B. Donnet, T.K. Wang, and J.C.M. Peng, *A comparison of diesel engine soot with carbon black.* Carbon, 1999. **37**(10): p. 1553-1565.

14.	Uy, D., M.A. Ford, D.T. Jayne, A.E. O'Neill, L.P. Haack, J. Hangas, M.J. Jagner, A. Sammut, and A.K. Gangopadhyay, *Characterization of gasoline soot and comparison to diesel soot: Morphology, chemistry, and wear.* Tribology International, 2014. **80**: p. 198-209.

15.	Regulations, E.E. *Standards for Light-duty Vehicles*. 2010 [cited 2015 March 7th]; Available from: http://upload.wikimedia.org/wikipedia/commons/c/c5/Euronorms_Diesel.png.

16.	Stanwick, P. and S. Stanwick, *Volkswagen Emissions Scandal: The Perils of Installing Illegal Software.* International Review of Management and Business Research, 2017. **6**(1): p. 18.

17.	Sanchez, F.P., A. Bandivadekar, and J. German, *Estimated cost of emission reduction technologies for light-duty vehicles.* A report by International Council of Clean Transportation (ICCT), 2012.

18.	Beat, T., *New method for measuring heavy-duty vehicle emissions*, *Tribology & Lubrication Technology (TLT)*. 2015, Society of Tribologists and Lubrication Engineers: Illinois, p. 12-13.

19.	Bishop, G.A., and R. Hottor-Raguindin, *On-road Heavy-duty Vehicle Emissions Monitoring System.* Environmental Science & Technology, 2015.

20.	Dougjack. *European Industry has Moved to Euro 6*. 2016 [cited 2018 January 11th] Available from: http://www.dougjack.co.uk/downloads/euro-6-european-emission-standards.pdf.

21.	Regulations, E.E. *Standards for Heavy-duty Vehicles*. 2013 [cited 2015 March 7th]; Available from: http://en.wikipedia.org/wiki/European_emission_standards.

22. Yamaguchi, E., and M. Untermann, *Soot wear in diesel engines.* Proceedings of the Institution of Mechanical Engineers, Part J: Journal of Engineering Tribology, 2006. **220**(5): p. 463-469.

23. Schoeffmann, W.J., C. Truffinet, M. Howlett and N. Ausserhofer, *Demands on Future Timing drives-Chain and Belt in Competition*. 2015, SAE Technical Paper.

24. Forsberg, P., F. Gustavsson, P. Hollman and S. Jacobson, *Comparison and analysis of protective tribofilms found on heavy duty exhaust valves from field service and made in a test rig.* Wear, 2013. **302**(1): p. 1351-1359.

25. Slatter, T., H. Taylor, R. Lewis and P. King., *The influence of laser hardening on wear in the valve and valve seat contact.* Wear, 2009. **267**(5): p. 797-806.

26. Lewis, R. and R. Dwyer-Joyce, *Wear of diesel engine inlet valves and seat inserts.* Proceedings of the Institution of Mechanical Engineers, Part D: Journal of Automobile Engineering, 2002. **216**(3): p. 205-216.

27. Forsberg, P., *Combustion Valve Wear: A Tribological Study of Combustion Valve Sealing Interfaces.* PhD Thesis, Department of Engineering Science, 2013, Uppsala University.

28. Gosvami, N., J.A. Bares, F. Mangolini and A.R. Konicek, *Mechanisms of antiwear tribofilm growth revealed in situ by single-asperity sliding contacts.* Science, 2015. **348**(6230): p. 102-106.

29. EU Council, *Vehicle emissions in real driving conditions: Council gives green light to second package*. 2016 [cited 2016 February 13th]; Available from: http://www.consilium.europa.eu/en/press/press-releases/2016/02/12-vehicle-emissions-in-real-driving-conditions-2nd-package/.

30. Vlachos, T.G., P. Bonnet, A. Perujo, and M. Weiss, *In-Use Emissions Testing with Portable Emissions Measurement Systems (PEMS) in the Current and Future European Vehicle Emissions Legislation: Overview, Underlying Principles and Expected Benefits.* SAE International Journal of Commercial Vehicles, 2014. **7**(1): p. 199-215.

31. Spikes, H., *Tribology research in the twenty-first century.* Tribology International, 2001. **34**(12): p. 789-799.

32. Canter, N., *GF-6, PC-11 and dexos1 (TM): New engine oil specifications mean new additive challenges.* Tribology & Lubrication Technology, 2015. **71**(9): p. 10-+.

33. McCarthy, S.A., *The future of heavy duty diesel engine oils.* Tribology and Lubrication Technology, 2014. **70**(10): p. 38-50.

34. Baş, H., A. Biyiklioğlu, and H. Cuvalci, *A new test apparatus for the tribological behavior of cam mechanisms.* Experimental Techniques, 2003. **27**(5): p. 28-32.

35. Ekberg, A., *Wear–some notes.* Dep. of Solid Mechanics, Chalmers University of Technology, 1997.

36. Blau, P.J., *How common is the steady-state? The implications of wear transitions for materials selection and design.* Wear, 2014.

37. Sahoo, P., *Engineering Tribology*. 2005: PHI Learning Pvt. Ltd, New Delhi.

38. Ludema, K.C., *Friction, Wear, Lubrication: A Textbook in Tribology*. 1996: CRC Press.

39. Scott, R., *Basic wear modes in lubricated systems.* Machinery Lubrication Noria Publication, 2008(1375).

40. Stachowiak, G. and A.W. Batchelor, *Engineering Tribology*. 2013: Butterworth-Heinemann, Oxford.

41. Holmberg, K., P. Andersson, and A. Erdemir, *Global energy consumption due to friction in passenger cars.* Tribology International, 2012. **47**: p. 221-234.

42. Yamaguchi, K., C. Sasaki, and R. Tsuboi, *Effect of surface roughness on friction behaviour of steel under boundary lubrication.* Proceedings of the Institution of Mechanical Engineers, Part J: Journal of Engineering Tribology, 2014: p. 1015-1019.

43. Van Basshuysen, R. and F. Schäfer, *Internal Combustion Engine Handbook-Basics, Components, Systems and Perspectives*. Vol. 345. 2004.

44.   Dardalis, D., R.D. Matthews, and A.O. Lebeck, *Design Details of the Compression Ignition Rotating Liner Engine. Reducing Piston Assembly Friction and Ring/Liner Wear in Heavy-Duty Diesel Engines*. 2012, SAE Technical Paper.

45.   Blau, P.J., *Friction Science and Technology: From Concepts to Applications*. 2008: CRC Press.

46.   Wang, Q. and Y. W. Chung, *Encyclopedia of Tribology*. 2013: Springer, New York.

47.   Hamid, B., *Maximizing Bearing Life with EHD Lubricants.* Machinery Lubrication, 2004: p. 28-30.

48.   Olsson, H., K.J. Astrom, C.C. De Wit, and M. Gafvert, *Friction models and friction compensation.* European Journal of Control, 1998. **4**(3): p. 176-195.

49.   Van Rensselar, J., *Beneath the surface: Why contact mechanics and tribology are a natural match.* Tribology & Lubrication Technology, 2015. **71**(7): p. 52-60.

50.   Dwyer-Joyce, R., *The life cycle of a debris particle.* Tribology and Interface Engineering Series, 2005. **48**: p. 681-690.

51.   La Rocca, A., G. Di Liberto, P.J. Shayler and M.W. Fay, *The nanostructure of soot-in-oil particles and agglomerates from an automotive diesel engine.* Tribology International, 2013. **61**: p. 80-87.

52.   La Rocca, A., G. Di Liberto, and P.J. Shayler, *Application of nanoparticle tracking analysis platform for the measurement of soot-in-oil agglomerates from automotive engines.* Tribology International, 2014. **70**: p. 142-147.

53.   Growney, D.J., O.O. Mykhaylyk, and L. Middlemiss, *Is carbon black a suitable model colloidal substrate for diesel soot?* Langmuir, 2015. **31**(38): p. 10358-10369.

54.   Jao, T.C., S. Li, K. Yatsunami and S.J. Chen, *Soot characterisation and diesel engine wear.* Lubrication Science, 2004. **16**(2): p. 111-126.

55.   Delvin, C.C., C.A. Passut, R.L. Campbell, and T.C. Jao, *Biodiesel Fuel Effect on Diesel Engine Lubrication*, in *Powertrains, Fuels & Lubricants Meeting*. 2008, SAE International: Rosemont, Illinois.

56.   Li, S., Csontos, B.M. Gable, C.A. Passut, and T.C. Jao, *Wear in cummins M-11/EGR test engines*. 2002, SAE Technical Paper.

57.   La Rocca, A., J. Campbell, M.W. Fay, and O. Orhan, *Soot-in-oil 3D volume reconstruction through the use of electron tomography: an introductory study.* Tribology Letters, 2016. **61**(1): p. 8.

58.   Bhowmick, H. and S. Biswas, *Relationship between physical structure and tribology of single soot particles generated by burning ethylene.* Tribology Letters, 2011. **44**(2): p. 139-149.

59.   Jayashankara, B. and V. Ganesan, *Effect of fuel injection timing and intake pressure on the performance of a DI diesel engine–A parametric study using CFD.* Energy Conversion and Management, 2010. **51**(10): p. 1835-1848.

60.   Woolley, R., *Reciprocating Engines, Lecture Notes*. 2014, University of Sheffield.

61.   Stone, R., *Introduction to Internal Combustion Engines.* 3rd Edition, 1999: Macmillan, London.

62.   Lahaye, J., *Mechanisms of soot formation.* Polymer Degradation and Stability, 1990. **30**(1): p. 111-121.

63.   Patel, M., Ricardo, C.L.A, Scardi, P. and Aswath, P.B., *Morphology, structure and chemistry of extracted diesel soot: Part I: X-ray absorption near edge structure (XANES) spectroscopy and high resolution transmission electron microscopy.* Tribology international, 2012. **52**: p. 29-39.

64.   ASTM International, *Standard Test Method for Field-Based Condition Monitoring of Soot in In-Service Lubricants Using a Fixed-Filter Infrared (IR) Instrument*. 2011, ASTM International.

65.   ASTM International, *Standard Test Method for Condition Monitoring of Soot in In-Service Lubricants by Trend Analysis using Fourier Transform Intrared (FT-IR) Spectrometry*. 2012, ASTM International.

66.   ASTM International, *Standard Practice for Condition Monitoring of In-Service Lubricants by Trend Analysis Using Fourier Transform Infrared (FT-IR) Spectrometry*. 2010, ASTM International.

67. Cheekala, N.R., R. Rohrbach, and P. Unger, *Soot Removal from Diesel Engine Lubrication Systems.* SAE International Journal of Fuels and Lubricants, 2010. **3**(2): p. 559-568.

68. Stone, R., *Introduction to Internal Combustion Engines*. 4th Edition, 2012: Palgrave Macmillan, Hampshire.

69. Diaby, M., M. Sablier, A. Le Negrate and M. El Fassi, *Understanding carbonaceous deposit formation resulting from engine oil degradation.* Carbon, 2009. **47**(2): p. 355-366.

70. Soejima, M., Y. Ejima, K. Uemori, and M. Kawasaki, *Studies on friction and wear characteristics of cam and follower: influences of soot contamination in engine oil.* JSAE Review, 2002. **23**(1): p. 113-119.

71. Gautam, M., K. Chitoor, M. Durbha, and J.C. Summers, *Effect of diesel soot contaminated oil on engine wear—investigation of novel oil formulations.* Tribology International, 1999. **32**(12): p. 687-699.

72. Nagai, I., H. Endo, H. Nakamura and H. Yano, *Soot and valve train wear in passenger car diesel engines*. 1983, SAE Technical Paper.

73. Antusch, S., M. Diewiebel, E. Nold, P. Albers and U. Spicher, *On the tribochemical action of engine soot.* Wear, 2010. **269**(1): p. 1-12.

74. George, S., S. Balla, and M. Gautam, *Effect of diesel soot contaminated oil on engine wear.* Wear, 2007. **262**(9): p. 1113-1122.

75. Rounds, F.G., *Carbon: cause of diesel engine wear?* 1977, SAE Technical Paper.

76. Penchaliah, R., T.J. Harvey, R.J.K. Wood, K. Nelson, and H.E.G. Powrie, *The effects of diesel contaminants on tribological performance on sliding steel on steel contacts.* Proceedings of the Institution of Mechanical Engineers, Part J: Journal of Engineering Tribology, 2011. **225**(8): p. 779-797.

77. George, S., S. Balla, V. Gautam, and M. Gautam, *Effect of diesel soot on lubricant oil viscosity.* Tribology International, 2007. **40**(5): p. 809-818.

78. Truhan, J.J., J. Qu, and P.J. Blau, *A rig test to measure friction and wear of heavy duty diesel engine piston rings and cylinder liners using realistic lubricants.* Tribology International, 2005. **38**(3): p. 211-218.

79. Truhan, J.J., J. Qu, and P.J. Blau, *The effect of lubricating oil condition on the friction and wear of piston ring and cylinder liner materials in a reciprocating bench test.* Wear, 2005. **259**(7): p. 1048-1055.

80. Fang, H.L. and M.J. Lance, *Influence of soot surface changes on DPF regeneration.* SAE transactions, 2004. **113**(4): p. 2053-2061.

81. Ivleva, N.P., A. Messerer, and X. Yang, *Raman microspectroscopic analysis of changes in the chemical structure and reactivity of soot in a diesel exhaust aftertreatment model system.* Environmental Science & Technology, 2007. **41**(10): p. 3702-3707.

82. Ruiz, M., R.G. de Villoria, A. Millera, and M.U. Alzueta, *Influence of the temperature on the properties of the soot formed from C 2 H 2 pyrolysis.* Chemical Engineering Journal, 2007. **127**(1): p. 1-9.

83. Dennis, A., C.P. Garner, and D. Taylor, *The effect of EGR on diesel engine wear*. 1999, SAE Technical Paper.

84. Hu, E., X. Hu, T. Liu, L. Fang, K.D. Dearn, and H. Xu, *The role of soot particles in the tribological behavior of engine lubricating oils.* Wear, 2013. **304**(1): p. 152-161.

85. Kaneta, M., T. Irie, and H. Nishikawa, *Effects of soot on wear in elastohydrodynamic lubrication contacts.* Proceedings of the Institution of Mechanical Engineers, Part J: Journal of Engineering Tribology, 2006. **220**(3): p. 307-317.

86. Gautam, M., M. Durbha, K. Chitoor, and M. Jaraiedi, *Contribution of soot contaminated oils to wear*. 1998, SAE Technical Paper.

87. Sato, H., N. Tokuoka, H. Yamamoto, and M. Sasaki, *Study on wear mechanism by soot contaminated in engine oil (first report: relation between characteristics of used oil and wear)*. 1999, SAE Technical Paper.

88.   Müller, J.O., D.S. Su, R.E. Jentoft, and U. Wild, *Diesel engine exhaust emission: Oxidative behavior and microstructure of black smoke soot particulate.* Environmental Science & Technology, 2006. **40**(4): p. 1231-1236.

89.   Guo, M., Z. Cai, Z. Zhang, and M. Zhu, *Characterization and lubrication performance of diesel soot nanoparticles as oil lubricant additives.* RSC Advances, 2015. **5**(123): p. 101965-101974.

90.   Hu, E., X. Hu, T. Liu, Y. Liu, R. Song, and Y. Chen, *Investigation of morphology, structure and composition of biomass-oil soot particles.* Applied Surface Science, 2013. **270**: p. 596-603.

91.   Hu, E., X. Hu, T. Liu, R. Song, K.D. Dearn, and H. Xu, *Effect of TiF 3 catalyst on the tribological properties of carbon black-contaminated engine oils.* Wear, 2013. **305**(1): p. 166-176.

92.   Smiechowski, M.F. and V.F. Lvovich, *Iridium oxide sensors for acidity and basicity detection in industrial lubricants.* Sensors and Actuators B: Chemical, 2003. **96**(1): p. 261-267.

93.   Olomolehin, Y., R. Kapadia, and H. Spikes, *Antagonistic interaction of antiwear additives and carbon black.* Tribology Letters, 2010. **37**(1): p. 49.

94.   Pahalagedara, L., H. Sharma, and C.H. Kuo, *Structure and oxidation activity correlations for carbon blacks and diesel soot.* Energy & Fuels, 2012. **26**(11): p. 6757-6764.

95.   Sharma, H.N., L. Pahalagedara, A. Joshi and S.L. Suib, *Experimental study of carbon black and diesel engine soot oxidation kinetics using thermogravimetric analysis.* Energy & Fuels, 2012. **26**(9): p. 5613-5625.

96.   Müller, J.O., D.S. Su, U. Wild, and R. Schlogl, *Bulk and surface structural investigations of diesel engine soot and carbon black.* Physical Chemistry Chemical Physics, 2007. **9**(30): p. 4018-4025.

97.   Warmuth, A., P. Shipway, and W. Sun. *Fretting wear mapping: the influence of contact geometry and frequency on debris formation and ejection for a steel-on-steel pair*. *Proceedings of the Royal Society of London A: Mathematical, Physical and Engineering Sciences*. 2015: The Royal Society.

98.   Fouvry, S., C. Paulin, and S. Deyber, *Impact of contact size and complex gross–partial slip conditions on Ti–6Al–4V/Ti–6Al–4V fretting wear.* Tribology International, 2009. **42**(3): p. 461-474.

99.   Merhej, R. and S. Fouvry, *Contact size effect on fretting wear behaviour: application to an AISI 52100/AISI 52100 interface.* Lubrication Science, 2009. **21**(3): p. 83-102.

100.   Mulik, R. and S.S. Ramdasi, *Development of Indigenous Methodology for Design and Dynamic Analysis of Engine Valve Train System with Timing Chain Drive for High Speed Applications*. 2015, SAE Technical Paper.

101.   Polat, O., A.A. Ebrinc, C. Ozen, and S. Akca, *Timing Chain Wear Assessment with Different Type of Oils*. 2009, SAE Technical Paper.

102.   Chagas, C.B., T.C. de Freitas, and R. Pederiva, *Approach to the Main Transmission Phenomena for Timing Chain Drive Systems*. 2014, SAE Technical Paper.

103.   Alajmi, M. and A. Shalwan, *Correlation between Mechanical Properties with Specific Wear Rate and the Coefficient of Friction of Graphite/Epoxy Composites.* Materials, 2015. **8**(7): p. 4162-4175.

104.   Conwell, J.C. and G. Johnson, *Design, construction and instrumentation of a machine to measure tension and impact forces in roller chain drives.* Mechanism and Machine Theory, 1996. **31**(4): p. 525-531.

105.   Troedsson, I. and L. Vedmar, *A method to determine the dynamic load distribution in a chain drive.* Proceedings of the Institution of Mechanical Engineers, Part C: Journal of Mechanical Engineering Science, 2001. **215**(5): p. 569-579.

106.   Eldiwany, B.H. and K.M. Marshek, *Experimental load distributions for double pitch steel roller chains on polymer sprockets.* Mechanism and Machine Theory, 1989. **24**(5): p. 335-349.

107.   Naji, M. and K. Marshek, *Experimental determination of the roller chain load distribution.* Journal of Mechanical Design, 1983. **105**(3): p. 331-338.

108.   Eldiwany, B.H. and K.M. Marshek, *Experimental load distributions for double pitch steel roller chains on steel sprockets.* Mechanism and machine theory, 1984. **19**(6): p. 449-457.

109. Peeken, H. and W. Coenen, *Influence of oil viscosity and various additives on the wear of roller chains.* Wear, 1986. **108**(4): p. 303-321.

110. Radcliffe, S., *Wear mechanisms in unlubricated chains.* Tribology International, 1981. **14**(5): p. 263-269.

111. Wada, M., S. Ide, S. Miki, and A. Ehira, *Development of a small pitch silent chain for a single-stage cam drive system*. 1999, SAE Technical Paper.

112. Ward, A. and R. Dwyer-Joyce, *Model experiments on automotive chain drive systems.* Tribology Series, 2001. **39**: p. 851-861.

113. Lee, P. and M. Priest, *An innovative integrated approach to testing motorcycle drive chain lubricants.* Tribology Series, 2003. **43**: p. 291-298.

114. Torrance, M.A., A.V. Olver, and M. Willcock. *Effect of soot on wear in conforming contacts*. in *Tribology 2006*. 2006. London: Institution of Mechanical Engineers (IMechE)-Tribology Group.

115. Bhowmick, H., S. Majumdar, and S. Biswas, *Influence of physical structure and chemistry of diesel soot suspended in hexadecane on lubrication of steel-on-steel contact.* Wear, 2013. **300**(1): p. 180-188.

116. Bolla, M., D, Farrace, Y.M. Wright, K. Boulouchos, and E. Mastorakos, *Influence of turbulence–chemistry interaction for n-heptane spray combustion under diesel engine conditions with emphasis on soot formation and oxidation.* Combustion Theory and Modelling, 2014. **18**(2): p. 330-360.

117. Cheng, X., L. Chen, F. Yan, and S. Dong., *Study on soot formation characteristics in the diesel combustion process based on an improved detailed soot model.* Energy Conversion and Management, 2013. **75**: p. 1-10.

118. Celnik, M.S., M. Sander, A. Raj, R.H West, and M. Kraft, *Modelling soot formation in a premixed flame using an aromatic-site soot model and an improved oxidation rate.* Proceedings of the Combustion Institute, 2009. **32**(1): p. 639-646.

119. Tao, F., R.D. Reitz, D.E. Foster, and Y. Liu, *Nine-step phenomenological diesel soot model validated over a wide range of engine conditions.* International Journal of Thermal Sciences, 2009. **48**(6): p. 1223-1234.

120. Cheng, X., L. Chen, G. Hong, F. Yan, and S. Dong, *Modeling study of soot formation and oxidation in DI diesel engine using an improved soot model.* Applied Thermal Engineering, 2014. **62**(2): p. 303-312.

121. Schejbal, M., J. Stepanek, M. Marek, P. Koci, and M. Kubicek , *Modelling of soot oxidation by NO2 in various types of diesel particulate filters.* Fuel, 2010. **89**(9): p. 2365-2375.

122. Singh, J., R.I.A. Patterson, M. Kraft, and H. Wang, *Numerical simulation and sensitivity analysis of detailed soot particle size distribution in laminar premixed ethylene flames.* Combustion and Flame, 2006. **145**(1): p. 117-127.

123. Singh, J., M. Balthasar, M. Kraft, and W. Wagner, *Stochastic modeling of soot particle size and age distributions in laminar premixed flames.* Proceedings of the Combustion Institute, 2005. **30**(1): p. 1457-1465.

124. Takagishi, H., N. Ohta, M. Nakajima, and A. Nagakubo, *Introduction of a New Method of Solving Wear Problems Caused by the Swing Motion Occurring between the Roller and the Sliding Contact Surface*. 2010, SAE Technical Paper.

125. Takagishi, H., K. Shimoyama, and M. Asari, *Prediction of camshaft torque and timing chain load for turbo direct injection diesel engine*. 2004, SAE Technical Paper.

126. Stehouwer, D.M., G. Shank, S.N. Herzog, and C.W. Hyndman, *Sooted Diesel Engine Oil Pumpability Studies as the Basis of a New Heavy Duty Diesel Engine Oil Performance Specification*. 2002, SAE Technical Paper.

127. Khonsari, M.M. and E.R. Booser, *Applied Tribology: Bearing Design and Lubrication*. 2nd Edition, 2008: John Wiley, West Sussex.

128. Hamrock, B.J., S.R. Schmid, and B.O. Jacobson, *Fundamentals of Fluid Film Lubrication*. 2004: CRC Press.

129. ASTM International, *Standard Test Method for Linearly Reciprocating Ball-on-Flat Sliding Wear*. 2008, ASTM International.

130. Booth, J., K.D. Nelson, T.J. Harvey, and R.J.K. Wood, *The feasibility of using electrostatic monitoring to identify diesel lubricant additives and soot contamination interactions by factorial analysis.* Tribology International, 2006. **39**(12): p. 1564-1575.

131. Zhang, J., E. Yamaguchi, and H. Spikes, *Comparison of Three Laboratory Tests to Quantify Mild Wear Rate.* Tribology Transactions, 2013. **56**(6): p. 919-928.

132. Berbezier, I., J. Martin, and P. Kapsa, *The role of carbon in lubricated mild wear.* Tribology International, 1986. **19**(3): p. 115-122.

133. Wu, Y., W. Tsui, and T. Liu, *Experimental analysis of tribological properties of lubricating oils with nanoparticle additives.* Wear, 2007. **262**(7): p. 819-825.

134. Uy, D., R.J. Zdrodowski, A.E. O'Neill, and S.J. Simko, *Comparison of the effects of biodiesel and mineral diesel fuel dilution on aged engine oil properties.* Tribology Transactions, 2011. **54**(5): p. 749-763.

135. Uy, D., A.E. O'Neill, and S.J. Simko, *Soot–additive interactions in engine oils.* Lubrication Science, 2010. **22**(1): p. 19-36.

136. CoolAirVW. *Rhino Foot Valve Adjuster Set*. 2017 [cited 2017 February 14th]; Available from: https://www.coolairvw.co.uk/Item/Shop_by_Vehicle~Beetle_Products~Beetle_Engine_Products~Valve_Train~Rockers_and_Tappets~Performance_Tappets/AC1091642/T1_-P-_T2_-P-_T3_1200cc-1600cc_9mm__Rhino_Foot_Valve_Adjuster_Set.html.

137. CoolAirVW. *Elephant Foot Valve Adjuster*. 2017 [cited 2017 February 14th]; Available from: https://www.coolairvw.co.uk/Item/Shop_by_Vehicle~Beetle_Products~Beetle_Engine_Products~Valve_Train~Rockers_and_Tappets~Performance_Tappets/AC1091518/T1-P-T2-P-T3_1200cc-1600cc_8mm_Elephant_Foot_Style_Valve_Adjusters.html.

138. Dwyer-Joyce, R.S. *Contact Mechanics*. Tribological Design Data 1997; Available from: http://www.leonardocentre.co.uk/media/default/documents/book_3_contact_mechanics.pdf.

139. Ajayi, O. and R. Erck. *Variation of nominal contact pressure with time during sliding wear*. *International Joint Tribology Conference*. 2001.

140. Hutchings, I.M., *Tribology: Friction and Wear of Engineering Materials.* 1992: Butterworth-Heinemann, Oxford.

141. Zammit, J.P., P.J. Shayler, and I. Pegg, *Thermal coupling and energy flows between coolant, engine structure and lubricating oil during engine warm up*, *Vehicle Thermal Management Systems Conference and Exhibition (VTMS10)*. 2010, IMechE. p. 177-188.

142. Roberts, A., R. Brooks, and P. Shipway, *Internal combustion engine cold-start efficiency: A review of the problem, causes and potential solutions.* Energy Conversion and Management, 2014. **82**: p. 327-350.

143. Will, F. and B. Alberto, *A new method to warm up lubricating oil to improve the fuel efficiency during cold start.* SAE International Journal of Engines, 2011. **4**(1): p. 175-187.

144. Samhaber, C., A. Wimmer, and E. Loibner, *Modeling of engine warm-up with integration of vehicle and engine cycle simulation*, *Vehicle Thermal Management Systems Conference & Exhibition*. 2001, SAE International.

145. Sharma, S., S. Sangal, and K. Mondal, *On the optical microscopic method for the determination of ball-on-flat surface linearly reciprocating sliding wear volume.* Wear, 2013. **300**(1): p. 82-89.

146. Qu, J. and J.J. Truhan, *An efficient method for accurately determining wear volumes of sliders with non-flat wear scars and compound curvatures.* Wear, 2006. **261**(7): p. 848-855.

147. Brunskill, H., P. Harper, and R. Lewis, *The real-time measurement of wear using ultrasonic reflectometry.* Wear, 2015. **332**: p. 1129-1133.

148. Dwyer-Joyce, R., B. Drinkwater, and C. Donohoe, *The measurement of lubricant–film thickness using ultrasound.* Proceedings of the Royal Society of London. Series A: Mathematical, Physical and Engineering Sciences, 2003. **459**(2032): p. 957-976.

149. Brunskill, H.P., *The real-time characterisation of dry machine element contacts using ultrasonic reflectometry*, PhD Thesis, *Department of Mechanical Engineering*. 2013, University of Sheffield.

150. Clarke, A., I.J.J Weeks, H.P. Evans, and R.W. Snidle, *An investigation into mixed lubrication conditions using electrical contact resistance techniques.* Tribology International, 2016. **93**: p. 709-716.

151. Beamish, S.A., *Dynamic oil film thickness measurement for sliding contacts using ultrasonics*, MEng Thesis, *Department of Mechanical Engineering*. 2017, University of Sheffield.

152. Bayer, R.G., *Wear Analysis for Engineers*. 2002: HNB Publishing, New York.

153. Blau, P.J., *Interpretations of the friction and wear break-in behavior of metals in sliding contact.* Wear, 1981. **71**(1): p. 29-43.

154. Pogačnik, A. and M. Kalin, *How to determine the number of asperity peaks, their radii and their heights for engineering surfaces: A critical appraisal.* Wear, 2013. **300**(1): p. 143-154.

155. Gadelmawla, E.S., M.M. Koura, and T.M.A. Maksoud, *Roughness parameters.* Journal of Materials Processing Technology, 2002. **123**(1): p. 133-145.

156. Asango, A., A. La Rocca, and P. Shayler, *Investigating the Effect of Carbon Nanoparticles on the Viscosity of Lubricant Oil from Light Duty Automotive Diesel Engines*. 2014, SAE Technical Paper.

157. Aworanti, O.A., S.E. Agarry, and A.O. Ajani, *A laboratory study of the effect of temperature on densities and viscosities of binary and ternary blends of soybean oil, soy biodiesel and petroleum diesel oil.* Advances in Chemical Engineering and Science, 2012. **2**(04): p. 444.

158. Ajayi, O.O., A. Erdemir, and R.H. Lee, *Sliding Wear of Silicon Carbide—Titanium Boride Ceramic-Matrix Composite.* Journal of the American Ceramic Society, 1993. **76**(2): p. 511-517.

159. Liu, C., S. Nemoto, and S. Ogano, *Effect of soot properties in diesel engine oils on frictional characteristics.* Tribology Transactions, 2003. **46**(1): p. 12-18.

160. Green, D., *The tribological effects of soot contaminated lubricants on engine components*. PhD Thesis, *Department of Mechanical Engineering*. 2007, University of Sheffield.

161. Mainwaring, R., *Soot and wear in heavy duty diesel engines*. 1997, SAE Technical Paper.

162. Ryason, P., I. Chan, and J. Gilmore, *Polishing wear by soot.* Wear, 1990. **137**(1): p. 15-24.

163. Lewis, R. and T. Slatter, *Design for Reduced Wear*, *Automotive Lubricants and Testing*, C.S. Tung and E.G. Totten, Editors. 2012, ASTM International; SAE International: Eagan, Minnesota.

164. Williams, J., *Engineering Tribology*. 2005: Cambridge University Press, Cambridge.

165. Ko, P., P.L., S.S. Iyer, H. Vaughan, and M. Gadala, *Finite element modelling of crack growth and wear particle formation in sliding contact.* Wear, 2001. **251**(1): p. 1265-1278.

166. Suh, N.P., *The delamination theory of wear.* Wear, 1973. **25**(1): p. 111-124.

167. Suh, N.P., *An overview of the delamination theory of wear.* Wear, 1977. **44**(1): p. 1-16.

168. Jahanmir, S. and N. Suh, *Mechanics of subsurface void nucleation in delamination wear.* wear, 1977. **44**(1): p. 17-38.

169. Fleming, J. and N. Suh, *Mechanics of crack propagation in delamination wear.* Wear, 1977. **44**(1): p. 39-56.

170. de Abreu Duque, P., M.M. de Souza, J. Savoy, and G. Valentina, *Analysis of the Contact Pressure between Cams and Roller Followers in Assembled Camshafts*. 2011, SAE Technical Paper.

171. Phoenix, *PLINT Tribology Products-TE 54 Mini Traction Machine*. 2011, Phoenix Tribology Limited.

172. Phoenix, *PLINT Tribology Products-TE 54 Mini Traction Machine*. 2011, Phoenix Tribology Limited.

173.   Escobar, J.A., *Stress and fatigue analysis of svi-tested camshaft lobes.* Master of Science Thesis in Materials Science and Engineering, Virginia Polytechnic Institute, 1996.

174.   Nallicheri, N.V., J.P. Clark, and F.R. Field, *An economic assessment of alternative manufacturing processes for the camshaft*. 1990, SAE Technical Paper.

175.   Khurram, M., R.A. Mufti, R. Zahid, N. Afzal, and U. Bhutta, *Experimental measurement of the roller slip in end-pivoted roller follower valve train.* Proc. of IMechE Part J: Journal of Engineering Tribology, 2015. **229**(9): p. 1047-1055.

176.   Skołek, E., K. Dudzinska, and J. Kaminski, *Corrosion Resistance of The Bearing Steel 67SiMnCr6-6-4 with Nanobainitic Structure.* Archives of Metallurgy and Materials, 2015. **60**(1).

177.   Skołek, E., K. Wasiak, and W.A. Świątnicki, *Structure and Properties of the Carburised Surface Layer on 35CrSiMn5-5-4 Steel after Nanostructurization Treatment.* Structure, 2015. **933**: p. 939.

178.   Ernesto, A., D. Mazuyer, and J. Cayer-Barrioz, *The combined role of soot aggregation and surface effect on the friction of a lubricated contact.* Tribology Letters, 2014. **55**(2): p. 329-341.

179.   Beschorner, K.E., M.S. Redfern, W.L. Porter, and R.E. Debski, *Effects of slip testing parameters on measured coefficient of friction.* Applied Ergonomics, 2007. **38**(6): p. 773-780.

180.   Meunier, C., D. Mazuyer, P. Vergne, and M. El Fassi, *Correlation between the film forming ability and rheological properties of new and aged low sulfated ash, phosphorus and sulfur (Low SAPS) automotive lubricants.* Tribology Transactions, 2009. **52**(4): p. 501-510.

181.   Kano, M., *Super low friction of DLC applied to engine cam follower lubricated with ester-containing oil.* Tribology International, 2006. **39**(12): p. 1682-1685.

182.   Heck, M., H.M. Ortner, S. Flege, and U. Reuter, *Analytical investigations concerning the wear behaviour of cutting tools used for the machining of compacted graphite iron and grey cast iron.* International Journal of Refractory Metals and Hard Materials, 2008. **26**(3): p. 197-206.

183.   Kowandy, C., C. Richard, Y.M. Chen, and J.J. Tessier, *Correlation between the tribological behaviour and wear particle morphology—case of grey cast iron 250 versus Graphite and PTFE.* Wear, 2007. **262**(7): p. 996-1006.

184.   Adachi, K., U. Cho, S.K. Sinha, and K. Kato, *Self-lubrication by formation of graphite films in the sliding of silicon nitride against cast iron.* Tribology Transactions, 2001. **44**(1): p. 41-46.

185.   Dienwiebel, M., N. Pradeep, and G.S. Verhoeven, *Model experiments of superlubricity of graphite.* Surface Science, 2005. **576**(1): p. 197-211.

186.   Diew, M., A. Ernesto, J. Cayer-Barrioz, D. Mazuyer, *Stribeck and traction curves under moderate contact pressure: from friction to interfacial rheology.* Tribology Letters, 2015. **57**(1): p. 8.

187.   Descartes, S., C. Godeau, and Y. Berthier, *Friction and lifetime of a contact lubricated by a solid third body formed from an MoS 1.6 coating at low temperature.* Wear, 2015. **330**: p. 478-489.

188.   Kuhnell, B.T., *Wear in rolling element bearings and gears- How age and contamination affect them.* Machinery Lubrication, 2004: p. 62-64.

189.   Komvopoulos, K., *Subsurface crack mechanisms under indentation loading.* Wear, 1996. **199**(1): p. 9-23.

190.   Jayaraman, S., K. Sadeghipour, and G. Baran, *Finite element analysis of horizontal and branched subsurface cracks in brittle materials.* Wear, 1997. **208**(1): p. 237-242.

191.   Liu, Y., L. Liu, and S. Mahadevan, *Analysis of subsurface crack propagation under rolling contact loading in railroad wheels using FEM.* Engineering Fracture Mechanics, 2007. **74**(17): p. 2659-2674.

192.   Johnson, K.L., *Contact Mechanics*. 2004: Cambridge University Press, Cambridge.

193.   Sun, Z. and C. Hao, *Conformal contact problems of ball-socket and ball.* Physics Procedia, 2012. **25**: p. 209-214.

194.   Liu, Y., B. Stratman, and S. Mahadevan, *Fatigue crack initiation life prediction of railroad wheels.* International Journal of fatigue, 2006. **28**(7): p. 747-756.

195. Fang, X., C. Zhang, X. Chen, Y. Wang, and Y. Tan, *A new universal approximate model for conformal contact and non-conformal contact of spherical surfaces.* Acta Mechanica, 2015. **226**(6): p. 1657-1672.

196. Blau, P. and S. Tung, *Bench performance test methods for lubricated engine materials.* Automotive Lubricants and Testing, ASTM International, 2012: p. 215-230.

197. Kruger, K.M., N.M. Tikekar, A.D. Heiner, and T.E. Baer, *Encoding scratch and scrape features for wear modeling of total joint replacements.* Computational and Mathematical Methods in Medicine, 2013.

198. Sopouch, M., Hellinger, W. and Priebsch, H. H., *Simulation of Engine's Structure Borne Noise Excitation Due to the Timing Chain Drive*, *SAE 2002 World Congress*. 2002, SAE Technical Paper.

199. Uysal, U. and O. Akalin, *Optimization of Timing Drive System Design Parameters for Reduced Engine Friction*. 2010, SAE Technical Paper.

200. Young, J.D., *Inverted Tooth Chain Sprocket with Frequency-Modulated Meshing Features to Reduce Camshaft Drive Noise*, *Noise and Vibration Conference and Exhibition*. 2007, SAE Technical Paper.

201. Young, J.D., Marshek, K. M., Poiret, C. and Chevee P., *Camshaft Roller Chain Drive with Reduced Meshing Impact Noise Levels*, *Noise & Vibration Conference and Exhibition*. 2003, SAE Technical Paper.

202. Liu, S.P., Dent, A. M., Thornton, J. W., Trethewey, M. W., Wang, K. W., Hayek, S. I., Chen, F. H. K., *Experimental Evaluation of Automotive Timing Chain Drive Impact Noise*, *SAE Noise and Vibration Conference and Exposition*. 1995, SAE Technical Paper.

203. Liu, J.S., D. Ramnath, and R. Adhikari, *Analytical predictions for the chain drive system resonance*. 2007, SAE Technical Paper.

204. Wos, S., W. Koszela, and P. Pawlus, *Tribological behaviours of textured surfaces under conformal and non-conformal starved lubricated contact conditions.* Proceedings of the Institution of Mechanical Engineers, Part J: Journal of Engineering Tribology, 2015. **229**(4): p. 398-409.

205. Elmatic. *Cartridge heaters applications*. 2015 [cited 2015 September 9th]; Available from: http://www.elmatic.co.uk/cartridge-heaters/.

206. Leespring. *Torsion springs data sheet*. 2015 [cited 2015 September 10th]; Available from: http://www.leespring.com/uk_browse_catalog.asp?CountryCode=011&rbunitOfMeasure=Metric&springType=T&partnum=&UnitOfMeasure=metric&specsCriteria=&subType=&isMIL=&pageNumber=89.

207. Wada, M., Ide, Shoichiro, Miki, Sadao and Ehira, Atsushi, *Development of a Small Pitch Silent Chain for a Single-Stage Cam Drive System*, in *International Congress and Exposition*. 1999, SAE Technical Paper.

208. Autoplius. *Mercedes-Benz M271 Engine*. [cited 2016, November 11th]; Available from: https://www.google.co.uk/url?sa=i&rct=j&q=&esrc=s&source=images&cd=&cad=rja&uact=8&ved=0ahUKEwiylO6317jUAhUHY1AKHRNoC7EQjRwIBw&url=https%3A%2F%2Fru.autoplius.lt%2Fobjavlenija%2Fmercedes-benz-c-klase-siulome-mercedes-benz-m271-a2710510003-5119805.html&psig=AFQjCNGBU8S4VO7HzJGbbpsEl9WB1MrdAw&ust=1497369688789666.

209. Dwyer-Joyce, R.S., Lewis, R., Ward, A. and Patterson, E. A., *Determination of Impact Stresses in an Automotive Chain Drive Component*, in *SAE World Congress*. 2006, SAE Technical Paper.

210. INA-Schaeffler, K., *Testing- Valvetrain Systems for Combustion Engines*. 2003.

Appendices

Appendix I – Technical Data Sheet of the Mineral Oil

Shell Helix *HX5 15W-40*

Premium multi-grade motor oil - Helps to remove sludge from dirty engines

Shell Helix HX5 is designed to help provide consistent engine performance. It works hard to help protect against engine sludge and reduce wear. It is suitable for a wide variety of vehicles for everyday driving conditions.

Proud Drivers Choose Shell Helix

Performance, Features & Benefits

- **Active cleansing technology**
  Actively locks away harmful performance-robbing deposits.

- **Active clean-up**
  Helps to remove sludge left behind by inferior oils [2]

- **Effective wear protection** [1]
  Helps to protect against wear and neutralise corrosive combustion acids.

- **Resistance to oil degradation** [2]
  Helps to maintain protection throughout the oil-drain interval.

- **Multi-fuel capability**
  Can be used for gasoline, diesel and gas engines, and is also suitable for biodiesel and gasoline/ethanol blends.

1 Based on Sequence IVA engine test carried out at an independent laboratory

2 Based on a severe sludge clean-up test

Main Applications

- Shell Helix HX5's premium multigrade formulation helps to provide protection in everyday daily driving conditions. Shell Helix HX5 can be used for gasoline, diesel and gas engines, and it is also suitable for biodiesel and gasoline/ethanol blends.

Specifications, Approvals & Recommendations

- API SN/CF
- ACEA A3/B3
- To find the right Shell Helix product for your vehicles and equipment, please consult Shell LubeMatch at: http://lubematch.shell.com
- Advice on applications not covered here may be obtained from your Shell or Shell Lubricants distributor representatives or technical help desks.

Typical Physical Characteristics

Properties			Method	Shell Helix HX5
SAE Viscosity Grade				15W-40
Kinematic Viscosity	@40°C	cSt	ASTM D445	106.00
Kinematic Viscosity	@100°C	cSt	ASTM D445	14.27
Viscosity Index			ASTM D2270	137
MRV	@-25°C	cP	ASTM D4684	17000
Density	@15°C	kg/m³	ASTM D4052	865.8
Flash Point		°C	ASTM D92	241
Pour Point		°C	ASTM D97	-45

These characteristics are typical of current production. Whilst future production will conform to Shell's specification, variations in these characteristics may occur.

Appendix II – Safety Data Sheet of the Carbon Black

Safety data sheet
according to 1907/2006/EC, Article 31

1 Identification of the substance/mixture and of the company/undertaking

Product identifier

Trade name	*Carbon black, acetylene, 100% compressed*
Stock number:	45527
CAS Number:	1333-86-4
EC number:	215-609-9

Relevant identified uses of the substance or mixture and uses advised against

Sector of Use   SU24 Scientific research and development

Details of the supplier of the safety data sheet

Manufacturer/Supplier:
Alfa Aesar, A Johnson Matthey Company
Shore Road
Port of Heysham Industrial Park
Heysham Lancashire LA3 2XY
United Kingdom
Office Tel: +44 (0) 1524 850506
Office Fax: +44 (0) 1524 850608
Email: uktech@alfa.com
www.alfa.com

Informing department: Product safety department.
Emergency telephone number: Call Carechem 24 at +44 (0) 1865 407333 (English only); +44 (0) 1235 239670 (Multi-language)

2 Hazards identification

Classification of the substance or mixture
Classification according to Regulation (EC) No 1272/2008

GHS02 flame

Flam. Sol. 2 H228 Flammable solid.

GHS08 health hazard

Carc. 2   H351 Suspected of causing cancer.

Classification according to Directive 67/548/EEC or Directive 1999/45/EC

Xn; Harmful

R40:   Limited evidence of a carcinogenic effect.

F; Highly flammable

R11:   Highly flammable.

Information concerning particular hazards
for human and environment: Not applicable

Label elements
Labelling according to Regulation (EC) No 1272/2008   The substance is classified and labelled according to the CLP regulation.

Hazard pictograms

GHS02 GHS08

Signal word	Warning
Hazard statements	H228 Flammable solid.
	H351 Suspected of causing cancer.
Precautionary statements	P210 Keep away from heat/sparks/open flames/hot surfaces. - No smoking.
	P241 Use explosion-proof electrical/ventilating/lighting/equipment.
	P280 Wear protective gloves/protective clothing/eye protection/face protection.
	P281 Use personal protective equipment as required.
	P405 Store locked up.
	P501 Dispose of contents/container in accordance with local/regional/national/international regulations.

Other hazards
Results of PBT and vPvB assessment

PBT: Not applicable.
vPvB: Not applicable.

3 Composition/information on ingredients

Chemical characterization: Substances

CAS# Designation:	Carbon black (CAS# 1333-86-4)
Identification number(s):	
EC number:	215-609-9

4 First aid measures

Description of first aid measures

After inhalation	Supply fresh air. If required, provide artificial respiration. Keep patient warm. Consult doctor if symptoms persist.
	Seek immediate medical advice.
After skin contact	Instantly wash with water and soap and rinse thoroughly.
	Seek immediate medical advice.
After eye contact	Rinse opened eye for several minutes under running water. Then consult doctor.
After swallowing	In case of persistent symptoms consult doctor.

Information for doctor
Most important symptoms and effects, both acute and delayed   No further relevant information available.
Indication of any immediate medical attention and special treatment needed   No further relevant information available.

5 Firefighting measures

Extinguishing media

Suitable extinguishing agents   In case of fire, use sand, carbon dioxide or powdered extinguishing agent. Never use water.

Special hazards arising from the substance or mixture   Can be released in case of fire:
Carbon monoxide and carbon dioxide

Advice for firefighters

Protective equipment: Wear self-contained breathing apparatus.
Wear full protective suit.

GB

Safety data sheet
according to 1907/2006/EC, Article 31

Trade name *Carbon black, acetylene, 100% compressed*

(Contd. of page 1)

6 Accidental release measures

Personal precautions, protective equipment and emergency procedures
Wear protective equipment. Keep unprotected persons away.
Ensure adequate ventilation
Keep away from ignition sources

Environmental precautions:
Do not allow material to be released to the environment without proper governmental permits.

Methods and material for containment and cleaning up:
Dispose of contaminated material as waste according to item 13.
Ensure adequate ventilation.
Keep away from ignition sources.

Reference to other sections
See Section 7 for information on safe handling
See section 8 for information on personal protection equipment.
See Section 13 for information on disposal.

7 Handling and storage

Handling
Precautions for safe handling
Keep containers tightly sealed.
Store in cool, dry place in tightly closed containers.
Ensure good ventilation/exhaustion at the workplace.

Information about protection against explosions and fires:
Protect against electrostatic charges.

Conditions for safe storage, including any incompatibilities
Storage
Requirements to be met by storerooms and containers:
Store in cool location.

Information about storage in one common storage facility:
Store away from oxidizing agents.

Further information about storage conditions:
Keep container tightly sealed.
Store in cool, dry conditions in well sealed containers.

Specific end use(s)
No further relevant information available.

8 Exposure controls/personal protection

Additional information about design of technical systems:
Properly operating chemical fume hood designed for hazardous chemicals and having an average face velocity of at least 100 feet per minute.

Control parameters
Components with critical values that require monitoring at the workplace:

Carbon black
mg/m3
ACGIH TLV   3.5; Not classified as a human carcinogen
Belgium TWA   3.5
Denmark TWA   3.5
Finland TWA   3.5; 7-STEL
France VME   3.5
Korea TLV   3.5; Not classified as a human carcinogen
Netherlands MAC-TGG 3.5
Norway TWA   3.5
Russia   4-STEL
Sweden NGV   3 (dust)
United Kingdom TWA 3.5; 7-STEL
USA PEL   3.5

Additional information:
No data

Exposure controls
Personal protective equipment
General protective and hygienic measures
The usual precautionary measures should be adhered to in handling the chemicals.
Keep away from foodstuffs, beverages and food.
Instantly remove any soiled and impregnated garments.
Wash hands during breaks and at the end of the work.

Breathing equipment:
Use breathing protection with high concentrations.

Protection of hands:
Check protective gloves prior to each use for their proper condition.

Material of gloves
Impervious gloves
The selection of the suitable gloves does not only depend on the material, but also on further marks of quality and varies from manufacturer to manufacturer.

Penetration time of glove material
Not determined

Eye protection:
Safety glasses
Face protection

Body protection:
Protective work clothing.

9 Physical and chemical properties

Information on basic physical and chemical properties
General Information
Appearance:

Form:	Powder
Colour:	Black
Smell:	Odourless
Odour threshold:	Not determined.
pH-value:	Not applicable.

Change in condition
Melting point/Melting range:	3652-3697°C
Boiling point/Boiling range:	4200°C
Sublimation temperature / start:	Not determined
Flash point:	Not applicable
Inflammability (solid, gaseous)	Highly flammable.
Ignition temperature:	900°C
Decomposition temperature:	Not determined
Self-inflammability:	Not determined.

(Contd. on page 3)
GB

Printing date 12.09.2011

Trade name *Carbon black, acetylene, 100% compressed*

(Contd. of page 2)

Critical values for explosion:	
Lower:	Not determined
Upper:	Not determined
Steam pressure:	Not applicable.

Density at 20°C	1.8-2.1 g/cm³
Relative density	Not determined.
Vapour density	Not applicable.
Evaporation rate	Not applicable.

Solubility in / Miscibility with	
Water:	Insoluble

Segregation coefficient (n-octanol/water):	Not determined.

Viscosity:	
dynamic:	Not applicable.
kinematic:	Not applicable.
Other information	No further relevant information available.

10 Stability and reactivity

Reactivity	
Chemical stability	
Thermal decomposition / conditions to be avoided:	No decomposition if used and stored according to specifications.
Possibility of hazardous reactions	No dangerous reactions known
Incompatible materials:	Oxidizing agents
Hazardous decomposition products:	Carbon monoxide and carbon dioxide

11 Toxicological information

Information on toxicological effects
Acute toxicity:

LD/LC50 values that are relevant for classification:

Oral	LD50	>15400 mg/kg (rat)
Dermal	LD50	>3 gm/kg (rabbit)

Primary irritant effect:	
on the skin:	No irritant effect.
on the eye:	May cause irritation
Sensitization:	No sensitizing effect known.
Other information (about experimental toxicology):	Mutagenic effects have been observed on tests with bacteria. Mutagenic effects have been observed on tests with laboratory animals.
Additional toxicological information:	To the best of our knowledge the acute and chronic toxicity of this substance is not fully known. IARC-2B: Possibly carcinogenic to humans: limited evidence in humans in the absence of sufficient evidence in experimental animals. ACGIH A4: Not classifiable as a human carcinogen: Inadequate data on which to classify the agent in terms of its carcinogenicity in humans and/or animals.
CMR effects (carcinogenity, mutagenicity and toxicity for reproduction)	Carc. 2

12 Ecological information

Toxicity	
Acquatic toxicity:	No further relevant information available.
Persistence and degradability	No further relevant information available.
Behaviour in environmental systems:	
Bioaccumulative potential	No further relevant information available.
Mobility in soil	No further relevant information available.
Additional ecological information:	
General notes:	Generally not hazardous for water. Do not allow material to be released to the environment without proper governmental permits.
Results of PBT and vPvB assessment	
PBT:	Not applicable.
vPvB:	Not applicable.
Other adverse effects	No further relevant information available.

13 Disposal considerations

Waste treatment methods	
Recommendation	Hand over to disposers of hazardous waste. Must be specially treated under adherence to official regulations. Consult state, local or national regulations for proper disposal.
Uncleaned packagings:	
Recommendation:	Disposal must be made according to official regulations.

14 Transport information

UN-Number	
ADR, IMDG, IATA	UN1325

UN proper shipping name	
ADR	1325 FLAMMABLE SOLID, ORGANIC, N.O.S. (carbon black)
IMDG, IATA	FLAMMABLE SOLID, ORGANIC, N.O.S. (carbon black)

Transport hazard class(es)
ADR

Class	4.1 (F1) Flammable solids, self-reactive substances and solid desensitised explosives.

GB

Safety data sheet
according to 1907/2006/EC, Article 31

Trade name *Carbon black, acetylene, 100% compressed*

(Contd. of page 3)

Label	4.1

IMDG, IATA

Class	4.1 Flammable solids, self-reactive substances and solid desensitised explosives.
Label	4.1
Packing group	
ADR, IMDG, IATA	III
Environmental hazards:	
Marine pollutant:	No
Special precautions for user	Warning: Flammable solids, self-reactive substances and solid desensitised explosives.
Kemler Number:	40
Transport in bulk according to Annex II of MARPOL73/78 and the IBC Code	Not applicable.
Transport/Additional information:	
ADR	
Limited quantities (LQ)	5 kg
Transport category	3
Tunnel restriction code	E
UN "Model Regulation":	UN1325, FLAMMABLE SOLID, ORGANIC, N.O.S. (carbon black), 4.1, III

15 Regulatory information

Safety, health and environmental regulations/legislation specific for the substance or mixture
Labelling according to Regulation (EC) No 1272/2008   The substance is classified and labelled according to the CLP regulation.
Hazard pictograms

GHS02 GHS08

Signal word	Warning
Hazard statements	H228 Flammable solid.
	H351 Suspected of causing cancer.
Precautionary statements	P210 Keep away from heat/sparks/open flames/hot surfaces. - No smoking.
	P241 Use explosion-proof electrical/ventilating/lighting/equipment.
	P280 Wear protective gloves/protective clothing/eye protection/face protection.
	P281 Use personal protective equipment as required.
	P405 Store locked up.
	P501 Dispose of contents/container in accordance with local/regional/national/international regulations.
National regulations	
Information about limitation of use:	Employment restrictions concerning young persons must be observed.
	For use only by technically qualified individuals.
Water hazard class:	Generally not hazardous for water.
Chemical safety assessment:	A Chemical Safety Assessment has not been carried out.

16 Other information

Employers should use this information only as a supplement to other information gathered by them, and should make independent judgement of suitability of this information to ensure proper use and protect the health and safety of employees. This information is furnished without warranty, and any use of the product not in conformance with this Material Safety Data Sheet, or in combination with any other product or process, is the responsibility of the user.

Department issuing data specification sheet: Health, Safety and Environmental Department.

Contact:	Zachariah C. Holt
	Global EHS Manager
Abbreviations and acronyms:	ADR: Accord européen sur le transport des marchandises dangereuses par Route (European Agreement concerning the International Carriage of Dangerous Goods by Road)
	RID: Règlement international concernant le transport des marchandises dangereuses par chemin de fer (Regulations Concerning the International Transport of Dangerous Goods by Rail)
	IMDG: International Maritime Code for Dangerous Goods
	IATA: International Air Transport Association
	ICAO: International Civil Aviation Organization
	GHS: Globally Harmonized System of Classification and Labeling of Chemicals
	EINECS: European Inventory of Existing Commercial Chemical Substances
	CAS: Chemical Abstracts Service (division of the American Chemical Society)
	LC50: Lethal concentration, 50 percent
	LD50: Lethal dose, 50 percent
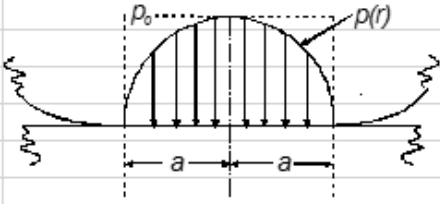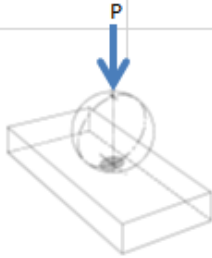
GB

Appendix III – Viscosity of the Sooty-oil Surrogates

		Spindle = RV2-6
		Speed = 70rpm-150rpm
		Torque = 10.4% (minimum)

Temp (°C)	Viscosity																	
	0%			3%			5%			7%			10%			12%		
	cP	Density	cSt	cP	Density	cSt	cP	Density	cSt	cP	Density	cSt	cP	Density	cSt	cP	Density	cSt
22	208.6	0.8622	241.94	251.7	0.8771	286.96	295.6	0.8871	333.23	373.3	0.897	416.15	729	0.913	798.51	1256	0.9239	1359.4
30	148.6	0.8578	173.23	201.1	0.8727	230.44	236.7	0.8826	268.19	320.8	0.8925	359.45	656	0.9083	722.2	1192	0.9192	1296.7
40	94.86	0.8524	111.29	159.7	0.8671	184.17	209.9	0.877	239.35	304.6	0.8868	343.48	515	0.9026	570.6	1056	0.9134	1156.1
50	72	0.8469	85.015	96.14	0.8616	111.59	160	0.8714	183.62	275.5	0.8811	312.67	457	0.8968	509.6	968	0.9075	1066.6
60	57.14	0.8414	67.907	78.29	0.856	91.458	128.8	0.8657	148.77	245	0.8755	279.85	428	0.891	480.36	912	0.9017	1011.4
70	42.29	0.836	50.587	67.43	0.8505	79.285	121.2	0.8601	140.91	230.3	0.8698	264.78	390	0.8852	440.57	840	0.8958	937.66
80	32	0.8305	38.529	55.86	0.8449	66.113	115	0.8545	134.58	216.2	0.8641	250.2	369	0.8794	419.58	804	0.89	903.37
90	23.43	0.8251	28.397	49.14	0.8394	58.544	113.1	0.8489	133.23	208.3	0.8584	242.65	358	0.8737	409.76	792	0.8842	895.77
100	14.86	0.8196	18.13	42.42	0.8338	50.874	111.2	0.8433	131.86	200.4	0.8528	235	347	0.8679	399.82	780	0.8783	888.07
Density at 15°C	0.866			0.881			0.891			0.901			0.917			0.928		

Appendix IV – Hertzian Point Contact Pressure Calculations

Contact Pressure Calculation (Hertzian)					
$$p_0 = \frac{3P}{2\pi a^2}$$					
Radius of Ball Specimen in x direction, R_{x1}	0.003	0.003	0.003	0.003	0.003 m
Radius of Flat Specimen in x direction, R_{x2}	1.00E+100	1.00E+100	1.00E+100	1.00E+100	1.00E+100 m
Radius of Ball Specimen in y direction, R_{y1}	0.003	0.003	0.003	0.003	0.003 m
Radius of Flat Specimen in y direction, R_{y2}	1.00E+100	1.00E+100	1.00E+100	1.00E+100	1.00E+100 m
Effective Radius in x direction, R_x	0.003	0.003	0.003	0.003	0.003 m
Effective Radius in y direction, R_y	0.003	0.003	0.003	0.003	0.003 m
Load, P	50	75	100	125	150 N
Ball Radius	3	3	3	3	3 mm
Sliding speed	0.133	0.133	0.133	0.133	0.133 m/s
Modulus of elasticity of Ball Specimen, E_1	215	215	215	215	215 Gpa
Modulus of elasticity of Flat Specimen, E_2	103	103	103	103	103 GPa
Poisson ratio of Ball Specimen, υ_1	0.3	0.3	0.3	0.3	0.3
Poisson ratio of Flat Specimen, υ_2	0.26	0.26	0.26	0.26	0.26
Reduced Radius, R'	0.0015	0.0015	0.0015	0.0015	0.0015 m
Effective Modulus of Elasticity, E'	1.505E+11	1.505E+11	1.505E+11	1.505E+11	1.505E+11 Pa
a	0.0001143	0.0001309	0.0001441	0.0001552	0.0001649 m
a	0.1143329	0.1308785	0.1440504	0.1551736	0.1648966 mm
Maximum contact pressure, p_o	**1.8262868**	**2.0905766**	**2.3009772**	**2.4786526**	**2.6339614** GPa
Average contact pressure, p_m	**1.2175246**	**1.3937177**	**1.5339848**	**1.6524351**	**1.7559743** GPa
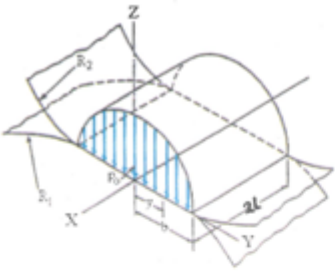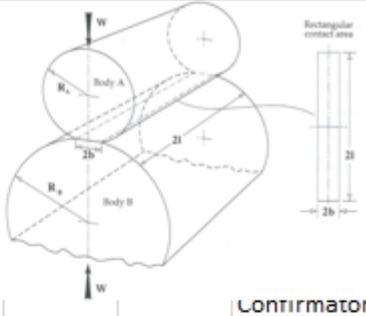
Appendix V – Minimum Film Thickness and Lambda Ratio Calculations

Film Thickness Calculation

Lubricant Temperature, T	100	°C
Load, w	50	N
Ball Radius	3	mm
Sliding speed	0.133	m/s
Modulus of elasticity of Ball Specimen	215	GPa
Modulus of elasticity of Flat Specimen	103	GPa
Poisson ratio of Ball Specimen	0.3	
Poisson ratio of Flat Specimen	0.26	
Reduced Radius of Curvature, R'	0.0015	m
Mean surface velocity, u	0.0665	m/s
Effective Modulus of Elasticity, E'	1.51E+11	Pa
Dimensionless Load Parameter, W	0.000148	
Elipticity Parameter, k	1.034	
r.m.s roughness, σ*	6.53E-07	m

Minimum Film Thickness, h_{min} (m) — bar chart with values for 0%CB, 3%CB, 5%CB, 7%CB, 10%CB, 12%CB

Lambda Ratio, λ — bar chart with values for 0%CB, 3%CB, 5%CB, 7%CB, 10%CB, 12%CB

$$H_{min} = 3.63 U^{0.68} G^{0.49} W^{-0.073} \left(1 - e^{-0.68k}\right)$$

Sooty oil	Kinematic Viscosity @40°C (cSt)	Kinematic Viscosity @100°C (cSt)	Density at 15°C (g/cm³)	Density at T°C (g/cm³)	Dynamic viscosity at temperature T & atm pressure, (Pa.s)	Pressure Viscosity-coefficient, αEHL (Pa⁻¹)	Dimensionless Material Parameter, G	Dimensionless Speed Parameter, U	Dimensionless Minimum Film Thickness, H_{min}	Minimum Film Thickness, h_{min} (m)	Lambda Ratio, λ
0%CB	106	14.27	0.866	0.819626	0.0116961	1.43E-08	2157.7593	3.44E-12	2.408E-06	3.61E-09	0.0055321
3%CB	184.17	50.874	0.881	0.833822	0.0424199	7.04E-09	1059.7723	1.25E-11	4.082E-06	6.12E-09	0.009377
5%CB	239.35	131.86	0.891	0.843287	0.1111958	2.29E-09	344.60256	3.27E-11	4.533E-06	6.8E-09	0.0104133
7%CB	343.44	235	0.901	0.852751	0.2003966	1.16E-09	174.22676	5.9E-11	4.844E-06	7.27E-09	0.0111274
10%CB	570.6	399.82	0.917	0.867895	0.3470016	9.72E-10	146.27867	1.02E-10	6.459E-06	9.69E-09	0.0148363
12%CB	1156.1	888.07	0.928	0.878306	0.7799969	5.82E-10	87.598742	2.3E-10	8.714E-06	1.31E-08	0.0200174

Appendix VI – Post-test Contact Pressure Calculations

$$P_n = \frac{P}{\pi a b}; \qquad a = \frac{1}{2} w_n; \qquad b = \sqrt{2rh - h^2}$$

Ball specimen radius, r   0.003 m

	0wt%CB	3wt%CB	5wt%CB	7wt%CB	10wt%CB	12wt%CB	D1-75N	D2-100N	D3-125N	D4-150N
Wear scar width, w_n (m)	3.84E-04	3.95E-04	4.55E-04	5.05E-04	5.39E-04	5.70E-04	4.92E-04	5.89E-04	6.51E-04	1.05E-03
Wear depth, h (mm)	0.0054	0.00552	0.00669	0.00924	0.01122	0.01313	0.00835	0.01259	0.01655	0.04312
Wear depth, h (m)	0.0000054	5.52E-06	6.69E-06	9.24E-06	1.12E-05	1.31E-05	8.35E-06	1.26E-05	1.66E-05	4.31E-05
Half-length of elliptical wear scar major axis, a (m)	1.92E-04	1.98E-04	2.28E-04	2.53E-04	2.70E-04	2.85E-04	2.46E-04	2.95E-04	3.26E-04	5.25E-04
Half-length of elliptical wear scar minor axis, b (m)	0.0001799	0.000182	0.0002	0.000235	0.000259	0.00028	0.000224	0.000275	0.000315	0.000507
Normal Load, P (N)	5.00E+01	50	50	50	50	50	75	100	125	150
Post-test nominal contact pressure, P_n (GPa)	4.61E-01	4.43E-01	3.49E-01	2.68E-01	2.28E-01	1.99E-01	4.34E-01	3.94E-01	3.88E-01	1.79E-01
Post-test nominal contact pressure, P_n (MPa)	4.61E+02	4.43E+02	3.49E+02	2.68E+02	2.28E+02	1.99E+02	4.34E+02	3.94E+02	3.88E+02	1.79E+02
P_n (GPa)	0.461	0.443	0.349	0.268	0.228	0.199	0.434	0.394	0.388	0.179

Appendix VII - Hertzian Line Contact Pressure Calculations

Line Contact Pressure Calculation (Hertzian)

$$b = \left(\frac{4PR'}{\pi l E'}\right)^{1/2}; \quad p_o = \frac{P}{\pi b l}$$

					Confirmatory	
Radius of Upper Disc, R_1	0.0125	0.0125	0.0125	0.0125	0.01	m
Radius of Lower Disc, R_2	2.50E-02	2.50E-02	2.50E-02	2.50E-02	1.50E-02	m
Width of Upper Disc, $2l$	8.00E-03	8.00E-03	8.00E-03	8.00E-03	1.00E-02	m
Width of Lower Disc	1.00E-02					m
Load, P	100	200	300	400	5	N
Nominal Desired Surface Speed (m/s)	0.5	1	1.5	2		m/s
Desired Slip (%)	5	10	15	20		%
Modulus of elasticity of Upper Disc, E_1	215	215	215	215	211	GPa
Modulus of elasticity of Lower Disc, E_2	215	215	215	215	211	GPa
Poisson ratio of Upper Disc, υ_1	0.3	0.3	0.3	0.3	0.3	
Poisson ratio of Lower Disc, υ_2	0.3	0.3	0.3	0.3	0.3	
Reduced Radius, R'	8.33E-03	8.33E-03	8.33E-03	8.33E-03	6.00E-03	m
Effective Modulus of Elasticity, E'	2.4E+11	2.4E+11	2.4E+11	2.4E+11	2.3E+11	Pa
Contact area dimensions, b	3.4E-05	4.7E-05	5.8E-05	6.7E-05	5.7E-06	m
Maximum contact pressure, p_o	2.37E+08	3.36E+08	4.11E+08	4.75E+08	5.55E+07	Pa
Average contact pressure, $p_{average}$	1.87E+08	2.64E+08	3.23E+08	3.73E+08	4.36E+07	Pa
Maximum deflection, δ	4.9E-07	9.4E-07	1.4E-06	1.8E-06	2.4E-08	m
Maximum shear stress, τ_{max}	7.22E+07	1.02E+08	1.25E+08	1.44E+08	1.69E+07	Pa
Depth at which τ_{max} occurs	2.6E-05	3.7E-05	4.6E-05	5.3E-05	4.5E-06	m
RPM Calculation for Top Disc (Wheel) Driving						
Lower Disc rotational speed	191	382	573	764		rpm
Upper Disc rotational speed	401	840	1318	1833		rpm

Appendix VIII – Central Film Thickness and Lambda Ratio Calculations

Central Film Thickness Calculation

Lubricant Temperature, T	100	°C
Load, w	50	N
Upper Disc Radius	12.5	mm
Sliding speed	1	m/s
Modulus of elasticity of Upper Disc	215	GPa
Modulus of elasticity of Lower Disc	215	GPa
Poisson ratio of Upper Disc	0.3	
Poisson ratio of Lower Disc	0.3	
Reduced Radius, R'	0.00833	m
Mean surface velocity, u	1.06	m/s
Effective Modulus of Elasticity, E'	2.36E+11	Pa
Dimensionless Load Parameter, W	3.05E-06	
Elipticity Parameter, k	6827.146	
r.m.s roughness, σ*	2.32E-07	m

For line contact, k = ∞

$$H_c = 2.69U^{0.67}G^{0.53}W^{-0.067}\left(1 - 0.61e^{-0.73k}\right)$$

Central Film Thickness, h$_c$ (m) — bar chart for 0%CB, 3%CB, 5%CB, 7%CB, 10%CB, 12%CB

Lambda Ratio, λ — bar chart for 0%CB, 3%CB, 5%CB, 7%CB, 10%CB, 12%CB

100N

Sooty oil	Kinematic Viscosity @40°C (cSt)	Kinematic Viscosity @100°C (cSt)	Density at 15°C (g/cm³)	Density at T°C (g/cm³)	Dynamic viscosity at temperature T & atm pressure, (Pa.s)	Pressure Viscosity-coefficient, αEHL (Pa⁻¹)	Dimensionless Material Parameter, G	Dimensionless Speed Parameter, U	Dimensionless Central Film Thickness, H$_c$	Central Film Thickness, h$_c$ (m)	Lambda Ratio, λ
0%CB	106	14.27	0.866	0.819626	0.0116961	1.43E-08	3386.3445	6.3E-12	1.464E-05	1.22E-07	0.5246408
3%CB	184.17	50.874	0.881	0.833822	0.0424199	7.04E-09	1663.1857	2.28E-11	2.381E-05	1.98E-07	0.8532734
5%CB	239.35	131.86	0.891	0.843287	0.1111958	2.29E-09	540.81242	5.99E-11	2.504E-05	2.09E-07	0.8972471
7%CB	343.44	235	0.901	0.852751	0.2003966	1.16E-09	273.42802	1.08E-10	2.588E-05	2.16E-07	0.9274946
10%CB	570.6	399.82	0.917	0.867895	0.3470016	9.72E-10	229.56684	1.87E-10	3.408E-05	2.84E-07	1.2212991
12%CB	1156.1	888.07	0.928	0.878306	0.7799969	5.82E-10	137.47573	4.2E-10	4.469E-05	3.72E-07	1.6013271

Appendix IX – Technical Specifications of Mercedes-Benz M271 Engine

General	C-class
Brand	**Mercedes-Benz**
Model	**C-class**
Generation	**C-class (W203)**
Engine	**C 180K (141 hp)**
Doors	**4**
Coupe type	**Sedan**
Seats	**5**
Engine and Drive Train	
Position of engine	**Front, longitudinal**
Engine displacement	**1796 cm³**
Torque	**220 Nm/2500 rpm.**
Fuel System	**Multi-point injection**
Turbine	**Mechanical supercharging (Compressor)**
Position of cylinders	**Inline**
Number of cylinders	**4 (Straight)**
Bore x Stroke	**82 x 85 mm.**
Bore/Stroke ratio	**0.96**
Compression ratio	**10.2**
Number of valves per cylinder	**4 (DOHC)**
Maximum power output	**141 hp (105 kW)@5200 rpm.**
Specific output	**78.5 hp/litre**
Maximum speed	**223 km/h**
Acceleration 0 - 100 km/h	**9.7 sec**
Fuel tank volume	**62 l**
Maximum torque	**Transverse stabilizer**
Specific torque	**220 Nm (22.4 kgm)@2500-4200 rpm.**
Fuel Type	**Petrol (Gasoline)**
Drive wheel	**Rear wheel drive**
Number of Gears (manual transmission)	**6**
Fuel Consumption	
Fuel consumption (economy) - urban	**11.4 l/100 km.**
Fuel consumption (economy) - extra urban	**5.9 l/100 km.**
Fuel consumption (economy) - combined	**7.9 l/100 km.**
Carbon dioxide emissions	**190.0 g/km.**